Characterization of active faults by 2D and 3D ground penetrating radar imaging technique and interpretation of the results

Tsend-Ayush Nyambayar

UNIVERSITÉ DE STRASBOURG

ÉCOLE DOCTORALE ***Sciences de la terre et Environnement ED 413***

UMR7063 Institut Terre et Environnement de Strasbourg

THÈSE présentée par :

Tsend-Ayush NYAMBAYAR

Soutenue le: **02 Septembre 2021**

Pour obtenir le grade de: **Docteur de l'Université de Strasbourg.**

Discipline/ Spécialité: Géophysique

Caractérisation des Failles Actives en 2D et 3D par la technique d'Imagerie géoradar et Interprétations des Résultats

THÈSE dirigée par:

Dr. Maksim BANO Directeur de thèse, Université de Strasbourg

Dr. Khuut TSEEDULAM Codirecteur de thèse, Mongolian University of Science and Technology

RAPPORTEURS:

Dr. Motoyuki SATO RAPPORTEUR externe, Tohoku University

Dr. Pascal SAILHAC RAPPORTEUR externe, Université Paris-Saclay

AUTRES MEMBRES DU JURY:

Dr. Antoine SCHLUPP Consultant de thèse, Université de Strasbourg

Dr. Munkhuu ULZIIBAT Consultant de thèse, Institute of Astronomy and Geophysics, MAS

ScD. Ochir GEREL Consultant de thèse, Mongolian University of Science and Technology

БОЛОВСРОЛ, ШИНЖЛЭХ УХААНЫ ЯАМ
ШИНЖЛЭХ УХААН, ТЕХНОЛОГИЙН ИХ СУРГУУЛЬ

СЭДЭВ: ГЕОРАДАРЫН ХОЁР БОЛОН ГУРВАН ХЭМЖЭЭСТ ДҮРСЛЭЛИЙН АРГА ТЕХНИКЭЭР ИДЭВХТЭЙ ХАГАРЛЫН ШИНЖ ЧАНРЫГ ТОДОРХОЙЛЖ ТАЙЛБАРЛАХ НЬ

ЦЭНД-АЮУШИЙН НЯМБАЯР

nyambayar@iag.ac.mn

Геологи-эрдэс судлалын ухааны доктор (PhD)-ын
зэрэг горилсон нэг сэдэвт бүтээл

Эрдэм шинжилгээний ажлын удирдагч:
Доктор (PhD), професор Maksim BANO, University of Strasbourg
Доктор (PhD), професор Х.Цээдулам, ШУТИС, Геологи Уул Уурхайн Сургууль

Эрдэм шинжилгээний ажлын шүүмжлэгч:
Доктор (PhD), професор Motoyuki SATO, Tohoku University
Доктор (PhD), професор Pascal SAILHAC, Paris-Saclay University

Эрдэм шинжилгээний зөвлөх:
Доктор (PhD), професор Antoine SCHLUPP, University of Strasbourg
Доктор (PhD), професор М.Өлзийбат, ШУА, Одон Орон Геофизикийн Хүрээлэн
Доктор (ScD), професор О.Гэрэл, ШУТИС, Геологи Уул Уурхайн Сургууль

Улаанбаатар хот 2021 он

Table of contents

Acknowledgements

I would like to thank all those who helped and supported me from the beginning to the end of this PhD dissertation work and gave me every opportunity to complete my doctoral dissertation. First of all, Dr. Maksim Bano taught me the techniques and development of GPR methodology and research work from the very beginning, and then who chose this PhD research topic, became my supervisor, and to help got a scholarship to study in France. Thank you very much.

I would also like to thank Dr. Tseedulam, the Mongolian supervisor of my thesis work, and Dr. Antoine Schlupp and Dr. Ulziibat Munkhuu, the co-supervisors, for their support during this time.

I would like to thank my thesis examiner and committee members for working as my dissertation reviewer Dr. Pascal SAILHAC, Dr. Motoyuki SATO, giving me valuable advice and helping me defend it.

I would like to express my deep gratitude to the staff of Campus France and all the staff of the French Embassy in Mongolia for providing me with the opportunity to get acquainted with the life and culture of France by conducting my thesis work at the University of Strasbourg. Please.

We would like to thank Dr. Jean-Rémi DUJARDIN and the Geophysical Team of the University of Strasbourg for their supported and helped of geophysical data processing and imaging technique.

I would like to thank Dr. Jérôme Van Der Woerd, Director of the Doctoral School of the University of Strasbourg, for his support and assistance in everything from the beginning to the end of this my thesis work. I would also like to thank all the faculty members of the Mongolian University of Science and Technology for teaching usefull geological lectures.

I would like to express my gratitude to Battogtokh, a friend of the active fault research team, and to the geophysical research team.

I would like to thank director Dr. S.Demberel, Dr. M.Ulziibat, Dr. Ts.Batsaikhan and the staff, researchers of the Institute of Astronomy and Geophysics, the project leader Dr. Odonbaatar and the project team.

Finally, I would like to express my deep gratitude to my wife, children, and mother for always being by my side and gived me hope, encouragement, and energy in the during of all this hard and endless work.

Résumé Etendu

Titre : *Caractérisation des failles actives par la technique d'imagerie géoradar en 2D et 3D et interprétation des résultats*

Tsend-Ayush NYAMBAYAR

La Mongolie est l'un des pays les plus exposés aux tremblements de terre, car ces derniers se produisent non seulement dans la zone de subduction des plaques tectoniques mais aussi entre les microplaques au milieu du continent. La Mongolie fait partie géologiquement de la zone orogénique de l'Asie centrale, et ses montagnes sont sismiquement actives en raison de leur faible taux de glissement. Sur les 44 tremblements de terre majeurs qui se sont produits en Asie depuis le début du siècle dernier, deux se sont produits en Mongolie. Les tremblements de terre de Bulnai (8.4Mw, 1905) et de Gobi-Altai (8.1Mw, 1957) étaient classés en neuvième et 12ème place, respectivement (voir tableau 1). L'urbanisation en Mongolie est à la hausse, en particulier dans la capitale, Oulan-Bator, qui compte environ 1,5 million d'habitants. Oulan-Bator est entouré de plusieurs failles actives, et l'augmentation cumulée du nombre des séismes depuis 2005 est devenue un réel problème (Figure 1).

Tableau 1. *Classement de la magnitude du moment sismique de 1900 à 2018. Tableau créé à partir des données de l'USGS sur les séismes de magnitude supérieure ou égale à 8,0 de 1900 à 2018.*

Rank	Number of quakes	Location name	Magnitude
1.	1	Chile	9.5
2.	1	Prince William Sound, Alaska, USA	9.2
3.	1	Indian Ocean, off west coast of northern Sumatra, Indonesia	9.1
4.	2	Tohoku, off east coast of Honshu, Japan; Kamchatka, Russia, USSR	9.0
5.	2	Ecuador-Colombia; Maule, Chile	8.8
6.	1	Rat Islands, Alaska, USA	8.7
7.	4	Assam-Tibet, China; Northern Sumatra	8.6
8.	5	Kamchatka, Russia; Banda Sea, Dutch East Indies (Indonesia); Kuril Islands, Russia; Southern Sumatra	8.5
9.	4	Bulnai, Mongolia; Sanriku, Japan; Tonga; Near coast of southern Peru	8.4
10.	9	Mindanao, Philippines; Kuril Islands, Russia; South of Sumbawa, Indonesia; Hokkaido, Japan; Sea of Okhotsk	8.3
11.	19	Panay, Philippines; Kuril Islands, Russia; Kamchatka, USSR; Irian Jaya region, Indonesia	8.2
12.	20	Gobi-Altai, Mongolia; Ryukyu Islands, Japan; Bihar, India; Nankaido, Japan; Hokkaido, Japan	8.1
13.	26	Taiwan region; Afghanistan; Pakistan; Mindanao, Philippines; New Guinea; Sea of Okhotsk; Kurile Islands; Loyalty Islands	8.0

L’objectif de cette thèse de doctorat est de déterminer et d'expliquer les caractéristiques et les paramètres des failles actives à l'aide de technologies modernes, telles que les techniques d'imagerie 2D et 3D de la méthode géoradar (ground penetrating radar ; GPR). Dans le cadre de ce travail de recherche doctorale les activités suivantes sont prévues :

1. Réaliser des mesures et des études avec plus de 2 antennes de fréquences différentes sur les principaux types de failles actives et faire des corrélations des images qui en résultent.

2. Développer la méthodologie, les principes et la conception de l'acquisition afin d’identifier les structures du sous-sol et d’étudier les principaux types de failles actives.

3. Faire des interprétations paléo-sismologiques et géologiques structurales de la faille de Songino, qui est la principale zone d'étude, en interprétant les résultats de mesure et d'imagerie détaillés de la méthode GPR.

Les méthodes paléo-sismologiques traditionnelles ont été utilisées pour étudier la géomorphologie des escarpements sur les sédiments fracturés par les séismes, ainsi que les mouvements des sédiments à traverser les traces de failles en surface ; l'objectif était d'ouvrir un paléo- tranchées à une profondeur de 1 à 3 mètres, de le comparer avec les résultats d'études GPR et de prélever des échantillons pour déterminer l'âge du dernier séisme. La recherche paléo-sismologique utilisant les mesures GPR permet une collecte plus rapide et plus précise de zones d'informations plus détaillées, plus profondes et plus larges que les études paléo-sismologiques traditionnelles.

Cette étude fait partie intégrante de l'évaluation de l'aléa sismique à Oulan-Bator. L'évaluation des risques sismiques est très importante pour le développement futur de la capitale d'Oulan-Bator qui est le seul centre économique, commercial et de services et dans laquelle vivent plus de 50% de la population de la Mongolie.

Déterminer la nature de la faille de Songino est essentiel pour comprendre les interactions entre les failles de Khustai et d’Emeelt, qui ont le plus grand impact sismique à Oulan-Bator. En outre, cela devrait également aider à expliquer les interactions et les modèles entre les différentes failles actives autour d'Oulan-Bator.

Le marqueur paléo-sismologique est toujours situé près de la surface, dans les premiers mètres du sous-sol. Au cours des deux dernières décennies, la méthode GPR est devenu de plus en plus populaire dans les études paléo-sismologiques en raison de ses propriétés non destructives, de sa rapidité de mis en œuvre et de son faible coût, permettant des mesures

précises sur de grandes surfaces. Le GPR est une méthode géophysique idéale afin d'étudier les sédiments quaternaires et les structures du sous-sol urbains, ainsi que pour identifier les zones appropriées d'excavations des tranchées et pour l'interpolation des données entre le paléo chenaux fluviaux.

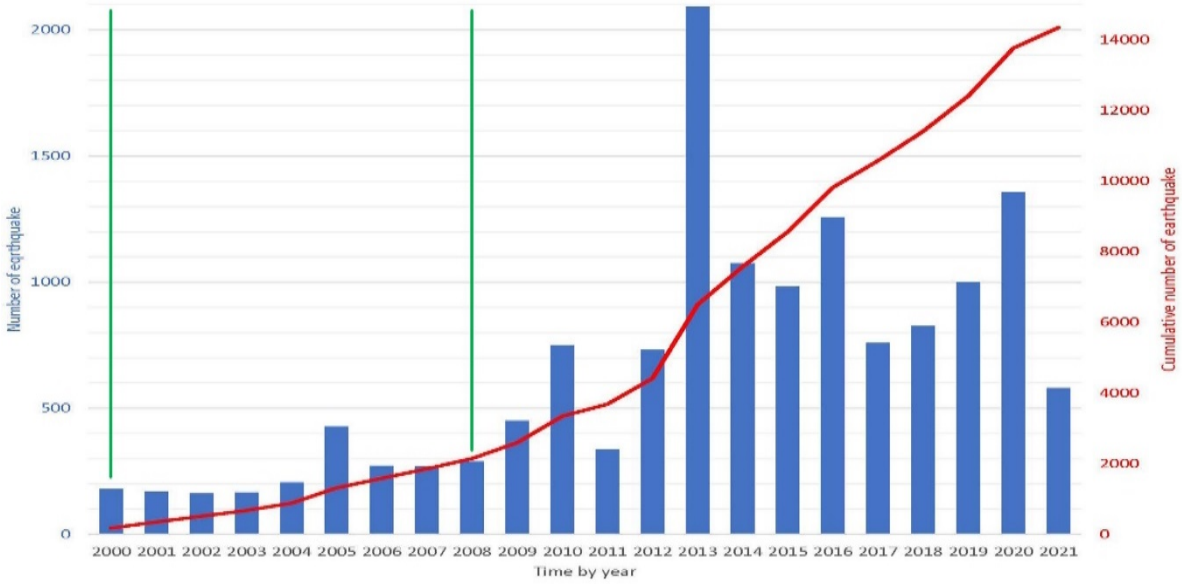

***Figure 1**. Nombre de séismes cumulé entre 2000 et 2021 (superficie de 140x140 km). La ligne verte est l'heure de début de l'installation de la nouvelle station, en 2000 l'installation du « tableau CTBT Songino » et en 2008 l'installation de « UB-mobile », MNDC data.*

Avant 2010, il n'y avait presque pas d'exemples d'études des failles actives par géoradar en Mongolie, le seul exemple-était effectué sur la faille active de Deren, Dundgovi dans laquelle un seul profil géoradar en mode CMP (Common Mid Point) à CO (Common Offset) a été mesuré en utilisant le système RAMAC avec une antenne de 100 MHz. Les résultats de l'étude géoradar ont été comparés avec les résultats d'une étude de paléo-tranchée.

Les failles de Khustai et d'Emeelt ont été étudiées et interprétées par des scientifiques de plusieurs pays, tandis que la faille Songino a été découverte en 2012 par une équipe de paléo-sismologie de l'Université de Strasbourg, France, en collaboration avec l'Institut d'astronomie et de géophysique de l'Académie des sciences, Mongolie. Avant cette étude, il n'y avait pas d'autres études sur la faille de Songino.

La thèse de doctorat intitulé "**Caractérisation des failles actives par la technique d'imagerie géoradar en 2D et 3D et interprétation des résultats**" se compose d'une introduction, de cinq chapitres, d'une bibliographie, il y a au total de 199 pages, dont 110 figures et 18 tableaux.

Le **premier chapitre**, qui inclue la méthode GPR et le traitement des données, présente un aperçu de la théorie, de la méthodologie et des applications de la méthode géoradar. Il détaille également la méthodologie des mesures géoradar 2D et 3D sur le terrain, le traitement de données, les concepts de l'imagerie géoradar, les principes et l'interprétation des résultats.

De longs enregistrements paléo-sismiques peuvent donc résider près de la surface dans les premiers mètres du sol (McCalpin, 2009). Au cours de la dernière décennie, la méthode GPR est devenu de plus en plus populaire pour les études paléo-sismologiques en raison de son caractère non destructif, de sa rapidité de mise en œuvre et de son faible coût, qui lui permettent d'être appliqué de manière dense sur de vastes zones. La méthode GPR se caractérise par le fait qu'elle collecte de grandes quantités de données plus rapidement que les autres méthodes géophysiques. La méthode GPR a été particulièrement adaptée afin de localiser les failles actives dans les formations quaternaires et les zones urbaines (Smith & Jol, 1995 ; Cai, et al., 1996 ; Audru, et al., 2001 ; Demanet, et al., 2001 ; Gross R. , et al., 2002), d'identifier des sites potentiels pour de futures excavations (Salvi, et al., 2003 ; Liberty, et al., 2003 ; Jewell & Bristow, 2004 ; Malik J. , et al., 2010) et pour interpoler les données entre les tranchées (Ferry, et al., 2004 ; Slater & Niemi, 2003). Dans de nombreux cas, elle est combinée à d'autres méthodes d'imagerie, notamment la électrotomographie (Demanet, et al., 2001 ; Lehmann, et al., 2001 ; Vanneste, et al., 2008). En termes de profondeur, de précision et de rapidité de mise en œuvre, la méthode GPR est la mieux adaptée pour déterminer le niveau cible aux profondeurs des premières dizaines de mètres au-dessus du sol. L'objectif ici est d'utiliser le GPR le long des failles actives pour détecter les déplacements accumulés au cours du temps par des marqueurs morphologiques enfouis.

La méthodologie de cette recherche est basée sur la combinaison de nombreuses technologies de pointe et suit la séquence suivante :

1. Télédétection et analyse d'images satellitaires.

2. Relevé géologique de la zone : traces de failles, escarpement, déplacement, points de contrôle, conditions de relevé GPR.

3. Levé GPR ; conception du levé GPR 2D et 3D, acquisitions de données, mesures de la topographie de la surface du sol.

4. Ouverture des paléo-tranchées, étude paléo-sismologique et échantillonnage afin de déterminer l'âge des failles.

5. Faire une interprétation complète des résultats de toutes les mesures, de la géologie structurale et de la géodynamique.

La méthodologie principale de cette recherche est la technique d'imagerie géoradar 2D et 3D, mais d'autres méthodes supplémentaires (Télédétection, DGPS) sont utilisées afin d'améliorer la qualité et l'efficacité de ce travail de recherche. La méthodologie de prospection géoradar est avant tout une technique qui cherche à expliquer la nature, l'origine, la cause et la régularité des failles.

Afin de vérifier la fiabilité et la précision de l'imagerie géoradar lors de la réalisation de mesures, 3 à 5 profils parallèles ont été réalisés à chaque point de ciblage à une distance de 1 à 2 mètres les uns des autres. Par conséquent, la qualité de l'imagerie du résultat final est élevée et il n'y a aucun doute sur la structure de l'image qui en résulte.

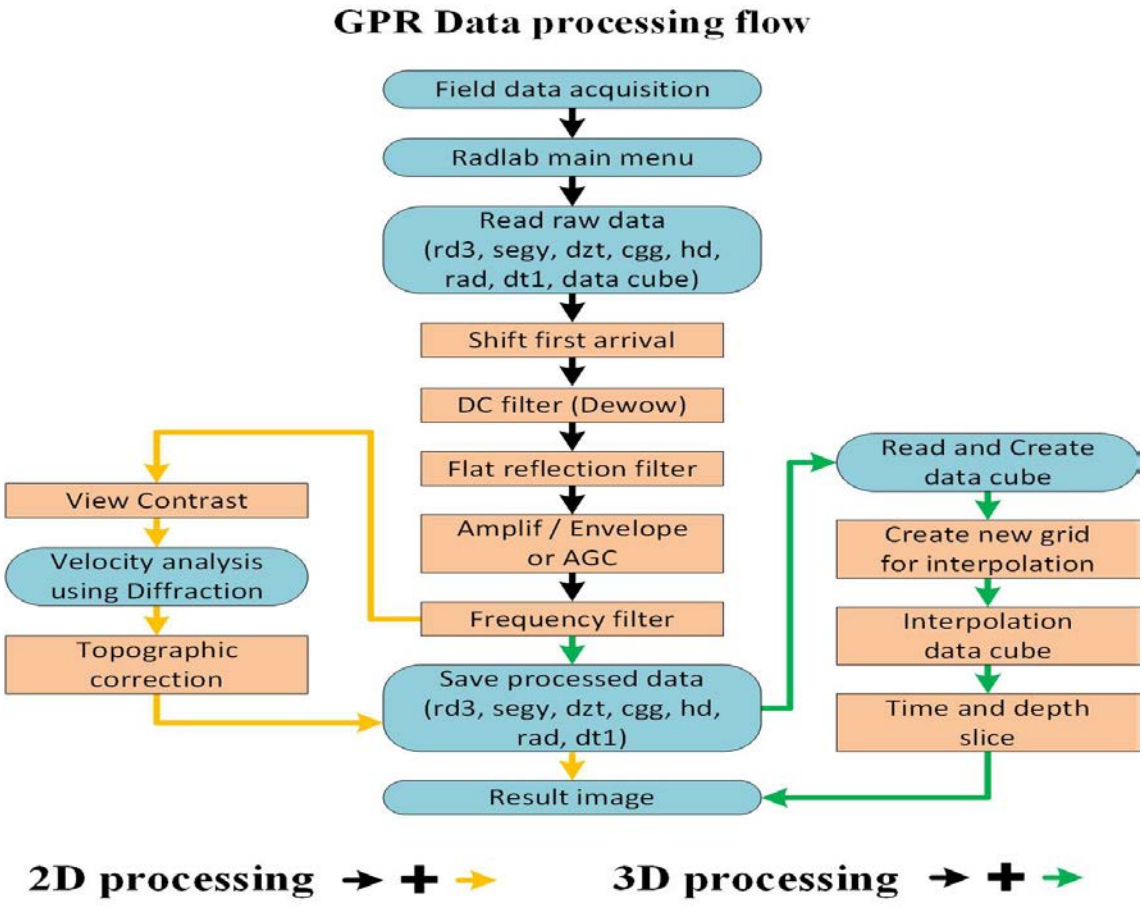

***Figure 2**. Schéma de traitement des données GPR. La couleur orange clair correspond à l'étape de filtrage et de traitement, tant disque le bleu clair correspond à l'étape d'entrée, de sortie et d'analyse des données*

Les données brutes géoradar nous les avons traités à l'aide de RadLab, un logiciel écrit en MATLAB. Le logiciel a été développé par l'Ecole et Observatoire des Sciences de la Terre

(EOST) d’Université de Strasbourg (EOST) en France. Nous avons également travaillé ensemble pour améliorer certains de ces modules logiciels (Figure 2).

En interprétant les résultats des images finales géoradar, nous avons pu déterminer les limites des différentes couches en les comparants à la géologie structurale de la proche surface du sous-sol. Nous avons analysé le décalage des réflexions des ondes radar afin de déterminer les déplacements dus aux failles actives.

Le **deuxième chapitre**, intitulé Applications et développement de la technique d'imagerie GPR aux structures des failles actives. Cette partie discute efficacité de la technique d'imagerie géoradar dans les études paléo-sismologiques, y compris l'interprétation des résultats de paléo-tranchés dans le cas de tous les types de failles actives. La méthodologie de l'imagerie 3D est également expliquée dans l'exemple d’étude de la faille d'Emeelt.

Au cours du XXe siècle, les connaissances sur les phénomènes sismiques ont beaucoup évolué grâce au développement de la sismologue, de la géodésie et de la paléo-sismologue. Alors que la sismologie et la géodésie fonctionnent sur des calendriers à court terme par rapport au temps de récurrence des séismes, la paléo-sismologie ouvre un champ d'observation couvrant plusieurs cycles de tremblements de terre. Les observations de répétitions de forts séismes en un ou plusieurs sites le long d'une faille ont permis d'établir des modèles conceptuels de successions de ruptures sismiques. Alors que certaines études décrivent les ruptures de surface avec des longueurs et des glissements différents d'un séisme à l'autre (Daëron, et al., 2007 ; Weldon, et al., 2004), d'autres décrivent des comportements répétitifs avec une distribution de glissement plus uniforme (Sieh K., 1981), (Schwartz & Coppersmith, 1984 ; Rubin & Sieh, 1997 ; Tapponnier, et al., 2001a).

Le gouvernement de la Mongolie a approuvé le « Programme national de réduction des risques de catastrophe sismique » en 2009, et conformément à ce plan, le ministère de la Construction et du Développement urbain a mis en place 12 centres provinciaux d'ingénierie-géologie, d'hydrogéologie, de cartographie sismique des microrégions et de bases de données sismologiques.

L'équipe de recherche de l'Institut d'astronomie et de géophysique a mené ce programme en 2012-2017. Dans le cadre de cette étude, l'équipe de recherche des failles actives a mené non seulement une étude GPR détaillée des failles autour d'Oulan-Bator et de la partie centrale de la Mongolie, mais aussi des études géologiques et paléo-sismologiques afin de combiner et comparer tous les résultats (Figure 3).

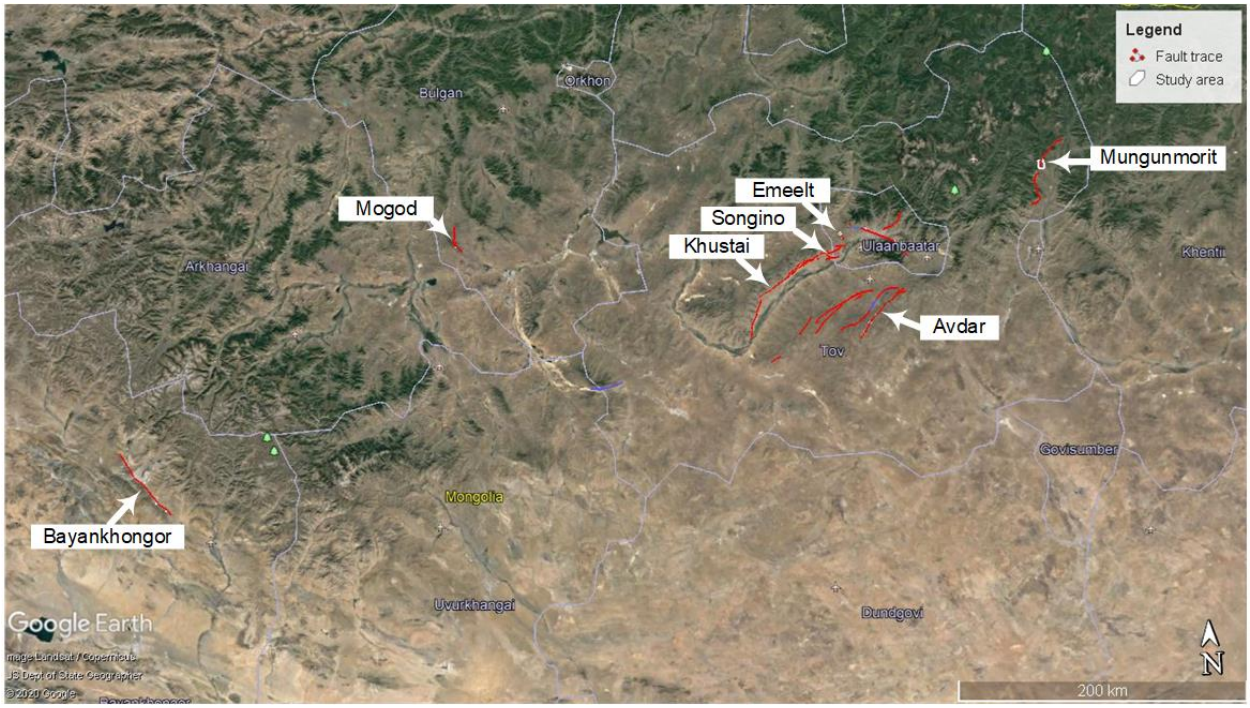

Figure 3. *Carte de localisation des failles actives à l'étude autour d'Oulan-Bator et de la région centrale de la Mongolie.*

La structure inverse de la partie sud de la faille de Mogod est nord-sud, tandis que la structure qui résulte de l'imagerie radar (Figure 4) est clairement dans la direction opposée. Au sommet de l'escarpement, il y a une démarcation visible de la faille du nord-est au sud-ouest. Les stratifications visibles à l'intérieur de la structure chevauchée, montrent clairement la direction du mouvement dans cette section. La figure 4 montre une interprétation des images radar obtenues avec les antennes 250 MHz et 500 MHz du profil-1, les deux images sont cohérentes.

L'étude de la tranchée paléo-sismologique a été menée en collaboration avec des scientifiques français et russes et comprend des photos de paroi de tranchée prises par les scientifiques français Laurent Bollinger (CEA) et Yann Klinger (IPGP). Diagraphie manuelle sur la paroi ouest de la tranchée paléo-sismologique montre clairement la couche jaune qui s'est disloquée et chevauchée (Figure 5).

Les résultats de la méthode des tranches de temps de profondeur du traitement, de l'imagerie et de l'analyse GPR pseudo-3D montrent que la méthode est plus efficace dans les études de failles actives ou les études paléo-sismologiques. Il est clairement montré que le déplacement horizontal de la faille active et la localisation de la trace de faille sont prédominants Figure 6. Les résultats des études et d'analyses 2D et 3D GPR, menées depuis 2010 sur les

failles actives de la région centrale de la Mongolie et autour de la capitale Oulan-Bator, ont été présentés. Nous avons imagé, cartographié, analysé et interprété les résultats des mesures géoradar pour tous les types de failles actives.

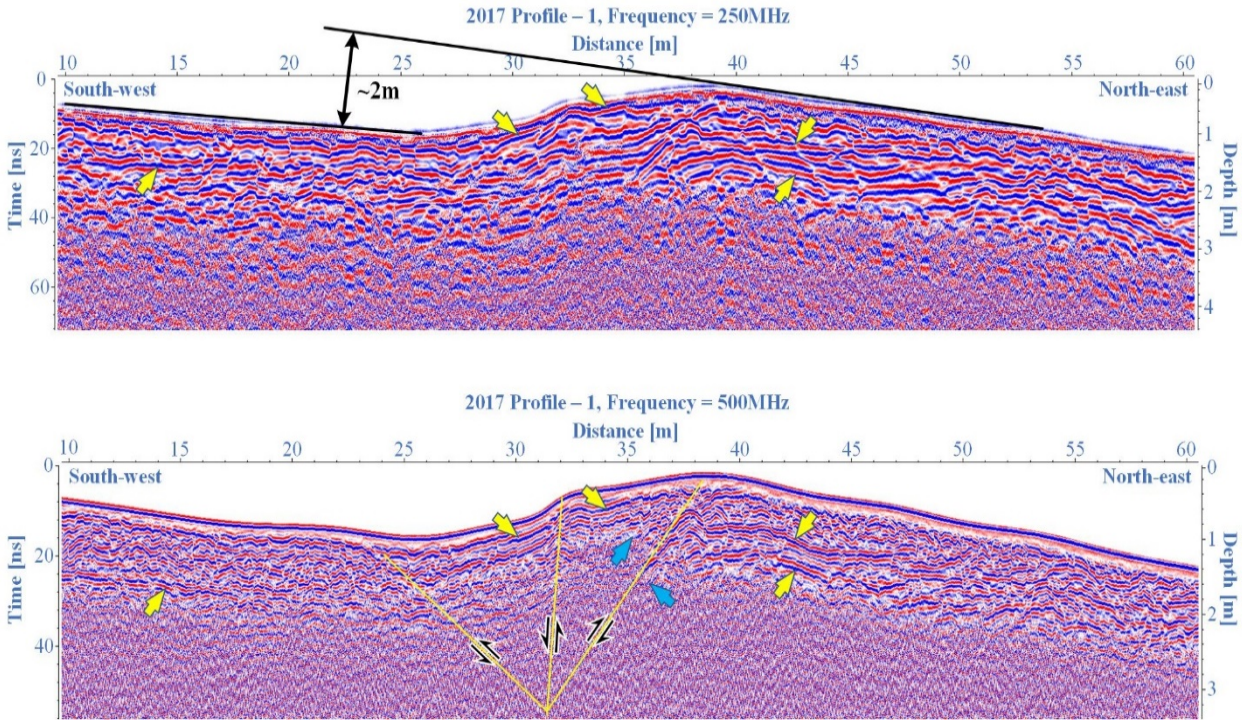

***Figure 4**. Résultat de l'interprétation de l'mage radar du profil-1 (acquis en juin 2017) de la zone 2 (structure chevauchée) de la faille de Mogod. La première figure est obtenue avec l'antenne de 250 MHz. La deuxième figure est obtenue avec l'antenne de 500 MHz. Les flèches jaunes montrent les réflexions des couches, les flèches bleues correspondent au même calque, les lignes orange correspondent aux couches réfléchissantes, les flèches noires indiquent la direction du mouvement.*

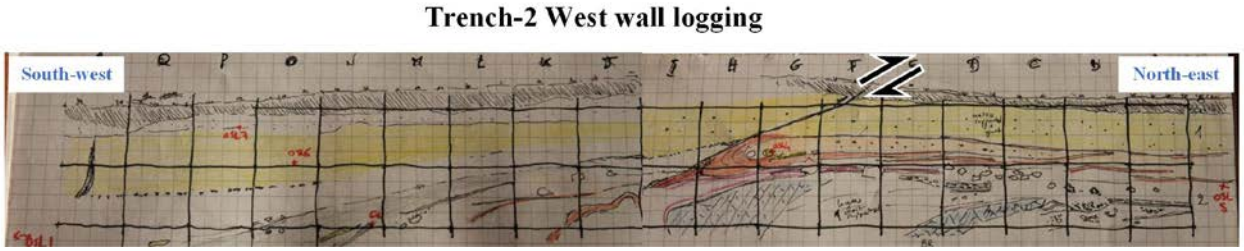

***Figure 5**. Diagraphie de la paroi ouest de la tranchée paléo-sismique 2. La couche indiquée en jaune a été fracturée et chevauchée. (D'après Laurent Bollinger (CEA), Yann Klinger (IPGP) 2017).*

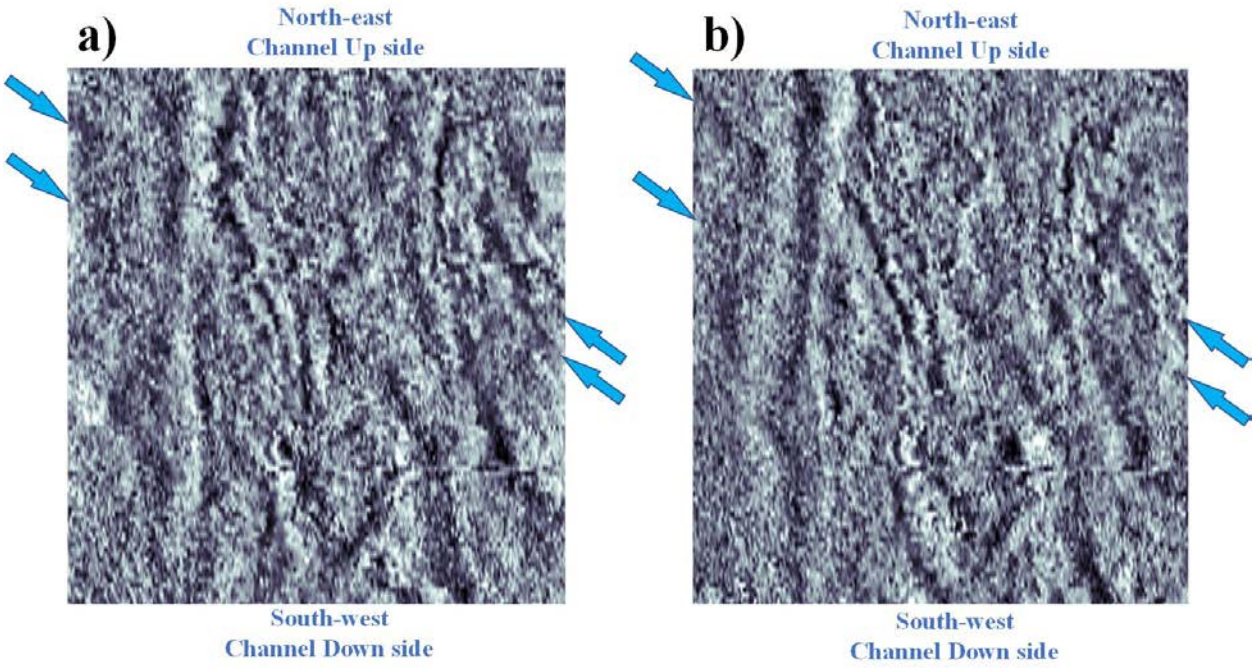

***Figure 6**. Résultat des 'depth slices' du cube de données pseudo-3D C1 (acquis en juin 2010) obtenu avec une antenne blindée de 500 MHz dans le paléo chenal fluvial de la faille active d'Emeelt. a) « Depth slice » à 0,48 m sous la surface du sol, b) « Depth slice » à0,53 m sous la surface du sol, flèches bleues indiquant les traces de faille.*

Le **troisième chapitre**, intitulé la technique de caractérisation paléo-sismologique de la faille active de Songino, Oulan-Bator, Mongolie, basée sur la méthode géoradar. En utilisant cette technique, l'étude présentée ici fournit des informations détaillées sur les structures des failles actives et explique les résultats de l'imagerie géoradar.

L'activité sismique observée aux alentours d'Oulan-Bator (UB), capitale de la Mongolie, est relativement faible par rapport à l'activité observée dans l'ouest de la Mongolie. Néanmoins, depuis 2005, l'activité sismique autour de UB a augmenté (Dugarmaa, et al., 2006), et s'organise à l'ouest de UB selon deux directions perpendiculaires : en 2009 année découverte de la faille Emeelt (environ 25 km de long) située à environ 10 km à l'ouest de UB (Schlupp, et al., 2012 ; Munkhsaikhan, 2016) et de la faille Hustai (le segment principal a une longueur d'environ 80 km) avec son plus proche segment à environ 15 km à l'ouest de UB (Ferry, et al., 2010 ; Ferry, et al. 2012).

La faille de Songino (20 km de long, localisée à 20 km à l'ouest d'UB) est située entre les failles d'Emeelt et de Hustai. La longueur et la morphologie de ces failles indiquent qu'elles

peuvent produire des séismes de magnitude 6,5 à 7,5 (Schlupp, et al., 2012 ; Dujardin J.-R., 2014 ; Munkhsaikhan, 2016).

L'équipe mixte franco-mongole de recherche sur les failles actives a d'abord réalisé des levés GPR sur les failles actives d'Emeelt et de Khustai en 2010, puis en 2011-2012 sur les failles acfives d'Avdar, Sharkhai, Gunj et Mogod. Les résultats de ces études ont été intégrés dans plusieurs thèses de maîtrise et de doctorat (Dujardin J.-R. , 2014), (Abeer, 2015), (Munkhsaikhan, 2016).

Après la reconnaissance géomorphologique de la faille de Songino en 2012, nous avons décidé d'utiliser des mesures GPR 2D pour étudier les dépôts souterrains potentiellement affectés par la faille sur une zone plus large. Les résultats devraient nous permettre de localiser avec précision les futures tranchées.

Les trois premières mesures de profils Ground Penetrating Radar sur la faille de Songino ont été collectées avec des antennes blindées 250 MHz et RTA non blindées 50 MHz en septembre 2012. Par la suite, en 2013, 2015 et 2017, plusieurs levés GPR 2D et 3D ont été effectués sur la faille Songino (voir figure 7), et en 2013, une étude de tranchée a été réalisée.

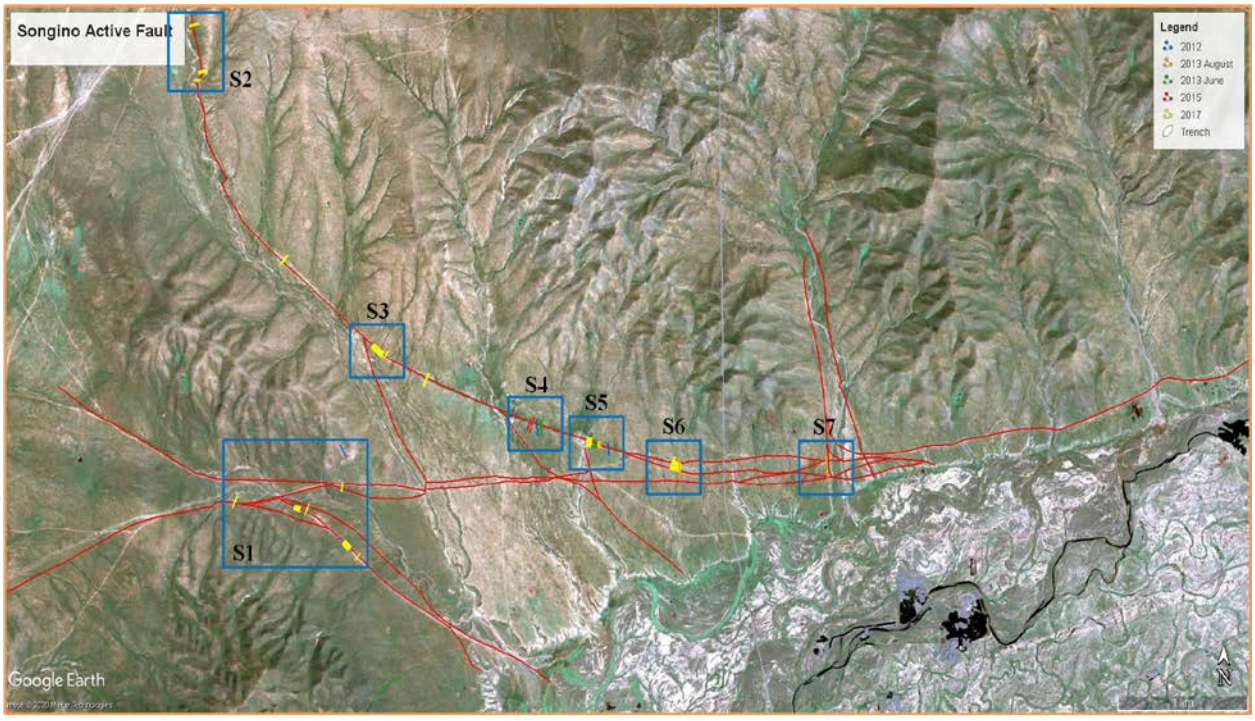

***Figure7**. Carte de localisation des zones d'étude de la faille de Songino. Les lignes rouges montrent les traces de la faille sur la rupture en surface de la faille de Songino, les carrés bleus montrent les zones étudiées par géoradar en 2012 et 2017*

Nous avons effectué des mesures GPR supplémentaires (Figure 8). Le 14 juin 2013, nous avons acquis le profil-2 et le 16 juin 2013, le même profil -2 (7 m de plus que celui du 14 juin), les profils sont quasiment identiques. De plus, deux longs et trois courts profils ont été réalisés en parallèle avec la trace de la faille dans la zone S5 (lignes blues figure 8a), et les résultats sont très importants pour comprendre les déplacements et les mouvements de faille.

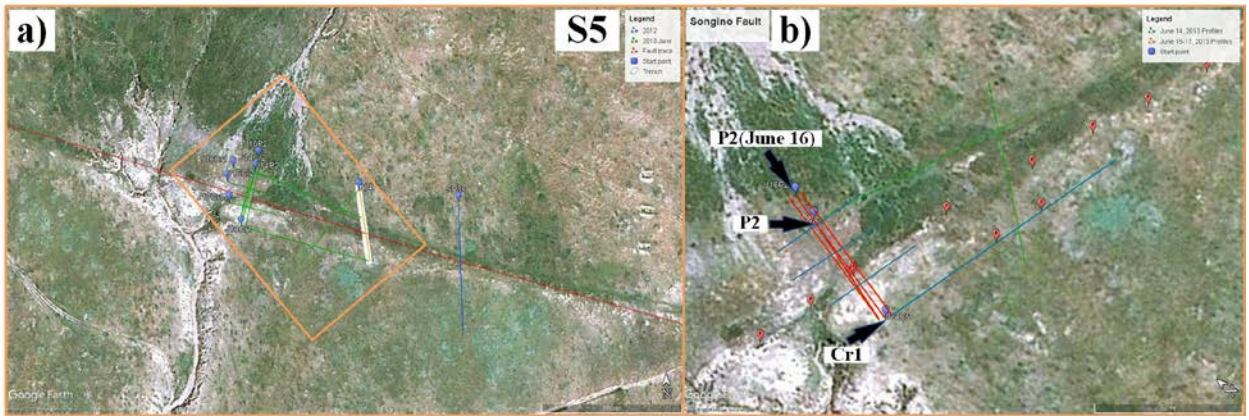

Figure 8*. Carte de localisation des profils GPR acquis en juin 2013. a) La zone d'étude GPR S5 (voir localisation à la figure 7). b) Une image agrandie de la zone des profils (carré orange) ; les lignes rouges représentent les profils GPR de juin 2012, la ligne bleue est le profil croisé Cr1, le symbole bleu indique la position initiale de la mesure, les symboles rouges (F) indiquent l'intersection des traces de faille en surface avec le profil.*

La figure 9a montre le profil-2 du 14 juin 2013, on remarque un événement radar de très forte amplitude qui est décalé par la faille. La zone 5 montre la structure d'érosion du sol sous l'escarpement de la faille, mais la localisation du plan de faille et l'angle de pendage du plan de faille ne sont pas visibles. Le résultat de l'image radar obtenu avec l'antenne blindée de 250 MHz, montre qu'il est possible d'analyser la direction du mouvement de la faille indiquant qu'il s'agit d'une faille normale sous l'escarpement. Cependant, sur la figure 9b la direction du pendage de la faille et la direction du mouvement sont similaires à celles de l'image du profil GPR de la Figure 9a.

La localisation du profil P1 de la zone 3D6 est montrée sur la Figure 10. L'image radar de ce profil (P1) est obtenu avec l'antenne blindée de 250MHz, montre des microplis formés sous le sol et sont indiqués par les flèches noires (Figure 11). De plus, les plis et les caractéristiques de mouvement des sédiments du sol sont clairement observés (marqués par des flèches noires et lignes blanches sur la Figure 11). La hauteur de l'escarpement dans cette zone est d'environ 2,1 mètres. L'angle créé par la hauteur de la surface pliée est de 5,7º

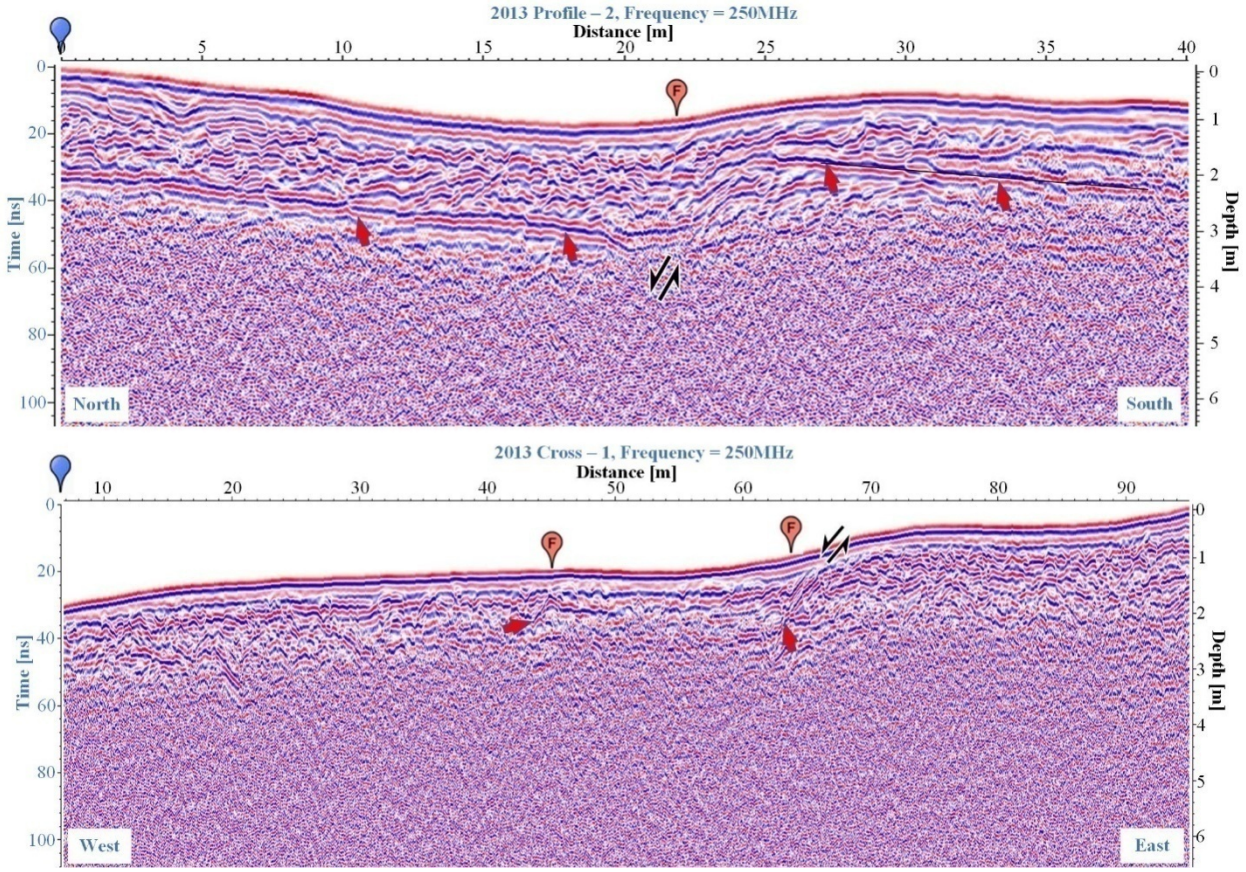

***Figure 9**. Le résultat des images GPR du profil P2 et du profil perpendiculaire Cr1 (acquis le 14 juin 2013) obtenu avec une antenne 250 MHz dans la zone d'étude principale de la faille de Songino S5 (voir localisation sur la Figure 7). a) Résultat de l'image GPR du profil P2, il montre une structure normale claire et un effet d'extension régional. b) Résultat de l'image GPR du profil perpendiculaire Cr1, la flèche rouge montre une zone très réflective. Les flèches noires indiquent la direction du mouvement des deux côtés.*

Une étude GPR détaillée de la faille Songino a révélé de nombreuses informations sur la structure, la direction du mouvement et l'accumulation de sédiments alluviaux des perturbations du sol causées par la faille. Sur la base de toutes ces données, une interprétation unifiée suggère que le mouvement principal de la faille Songino est une structure de décrochement latéral gauche du sud-est au nord-ouest. L'effet de compression sur la partie ouest, ou la structure sédimentaire d'escarpement formée à la surface du sol, est l'effet de l'excavation à un angle d'environ 40° par rapport à la direction de mouvement de la faille. Le sédiment avec un escarpement de structure normale, à l'est, est l'effet de la tension de la structure qui se courbe dans le sens du mouvement de la faille de Songino et forme un angle d'environ 21°.

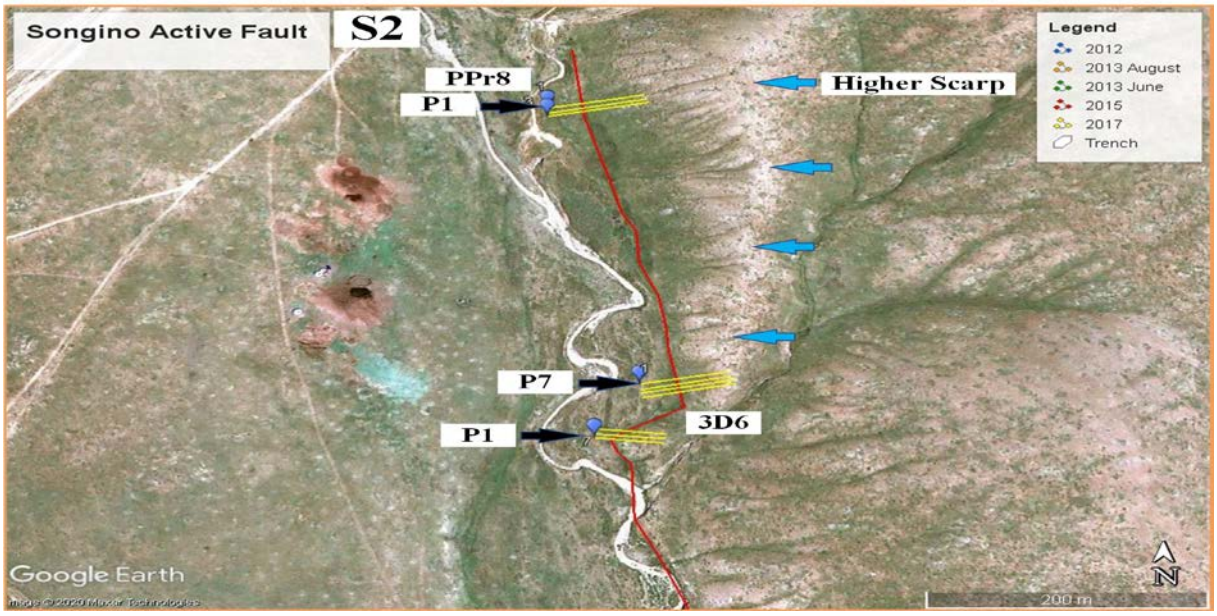

***Figure 10**. Carte de localisation des profils GPR mesurés en aout 2017, la zone d'étude GPR S2 est montrée sur la Figure 7. Les lignes jaune indiquent les profils GPR perpendiculaire à la faille, la ligne rouge est la trace de la faille, les symboles bleus indiquent le début des profils. Les flèches bleues pointent le chevauchement de l'escarpement de la faille.*

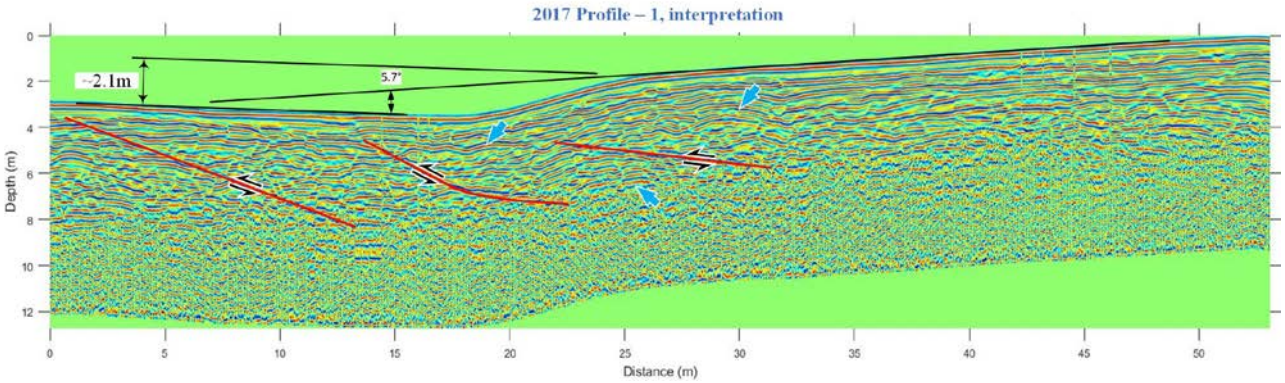

***Figure 11.** Le résultat de l'image GPR du profile P1 de la zone 3D6 (acquis en 2017, voir aussi Figure 10) obtenu avec l'antenne de 250 MHz (voir la localisation sur la Figure 7). Interprétation de l'image radar du profil P1. L'image radar montre clairement une structure chevauchée (lignes rouges), les flèches noires montrent la direction de la déformation. La hauteur de l'escarpement est, de 2.1 m.*

Le **quatrième chapitre** est intitulé '*Le contexte géologique de la caractérisation paléo-sismologique de la faille active de Songino, Oulan-Bator, Mongolie'*. Le but est non seulement d'étudier les causes des structures identifiées et l'environnement géologique sur la faille de

Songino, mais aussi d'expliquer les interactions avec les failles de Khustai et d'Emeelt. Les résultats de datation sur les failles de Khustai, Emeelt et Songino sont également décrits.

La géologie régionale de la Mongolie est couramment abordée en utilisant une analyse tectono-stratigraphique des terrains pour aider à interpréter sa structure et son histoire. En ce sens, un terrain est défini comme une entité ou un fragment géologique limité par une faille qui se caractérise par une taille régionale et une histoire géologique distinctive qui diffère sensiblement de celle des blocs crustaux voisins (Tomurtogoo & al, 2002).

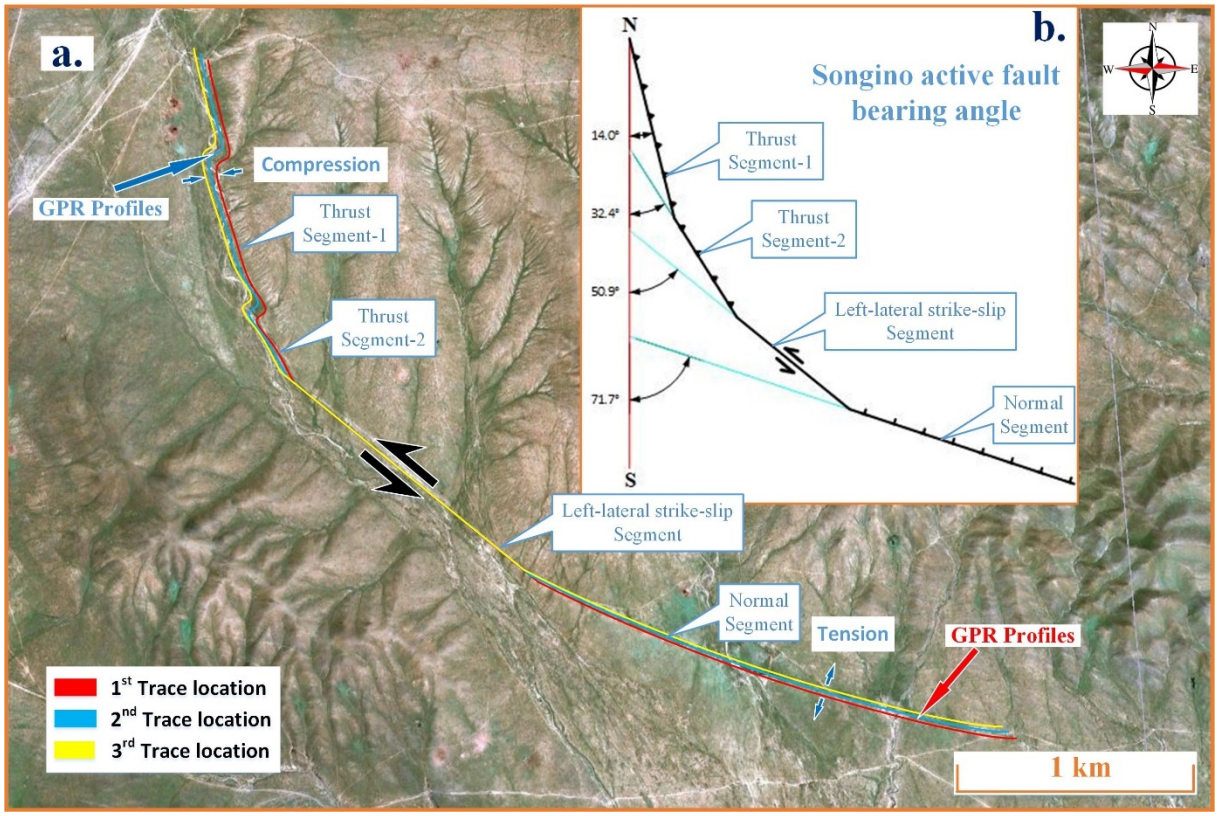

***Figure 12**. La faille active de Songino, a) la ligne rouge indique la première trace de la faille, la ligne bleu est la 2nde trace et la ligne jaune la 3eme trace après le 2eme événement. b) Quatre différents directions de la trace de la faille avec les angles correspondants.*

La principale caractéristique distinctive de la carte satellitaire de la faille de Songino est qu'elle se compose de trois principaux types de sous-structures, qui peuvent être en compression, en extension et en décrochement (strike-slip), voir Figure 12. À l'extrême ouest, à la pointe avec l'effet de compression, il y a trois sous-sections avec une structure en escalier, qui sont clairement visibles avec une zone de cisaillement (strike-slip) au milieu de deux sous-sections qui ressemble également à un effet de pliage horizontal.

De plus, les trois sous-sections de la hiérarchie montrent des azimuts différents, se déplaçant du sud au sud-est. L'escarpement crée dans la zone de compression mesure plus de 22 m de hauteur à l'extrémité nord et disparaît à mesure qu'il avance. L'autre type de structure (au milieu) est à décrochement latéral dextre qui se déplace dans une direction horizontale. On peut remarquer que ce décrochement latéral se déplace en ligne presque droite. Il n'y a presque pas d'escarpement de faille dans cette zone de transition horizontale du décrochement latéral dextre, et il n'est pas possible d'identifier la zone de faille et les traces à la surface du sol. L'escarpement de cette structure normale a également une structure d'escarpement progressivement croissante depuis la structure de décrochement jusqu'à l'extrémité est. La figure 12a montre le déplacement de trois séismes sur la faille de Songino, et l'emplacement de la première trace de la fissure est indiqué en rouge. Les couleurs bleu et jaune montrent comment les traces de la faille changent et se déplacent au cours des deux prochains séismes. La flèche noire indique la direction générale de la faille de Songino, et les trois courbes de couleurs différentes et la distance entre elles indiquent la quantité de mouvement dans quelle partie de la faille Songino. La figure 12b montre comment la direction d'allongement de la faille de Songino change et de combien de degrés. La Figure 12 et montre aussi quels effets de déformation se produisent et dans quelle partie.

Il y a une différence d'environ 20,5º entre les structures normales et décrochantes, et d'environ 37,1º entre les structures décrochantes et de compression, et un total d'environ 58º de différence entre les structures normales et de compression.

Enfin, la correction entre la carte géologique et les traces d'allongement de la ligne de faille détermine la direction du mouvement de la faille Songino et des sédiments environnants, la cause des dommages accumulés et leur relation.

Le **cinquième chapitre** présente la discussion générale et la conclusion. La discussion s'est concentrée sur l'interprétation et les hypothèses des résultats de l'étude de la faille de Songino et termine par une conclusion générale de la dissertation.

L'objectif de ce travail de thèse, et plus largement du cadre d'un projet de micro-zonage et de cartographie sismique de la capitale Oulan-Bator, était de développer une nouvelle approche paléo-sismologique basée sur l'imagerie GPR à haute résolution, qui permettrait de trouver les traces d'un plus grand nombre de forts séismes passés. Qu'il a été possible de faire une structure peu profonde à 2-3 mètres et mais limité pour la structure profonde à 5-30 mètres jusqu'à présent avec les méthodes paléo-sismologiques existantes.

Accomplissement avec succès des travaux prévus dans le cadre de l'objectif du travail d'étude de thèse de doctorat "Caractérisation des failles actives par technique d'imagerie radar à pénétration de sol 2D et 3D et interprétation des résultats". De plus, trois antennes de fréquences différentes ont été utilisées pour les principaux types de failles actives conformément à la tâche de recherche planifiée dès le départ. Et des mesures ont été effectuées afin de déterminer la corrélation des résultats d'imagerie. Les principes de mesure géoradar ont été développés et testés sur plusieurs types de failles actives. Nous avons pu identifier et imager différents types de structures et les résultats obtenus sont pertinents.

Des informations détaillées sur les mesures GPR et l'imagerie de la faille de Songino, la principale zone de recherche, ont été compilées et interprétées, et des explications paléo-sismologique et géologie structure de la faille ont été faites, et les réponses suivantes ont été répondues. Ceux-ci inclus :

La faille Songino n'est pas une faille auto-activant et se déplace uniquement sous l'influence de la faille de Khustai, elle est contrôlée par les failles actives de Khustai et d’Emeelt.

L'environnement géodynamique de la faille de Songino est dû au déplacement horizontal et au mouvement de rotation du bloc frontal de la faille de Khustai vers la faille d'Emeelt.

La structure arrondie de la faille de Songino crée trois types de structures différente lors du mouvement de décrochement horizontal.

Le mouvement principal de la faille de Songino est un décrochement latéral dextre, et son chevauchement (compression) et sa structure normale (extension) des deux côtés sont dues à la structure en courbure de cette faille.

Puisque la faille de Songino est une structure directement liée à la faille active de Khustai son mouvement de retrait est lié au mouvement de faille de Khustai.

Il est évident que le mouvement de la faille de Songino est un décrochement latéral dextre, mais la structure de la microplaque dans la région ne bouge pas d'elle-même et la plaque frontale de Khustai se déplace vers l’est, comprimant ainsi la faille de Songino et provoquant le mouvement de l’faille Songino.

Alors que d'autres études paléosismologiques n'ont comparé les profils GPR du seul type de faille active étudiée avec les résultats de la tranchée, mes travaux de thèse ont montré en pratique qu'il est possible de déterminer la structure de faille active pour tous les types.

En outre, il a été démontré que l’ensemble de nombreuses mesures radar effectuées le long de la trace de faille active peut déterminer le déplacement principal de toute faille active.

Il est plus raisonnable de déterminer le mouvement principal des failles actives en identifiant avec précision les déplacements et les structures fracturées en plusieurs points cibles le long de la trace de faille, en les analysant.

Le déplacement vertical de l'escarpement de la section à structure normale était d'environ 1,5 m dans le profil perpendiculaire à la trace de la faille Songino, et le déplacement vertical était d'environ 0,8 m dans le profil parallèle le long de la faille, tandis que la hauteur du déplacement vertical dans la structure de chevauchement nord-ouest de la faille de Songino était la plus élevée, son point culminant mesurait environ 22 m de haut.

Il y a une différence d'environ 20,5º entre les structures normales et décrochantes, et d'environ 37,1º entre les structures décrochantes et poussées, et un total d'environ 58º de différence entre les structures normales et poussées.

ӨРГӨТГӨСӨН ТОВЧЛОЛ

ГЕОРАДАРЫН ХОЁР БОЛОН ГУРВАН ХЭМЖЭЭСТ ДҮРСЛЭЛИЙН АРГА ТЕХНИКЭЭР ИДЭВХТЭЙ ХАГАРЛЫН ШИНЖ ЧАНРЫГ ТОДОРХОЙЛЖ ТАЙЛБАРЛАХ НЬ

УДИРТГАЛ

Тулгамдсан асуудал

Газар хөдлөлт нь зөвхөн тектоник хавтангуудын субдукцийн бүсэд төдийгүй тивийн дунд бичил хавтангуудын хооронд тохиолддог тул Монгол улс нь газар хөдлөлтийн эрсдэлтэй орны нэг юм. Монгол улс геологийн хувьд Төв Азийн орогенийн бүсэд багтдаг бөгөөд эдгээр уулс нь гулсалтын хурд багатай хөгжиж байдаг тул газар хөдлөлтийн идэвхтэй байдаг. Өнгөрсөн зууны эхэн үеэс хойш дэлхий дээр 8.0-аас дээш баллын 100 орчим газар хөдлөлт болж, үүний бараг 50% нь Ази тивд болжээ. Эдгээрээс Ази тивд болсон 44 хүчтэй газар хөдлөлтийн дотроос хоёр нь Монгол улсад болсон ба газар хөдлөлтийн магнитудын эрэмбээрээ Булнайн газар хөдлөлт (1905) ес дүгээрт, Говь-Алтай (1957) газар хөдлөлт нь 12 дугаарт бичигджээ. Гэсэн хэдий ч эдгээр газар хөдлөлт нь хүн амын нягтрал багатай, нүүдэлчин амьдралын хэв маягаас шалтгаалан гамшиг, хохирол багатай байсан. Гэвч өнөөдөр Монгол улс дахь хотжилт улам бүр нэмэгдэж, ялангуяа 1.5 сая орчим хүн ам төвлөрсөн нийслэл Улаанбаатар хотод эрчимтэй суурьшилт явагдаж байна. Улаанбаатар хот нь олон идэвхтэй хагарлаар хүрээлэгдсэн байдаг бөгөөд 2005 оноос хойш газар хөдлөлтийн идэвхжил нь огцом нэмэгдэж байгаа нь тулгамдаад буй бодит асуудал болж байна.

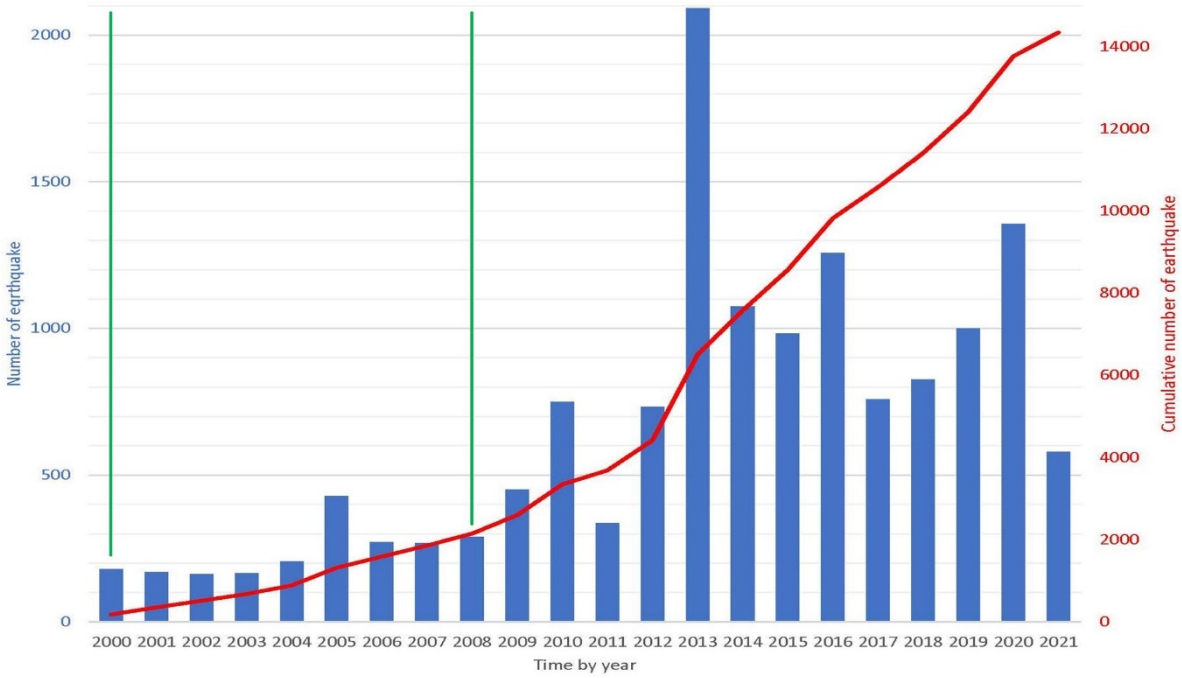

Зураг 1. 2000-2021 оны хооронд болсон газар хөдлөлтийн нийт тоо (140x140 km талбай). Ногоон шугам нь шинэ станц суурилуулсан хугацаа, 2000 онд "СТВТ-ийн Сонгино дахь сүлжээ станц" ба 2008 онд "UB-mobile"станцууд, MNDC-ийн мэдээллийн сан.

Хүснэгт 1. 1900 -аас 2018 он хүртэлх газар хөдлөлтийн момент магнитудийн зэрэглэл. Хүснэгтийг USGS-ийн 1900-2018 онуудад бүртгэгдсэн 8.0 ба түүнээс дээш момент магнитудтай хүчтэй газар хөдлөлтийн мэдээллээр үүсгэсэн болно.

Rank	Number of quakes	Location name	Magnitude
14.	1	Chile	9.5
15.	1	Prince William Sound, Alaska, USA	9.2
16.	1	Indian Ocean, off west coast of northern Sumatra, Indonesia	9.1
17.	2	Tohoku, off east coast of Honshu, Japan; Kamchatka, Russia, USSR	9.0
18.	2	Ecuador-Colombia; Maule, Chile	8.8
19.	1	Rat Islands, Alaska, USA	8.7
20.	4	Assam-Tibet, China; Northern Sumatra	8.6
21.	5	Kamchatka, Russia; Banda Sea, Dutch East Indies (Indonesia); Kuril Islands, Russia; Southern Sumatra	8.5
22.	4	Bulnai, Mongolia; Sanriku, Japan; Tonga; Near coast of southern Peru	8.4
23.	9	Mindanao, Philippines; Kuril Islands, Russia; South of Sumbawa, Indonesia; Hokkaido, Japan; Sea of Okhotsk	8.3
24.	19	Panay, Philippines; Kuril Islands, Russia; Kamchatka, USSR; Irian Jaya region, Indonesia	8.2
25.	20	Gobi-Altai, Mongolia; Ryukyu Islands, Japan; Bihar, India; Nankaido, Japan; Hokkaido, Japan	8.1
26.	26	Taiwan region; Afghanistan; Pakistan; Mindanao, Philippines; New Guinea; Sea of Okhotsk; Kurile Islands; Loyalty Islands	8.0

Судалгааны асуулт

Монгол улсын нийслэл Улаанбаатар хотын баруун талд орших Хустай болон Эмээлт хоёр том идэвхитэй хагарлын дунд орших Сонгино хагарал нь:

Бие даасан идэвхитэй хагарал мөн үү?

Ямар геодинамикийн орчинд яагаад үүсэв?

Яагаад өөр өөр харилцан адилгүй мөргөцөгүүдтэй байгаа вэ?

Ямар төрлийн хагарал вэ?

Цаашид хэрхэн яаж, хэзээ хөдлөх магадлалтай вэ?

Сонгино хагарлын хөдөлгөөн нь дээрхи хоёр том хагарлын шилжилт хөдөлгөөнтэй хэрхэн яаж уялдаж байна вэ? зэрэг асуултуудад энэхүү судалгааны ажлын хүрээнд хариулах шаардлагатай болно.

Судалгааны зорилго, зорилт

Орчин үеийн дэвшилтэд технологи болох Георадарын 2 болон 3 хэмжээст зураглалын техникээр идэвхитэй хагарлын шинж чанар, параметрүүдийг тодорхойлж, тайлбарлахад энэхүү докторын судалгааны ажлын зорилго оршино.

Уг судалгааны ажлын хүрээнд дараахи ажлуудыг хийж гүйцэтгэхээр төлөвлөсөн. Үүнд:

1. Идэвхитэй хагарлын үндсэн төрлүүд дээр 2-оос дээш хэд хэдэн өөр давтамжийн антенүүд ашиглан хэмжилт судалгаа гүйцэтгэж үр дүнгийн зураглалын харилцан уялдааг гаргах.

2. Идэвхитэй хагарлын үндсэн төрлүүд дээрхи бүтцүүдийг хэрхэн тодорхойлох, зураглах арга зүй, хэмжилтийн зарчмийг боловсруулах.
3. Георадарын хэмжилтийн мэдээлэл боловсруулах программ хангамжын зарим модулиудыг бичиж туршин зүгшрүүлэх.
4. Судалгааны гол талбар болох Сонгино хагарлын нарийвчилсан хэмжилт, зураглалын мэдээлэл бүрдүүлж тайлал хийснээр уг хагарлын талаархи палеосейсмологи болон структур геологийн тайлбар хийх.

Судалгааны хамрах хүрээ

Уламжлалт палеосейсмологийн судалгааны арга нь газар хөдлөлтөөр үүссэн хагарлын хөрсөн дээр үүсгэсэн мөргөцөгийн геоморфологи, болон хөрсний шилжилт хөдөлгөөнүүдийг газрын гадаргуу дээрхи эвдрэлийн ул мөрөөр дамжуулан судалдаг бөгөөд доош гүний хувьд 1-3 м гүний шруф болон тренчийн судалгааг гүйцэтгэдэг байсан. Тэгвэл георадарын тандан судалгааны тусламжтай палеосейсмологийн судалгааг хийснээр илүү гүний буюу 4-40м гүний мэдээллийг үл эвдэх аргаар хурдан шуурхай өндөр нарийвчлалтайгаар авах боломж бүрдэж байгаа болно. Бидэнд байгаа MALA брендийн 4 өөр давтамжийн антенаар бид 4-40м гүний зураглал хийх боломжтой боловч тухайн газар нутгийн хөрсний онцлог болон ус чийгний агууламж, мөн хүчтэй ойлгогч давхаргууд зэргээс хамаарч георадарын сигналын нэвтрэх гүн нь өөрчлөгддөг гэдгийг хэлэх хэрэгтэй болов уу. Мөн георадар нь биет болон давхаргуудаас буцаж ойсон ойлтын сигналыг бүртгэдэг учир долгионы ойлтын хуулийн хүрээнд л зураглал хийгддэг болно. Тиймээс 45^{0} аас илүү унлын өнцөг бүхий налуу бүтцийн хувьд радио долгионыг хажуу тийш сарниулах тул ийм бүтцийг тухайн орчний хэвтээ давхаргуудын шилжилт, өөрчлөлтөөр нь анализ хийдэг.

Судалгааны ач холбогдол

Энэхүү судалгааны ажил нь нийслэл Улаанбаатар хотын газар хөдлөлтийн аюулын үнэлгээний ажлын хүрээнд хийгдсэн тус ажлын нэг салшгүй хэсэг юм. Газар хөдлөлтийн аюулын үнэлгээний ажил нь Монгол орны хүн амын 50% аас илүү хувь нь суурьшсан, эдийн засаг, худалдаа үйлчилгээ дэд бүтцийн цор ганц төв болоод байгаа нийслэл хотын цаашдын төлөвлөлтөд маш чухал ач холбогдолтой ажил юм.

Сонгино хагарлын шинж чанрыг нарийвчлан тогтоосноор Улаанбаатар хотын газар хөдлөлтийн аюулын хамгийн том нөлөө бүхий Хустай болон Эмээлт хагарлуудын зүй тогтол хөдөлгөөнийг зөвөөр үнэлэх, харилцан уялдааг ойлгоход нэн чухал ач холбогдолтой юм. Цаашлаад Улаанбаатар хотын эргэн тойрны идэвхитэй хагарлуудын хоорондын харилцан хамаарал, зүй тогтлуудыг тайлбарлахад мөн адил дөхөм болох учиртай юм.

Нэр томьёоны тодорхойлолт

GPR-Ground Penetrating Radar гэдэг газрын гүний хөрс шороо чулуулаг болон барилга байшин, авто зам, уул уурхайн далан хучилт зэрэг хатуу бие доторх бүтцийг судалдаг арга зүй бөгөөд монголоор Георадар гэж нэршиж байгаа болно.

GPS-Global Position System гэдэг байрлал тогтоох хиймэл дагуулын төхөөрөмж бөгөөд дифференциал горимын хос төхөөрөмж ашиглаж RTK-Real Time Kinematic горимд хэмжилт хийснээр 1 сантиметрийн өндөр нарийвчлалтайгаар байрлалыг тодорхойлж өгдөг учраас геологи, геофизикийн хээрийн судалгааны ажилд өргөн ашиглагддаг.

2D гэдэг нь геологи, геофизикийн зүсэлтүүдийг хоёр хэмжээст зураглалын аргаар дүрслэн харуулах хэлбэр бөгөөд харин 3D гэдэг нь геологи, геофизикийн зүсэлтүүдийг гурван хэмжээст зураглалын аргаар дүрслэн харуулах хэлбэр юм.

GPR-Slice гэдэг нь гурван хэмжээст хэмжилт, зураглалын үед өргөн ашиглагддаг анализын нэг төрөл бөгөөд өндөр нарийвчлал бүхий гурван хэмжээст мэдээллийн кубыг үүсгэсний дараа газрын гадаргуутай паралелаар дурын гүнд хийсэн хэвтээ зүэлтүүдийг хэлдэг.

Палеосейсмологи- Палеосейсмологи нь эртний газар хөдлөлтийн шинж тэмдгүүдийг илрүүлж, газар хөдлөлтийн аюулыг тооцоолох зорилгоор геологийн хурдас, чулуулгийг судалдаг. Палеосейсмологи нь ихэвчлэн намаг, нуур, голын эрэг зэрэг сүүлийн хэдэн мянган жилийн турш хурдас тасралтгүй бий болсон геологийн дэглэмээр хязгаарлагддаг.

Геоморфологи- Геоморфологи нь дэлхийн гадаргуу дээр эсвэл түүний ойролцоо үйл ажиллагаа явуулж буй физик, хими, биологийн процессоос үүссэн топографи ба батиметрийн шинж чанаруудын үүсэл, хувьслын талаархи шинжлэх ухааны судалгаа юм.

Структур геологи- Структур геологи нь геологийн хурдас, чулуулгийн нэгжийн хэв гажилтын түүхийг харгалзан гурван хэмжээст тархалтыг судалдаг.

Судалгааны ажлын бүтэц

Георадарын хоёр болон гурван хэмжээст дүрслэлийн арга техникээр идэвхтэй хагарлын шинж чанрыг тодорхойлж тайлбарлах нь сэдэвт докторын нэг сэдэвт судалгааны бүтээл нь удиртгал, 5 бүлэг, ном зүй, гэсэн үндсэн бүтэцтэй ба зураг-110, хүснэгт-18 багтаасан нийт 199 хуудас бүхий материал болсон байна.

Удиртгал хэсэгт судалгааны ажлын үндэслэл, тулгамдаж буй асуудлууд, зорилго, зорилтыг тусгасан. Мөн уг судалгааны ажлын үр өгөөж, ач холбогдол, судлагдсан байдал зэргийг тусгаж өгөхийг зорьсон болно.

Нэгдүгээр бүлэг нь Георадарын тандан судалгааны арга зүй, мэдээлэл боловсруулалт нэртэйгээр Георадарын тандан судалгааны онол, арга зүйн үндэс болон хэрэглээний талаар оруулж өгсөн. Мөн георадарын хээрийн хэмжлтийн арга зүй, мэдээлэл боловсруулалт, 2 болон 3 хэмжээст хэмжилт, зураглалын ажлын үндэс, зарчим, үр дүнгийн тайллын талаар дэлгэрэнгүй тусгаж өгсөн.

Хоёрдугаар бүлэг нь идэвхтэй хагарлын бүтцийн судалгаан дээр Георадарын зураглалын арга техникийг ашиглах, хөгжүүлэх нэртэйгээр Георадарын тандан судалгааны арга зүйг палеосейсмологийн судалгаанд хэрхэн үр дүнтэйгээр ашиглах талаар оруулж хагарлын бүх төрлүүд дээр хийгдсэн хэмжилт зураглалын үр дүнгүүдийг тайлал болон палео-тренчийн судалгааны үр дүнгүүдийн хамтаар оруулж өгсөн. Мөн 3

хэмжээст зураглалын арга зүйг Эмээлтийн хагарлын судалгааны жишээн дээр оруулж тайлбарласан.

Гуравдугаар бүлэг нь Монгол улсын нийслэл Улаанбаатар хотын Сонгино хагарлын палеосейсмологийн шинж чанрыг Георадарын зураглалын арга техник ашиглан тодорхойлох нэртэйгээр уг хагарлын сунлын дагуух бүтцүүдийг нарийвчлан зураглаж, гарсан үр дүнгүүдийг нэг бүрчлэн тайлал хийсэн бөгөөд энэхүү судалгааны ажлын талаар мэдээллүүдийг дэлгэрэнгүй оруулсан болно.

Дөрөвдүгээр бүлэг нь Монгол улсын нийслэл Улаанбаатар хотын Сонгино идэвхтэй хагарлын палеосейсмологийн шинж чанарын геологийн нөхцөл нэртэйгээр Сонгино хагарлын Георадарын судалгааны үр дүн тайллаар тодорхойлогдсон бүтцүүдийн үүсэх шалтгаан, геологийн орчин нөхцөл болон Хустай, Эмээлт хагарлуудтай хэрхэн уялдах талаар оруулсан. Мөн Хустай, Эмээлт болон Сонгино хагарлууд дээр хийгдсэн нас тогтоох ажлын үр дүнгүүдийг оруулж тайлбарласан байгаа болно.

Тавдугаар бүлэг нь ерөнхий хэлэлцүүлэг, дүгнэлт гэсэн нэртэйгээр Сонгино хагарлын судалгааны үр дүнгүүдийн тайлал, дэвшүүлсэн таамаглалын талаар орсон ба энэхүү Георадарын хоёр болон гурван хэмжээст дүрслэлийн арга техникээр идэвхтэй хагарлын шинж чанрыг тодорхойлж тайлбарлах нь сэдэвт докторын нэг сэдэвт судалгааны бүтээлийн нэгдсэн дүгнэлтүүдийг оруулж өгсөн.

СУДЛАГДСАН БАЙДАЛ

Палеосейсмологийн талаархи ул мөрүүд нь газрын гадаргуугийн ойролцоо, газрын эхний метрт байрладаг (McCalpin, 2009). Сүүлийн хорь гаруй жилийн хугацаанд Георадар нь хөнөөлгүй шинж чанар, хэмжилтийн хурд, өртөг багатай учраас өргөн уудам газар нутагт нарийвчилсан хэмжилт хийх боломжийг олгодог тул палеосейсмологийн судалгаанд улам бүр түгээмэл хэрэглэгдэх болж байна. Георадар нь одоо байгаа бусад геофизикийн аргуудаас өндөр нарийвчлалтай байдаг. Георадар нь дөрөвдөгчийн хурдсын тогтоц, хот суурин газрын хөрсний бүтцийн судалгаа, төлөвлөлтийн ажилд нэн тохиромжтой байсан (Smith & Jol, 1995; Cai, McMechan, & Fisher, 1996; Audru, et al., 2001; Demanet, et al., 2001; Gross, et al., 2002), мөн судалгааны палеотренч малтлага хийх өндөр магадлалтай газрыг тодорхойлох зорилгоор (Salvi, et al., 2003; Liberty, et al., 2003; Jewell & Bristow, 2004; Malik J. , et al., 2010), болон суваг хоорондын өгөгдлийг интерполяцлахад нэн тохиромжтой (Ferry, et al., 2004; Slater & Niemi, 2003). Ихэнх тохиолдолд үүнийг бусад геофизикийн дүрслэх аргуудтай хослуулдаг ба ялангуяа цахилгаан томографи аргатай хослуулах нь өндөр үр дүнтэй (Demanet, et al., 2001; Lehmann, et al., 2001; Vanneste, et al., 2008). Гүний тандан судалгааны гүн, нарийвчлал, хэмжилтийн хурдны хувьд Георадар нь өргөн цар хүрээг хамарсан талбайн хэдэн арван метрийн хэмжээтэй бүтцийг тодорхойлоход хамгийн тохиромжтой арга юм.

Георадарын судалгааны арга, техник нь геофизикийн судалгааны салбар дахь хамгийн залуу бөгөөд хамгийн хурдацтай хөгжиж буй арга, техник бөгөөд Монгол орны хувьд өргөн дэлгэр ашиглагдаагүй байсан. 2010 оноос өмнө Монгол улсад хийгдсэн Георадарын судалгааны ажлын жишээнүүд бараг байхгүй байсан бөгөөд идэвхитэй хагарлын судалгааны ганц жишээ байсан. Энэ нь Дундговь аймгийн Дэрэнгийн идэвхтэй

хагарал дээр Швед улсын MALA Geoscience компаний 100 МГц-ийн антентай RAMAC GPR системээр CMP (Common Mid-Point) аргачлалаар зөвхөн нэг профайл дээр хийж, палео-тренчийн судалгааны үр дүнтэй хослуулан хийсэн байсан (Lu, et al., 2010).

Хустай, Эмээлт хагарлуудыг олон орны эрдэмтэн судлаачид судалсан байдаг бөгөөд өөр өөрсдийн зүгээс тайлбарласан байдаг бол харин Сонгино хагарлыг 2012 онд Франц улсын Страсбургийн Их Сургуулийн палеосейсмологийн судалгааны баг илрүүлж Шинжлэх Ухааны Академийн Одон Орон Геофизикийн Хүрээлэнгийн судалгааны багтай хамтран нарийвчилсан судалгааг эхлүүлсэн. Сонгино хагарлын талаар өөр ямар нэгэн судалгаа байхгүй болно.

СУДАЛГААНЫ АРГА ЗҮЙ

Судалгааны ажлын арга зүй нь орчин үеийн дэвшилтэд технологиудын олон арга зүйг хослуулан ашиглаж хийгддэг ба доорхи дарааллийн дагуу явагддаг.

1. Зайнаас тандан судлал, сансрын зургын анализ (Хагарлын ул мөр, мөргөцөг, шилжилт хөдөлгөөнийг илрүүлэх зураглах)
2. Талбайн геологийн судалгаа (Хагарлын ул мөр, мөргөцөг, шилжилт хөдөлгөөн, шалгах цэгүүд, георадарын судалгааны орчин нөхцөл шалгах)
3. Георадарын судалгаа (2D ба 3D георадарын хэмжилт, мэдээлэл цуглуулах, гадаргын топографын хэмжилт хийж гүйцэтгэх)
4. Палеосейсмологийн судалгааны тренч ухах, хагарлын нас тогтоох дээж авах.
5. Бүх хэмжилт судалгааны үр дүн, структур геологи, геодинамикийн нэгдсэн тайлал хийх.

Уг судалгааны ажлын гол арга зүй нь Георадарын 2 болон 3 хэмжээст зураглалын техник боловч судалгааны ажлын чанрыг дээшлүүлж өндөр үр дүнтэй болгохын тулд бусад нэмэлт арга зүйг хослуулан хэрэглэдэг болно. Георадарын тандан судалгааны арга зүй нь үндсэндээ тайлбар судалгаа бөгөөд хагарлын шинж чанар, үүсэл хөгжил, шалтгаан болон зүй тогтлыг тайлбарлахыг эрэлхийлж байгаа юм.

Өгөгдөл цуглуулах

Георадарын хэмжилтийг гүйцэтгэхдээ зураглалын найдвартай, үнэн зөв байдлыг нягтлан шалгах зорилгоор, хэмжилт хийсэн цэг бүр дээр хоорондоо 1-2 метрийн зайтай 3-5 паралел зүсэлтүүдийг хийж байсан болно. Тийм учраас эцсийн үр дүнгийн зураглалын чанар өндөр байгаа бөгөөд гарч буй бүтцийн хувьд эргэлзээ байхгүй юм.

ӨГӨГДЛИЙН БОЛОВСРУУЛАЛТ, ҮР ДҮН

Бид Георадарын хэмжилтийн хөндлөн зүсэлтүүдийн боловсруулалтыг MATLAB – ийн хэсэгчилсэн программын хэсгүүдийг ашиглаж мэдээлэл боловсруулалтад зориулж бичигдсэн RadLab гэдэг программ хангамжаар гүйцэтгэсэн. Уг программ хангамжийг Франц улсын Страсбургын Их Сургуулийн (EOST) хамт олон боловсруулсан бөгөөд бид хамтын ажиллагааныхаа хүрээнд уг программ хангамжийг ашиглаж, хөгжүүлэлт хийж байгаа болно.

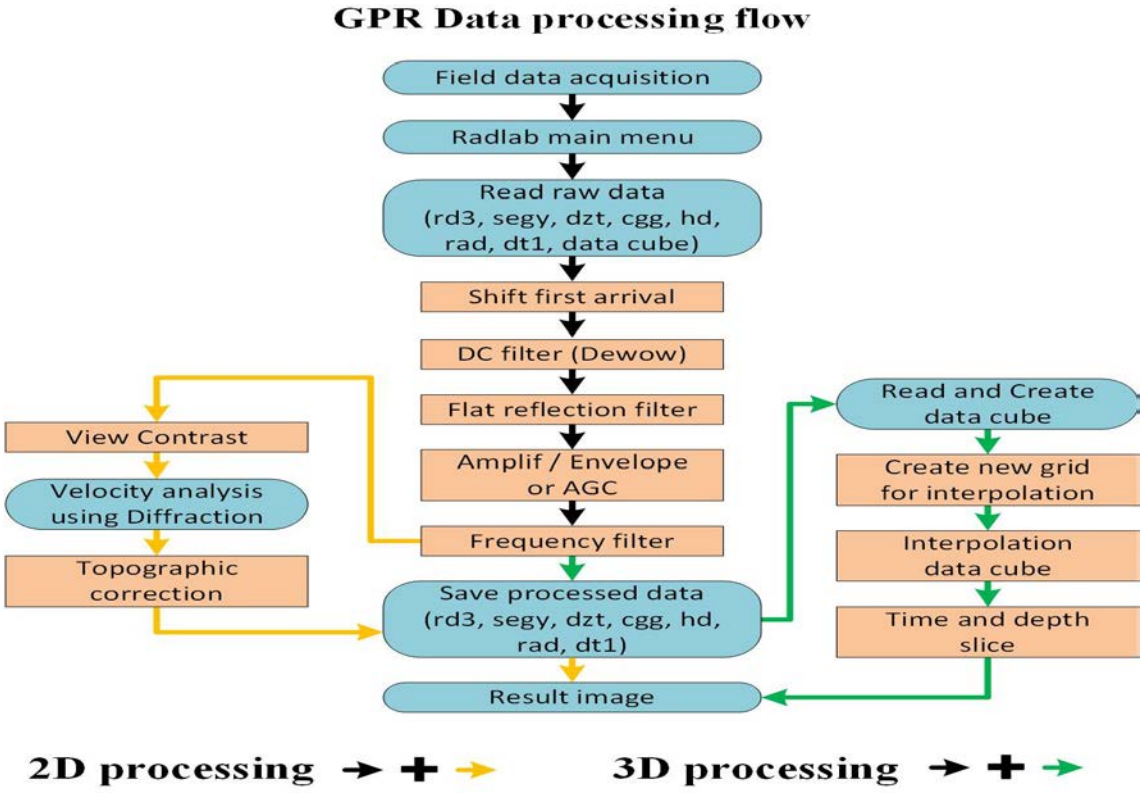

Өгөгдөлд шинжилгээ, анализ хийх

Георадарын зураглалын эцсийн үр дүнд тайлал хийхдээ ялгаатай үе давхаргуудын хил зааг тэдгээрийн шилжилт хөдөлгөөн болон долгионы ойлт, хугарал, замхрал, долгионы фазын гажилт өгч байгаа хэсгүүдэд анализ хийх замаар тухайн хөрс, хурдас чулуулгын геолегийн бүтэцтэй харьцуулан эцсийн дүгнэлт хийдэг.

ДҮГНЭЛТ

Георадарын 2 болон 3 хэмжээст зураглалын техникээр идэвхитэй хагарлын шинж чанар, параметрүүдийг тодорхойлж, тайлбарлах докторын судалгааны ажлын тавьсан зорилгын хүрээнд гүйцэтгэхээр төлөвлөсөн ажлуудыг амжилттай хийж гүйцэтгэсэн ба

Идэвхитэй хагарлын үндсэн төрлүүд дээр 3 өөр давтамжийн антенүүдийг тухайн судалгааны даалгавартаа тохируулан ашиглаж, хэмжилт судалгаа гүйцэтгэж үр дүнгийн зураглалын харилцан уялдаа хамаарлыг гаргаж чадсан.

Идэвхитэй хагарлын үндсэн төрлүүд дээрхи өөр өөр бүтцүүдийг хэрхэн тодорхойлох, зураглах арга зүй, хэмжилтийн зарчмийг боловсруулж түүнийхээ дагуу хэд хэдэн идэвхитэй хагарлууд дээр судалгаа хийж зохих үр дүнгүүдийг гаргасан.

Георадарын хэмжилтийн мэдээлэл боловсруулах RadLab программ хангамжын зарим модулиудыг MATLAB программын хэл дээр бичиж туршин зүгшрүүлсэн.

Судалгааны гол талбар болох Сонгино хагарлын нарийвчилсан хэмжилт, зураглалын мэдээлэл бүрдүүлж тайлал хийснээр уг хагарлын талаархи палеосейсмологи болон структур геологийн тайлбар хийж дараахи судалгааны асуултууддаа хариулт авсан болно. Үүнд:

Сонгино хагарал нь бие даасан идэвхижил бүхий хагарал биш бөгөөд зөвхөн Хустайн хагарлын нөлөөн дор хөдөлдөг ба Хустайн хагарал болон Эмээлтийн хагарлуудын дунд хянагддаг хагарал юм.

Сонгино хагарлын геодинамик орчин нь Хустайн зүүн хойд булан нь хагарлын зүүн гарын хэвтээ шилжилт болон Хустайн урд талын блоны эргэлтийн хөдөлгөөнөөр Эмээлтийн хагаралд шахагдан гэдрэг сөрж эвдэрсэн бүтцээс үүсэлтэй бөгөөд хөдөлгөөний чиглэл нь Хустайн хагарлын шилжилтийн эсрэг байна.

Сонгино хагарлын дугуйрсан бүтэц нь хэвтээ шилжилт хөдөлгөөн хийх явцдаа 3 төрлийн өөр бүтэц үүсгэж байгаа болно.

Сонгино хагарлын үндсэн хөдөлгөөн нь зүүн гарын хэвтээ шилжилттэй хагарал бөгөөд түүний хоёр талын тохрол болон зөрөл бүтэц нь хагарлын сунлын муруй бүтцээс хамаарч үүсэж байгаа юм.

Сонгино хагарал нь Хустай хагарлаас шууд хамааралтай бүтэц учраас дахин хөдлөх хөдөлгөөн нь Хустайн хөдөлгөөнтэй хамааралтай болно.

Сонгино хагарлын хөдөлгөөн зүүн гарын шилжилттэй гэдэг нь илт харагдаж байгаач уг хэсгийн бичил хавтан нь өөрөө хөдлөхгүй бөгөөд Хустайн хавтан нь зүүн тийш хөдөлснөөр Сонгино хагарлын хавтанг шахаж шилжилт хөдөлгөөн үүсгэж байгаа юм.

Судалгааны үр дүнгийн шинжлэх ухааны шинэлэг байдал;

Олон улсын хэмжээнд хийгдсэн палеосейсмологийн судалгааны ажлууд дээр зөвхөн тухайн хагарлынхаа георадарын зүсэлтүүдийг палеотренчийн үр дүнтэй харьцуулсан байдаг бол миний судалгааны ажлын хувьд хагарлын төрлийг тодорхойлох боломжтой гэдгийг жишээ судалгаанууд дээр бодит байдлаар үзүүлэн гаргаж ирсэн.

Хагарлын сунлын дагуу хийгдсэн олон хэмжилтийн үр дүнгүүдийн нийлбэрээр тухайн хагарлын үндсэн шилжилт хөдөлгөөнийг тогтоох боломжтой гэдгийг харуулсан.

Идэвхитэй хагарлын үндсэн хөдөлгөөнийг хагарлын сунлын дагуу олон цэг дээр шилжилт хөдөлгөөн, эвдэрлийн бүтцүүдийг нарийн тогтоож, тэдгээрт нэгдсэн анализ хийж тогтоох нь илүү үндэслэлтэй юм.

List of figures

List of tables

Introduction

Several active faults have been identified around Ulaanbaatar (UB) city, and in this doctoral dissertation we present the results ground penetrating radar (GPR) obtained on these faults. We will first need to answer the following questions:

Is Mongolia a seismically active and dangerous country? If so, how dangerous is the country? Why is Mongolia so seismically active? And so many questions will arise. Therefore, in order to answer the above questions, it is necessary to first compare the historical earthquakes that took place in the world with the historical earthquakes that took place in Mongolia.

Most people believe that earthquakes often occur on the plate boundary of the world's continents, and that Mongolia is safe because it is in the center of the Central Asia. Mongolia is an earthquake risk country because earthquakes occur not only within the subduction zones of the plates, but also between the micro-plates in the middle of the continent. Mongolia is in the orogeny's region of the Central Asia in terms of geology, and these mountains are seismically active due to their ongoing development by low slip rate. One century of seismicity in Mongolia (1900-2000) show where and how much land are active in the whole territory (Figure 0.5). Since the beginning of the last century, there have been about 100 earthquakes with a magnitude of more than 8.0 on the Earth, almost 50% of which occurred in Asia. From Figure 0.1 we remark that among 44 strong earthquakes in Asia, two of them occurred in Mongolia The Bulnai earthquake (1905) is the ninth strongest and the Gobi-Altai earthquake (1957) is the 12th ranked of the earthquake magnitude from 1900 to 2018 year in the world (Table 0-1). However, these earthquakes are less catastrophic and less damaging, due to the low population density and nomadic lifestyle of this time. However, the urbanization in Mongolia is continually increasing, especially in the capital city of Ulaanbaatar where a population of around 1.5 million is concentrated. Hence, the study of seismic hazard is of first importance for the UB capital which is surrounded by several active faults and showing an increasing of seismic activity since 2005 (See (Dugarmaa, et al., 2003; Schlupp, et al., 2012; Ferry, et al., 2010; Munkhsaikhan, 2016).

From the beginning of the last century to the present, data on the magnitude and damage caused by earthquakes and catastrophes around the world clearly show that damages after earthquakes are directly related to the concentration of population and urbanization (Table 0-2). Although the Bulnai (1905) and Gobi-Altai (1957) earthquakes caused less damages and victims than the other earthquakes of the same magnitude in the world (Figure 0.3), nowadays

the urbanization in Mongolia is continually increasing especially in the capital city of UB which presents a high seismic hazard risk. Figure 0.2 shows the seismic activity around Ulaanbaatar capital city since 2000 and the dates of installation of the seismic array stations for the seismic monitoring.

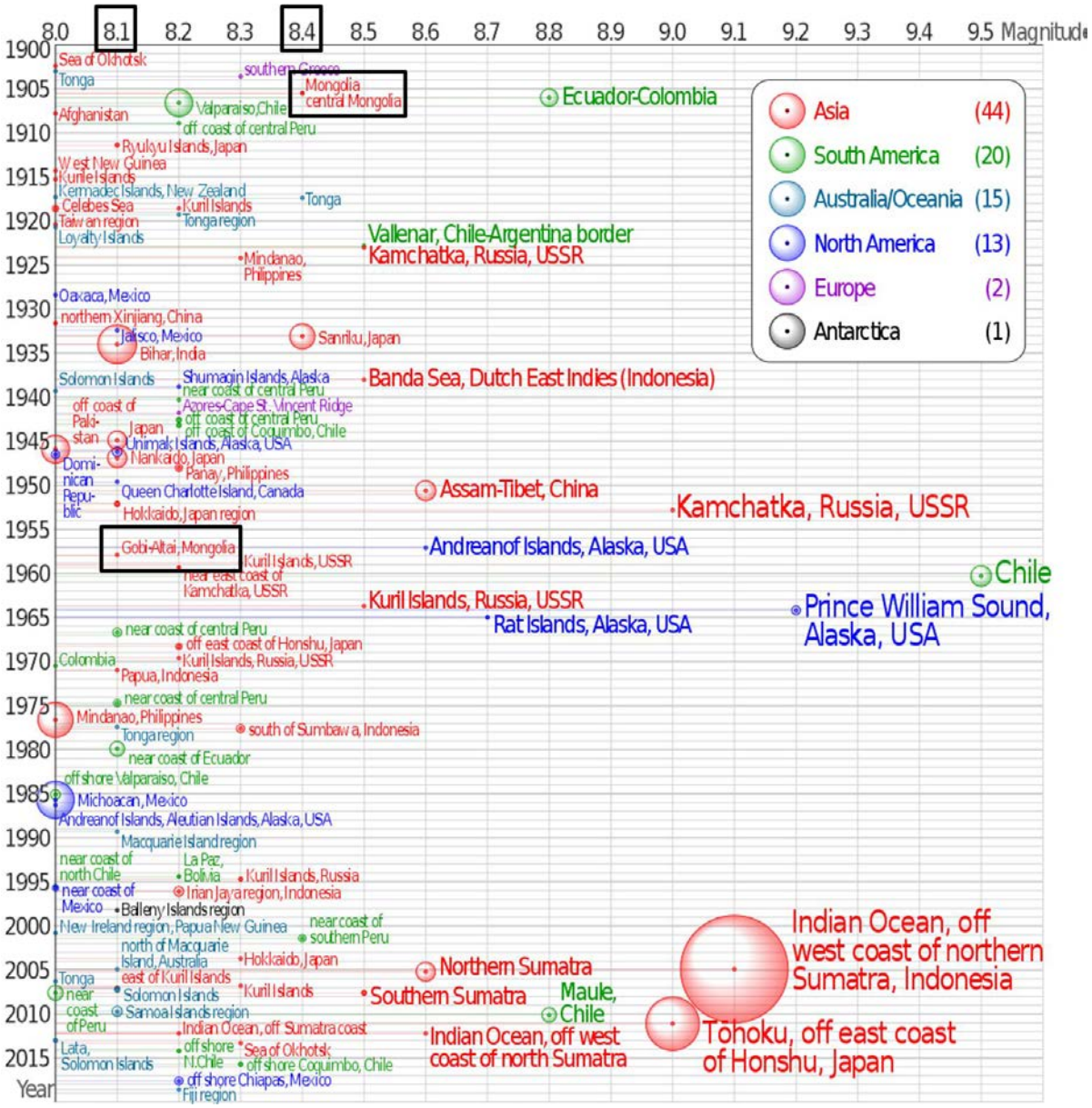

Figure 0.1 Earthquakes of moment magnitude 8.0 and greater from 1900 to 2018. The apparent 3D volumes of the bubbles are linearly proportional to their respective fatalities. The color indicates the continent, and the legend counts the number of quakes for each, black square surrounds the two earthquakes of Mongolia, (USGS sources).

Numerous studies by various researchers on the origin of Mongolia's mountains and current active tectonics have explained that the active deformation and active fault systems in

western and central Mongolia are dominantly the result of the Indo-Eurasian collision (Tapponnier & Molnar, 1979) (Figure 0.4).

The current deformation of Central Asia due to the Indo-Asian collision is estimated by the Global Positioning System (GPS) at about 4 cm/year (Calais, et al., 2006), while the South China block is compressed at 1 cm/year (Figure 0.4). The first GPS observations in Mongolia began in 1994 and showed that all deformations were much smaller than in the south (Calais & Amarjargal, 2000; Calais, et al., 2003; Calais, et al., 2006).

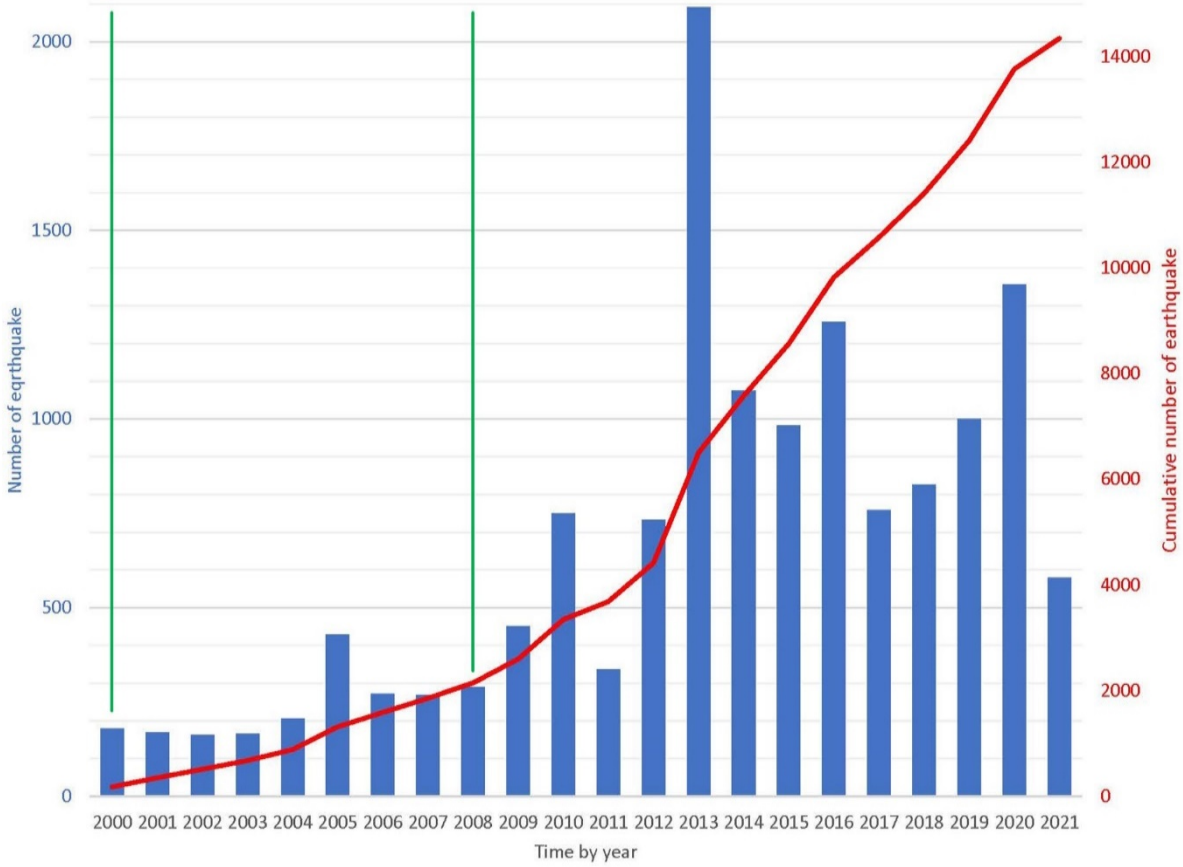

Figure 0.2 Cumulative number of earthquakes between 2000 and 2021 (area of 140x140 km). Green line is starting time of new station installation, in 2000 installation of "CTBT Songino array" and in 2008 installation of "UB-mobile", MNDC data.

It is well known that strong earthquakes (Mw ≥ 6) are relatively rare on the human time scale, but they cause significant damage and often many victims. This is the reason why we seek to better understand and anticipate earthquakes. The major questions we would like to be able to answer are: where and when will the next strong earthquake occur on a given fault? What will be its magnitude and its effects in terms of strong movements of the ground? While most major 'active' faults are now known (Tapponnier, et al., 2001a; Bozkurt, 2001; Prentice,

et al., 2003) and with them the location of future great earthquakes, the anticipation of the date-magnitude effects parameters of the strong events to come remains a challenge not attained to date despite a very large number of studies. One of the difficulties of difficulties often are these strong events often long (several hundred and thousands of years), especially than the person's observation period. It is then impossible to know whether the strong earthquakes on a fault are similar or dissimilar, whether they repeat regularly or irregularly, whether they produce the same effects, etc. Only the Park field segment on the San Andreas fault broke during 5 'successive' events of Mw ≈ 6 (1881, 1901, 1922, 1934, 1966, 2004) which could have been observed during the last two centuries.

Table 0-1 Rank of the earthquake moment magnitude from 1900 to 2018. Table created by USGS data of the Earthquakes of moment magnitude 8.0 and greater from 1900 to 2018, (USGS sources).

Rank	Number of quakes	Location name	Magnitude
27.	1	Chile	9.5
28.	1	Prince William Sound, Alaska, USA	9.2
29.	1	Indian Ocean, off west coast of northern Sumatra, Indonesia	9.1
30.	2	Tohoku, off east coast of Honshu, Japan; Kamchatka, Russia, USSR	9.0
31.	2	Ecuador-Colombia; Maule, Chile	8.8
32.	1	Rat Islands, Alaska, USA	8.7
33.	4	Assam-Tibet, China; Northern Sumatra	8.6
34.	5	Kamchatka, Russia; Banda Sea, Dutch East Indies (Indonesia); Kuril Islands, Russia; Southern Sumatra	8.5
35.	4	Bulnai, Mongolia; Sanriku, Japan; Tonga; Near coast of southern Peru	8.4
36.	9	Mindanao, Philippines; Kuril Islands, Russia; South of Sumbawa, Indonesia; Hokkaido, Japan; Sea of Okhotsk	8.3
37.	19	Panay, Philippines; Kuril Islands, Russia; Kamchatka, USSR; Irian Jaya region, Indonesia	8.2
38.	20	Gobi-Altai, Mongolia; Ryukyu Islands, Japan; Bihar, India; Nankaido, Japan; Hokkaido, Japan	8.1
39.	26	Taiwan region; Afghanistan; Pakistan; Mindanao, Philippines; New Guinea; Sea of Okhotsk; Kurile Islands; Loyalty Islands	8.0

Although earthquakes have something in common, they are not similar in terms of location of epicenter and direction of propagation of the rupture and they are not repeated regularly (Bakun & Lindh, 1985; Jackson & Kagan, 2006). If such irregularities are the norm, anticipating the parameters of future strong earthquakes could be difficult, if not impossible.

One way to expand our knowledge of strong earthquakes and how they repeat themselves is to investigate the past and determine the characteristics (where, when, what magnitude) of strong prehistoric events. Getting to know these characteristics would be a great help in anticipating those of future events. This field of study of past earthquakes (i.e., prior to the historical period and therefore generally in the last ≥ 2000 years) is that of paleo-seismology (Yeats, et al., 1997; Weldon, et al., 2004; McCalpin, 2009).

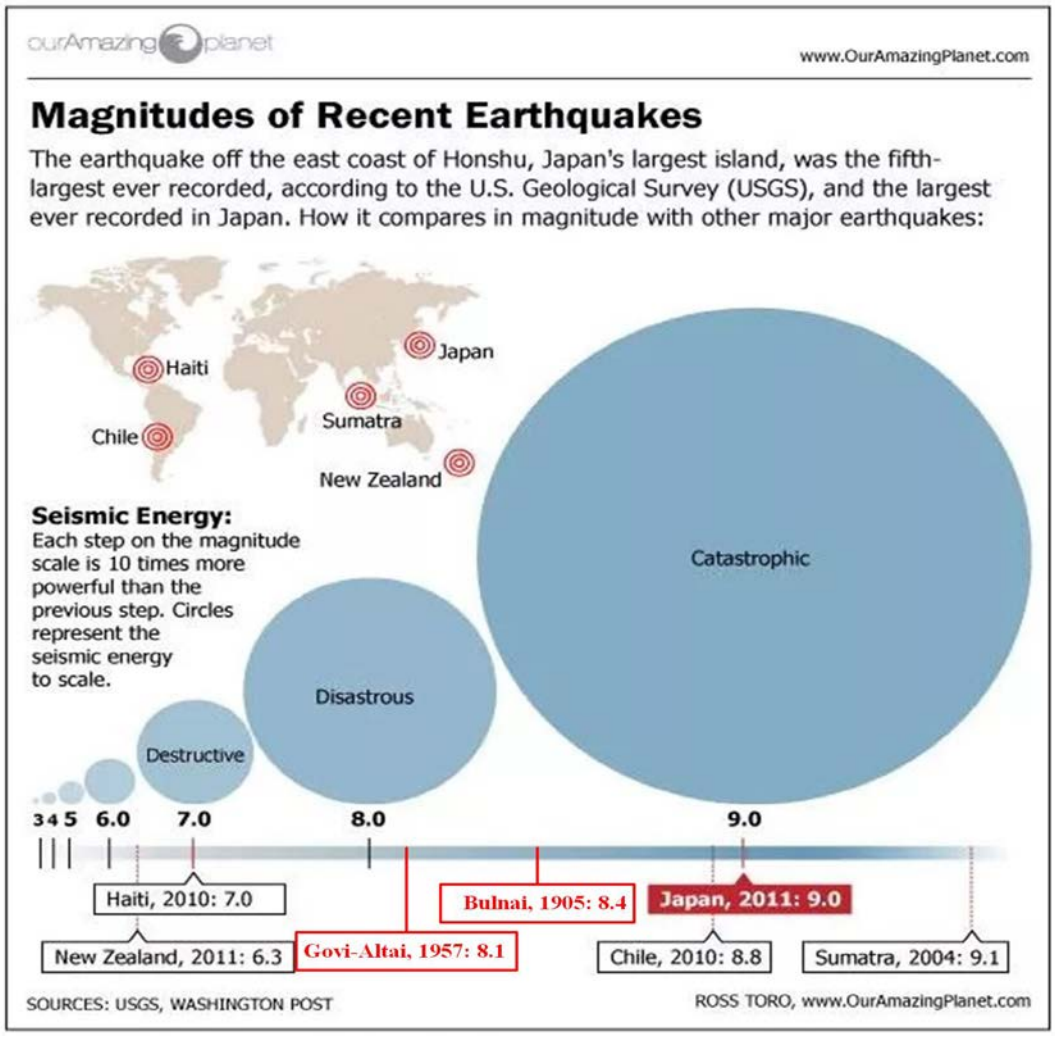

Figure 0.3 Earthquake magnitude comparison. Each step on the magnitude scale is 10 times more powerful than the previous step. Radiuses of circles represent the seismic energy to scale. The two strongest Mongolian's earthquakes (indicated in red) are compared in magnitude with other major earthquakes (USGS sources).

The objective of paleo-seismology is to document the seismic history of a fault (i.e., location, age, and displacements associated with the largest ruptures on the fault) over a sufficiently long period of time (several thousands to tens of thousands of 'years) to include

many successive events. First, only earthquakes of relatively large magnitude (Mw ≥ 6) and shallow (≤ 30 km) leave traces of rupture at the surface or very close to the surface. Whatever their nature (displacement of morphological markers, portions of escarpment exhumed, uplift of coastal markers, etc.), these traces are rapidly degraded by erosion or buried by sedimentation, and therefore diminish or disappear over time. In addition, earthquakes repeating over time, their traces overlap and produce a complex signal to analyze. Another difficulty is methodological; not only the traces of old strong earthquakes are difficult to detect and analyze, but the methods which allow these detections and analyzes are few and often only applicable on structures locally known.

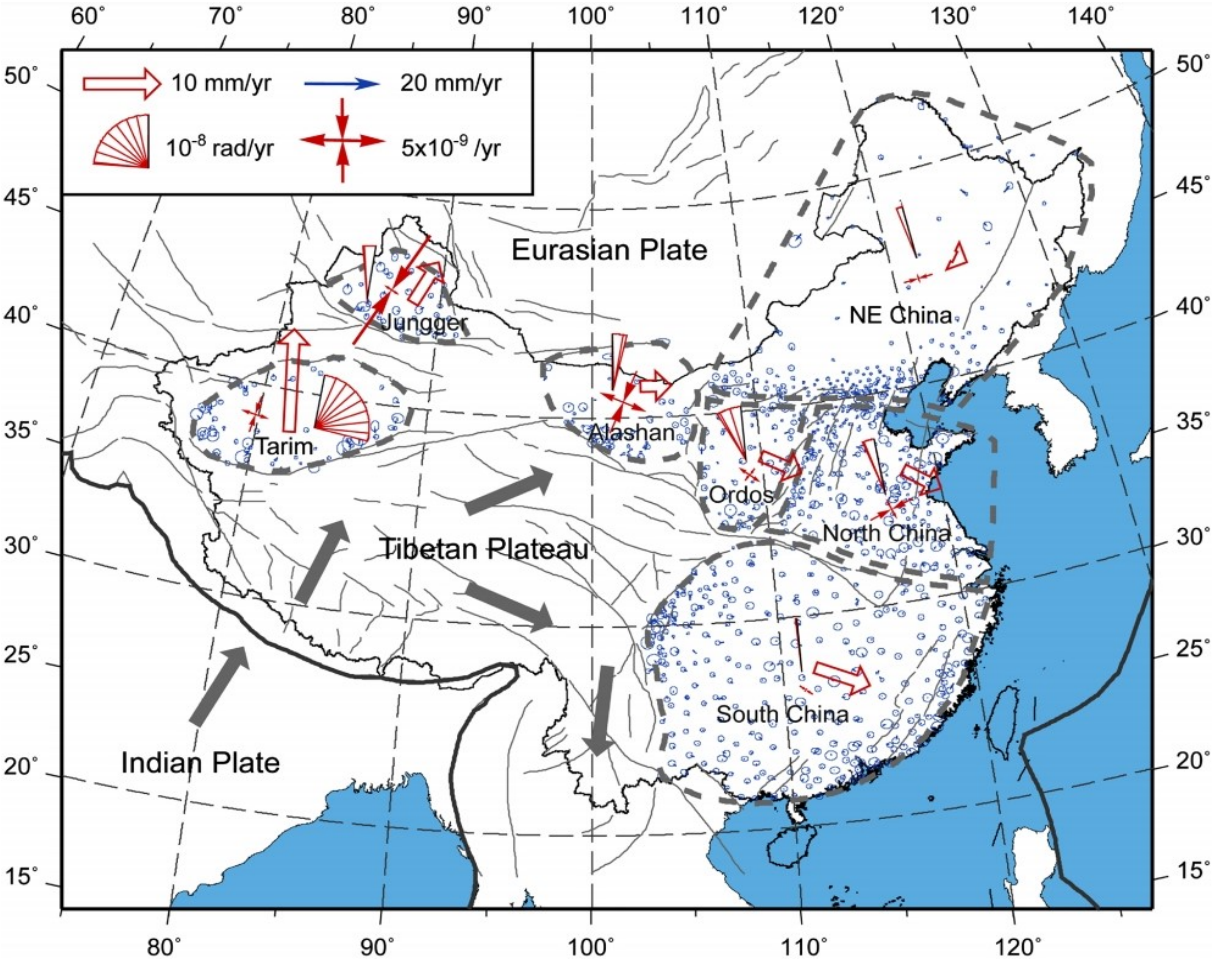

Figure 0.4 Block motion model. Thick gray dashed lines are the block boundaries. Red fan shapes and hollow arrows denote block rotation rates and translation rates with respect to the Eurasian plate, respectively. Red thin vector pairs denote principal strain rates. Black arrows indicate motion directions of the Indian plate and Tibetan plateau (Wang & Shen, 2020).

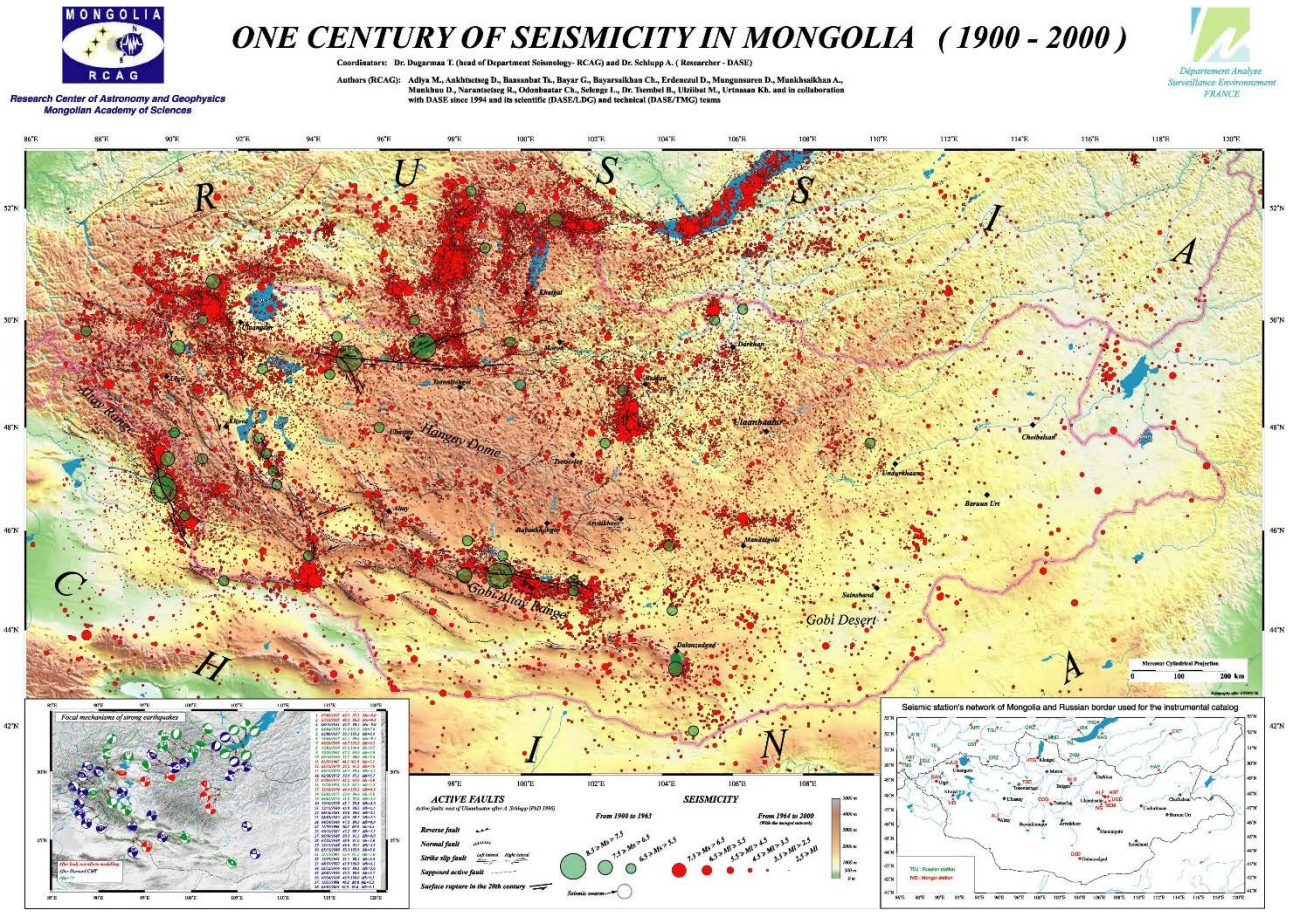

Figure 0.5 One century (Benedetti, et al., 2003)of seismicity in Mongolia (1900-2000), RCAG and DASE team.

This is notably the case of paleo-seismological trenches (Rockwell, et al., 2009c; McCalpin, 2009) samples of escarpments exhumed to measure the content of cosmogenic isotopes (Schlagenhauf, et al., 2010; Schlagenhauf, et al., 2011; Palumbo, et al., 2004) samples of corals raised seismically (Zachariasen, et al., 1999; Sieh, et al., 2008) etc. Finally, it is rare that a paleo-seismological method makes it possible to determine both the displacements produced by the earthquake and the age of the earthquake. Most paleo-seismological studies carried out to date only document the age of some past earthquakes (Weldon, et al., 2004; Daëron, et al., 2007; Marco, et al., 1996) but not their movements.

A good documentation is rarely documented by measurement of the earthquake transitions (Sieh K. , 1996; Yeats, et al., 1997; Weldon, et al., 2004). There is a long time that observed to the extended period observed to the extended transition, but they do not have a precision because they are based on indirect evidence (Liu-Zeng, et al., 2006).

Table 0-2 List of deadliest 20th century earthquakes (USGS sources).

Rank	Fatalities	Magnitude	Event	Location	Date
1	273,400	7.8 M_s	1920 Haiyuan earthquake	China	16 December 1920
2	242,000	7.6	1976 Tangshan earthquake	China	28 July 1976
3	142,800	8.2	1923 Great Kantō earthquake	Japan	1 September 1923
4	110,000	7.3 M_s	1948 Ashgabat earthquake	Turkmen SSR	5 October 1948
5	82,000	7.1 M_s	1908 Messina earthquake	Italy	28 December 1908
6	70,000	7.9	1970 Ancash earthquake	Peru	31 May 1970
7	60,000	7.7	1935 Quetta earthquake	Pakistan	31 May 1935
8	50,000	7.4	1990 Manjil–Rudbar earthquake	Iran	21 June 1990
9	40,900	7.6	1927 Gulang earthquake	China	22 May 1927
10	32,700	7.8	1939 Erzincan earthquake	Turkey	26 December 1939
11	32,610	6.7 M_s	1915 Avezzano earthquake	Italy	13 January 1915
12	28,000	8.3 M_s	1939 Chillán earthquake	Chile	24 January 1939
13	25,000	6.8 M_s	1988 Armenian earthquake	Armenian SSR	7 December 1988
14	23,000	7.5	1976 Guatemala earthquake	Guatemala	4 February 1976
15	20,000	7.8 M_s	1905 Kangra earthquake	India	4 April 1905
16	17,127	7.6	1999 İzmit earthquake	Turkey	17 August 1999
17	15,621	7.1	1970 Tonghai earthquake	China	5 January 1970
18	15,000	7.4	1978 Tabas earthquake	Iran	16 September 1978
18	15,000	7.4	1968 Dasht-e Bayaz and Ferdows earthquakes	Iran	31 August 1968
20	12,225	7.1 M_L	1962 Buin Zahra earthquake	Iran	1 September 1962
21	12,000	7.3 M_s	1907 Qaratog earthquake	Tajikistan	21 October 1907
21	12,000	8.0	1934 Nepal–India earthquake	India	15 January 1934
21	12,000	5.8	1960 Agadir earthquake	Morocco	29 February 1960
24	11,000	6.3	1972 Nicaragua earthquake	Nicaragua	23 December 1972
25	10,000	8.0	1931 Fuyun earthquake	China	11 August 1931
25	10,000	7.8	1944 San Juan earthquake	Argentina	15 January 1944
25	10,000	8.0	1985 Mexico City earthquake	Mexico	19 September 1985

However, if the determination of the dates of occurrence of strong past earthquakes is crucial, that of the displacements produced is also very important. As the earthquake displacement varies along the ruptures (Manighetti, et al., 2005), it is a priori necessary to document the slip produced by each of the earthquakes passed through several points of the breaking length. The maximum and average displacements produced at the surface can then be determined, and these quantities are fundamental for estimating the magnitude of past events. It is important to note that the displacements produced on the ground surface are often only a fraction of the displacements produced in depth by the earthquake (Manighetti, et al., 2007). The magnitudes estimated at the surface are therefore always minimum values.

The motivation for this thesis work was to help developing a new methodology and acquire new data to better estimate the seismic hazard relating to active faults. These

developments and acquisitions have targeted active faults but will eventually be applied to other active faults around Mongolia.

Therefore, this doctoral thesis work was carried out in 5 chapters: GPR method and data processing, applications of GPR imaging technique for active fault structures, paleo-seismological characterization GPR-based technique of the Songino active fault, Ulaanbaatar, Mongolia., and geological context of the paleo-seismologic characterization of the Songino active fault, Ulaanbaatar, Mongolia.

GPR research methods and techniques are the fastest-growing methods and techniques in geophysical research fields and now is widely used in a lot of branches around the world. Mongolia was only a few examples of GPR research before 2010 (Since 1998, GPR survey has been conducted jointly by MUST and Tohoku University) and only one instance used in active fault studies. This was performed on a single profile in the Common Offset (CO) survey design with a RAMAC GPR system (MALA Geoscience, Sweden) 100 MHz antenna on the Deren active fault (Dundgovi, Mongolia) and combined with trench studies (Figure 0.6) (Lu, et al., 2010). The velocity of the electromagnetic wave in the subsurface was measured by Common-Mid-Point (CMP) data (Lu, et al., 2010).

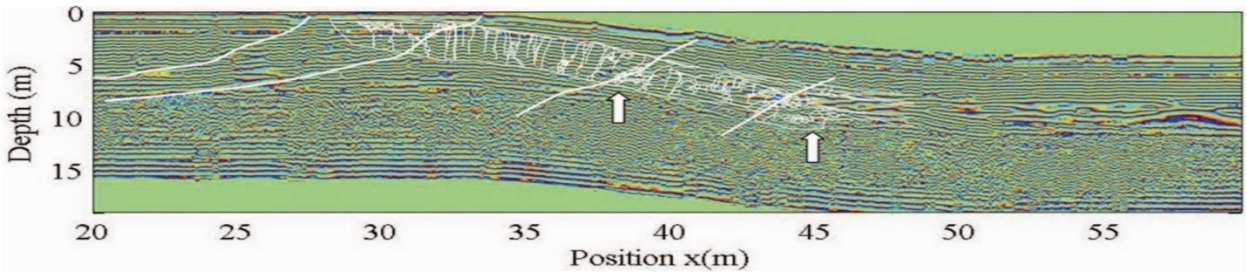

a) Correlation of GPR data with trench observation

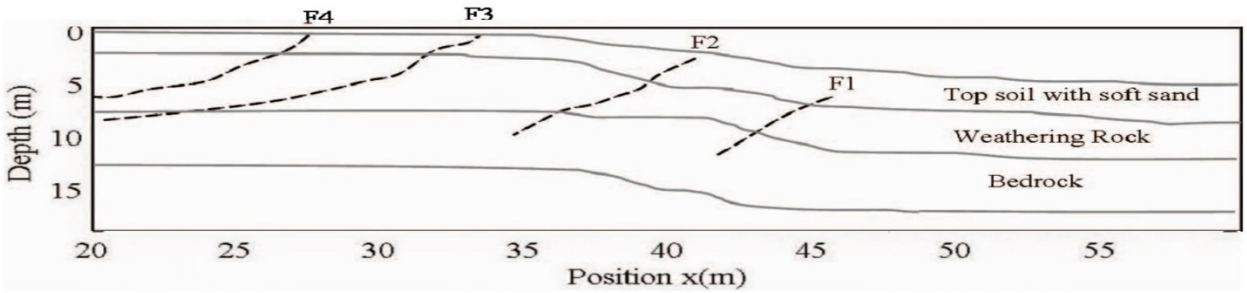

b) Simple geological model interpreted from GPR result image

Figure 0.6 Characterization of the Deren fault by GPR. a) GPR result image with trench observations, b) Geological model interpreted from GPR result image (Lu, et al., 2010).

Chapter 1 : GPR (Ground Penetrating Radar) method and data processing

1 Introduction

The dropping faults move the morphological markers in an approximately horizontal plane and parallel to the surface of the ground. Long records of paleo seismic can therefore reside close to the surface, in the first meters of the ground (McCalpin, 2009). Geophysical imagery is a potential means of detecting and imaging these records. The choice of the most appropriate geophysical imaging method to image the first meters of soil and detect possible buried objects or structures depends mainly on the geological context, the depth and size of the target, the resolution required, but also of more practical aspects such as the type of land (reliefs, vegetation), the financial cost and the difficulty of data acquisition and processing. Indeed, many geophysical methods exist (Reynolds, 2011; Telford, et al., 1990) and are distinguished by their sensitivity, depth of investigation and resolution. Most have already been applied to active faults in terrestrial and marine environments (McCalpin, 2009). The most common are seismic reflection and refraction, electrical tomography, electromagnetism, magnetism and gravimetry. The scale of application and the resolution of these methods are of the order of a few centimeters (GPR) to ten kilometers (seismic reflection). They are generally applied in fault studies and in paleo seismology in particular in order to 1) recognize sites before slicing or drilling (Salvi, et al., 2003; Vanneste, et al., 2006), 2) define the geometry of the fault plane in depth (up to the crustal scale) (Vergne, et al., 2002; Wittlinger, et al., 1998; Nguyen, et al., 2003), 3) detect faults that do not reach the surface (Cavinato, et al., 2002; Caputo, et al., 2007), 4) measure the vertical displacements of the stratigraphic layers (McClymont, et al., 2009a; Yetton & Nobes, 1998a). Over the past decade, the GPR has become more and more popular in paleo seismological studies due to its non-destructive nature, its speed of implementation and its low cost, which allow it to be densely applied over large areas. GPR also achieves higher resolutions than other existing geophysical methods. The GPR has been particularly suitable for locating fault plans in quaternary formations and urban areas (Smith & Jol, 1995; Cai, et al., 1996; Audru, et al., 2001; Demanet, et al., 2001; Gross, et al., 2002), to identify sites with high potential for future excavations (Salvi, et al., 2003; Liberty, et al., 2003; Jewell & Bristow, 2004; Malik J. , et al., 2010) and to interpolate data between trenches (Ferry, et al., 2004; Slater & Niemi, 2003). In many cases, it is combined with other imaging methods, notably electric tomography (Demanet, et al., 2001; Lehmann, et al., 2001; Vanneste, et al., 2008). In terms of

depth of investigation, resolution, and speed of implementation, the GPR is the most suitable method for detecting metric-sized targets in the first ten meters of the ground over wide areas. The objective here is to use the GPR along active faults in order to detect the displacements accumulated over time by buried morphological markers. The existence of such markers in the first meters of the ground, mainly abandoned rivers, has been highlighted in some 3D trenches (Wesnousky, et al., 1991; Marco, et al., 2005; Noriega, et al., 2006; Rockwell, et al., 2001; Rockwell, et al., 2009c; Liu-Zeng, et al., 2006) or by geophysical imagery (McNeilan, et al., 1996; Ferry, et al., 2004). The low spatial extent of these studies, however, limits the detection of these shifts to only around ten meters, or the displacement produced by the last few strong events.

We describe in this chapter the different steps that we followed during our application of the GPR to paleo seismology. At each step, we describe the necessary data and the methods of processing and analysis. We can thus conclude on the reliability, objectivity, and advantages of this approach, as well that discuss the uncertainties, the drawbacks, and the subjectivity of the results.

2 Principle of the GPR

Ground Penetrating Radar (GPR) is a high-resolution, near surface, geophysical method based on the propagation, reflection and scattering of high frequency (from 10 MHz to 2 GHz) electromagnetic (EM) waves in the Earth (Daniels, et al., 1988; Jol, 2009; Van Dam, 2012). EM waves sent into the ground are reflected at interfaces of electric and dielectric contrast and the reflected signals are recorded. Those discontinuities can result from changes in the water content, the chemical composition, or the texture of the deposits. In sedimentary deposits, variations in grain size and water saturation are the main factors triggering reflections. GPR has proven its efficiency in many fields of geosciences but seems generally most efficient in sedimentary deposits, marked lithological boundaries, fractures and/or faults (Gross, et al., 2004; Deparis, et al., 2007; McClymont, et al., 2010), even for subtle changes in the nature, size, shape, orientation and packing of grains (Guillemoteau, et al., 2012). In the sedimentological context, interpretation generally uses GPR-facies analysis, analogous to their use in seismic studies (Jol & Bristow, 2003; Neal, 2004). Ground Penetrating Radar (GPR) is a geophysical imaging method that detects reflections and diffractions of electromagnetic waves occurring at the dielectric, electrical and magnetic contrasts of the sub-surface within an electrically resistive medium. This is a relatively recent geophysical method which has found a

wide field of applications over the last twenty years (Annan, 2002) for a background, and (Jol, 2009; Beres & Haeni, 2005) for a review. description of the main applications).

In the context of actives faults, the ground penetrating radar (GPR) method gives good and useful results. It can help to characterize faults by identifying offsets of radar reflections and buried fluvial channel deposits (Beauprêtre, et al., 2012). The investigation depth depends on the electromagnetic (EM) attenuation of the medium and the frequency of the antenna used. The lower the frequency, the greater the penetration depth, which varies from a few centimeters in conductive materials up to 50 m for low conductivity (less than 1 mS m^{-1}) media (Jol, 2009). The vertical resolution depends on the velocity of EM waves and the frequency used. In general, features such as sedimentary structures, lithological boundaries, fractures and/or faults are clearly visible with GPR (Deparis, et al., 2007; Christie, et al., 2009; McClymont, et al., 2010) even when these features differ only by small changes in the nature, size, shape, orientation and packing of grains (Guillemoteau, et al., 2012).

By describing in the following the principle of electromagnetic (EM) wave propagation, we will introduce the concepts and vocabulary inherent in this method, as well as the signal and noise sources that we will try to amplify and to reduce, respectively, during processing.

2.1 Propagation of electromagnetic waves

The principle of GPR is based on the ability of materials to polarize under the presence of an electromagnetic field. This electromagnetic (EM) field propagates in the ground in the form of electromagnetic waves. This propagation is expressed by the equation EM waves obtained from Maxwell's equations, eliminating either the field electric, or the magnetic field. We obtain the following wave equation by eliminating the magnetic field in a homogeneous and isotropic medium:

$$\nabla^2 E + k^2 E = 0 \qquad 1.1a \qquad\qquad \nabla^2 E - \mu\sigma \cdot \frac{\partial E}{\partial t} - \mu\varepsilon \cdot \frac{\partial^2 E}{\partial t^2} = 0 \qquad 1.1b$$

(1) (2) (3)

with E the electric field, k the wave number, μ the magnetic permeability ($H.m^{-1}$), ε the dielectric permittivity ($F.m^{-1}$), σ the electrical conductivity ($S.m^{-1}$). For the sedimentary (no-magnetic) rocks, the magnetic permeability (μ) is supposed to be equal to $\mu_o = 4\pi * 10^{-7} H.m^{-1}$, the magnetic permeability of the free space. In that case $\mu_r = \mu/\mu_o$ the relative permeability is equal to 1. The speed of the waves will therefore be essentially dependent on the dielectric permittivity, some values of which for rocks are given in (Annan, 2009). (Eqns. 1.1a) characterized by the vector

Helmholtz equation. In electromagnetics, the vector Helmholtz equation is the frequency-domain equivalent of the lossy wave equation (Eqns. 1.1b). The first term (1) is called the Laplacian (∇^2). The second term (2), which contains a first order time derivative, controls the diffusive behavior of the electromagnetic signal and the third term (3), which contains a second order time derivative, represents an energy conservation term in (Eqns. 1.1b). The electromagnetic waves will be able to propagate in the medium when the diffusive term is weak compared to the propagative term, that is, in a weakly conductive medium and at high frequencies. Indeed, the behavior of the waves is depending on the frequency and the physical properties of the medium. At low frequencies, the behavior of the waves will be diffusive, and the wave will diffuse with different speeds depending on the frequency (dispersion). At high frequencies (> 10 MHz), the speed of the waves becomes independent of the frequency; this is the case of ground penetrating radar (GPR) method. The transition frequency ft between diffusive/propagative regimes for a simple material, is given by equation (Annan, 2009):

$$f_t = \frac{\sigma}{2\pi\varepsilon} \qquad 1.2$$

For frequencies higher than this value, all frequency components have the same propagation speed and attenuation; the medium is non-dispersive. The propagation speed *V* of an impulsive signal in the absence of dispersion is given by equation (Annan, 2009):

$$V = \frac{1}{\sqrt{\mu\varepsilon}} = \frac{c}{\sqrt{\kappa}} \qquad 1.3$$

Since $\mu = \mu_o$, the speed of the waves will therefore be essentially dependent on the dielectric permittivity, c is the speed of light ($3*10^8$ m/s). During its propagation, the amplitude of the radar signal decreases exponentially with the propagation distance *z* ($e^{-\alpha z}$) in the medium, where the attenuation α is given by (Annan, 2009):

$$\alpha = \sqrt{\frac{\mu}{\varepsilon}} \cdot \frac{\sigma}{2} \qquad 1.4$$

In addition to the intrinsic attenuation α (ohmic or geometrical attenuation), there is another attenuation (scattering attenuation) due to the presence of heterogeneities (scatters) which diffract or reflect the energy in all directions. Another characteristic of the EM wave propagation is the impedance *Z* which describes the resistance of the medium to the passage of the wave and is given by (Annan, 2009):

$$Z = \sqrt{\frac{\mu}{\varepsilon}} = \frac{Z_0}{\sqrt{\kappa}} \qquad 1.5$$

Z_0 is the impedance of free space and κ is the dielectric constant ($\kappa = {}^{\varepsilon}/_{\varepsilon_0}$, *where* ε_0 *is the permittivity of vacuum, 8.89*10^{-12} F/m*), Equation (1.5) is valid in the case of GPR frequency range between 10 MHz – 2 GHz (Cassidy N. , 2009). An impedance contrast between two layers describes an interface on which the reflections are characterized by their reflectivity; a crucial property for reflection imaging.

Table 1-1 Typical values of relative permittivity and conductivity for materials conventional sub-surface for an antenna frequency of 100 MHz, after (Annan, 2009).

Matériaux	Conductivité (σ, mS/m)	Permittivité relative (ε)
Air	0	1
Argile sèche	1–100	2–20
Argile humide	100–1000	15–40
Béton sec	1–10	4–10
Béton humide	10–100	10–20
Eau douce	0.1–10	78 (25°C)–88
Glace d'eau douce	10^{-6}–1	3
Eau de mer	4000	81–88
Glace de mer	10–100	88
Permafrost	0.1–10	2–8
Granite sec	10^{-3}–10^{-6}	5–8
Granite fracturé et humide	1–10	5–15
Calcaire sec	10^{-3}–10^{-7}	4–8
Calcaire humide	10–100	6–15
Grès sec	10^{-3}–10^{-7}	4–7
Grès humide	10^{-2}–10^{-3}	5–15
Argile marine saturée	10–100	6–9
Sable sec	10^{-4}–1	3–6
Sable humide	0.1–10	10–30
Sable côtier sec	0.01–1	5–10
Sol sableux sec	0.1–100	4–6
Sol sableux humide	10–100	15–30

2.2 Reflection, refraction, transmission, and reception of EM signals

Transmitted signal - The EM signal transmitted by the transmitting antenna is a pulse signal of a given frequency and duration. It is characterized by a center frequency fc and a band-pass of width B (in Hz), linked by the ratio $R = \frac{B}{f_c}$, generally equal to 1. For an antenna of center frequency f_c = 100 MHz, the transmitted signal will therefore have a frequency band B of 100 MHz centered in 100 MHz, and a duration of 10 ns. The ratio R tends to be maximized,

so to widen the frequency band while reducing the center frequency and thus increasing both the resolution and penetration depth. The transmitting antenna emits in all directions defined by the radiation diagram close to the air-ground interface. Therefore, part of the energy will be transmitted into the ground, and some energy will travel through the air. When the source is located exactly at the air-ground interface, the entire downward energy is transmitted into the ground. When the source is above the air-ground interface most of the energy is reflected at the air-ground interface. Therefore, a good coupling between the transmitting antenna and the ground is therefore essential for a maximum signal to be transmitted into the ground.

Reflection, diffraction, refraction, transmission - The emitted EM waves will then follow the principles of reflection, transmission and refraction according to Snell-Descartes and Huygens-Fresnel diffraction laws (Figure 1.1). The reflection and transmission coefficients (Eqns. 1.6, 1.7, 1.8 and 1.9, (Cassidy N. J., 2009) describe how the amplitude of EM waves is varying when waves meet an interface between two different media depending on the angle of incidence (Zoepritz equations). These coefficients are different depending on the transverse electrical (TE) or transverse magnetic (TM) component of the EM field.

$$R_{TE} = \frac{Z_1^{-1} \cos\theta_1 - Z_2^{-1} \cos\theta_2}{Z_1^{-1} \cos\theta_1 + Z_2^{-1} \cos\theta_2} \qquad 1.6$$

$$R_{TM} = \frac{Z_1 \cos\theta_1 - Z_2 \cos\theta_2}{Z_1 \cos\theta_1 + Z_2 \cos\theta_2} \qquad 1.7$$

$$T_{TE} = 1 - R_{TE} \qquad 1.8$$

$$T_{TM} = 1 - R_{TM} \qquad 1.9$$

Where Z_1 is the impedance in the first medium, Z_2 is the impedance in the second medium, θ_1 is the incident/reflection angle, and θ_2 is the transmission angle.

Received Signal - The receiving antenna first receives the direct wave in the air (V = 0.3 m/ns), then the direct wave in the ground ($V \approx 0.1$ m/ns), and then the various reflected and diffracted waves in air and in the ground. When the source-to-receiver distance is small (offset and angle of incidence almost zero), which is generally the case for ground penetrating radar acquisition in common offset, the arrival times are close, and some arrivals may interfere with each other.

The received EM signals are converted into an electrical signal which is digitally reduced under the shape of an amplitude as a function of time called the trace shown in Figure

1.2. These traces are then juxtaposed to obtain an image of the reflectivity (radar section) of the subsoil.

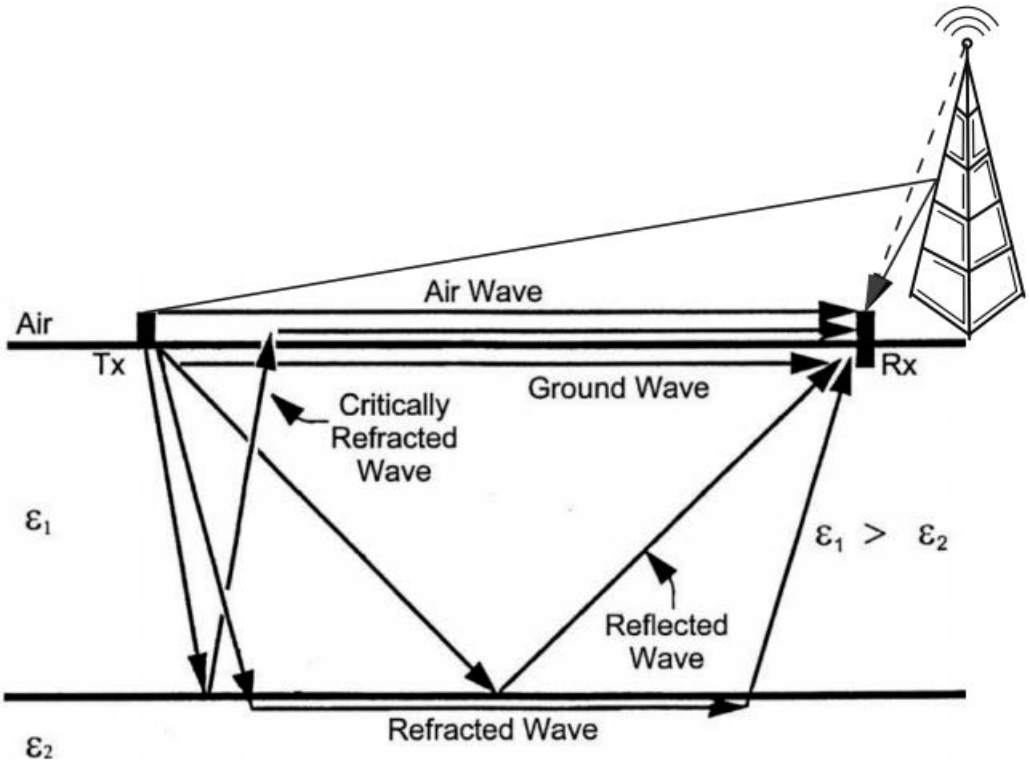

Figure 1.1 Path of propagation of electromagnetic waves in the ground in the case of a two-layer medium with contrasting dielectric permittivity (ε_1 and ε_2), after (Sperl, 1999).

2.3 Resolution and penetration depth

Ground penetrating radar performance can be described in terms of two interrelated characteristics: maximum penetration depth and resolution (Davis & Annan, 1989). The maximum penetration depth refers to the maximum depth at which a buried target can be detected, and the resolution is the minimum separation between two buried targets so that they remain discernible. These two characteristics are strongly influenced by the electromagnetic properties of the medium (Noon, et al., 1998). In addition, there is a trade-off between penetration and resolution due to the dependence opposite of these two characteristics to frequency. For example, to penetrate the ground efficiently, low frequency signals are needed because the subsoil acts as a low pass filter. However, if the targets to be imaged are relatively close to each other, a wide bandwidth with a good resolving power is necessary, high-frequency signals.

Resolution is a concept common to all detection methods based on wave propagation and can be described in terms of received echoes: echoes can happen simultaneously, overlap

or be separated in time (Annan, 2009). The resolution therefore depends directly on the width (or center frequency) of the pulse propagating in the soil and is divided into two components, one lateral and one deep (Figure 1.3).

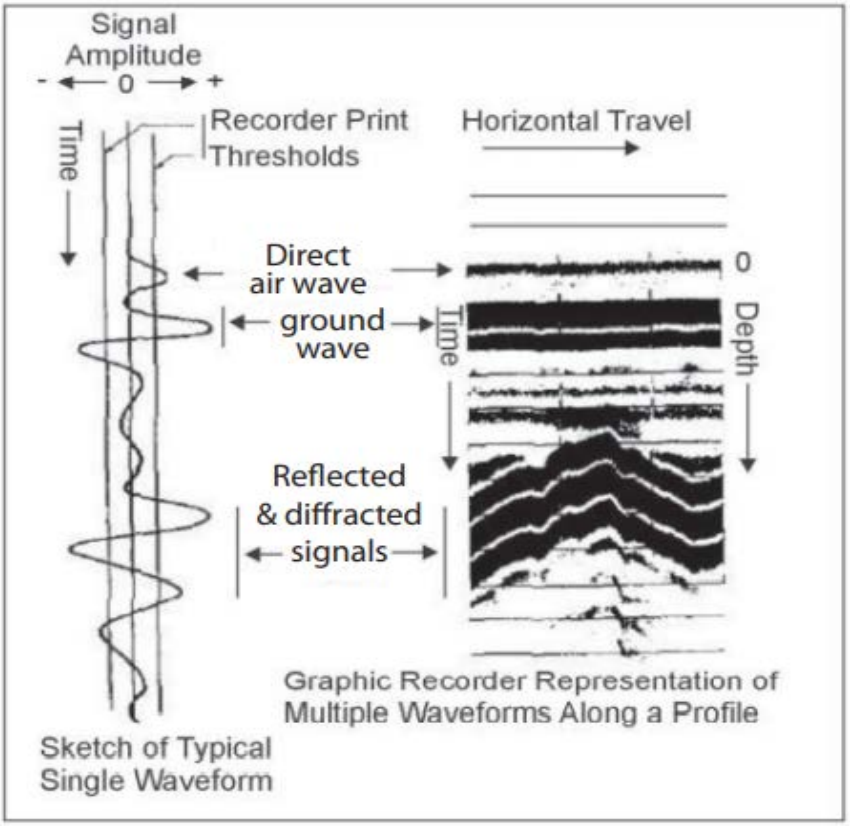

Figure 1.2 Signal received by the receiving antenna and the graphic profile display (radar section), after (Benson, et al., 1984).

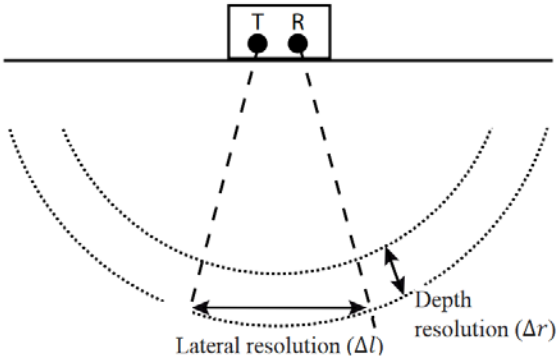

Figure 1.3 Ground penetrating radar resolution is divided into two components, depth resolution and lateral resolution, after (Annan, 2009).

In-depth (or vertical) resolution (Δr) is defined according to the Rayleigh criterion:

$$\Delta r \geq \frac{W_v}{4} \qquad 1.10$$

With *W* the width of the pulse and *V* the speed of EM waves. The width of the pulse is directly linked to the frequency band *B* which is equal to the center frequency f_c of the antenna, thus we have.

$$W = \frac{1}{B} = \frac{1}{f_c} \qquad 1.11$$

Therefore, the vertical resolution can then be expressed:

$$\Delta r \geq \frac{v}{4f_c} = \frac{\lambda_c}{4} \qquad 1.12$$

With λ_c the wavelength of the center frequency.

In an ideal case of a medium without attenuation, the vertical resolution is independent of the distance to the source. In practice, the attenuation causes a shift in the spectrum towards the low frequencies and therefore a decrease in fc (or frequency band *B*) with depth. The lateral resolution depends on the speed, the pulse width and distance to the source.

The lateral resolution (Δl) is equal to the radius of the first Fresnel zone for a monochromatic signal of frequency f_c and can be expressed (Annan, 2009):

$$\Delta l = \sqrt{\frac{d\lambda_c}{2}} \qquad 1.13$$

Where d is the depth of the target. If we calculate these resolutions for different values of antenna frequencies on the market, we obtain the values described in.

The maximum penetration depth is governed by the attenuation which characterizes the exponential decay of the signal as it propagates in the soil. For the EM waves, attenuation is mainly controlled by the conductivity of the medium. More the medium is conductive (like clays, or rocks saturated with water), the stronger the attenuation. Part of the energy is also dissipated by the phenomena of diffraction (scattering) in very heterogeneous media. The attenuation also increases with the frequency. Finally, the penetration depth also depends on the strength of the signal emitted, but this is limited by legislation so as not to interfere with other instruments (TV, radio, navigation instruments, etc.).

In the first order, the penetration depth (δ) of an GPR wave is given by:

$$\delta = \frac{2}{\sigma} * \sqrt{\frac{\varepsilon}{\mu}} \qquad 1.14$$

with μ the magnetic permeability, σ the conductivity, ε the dielectric permittivity. The penetration depth is of the order of 2 m at 800 MHz, 10 m at 250 MHz and may reach 30 m at 100 MHz, if the medium is moderately electrically resistive (see (Annan, 2009).

The success of a GPR survey therefore depends on an important factor, the prior knowledge of the target. The choice of acquisition parameters will depend on the depth, size, and nature of the target's cash flow, depending on the capacities and limits of GPR method that we have just described. We can also bypass this duality between resolution and penetration depth by performing multiscale imaging, i.e., multi-resolution, thanks to broadband or multi-frequency radar measurements.

Table 1-2 - Depth resolutions and lateral resolutions as a function of the center of the antenna, calculated from equations 1.12 and 1.13 for a constant speed in the medium of 0.1 m/ns and a target located at a depth of 1 m. These values are only indicative.

Frequency (MHz)	Depth resolution (m)	Lateral resolution (m)
50	0.5	1
100	0.25	0.7
250	0.1	0.45
400	0.06	0.35
800	0.03	0.25
1000	0.025	0.22
1500	0.017	0.18
2000	0.013	0.16

3 Data acquisition

3.1 Acquisition and topographic data

Topographic data has two interests in our approach. The first is from accurately position GPR profiles and correct topographic variations along the profiles. For 3D and pseudo 3D campaigns, precise positioning of GPR profiles relative to each other is vital for making correlations of a side to side or horizontal sections. For a GPR acquisition at 100 MHz and 250 MHz, topographic data should have a sampling interval of 2 m and 1 m, respectively, and a spatial precision of 5 cm and 3 cm (Cassidy N. J., 2009). The second interest is knowing the topography of the surface in detail to perform a morphological analysis marker present and then compare them with information from the data GPR.

During all acquisition missions, we used differential GPS systems for the topographic surveys, RTK survey method. We used this information during morpho-tectonic analyzes, and

for topographic corrections of our GPR profiles. The data are in the form of point clouds with *XYZ* coordinates. The topographic data corresponding to the GPR profiles are linearly interpolated to get a point every 20 cm. The 3D set of points is interpolated by the kriging method on grids, according to the density of points, of 2 x 2 m2 for GPS data using SURFER software, in order to obtain digital elevation models (DEM) that can be used in GIS software.

3.2 Differential RTK GPS

Principle - As its name suggests, the principle of differential GPS is based on difference of two signals received at two neighboring points which makes it possible to reduce the effects measurement errors. It is therefore enough to observe at a known point the fluctuations of measurements and subtract them from a second point observing the same satellites Figure 1.4. This corrects a large part of the measurement errors, whether they are related satellites (clock, orbits), propagation conditions (tropospheric effects, ionospheric, atmospheric) or to voluntary fluctuations in the transmitted signal. The positioning accuracy then drops from around 10-20 meters to a few centimeters and more so as the distance between the measuring points is small.

The "differential" mode exists in several variants. The most elaborate uses the measure of several phase differences, thus increasing the accuracy of the measurements. The RTK GPS we used, is that the receivers communicate by radio to transmit the corrections in real time and the data is processed also in real time. A disadvantage of RTK GPS is that it uses radio waves like ground penetrating radar. RTK GPS systems must therefore stay at an enough distance from ground penetrating radar not to disturb the measurements.

GPS data acquisition and processing - During the GPR mission, we had two Trimble 5700 RTK GPS systems and Piksi Multi RTK GNSS system, each made up of a rover, a base and a controller, transmitting corrections and data to each other in real time by radio. That system is dedicated to locating GPR profiles, and the other to topographic surveying. Indeed, even though the relative positions of the RTK GPS data are known to an accuracy of a centimeters, it is necessary to precisely know their absolute position in order to import them into GIS software and superimpose them on other geo referenced data (high resolution). The relative position of the mobile RTK GPS data is already corrected in real time, their position is simply translated by the same quantity as the translation of the base position after correction. The relative positions of the mobile receiver with respect to the base are calculated in a second step for the data from kinematic systems.

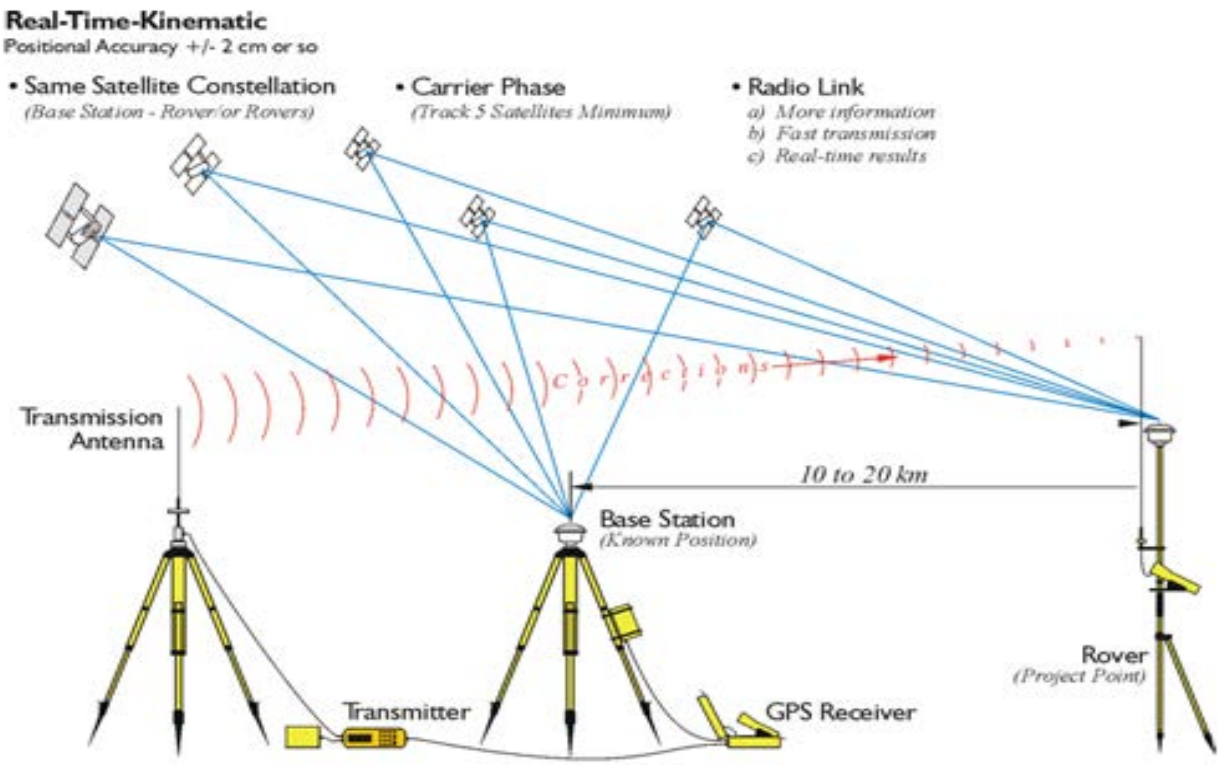

Figure 1.4 RTK and DGPS/GNSS. Source: after (Jan, 2015)

3.3 GPR data acquisition

The type of GPR system and the acquisition geometry are parameters to be chosen before to start the acquisition according to the depth of the target, its geometry (size, composition, orientation), the nature of the target and its surrounding.

Description of the GPR system. A ground penetrating radar system is made up of two antennas and their electronics, a control (recorder, analog-to-digital converter), a trigger, a computer, and a power supply Figure 1.5.

There are different types of GPR antennas; we can distinguish them according to:

• Their center frequency generally offered by manufacturers between 25 MHz and 2.5 GHz. The lower limit is constrained by the physical limits of propagation EM waves in sub-surface materials. Depending on the size of the target, the center frequency, on which the resolution depends, should be minimized to avoid energy losses associated with attenuation of high frequencies.

Figure 1.5 The different components of a GPR system. Image Source: (Canada: Geoscan)

• The absence or presence of shielding around the antennas. The shielding is intended to maximize the energy transmitted into and received from the ground, and minimize the energy of direct waves, waves reflected in the air, external electromagnetic noise. The downside to shielding is that it generates additional responses, which can be reverberate for a long period of time (ringing). Generally, the antennas large sizes and therefore low frequency (less than or equal to 100 MHz) are not shielded and should preferably be used on an open site.

• Separation of antennas. Generally shielded antennas contain the transmitter and the receiver on the same box, and the distance (offset) between them is constant, while unshielded antennas are generally separable.

• The transmission/reception mode which depends on the orientation of the antennas with respect to each other. If the transmitting and receiving antennas are parallel, we will speak of Transverse Electric (TE) mode, with reference to the electrical component of the field waves. When the antennas are one after the other, it is called Transverse Magnetic (TM) mode in reference to the magnetic component of the wave field.

The acquisition unit is the heart of the system and controls the time of generation and signal reception. The required precision is less than 10^{-12}s over a signal duration of 1000 ns. It is connected by optical fiber to the electronics of the antennas. The generation of the signal can be triggered manually (computer keyboard), or automatically in time or in distance by an encoder wheel or tachometer (Lehmann & Green, 1999), GPS). The acquisition software, installed in a laptop, is used to define the acquisition parameters (frequency, spatial acquisition,

duration, summation) and to view the profile during the acquisition. The GPR has long been the only geophysical imaging method capable of display in real-time reflectivity images; recently joined by the last generation of resistivity meters that display the pseudo-sections of the conductivity.

When acquiring the GPR profiles, we used a MALA series GPR instruments manufactured by Guidelinegeo AB (MALA Geoscience AB) company. That is MALA Professional Explorer (ProEx) control unit with MALA GPR antennas (MALA 250 MHz and 500 MHz center-frequencies shielded antenna and the MALA RTA (Rough Terrain Antenna) 50 MHz unshielded antenna (MALA Swedish trademark) (Guideline Geo, 2021).

The MALA ProEx control unit is the most versatile control unit in the MALA Geoscience range and the high-end full range system. The antennas are connected to the optical module, via their electronics, to a ProEx control unit, allowing optical acquisition (Guideline Geo, 2021).

The MALA RTA 50 MHz unshielded antenna is resistance decade designed antenna and center frequency is 50 MHz. The antenna offset is 4.2 m and ground coupled, pulsed technology antenna (Guideline Geo, 2021).

But MALA 250 MHz and MALA 500 MHz shielded antennas are both bow-tie designed antennas and their center frequencies are 250 MHz and 500 MHz. The offset of the antenna 0.31 m for the 250 MHz antenna and 0.18 m for the 500 MHz antenna. There is also ground coupled, pulsed technology antennas (Guideline Geo, 2021).

3.3.1 Mode of acquisition

The purpose of GPR is to receive the signal reflected by the interfaces of the subsoil. It is a geophysical method analogous to seismic reflection. Therefore, the modes of acquisition, processing and representation are similar. The constant offset acquisition mode is characterized by a constant distance (S) and the same orientation between transmitting and receiving antennas at each measurement point. These measurement points are equidistant (Δx) and distributed along profiles. In each point, the recorded trace describes the amplitude variations of the reflected signal as a function of time. The tracks are then represented as a function of the distance along the profile in order to obtain an image of the reflectivity (radar section) of the ground (Figure 1.6). Variations in amplitude and time reflections indicate variations in speed, attenuation, contrast of impedances and geometry of interfaces.

The second acquisition mode in the common midpoint (multiple offsets, CMP, Figure 1.6) is carried out by gradually moving the antennae away from each other at regular intervals relative to a central point (Mid-Point). The reflections then appear in the form of hyperbolas and the equation for a tabular medium can be expressed as follows:

$$t^2 = t_0^2 + \frac{x^2}{v^2} \qquad 1.15$$

with t the arrival time of the reflection, t_0 the arrival time at zero offset, x the offset and V the average speed between two interfaces, the unknowns being the speed and the time arrival at zero offset (t_0).

CMPs are mainly used to determine speed of the radar waves in the medium as a function of depth and are achieved at a few points of the investigated area. The ideal would be to know the speed at any point in the medium, this is called multi-offset acquisitions or multiple coverage reflection. This method of acquisition (as in seismic reflection) reduces the signal / noise ratio by summing the traces and providing knowledge of the speed at any point in the medium. This type of data can be inverted in order to find the physical properties of the medium (dielectric permittivity, conductivity). However, given the distances considered here and the number of profiles, this heavy acquisition had to be abandoned. Only a few (3-4) CMPs were therefore acquired in order to estimate the speeds of radar waves.

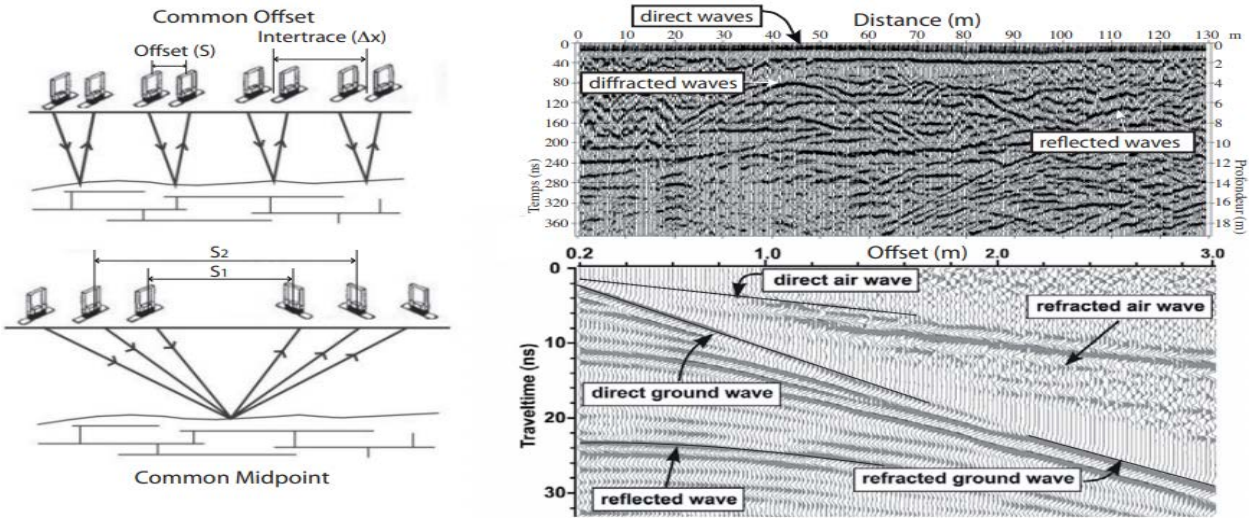

Figure 1.6 The different acquisition modes typical of ground penetrating radar, with constant offset at the top, in the CMP mode at the bottom. On the right, an example of the typical image obtained for each of the modes with the different types of arrivals indicated (Figure 1.1) after (Bano, 2000; Steelman & Endres, 2011).

3.3.2 Acquisition parameters

The triggering of the acquisition is controlled by a coding wheel (pre-calibrated) attached to the antenna. The center frequencies of the chosen antennas impose a sampling in time (Δt) and in space (Δx) respecting the Nyquist criterion:

$$\Delta t \leq \frac{1}{2 f_{max}} \qquad 1.16$$

$$\Delta x \leq \frac{v}{2 f_{max}} \qquad 1.17$$

Given the relationship between frequency band and center frequency, it is recommended to use a sampling frequency greater than 6 to 10 times the center frequency (no anti-aliasing filter), i.e., a sampling frequency of 1000 MHz and of 2500 MHz for the selected antennas ($\Delta t \leq 1$ ns and 400 ps respectively). For an average speed of 0.1 m.ns–1, the sampling interval between the measurement points must be less than 4 cm. In order to optimize the speed acquisition time, we also adapt the acquisition time and therefore the number of samples per trace. In addition, at each point, a trace is issued and received several times, then stacked (summed). By increasing the number of traces summed up, the signal/noise ratio is increased but the acquisition speed is reduced. These last two parameters are adapted to each site investigated, depending on the estimated penetration depth from initial test of measurements.

3.3.3 Acquisition geometry

The acquisition geometry depends on the size and orientation of the target. It is one the originalities of our application of ground penetrating radar to paleo seismology. Indeed, the first objective is to image buried morphological markers on both sides of a fault and not the fault plane itself. More specifically, the purpose of this application is to measure the amount of displacement accumulated on buried markers. We are therefore looking for markers oriented perpendicularly at the fault plane, or close to perpendicular. In order to cut these markers perpendicularly, we make the GPR profiles parallel to the fault. These profiles have been conducted closest to the fault trace in order to determine precisely where the markers morphological intersect it and cover minimum 50 m on either side of the fault in order to define the geometry of these markers. We also performed 3 to 4 perpendicular profiles to the fault on each site in order to image the fault zone and help us correlating reflectors on both sides of the fault. We have just described the different types of data acquired as well as the signals and sources of noise and EM wave attenuation. The objective of Signal processing described below is to reduce these effects in order to highlight the reflections.

4 Processing

4.1 GPR data processing

The processing of GPR data includes a subjective part because it depends on the opinion and the experience of the interpreter as well as the nature of the dataset and the targets. We have followed the classic steps of advanced GPR data processing as described in reference books and articles (give a reference here). The goal of these treatments is to increase the signal to noise ratio, to image as correctly as possible the various complex interfaces, while avoiding or correcting artifacts. The flow chart of the processing is given in Figure 1.7.

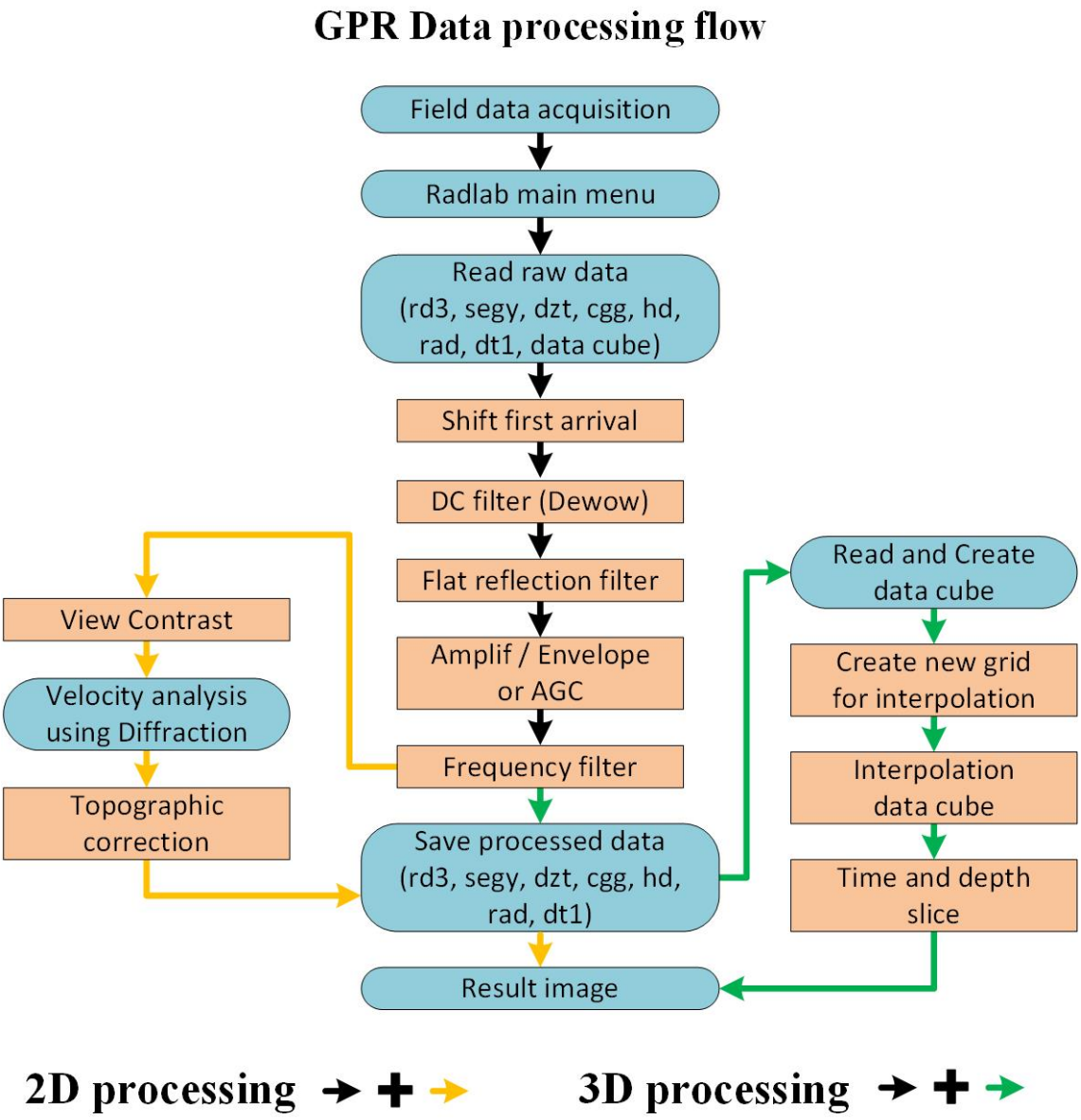

Figure 1.7 GPR data processing diagram. Lighter orange is filter and processing step, lighter blue is data in, out and analyzing step.

4.2 Time-zero corrections

The data is first converted from commercial Ramac format to Seismic Unix format, software that we used for data processing. The arrival time of the direct wave (T_0) is then aligned in all the profiles to correct the offsets or drifts in recording time that may result from stopping/resuming the acquisition, too low battery problem, the length and tension of the optical fibers, etc. In order to detect and realign the arrival times we have chosen as a criterion the first passage from a positive amplitude (in black in Figure 1.8a) to a negative amplitude (in white in Figure 1.8a) or vice versa.

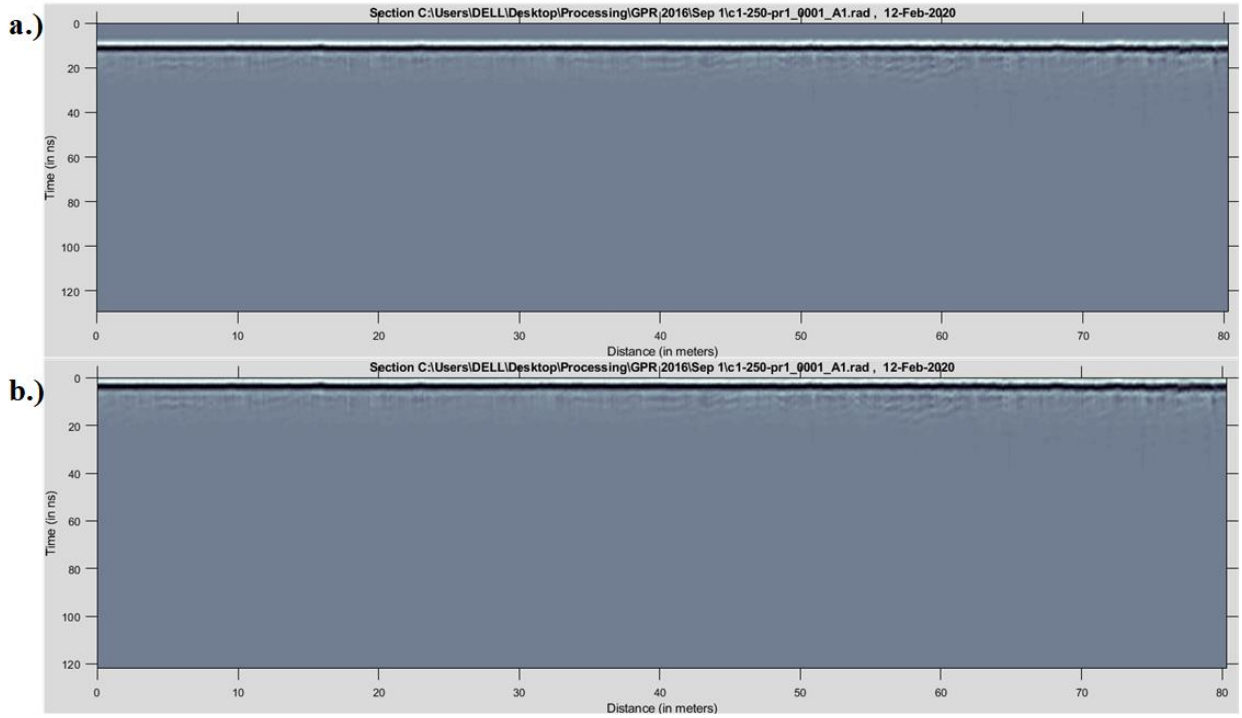

Figure 1.8 a) Example of raw GPR profile before processing; b) GPR profile after time-zero correction.

4.3 Editing data

This step is essential and tedious. It asks beforehand to have the location and topography of profiles obtained from GPS data and LiDAR. Due to acquisition conditions, errors, and obstacles in the field, the profiles must be combined, reversed, sorted. White traces must be added in order to fill acquisition stops when crossing fences, streams and other obstacles. When all the GPR profiles are corrected, it is necessary to check and correct the acquisition parameters entered in the headers of each trace as well as adding the position in *XYZ* of each track obtained from GPS data. Like GPR profiles and GPS were acquired separately, landmarks were placed

in the field every 30-50 m and read by the two systems in order to readjust the two data sets. The localization traces can also be used to correct the triggering irregularity problems associated with the roughness of the ground, the jamming of the encoder wheel etc. This is done by interpolating the traces to ensure regular spacing, necessary during subsequent processing steps such as migration.

4.4 De-wow, ringing reduction and lateral equalization of the traces

This step consists of removing the noise created by the fitting and the acquisition. The "wow" is the result of the saturation of the signal by the first arrivals of the direct waves and inductive coupling (Annan, 1993). The ringing is due to the multiple reflections on the shielded antenna or the air/ground interface due to poor antenna coupling with the ground. In addition, as this coupling is not regular along the profile, the amplitude of the signal transmitted in the soil varies laterally and is not related to the changes of physical properties of the medium (see Figure 1.9).

The "de-wow" consists in reducing the DC component of the signal and its drift in time by subtracting the average value of each trace and applying a high pass filter, respectively. The ringing is reduced by subtracting from each trace, the trace averaged over a sliding window of a given width, this also reduces the amplitude of the horizontal reflectors. (Kim, et al., 2007) propose other methods more sophisticated in order to suppress the ringing.

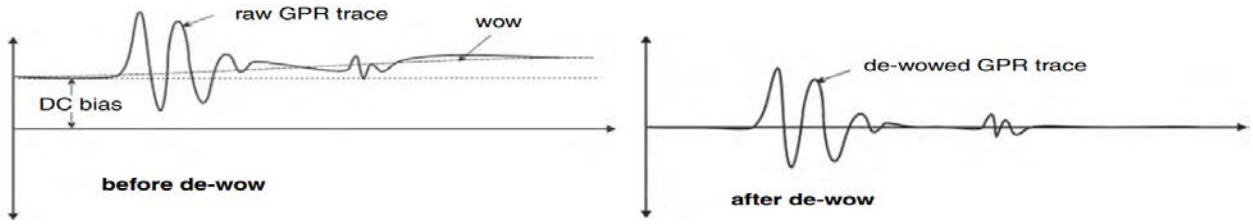

Figure 1.9 Effect of de-wow filter. After (Cassidy N. J., 2009).

The amplitude of the traces is equalized laterally by normalizing each trace by its maximum amplitude value or its RMS value. In (Figure 1.10), we notice in particular the reduction of the wave in the air which increases the dynamics of the image: the reflections appear better, as well as the beats which have been reduced but not suppressed.

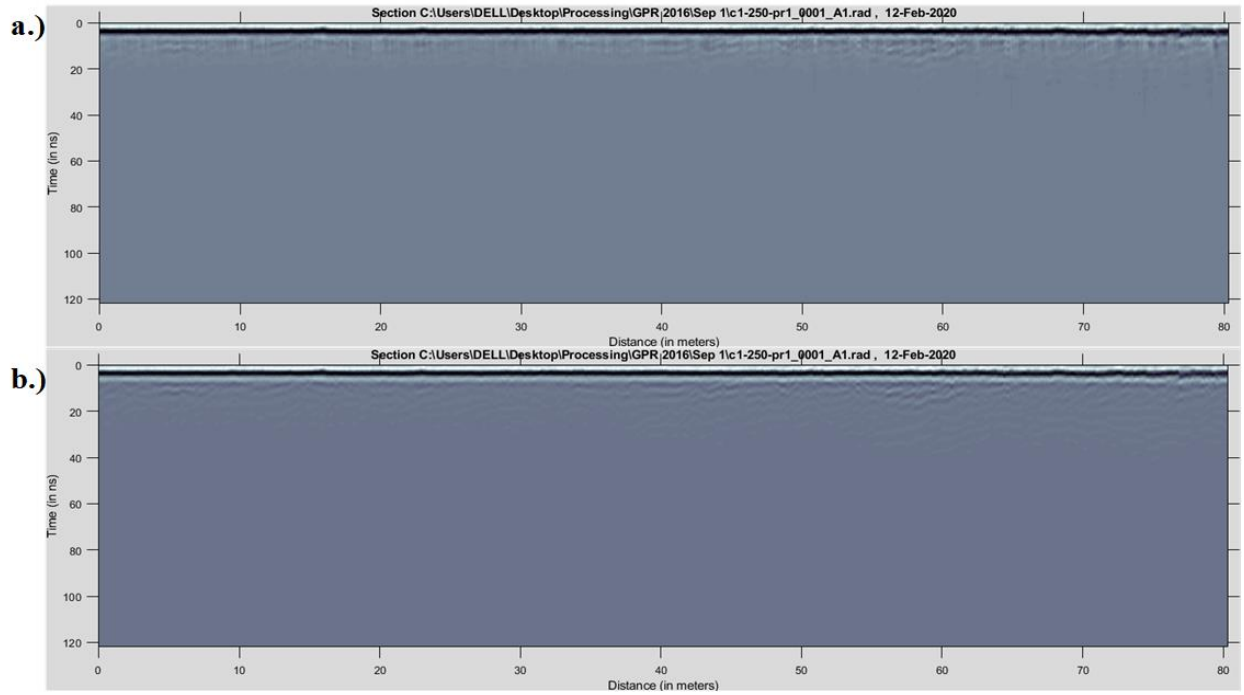

Figure 1.10 De-wow processing. a) Example of GPR profile before De-wow processing; b) GPR profile after De-wow processing.

4.5 Filtering

Filters are typically applied to remove human induced noise and to improve the visual quality of the data. They are also useful to highlight certain aspects of the data to facilitate interpretation. There are many filter types, 1D (temporal or spatial) or 2D, simple or sophisticated, in time or frequency domain. We used a first filter, high pass during the de-wow, and a band pass filter to remove all signals of lower frequencies or greater than the signal frequency band determined from the data spectrum. Depending on the medium, the frequency band will be translated towards the low frequencies relative to the frequency band of the source signal. We also apply a spatial filter, in the form of a weighted sliding average, which improves the continuity of reflectors. This sliding average manages to reduce air diffraction hyperbolas when applied to a window wide enough but tends to smooth the data and therefore reduce the resolution. (Bano, et al., 1999; Sun & Young, 1995) have proposed a method to remove these diffractions in air but this method cannot be fully automated and requires the presence of the vertex of the diffraction hyperbola on the profile.

4.6 Flat Reflection Filter

Ground penetrating radar data often presents noise that appears as coherent horizontal reflections and periodic. This is a ringing noise effect, due to the instrumentation. This noise appears when the signal-to-noise ratio is less than 1. If it is not subtracted, this noise can completely mask reflections from deep geological structures. These exists several methods to remove these flat reflections (Kim, et al., 2007). The method used by Radlab (Software developed at EOST, Strasbourg) is a subtraction of an average trace, or background removal. As this noise is consistent over the entire length of the section (real reflections are much less consistent), if we take the average of the traces on a sliding window in x, we thus obtain an average trace containing only resonant noise. By subtracting this mean trace from the data, we thus remove the flat reflections noise (Figure 1.11). However, there is always a risk of removing real horizontal reflections appearing at the same time and coming from geological structures, such as water tables. In our case, however, this has an advantage because it allows sloping reflectors to appear better. Figure 1.11 shows a GPR profile with and without the Flat Reflection Filter applied. The data is much less noisy, and we see appearing the reflections coming from a channel structure.

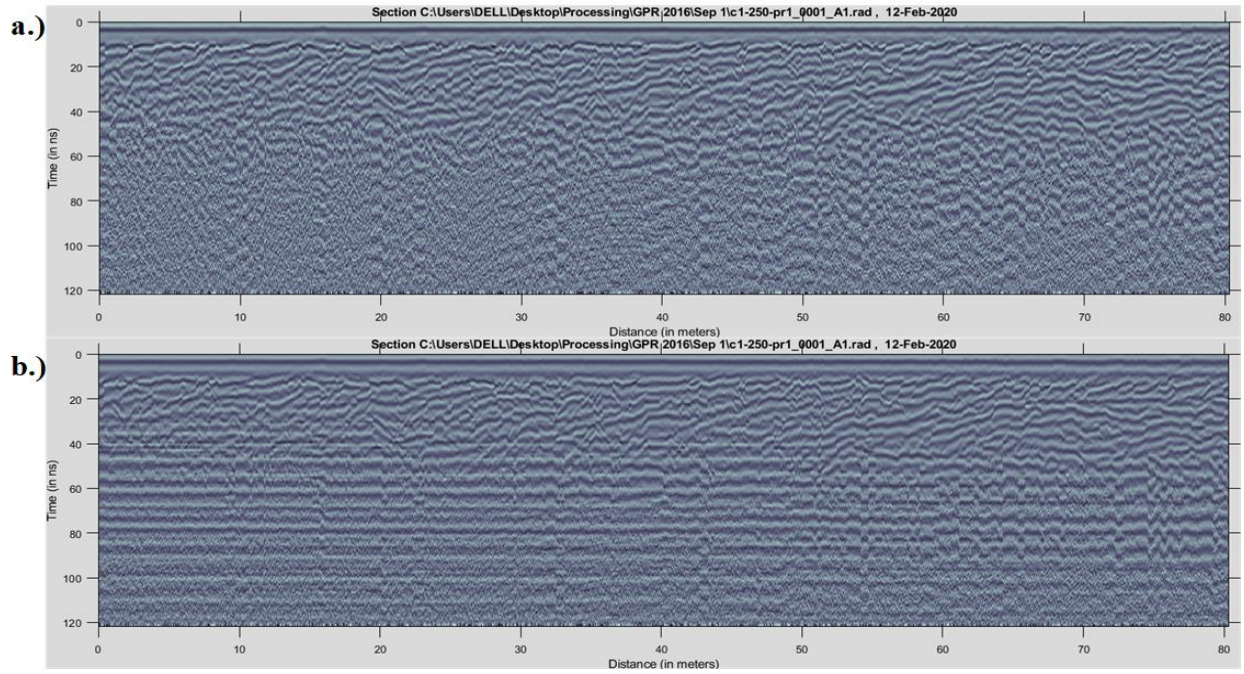

Figure 1.11 Flat reflection filter processing. a) Example of GPR profile with Flat reflection filter processing; b) GPR profile without Flat reflection filter processing.

4.7 Amplification - Time gain

The signal is then amplified in order to better see the low amplitudes. We give a value of 80 dB: the factor between signals of smaller amplitude and signals of higher amplitude is 40 in this case (Figure 1.12).

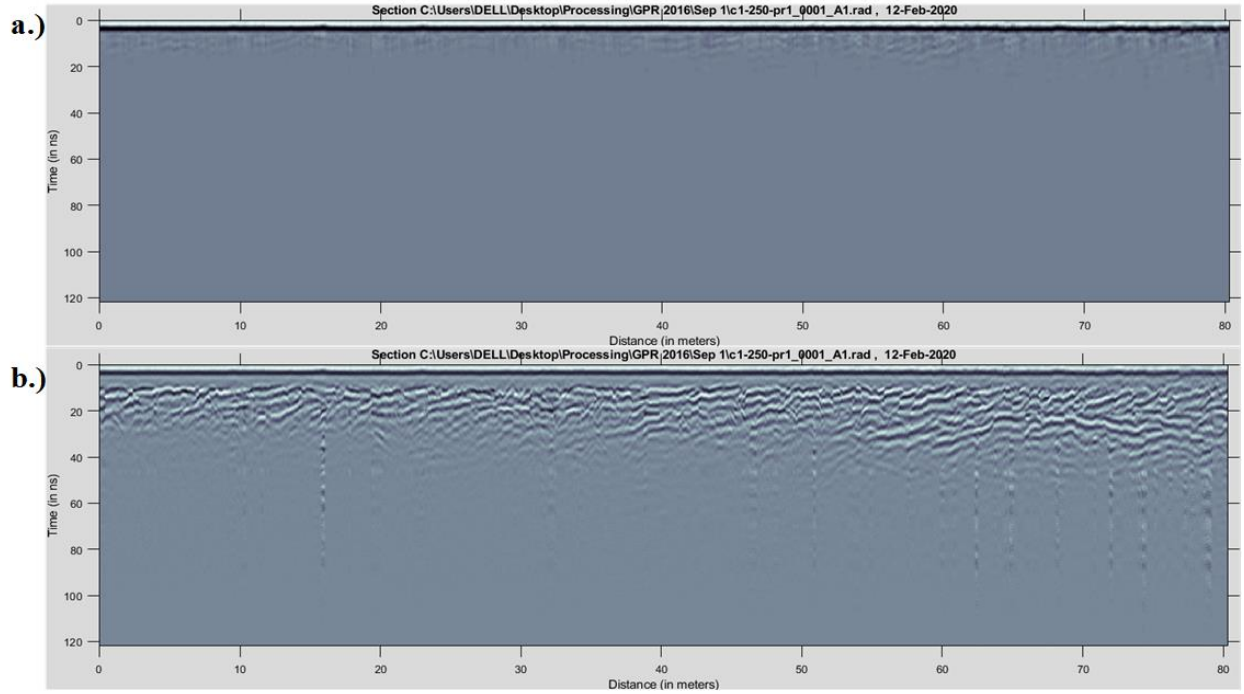

Figure 1.12 Amplification processing. a) Example of GPR profile before Amplification processing; b) GPR profile after Amplification processing.

4.8 Frequency Filter

Band pass filters are used to remove unwanted frequencies from the traces. Frequencies below the lower cut-off frequency and above the upper cut-off frequency are attenuated. The band pass filter dialog is used to adjust the settings for band pass filters applied to the data. Both FIR (finite impulse response) and IIR (infinite impulse response) filters are available. FIR-filters are slower but generally provide better results. The upper and lower cut-off frequencies define the boundaries of the band pass of the filter (Figure 1.13).

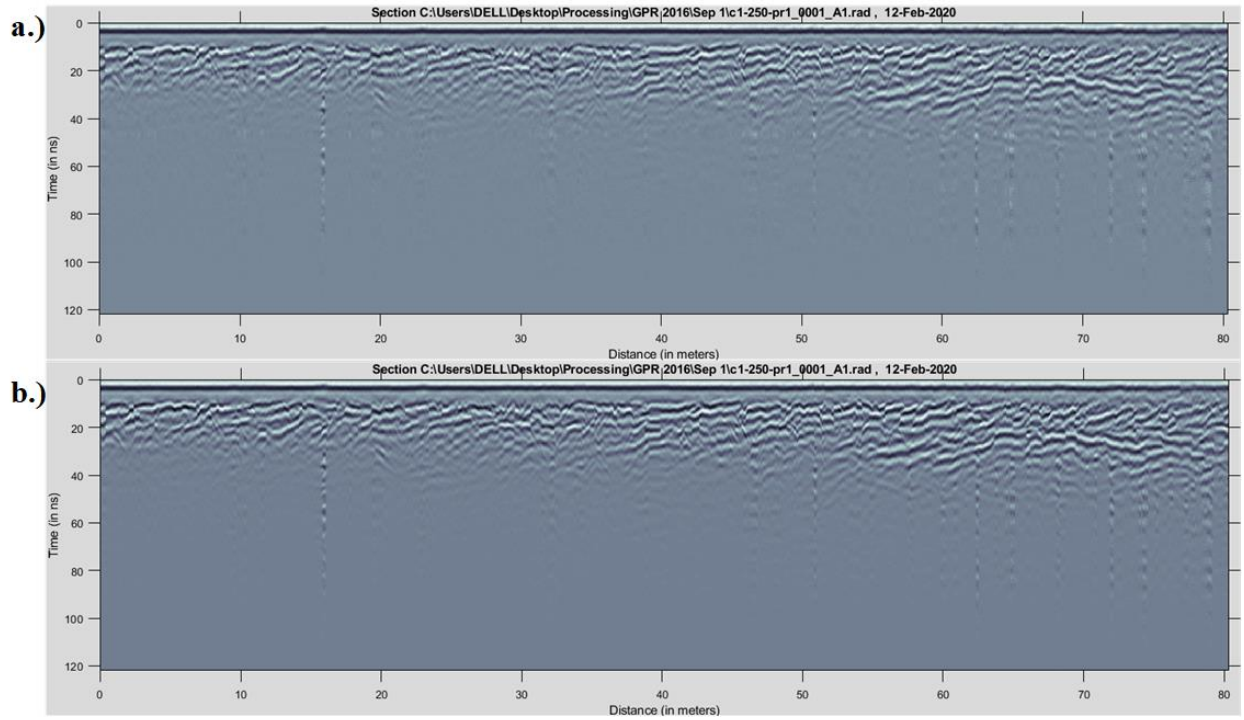

Figure 1.13 Frequency filter processing. a) Example of GPR profile before frequency processing; b) GPR profile after frequency processing.

4.9 Automatic gain control

This filter attempts to adjust the gain of each trace by equalizing the mean amplitudes observed in a sliding time window. A short window gives a more pronounced effect, the extreme of which would a one-sample window which would cause all amplitudes to be equal. The other extreme would be a time window of the same length as the trace. This would have no effect on the trace. After equalization a constant multiplier is applied to the trace to make the resulting amplitudes reasonable (Figure 1.14, Figure 1.17).

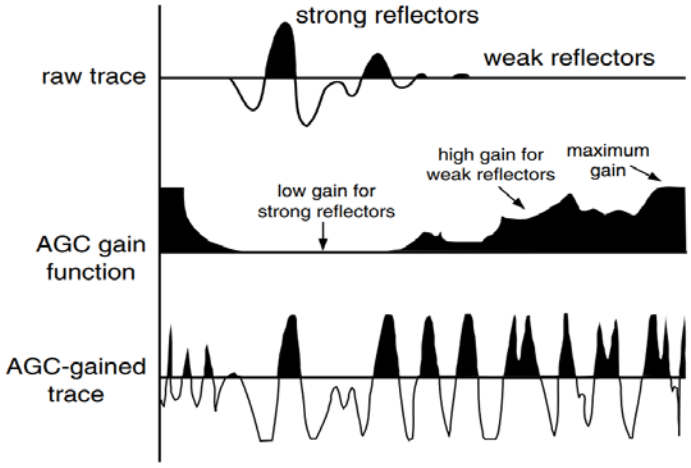

Figure 1.14 The effect of an AGC function applied to a radar trace. See (Inc., 2001; Inc, 2020).

4.10 Velocity analysis

In order to convert the time radar section into depth radar section we need to know the speed of radar waves in the medium. A common method (coming from seismic) is by analyzing the common mid-point CMP) profiles. For a range of velocities, the CMP data are corrected for NMO (normal move out) with a constant velocity and then a summation (stack) is preformed (See Figure 1.15 below, (Yilmaz O. , 1987)).

A 2010 GPR study jointly by Jilin University and Tohoku University of the Deren active fault determined that the velocity of radar waves within the subsurface sediment was 0.12 m/ns (Lu, et al., 2010).

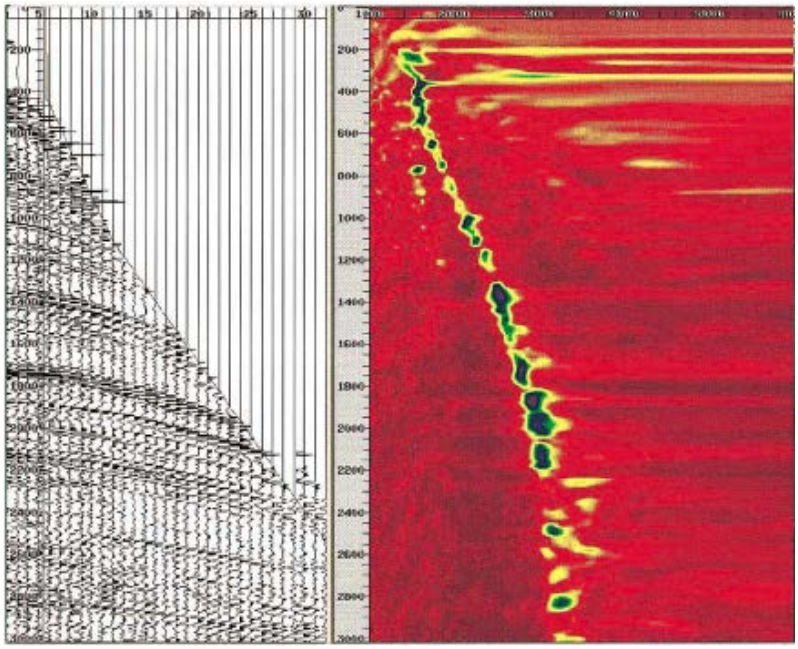

Figure 1.15 Velocity analysis by calculating the semblance over reflections hyperbolas (Yilmaz O. , 1987) the maximum of the energy gives the value of the velocity for the given time.

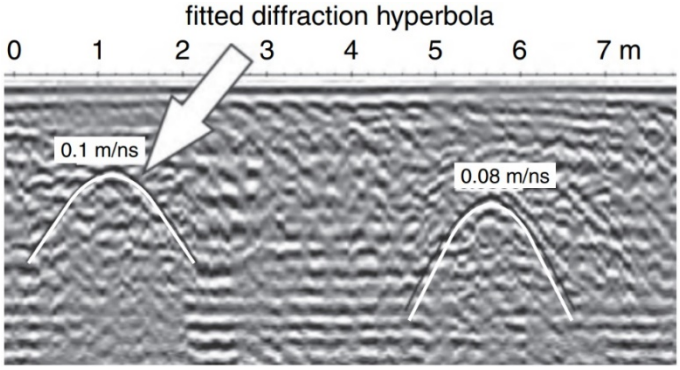

Figure 1.16 Radar velocity analysis by diffraction hyperbola fitting. After (Cassidy N. , 2009).

Another kind of velocity analysis is by analyzing the diffractions hyperbolas on the common offset (CO) GPR data. This type of analysis provides an estimate of speeds with an uncertainty of 10% (Figure 1.16) (Cassidy N. J., 2009).

A velocity estimation by diffraction analysis (not shown here) on CO GPR data gives a mean velocity of 0.135 and 0.095 m/ns for the data collected in all the GPR survey. The difference in velocity is explained by the soil humidity for the weather condition period during the GPR survey. We have been used a constant average speed for all active fault study area, because we have just CO GPR data (Figure 1.18). (Table 1-3)

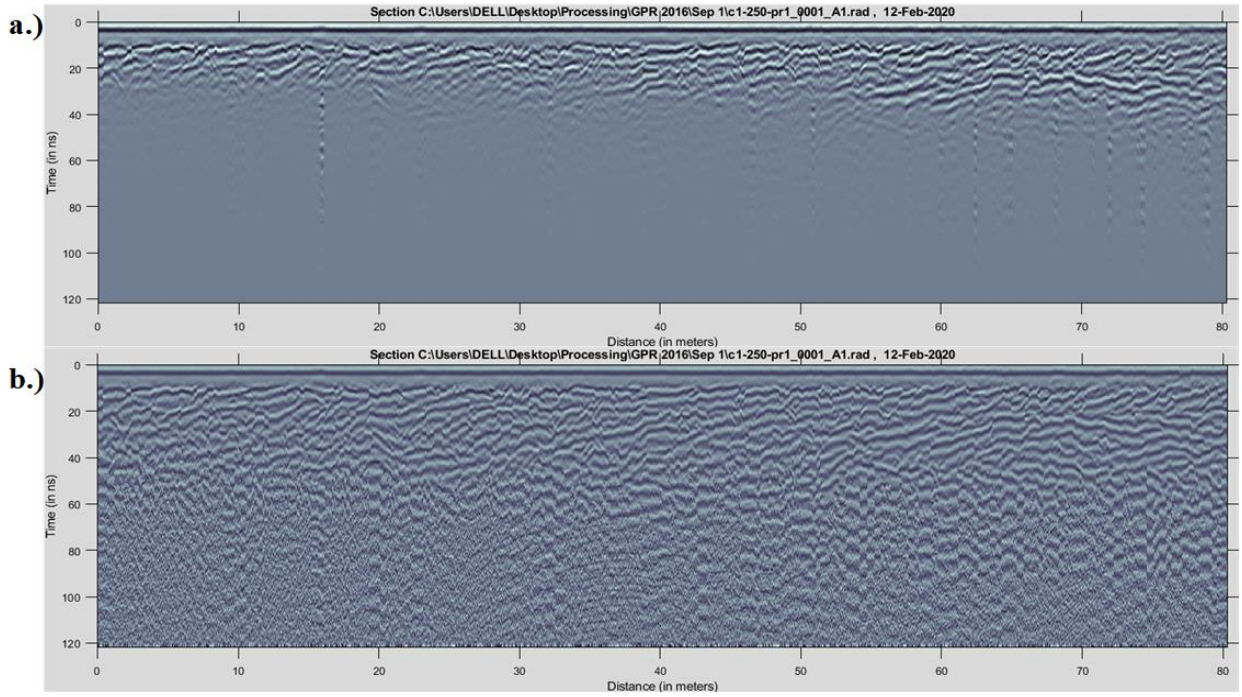

Figure 1.17 AGC processing. a) Example of GPR profile before AGC processing; b) GPR profile after AGC processing.

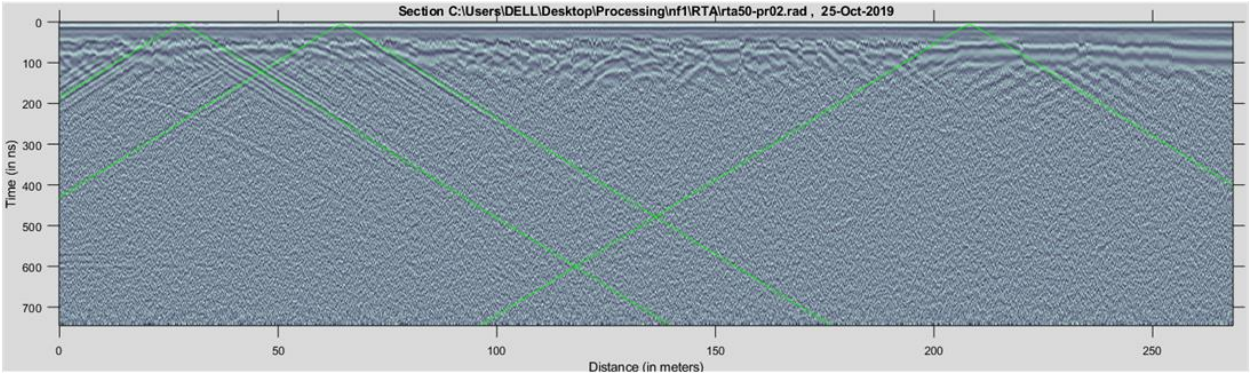

Figure 1.18 Hyperbola analyze. Green line is surface reflected air wave hyperbola, air wave velocity is 0.3 m/ns.

4.11 Migration

The aim of migration is to spatially reconstruct the structures visible in the GPR profiles, focusing the diffraction hyperbolas (coming from the subsoil) into one-point source and repositioning sloped or non-planar reflectors in their actual position. This process, which we applied in 2D, uses the speed of the waves in the medium estimated from the CMP/diffractions analysis. We used the migration of Stoltz (or F-K migration) which is one of the most common methods (Stolt, 1978). Migration was only kept in the processing chain when it improves the GPR images. Indeed, intended for seismic signals, migration is not very efficient for GPR signals in a complex and heterogeneous medium due to the differences in wave propagation properties (Cassidy N. J., 2009). Recently, adapted algorithms to GPR data presenting a strong topography have been developed (Lahmann & Green, 2000; Streich, et al., 2007; Dujardin & Bano, 2013).

Table 1-3 GPR velocity chart.

Material	Velocity m/ns	Velocity ft/ns
Air	0.3	0.98
Ice	0.16-0.17	0.52
Dry Soil	0.15	0.49
Dry Sand	0.15	0.49
Granite	0.13	0.43
Dry Salt	0.13	0.43
Dry Rock	0.12	0.39
Limestone	0.12	0.39
Wet Rock	0.10	0.33
Concrete	0.08-0.12	0.26-0.39
Pavement	0.10	0.33
Shales	0.09	0.30
Silts	0.07	0.23
Wet Soil	0.06	0.20
Wet Sand	0.06	0.20
Clays	0.06	0.20
Fresh Water	0.033	0.11
Sea Water	0.033	0.11

Chapter 2 Applications and development of GPR imaging technique for active fault structures.

1 Introduction

During the 20th century, knowledge about the seismic phenomenon greatly evolved thanks to the development of seismology, geodesy, and paleo-seismology. While seismology and geodesy work on very short time scales compared to the earthquake recurrence time, paleo-seismology opens a field of observation covering several seismic cycles. These observations of repetitions of strong earthquakes at one or more sites along a fault made it possible to establish conceptual models of successions of seismic ruptures (Figure 2.1 and Figure 2.2). While some studies describe surface ruptures with different lengths and slides from one earthquake to another (Figure 2.1a) (Daëron, et al., 2007; Weldon, et al., 2004), others describe repetitive behaviors with a more uniform slip distribution (Figure 2.1b) (Sieh K. , 1981), or even characteristic behaviors (Figure 2.1c) (Schwartz & Coppersmith, 1984; Rubin & Sieh, 1997; Tapponnier, et al., 2001a).

A study compiling the results obtained from 45 trenches carried out in a single site of the San Andreas fault (displacements and ages of the last 15 strong earthquakes) suggests the possible role of a threshold of relative deformation accommodated on the fault, in the ' triggering of phases of strong seismic activity (Weldon, et al., 2004) (Figure 2.3). Similar observations have been made very recently on a normal fault in Italy (Schlagenhauf, et al., 2011). In these two studies, it appears that the quantity of stresses released by each earthquake varies from one earthquake to another and that the earthquakes do not release all the stresses accumulated during the interseismic period which precedes them. The repetition of earthquakes also does not appear regular over time but seems to alternate between periods of quiescence during which the stresses accumulate up to a certain threshold and the apparent sliding speed is therefore relatively low, and periods of high activity during which a large part of the stresses are relaxed during several strong earthquakes following each other over a short period of time. During these seismic swarm periods, the apparent slip speed over the fault is therefore much higher (Figure 2.3), (Weldon, et al., 2004). The intense activity phases would possibly be triggered by the fact that the fault has reached a maximum threshold of accumulation of relative deformation.

Whatever the interpretations, these studies confirm that knowledge of the earthquake slip as well as the age of earthquakes are two essential parameters for a better understanding of the repetition modes of earthquakes. On the other hand, due to the lack of regular behavior of earthquakes in the medium term, this study suggests the need to know more precisely the displacement and the date of the last 10-20 strong earthquakes at several points of a fault in order to better understand the mechanisms responsible for triggering, repetition and pruning earthquakes. Finally, this study also suggests the need to develop new methods, less expensive in time and less destructive than the trenches, allowing to find this information preserved in the first few tens of meters of the ground.

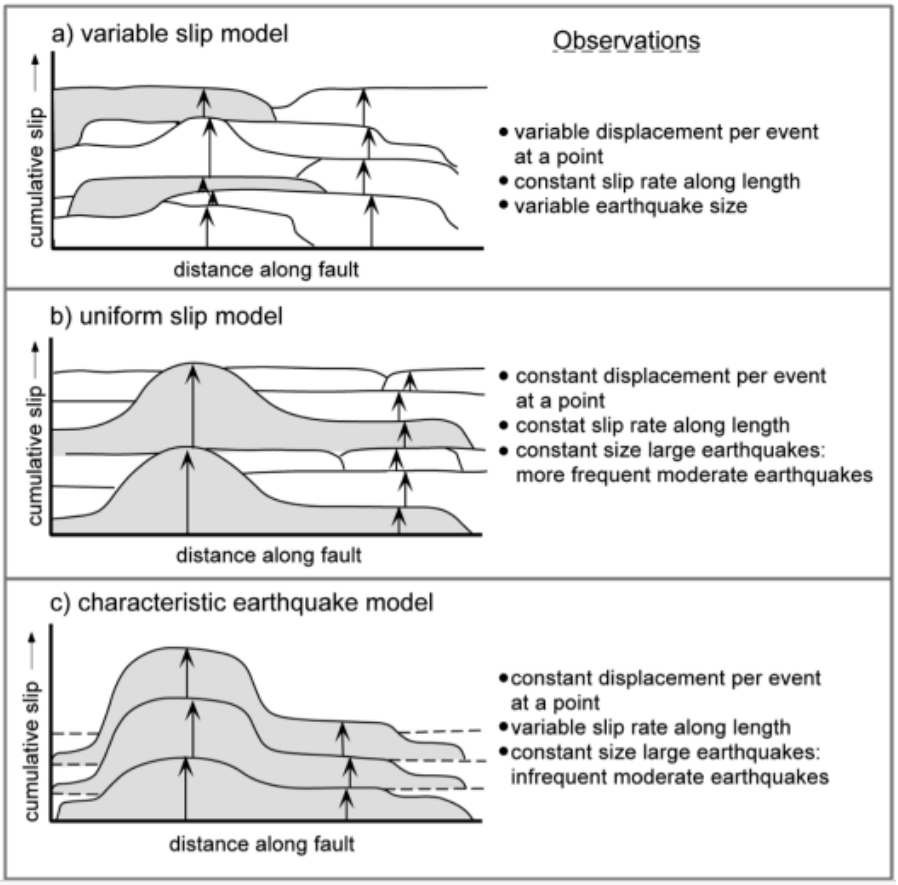

Figure 2.1 Conceptual models of succession of coseismic shifts. Different paleo seismological studies illustrate each of these models. a) the variable slip model describes earthquakes of variable magnitudes occurring randomly on the fault, b) the uniform slip model, after (Sieh K. , 1981) describes earthquakes repeating periodically on the same segment of the fault. Large earthquakes that can break several segments and moderate earthquakes accommodating slip deficits, c) the characteristic model describes earthquakes repeating periodically over the same rupture length and with similar magnitudes, after (Schwartz & Coppersmith, 1984)

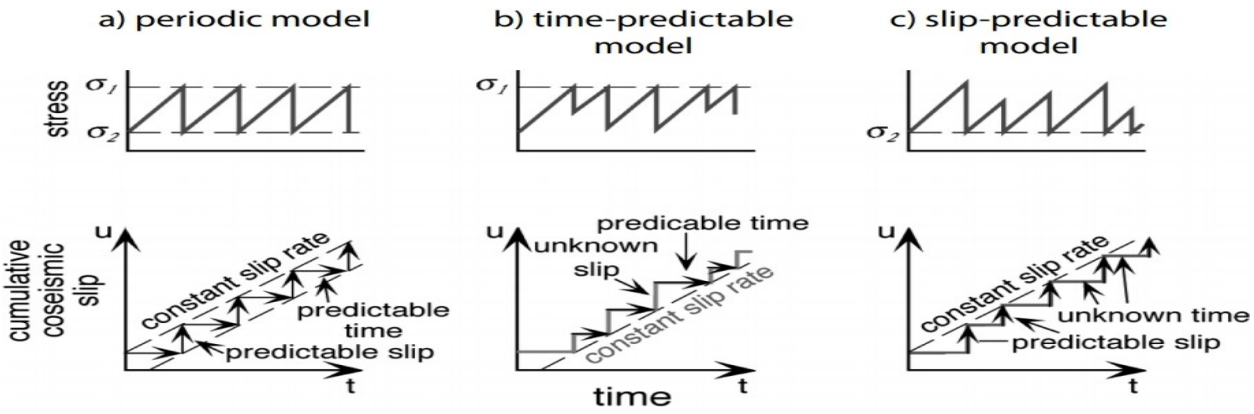

Figure 2.2 a) Periodic model of earthquake recurrence for which the levels of stresses before and after rupture are constant. This implies a predictable date and slip for each earthquake, b) Predictable time model based on a constant level of breaking stress. The stress drop and the amount of slip are not predictable, but if the last slip is known, the time to the next earthquake is predictable, c) Predictable slip model based on a constant level of stress after each earthquake. Depending on the time since the last break, the amount of slip is predictable, after (Shimazaki & Nakata, 1980).

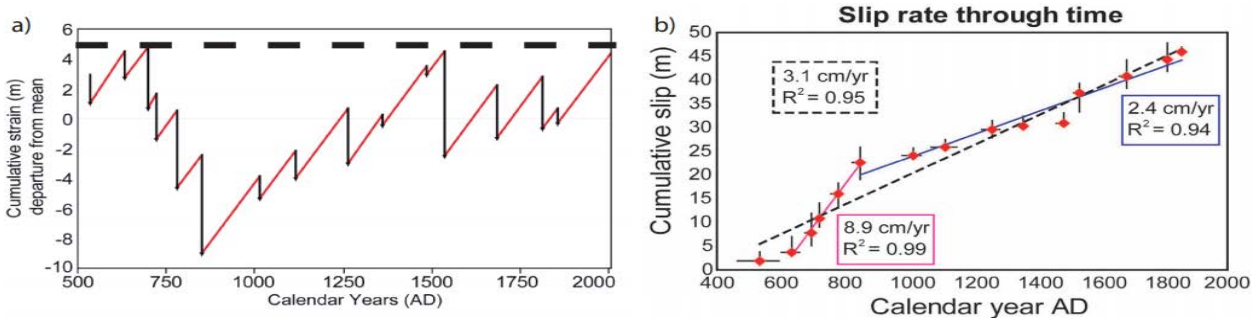

Figure 2.3 Identification of the last 15 strong earthquakes on the San Andreas fault reveals differences between each event, and variations in accommodation and relaxation slip over short periods of time including several seismic cycles, after (Weldon, et al., 2004). 'Seismic cycles' are nevertheless suggested, no longer on the scale of a single event, but to that of several events.

This chapter provides a brief overview of how Ground Penetrating Radar survey methods have been used in active faults in Mongolia and the results obtained on them. The main purpose of Ground Penetrating Radar surveys conducted on active faults since 2010 is to develop Ground Penetrating Radar surveys in Mongolia, to determine all types of active fault parameters, and to obtain a methodology for using a combination of Ground Penetrating Radar surveys and other modern technologies. To do this, we used many advanced research methods, such as Ground Penetrating Radar and remote sensing, and high-precision differential

positioning system, on several active faults, and as a result, we were able to achieve good results on all types of active faults. The results of these studies are classified by types of active faults and included in this chapter. Also, examples of three-dimensional survey and analysis, an advanced method of Ground Penetrating Radar research, are also presented in this chapter.

2 The GPR applications and method development for the active fault structures of the central Mongolia.

The GPR technique has been shown to be very effective in determining the horizontal and vertical displacement of faults, and in mapping old channels and ravines. GPR imaging results in the analysis of the boundaries of different layers and the areas where the reflections, refraction, deformation, and distortion of the waves occur, and a conclusion is made concerning the geological structure of the area (Davis & Annan, 1989).

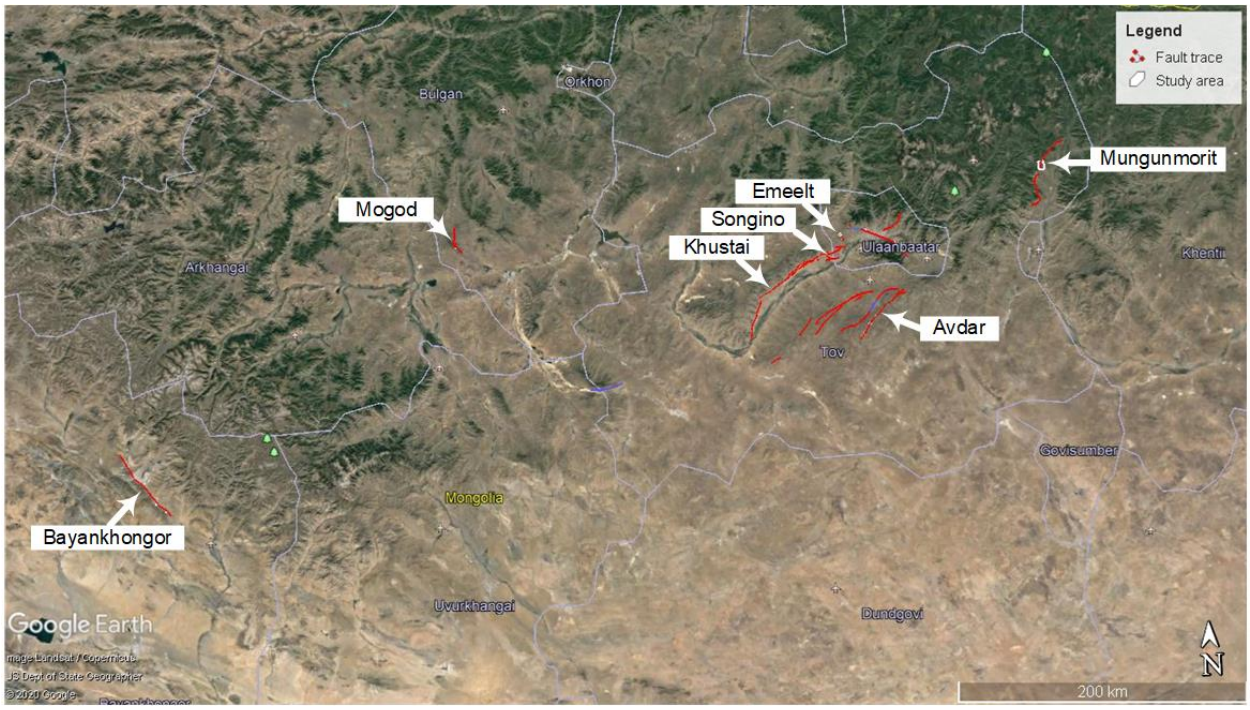

Figure 2.4 Location map of the studying active faults around Ulaanbaatar and the central region of Mongolia.

The Government of Mongolia approved the "National Earthquake Disaster Risk Reduction Program" in 2009, and according to this plan, the Ministry of Construction and Urban Development commissioned 12 province center engineering-geology, hydrogeology, seismic micro-region mapping and seismic databases. The research team of the Institute of Astronomy and Geophysics conducted it in 2012-2017. Within the framework of this study, the active fault research team conducted a detailed study of the active faults around Ulaanbaatar

and the central region of the Mongolia in the form of GPR studies, geological surveys and paleo-seismological trench surveys and then the results were combined (Figure 2.4).

3 Compressional structured fault examples

3.1 The Mogod active fault zone

3.1.1 Study area and geological environment

The center of Mogod soum is located 131 km from Bulgan province center and 340 km from Ulaanbaatar capital city of Mongolia. The territory is dominated by medium-high mountains and intermountain valleys with mountain black soil. There are Bayan, Mogod, Jargalant, Tulee and Dulaan Khar mountains. There are extinct Holocene volcanoes called Big and Small Togoo (Wikipedia, 2001).

The 1967 January 5 Mogod main shock (Mw 7.1) and its principal aftershock of January 20 (Mw 6.4 and below) occurred east of the Hangay dome in central Mongolia, a site of significant Quaternary volcanism (Barry & Kent, 1998), and involved principally N-S right-lateral strike-slip faulting (Natsag-YÏm, et al., 1971; Khil'ko, et al., 1985; Huang & Chen, 1986; Baljinnyam, et al., 1993). Right-lateral strike-slip faulting also occurs in western Mongolia, parallel to the NW-SE ranges of the Mongolian Altay (Bayasgalan & Jackson, 1999b).

The main co-seismic surface ruptures in 1967 occurred in four segments or zones. The segments with the largest and most continuous offsets consist of ~20 km of N-S right-lateral strike-slip faulting (Figure 2.5b) and ~10 km of thrust faulting with a NW-SE strike dipping NE (Figure 2.5c). In addition, less continuous and smaller-offset N-S ruptures (Figure 2.5a) occurred further north of the main strike-slip faulting, following the western side of the range front east of Mogod town. Other minor cracks occurred in the valley floor (Figure 2.5d). A brief description of the main characteristics of these ruptures is necessary to help constrain the seismological analysis and the geo-morphological interpretation.

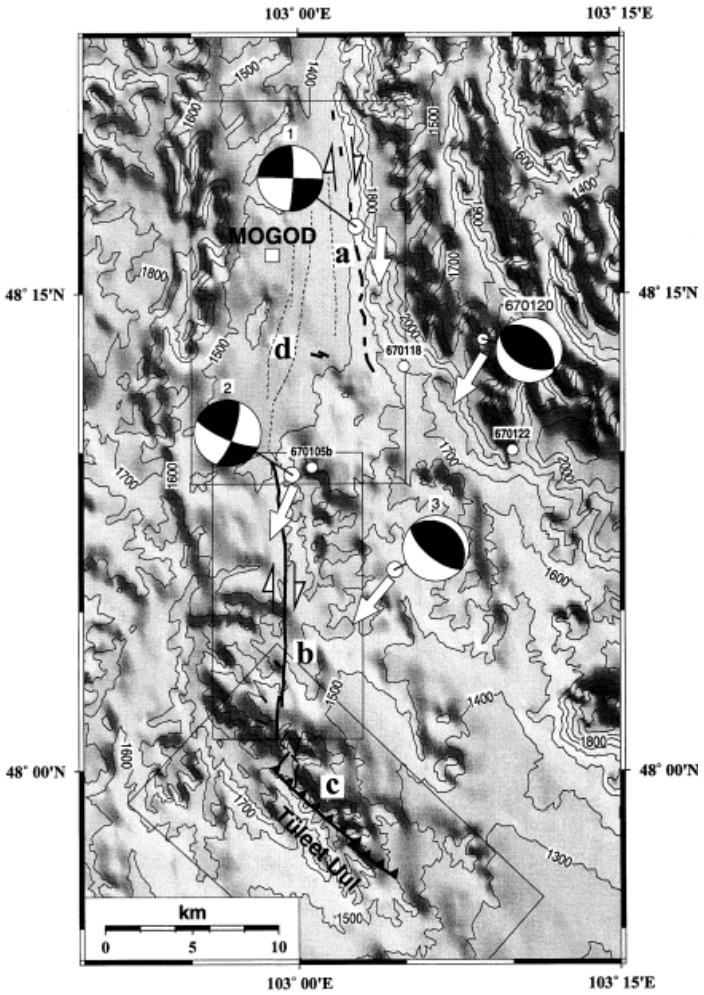

Figure 2.5 Summary map of the 1967 Mogod earthquakes (see Figure 2.4 for location). The main surface fault ruptures (b and c) are shown as heavy lines and are taken from (Baljinnyam, et al., 1993). The three main shock sub events (marked 1, 2 and 3) and the mechanism of the principal aftershock (670120) are taken from our analysis of the P and S waveforms. Slip vectors are shown as large white arrows, after (Bayasgalan & Jackson, 1999b).

3.1.2 Data acquisition method and survey parameters

A detailed study of Mogod active fault was conducted in August 2012 by a team of scientists from the University of Strasbourg, France, and researchers from the Institute of Astronomy and Geophysics, Mongolian Academy of Sciences. A comprehensive geological field investigation and geophysical survey (GPR, GPS, Magnetic) was conducted over a three-day period from 21 August to 23 August 2012 year.

In 2017, as part of the 60th anniversary conference of the Institute of Astronomy and Geophysics, a field trip to the Mogod active fault zone of the conference team was planned organize. The paleo-seismic trenches were excavating after a detailed geophysical study was

carried out in the area where the paleo-seismic trench was planned to be excavated. Geophysical surveys were conducted from June 13 to June 18 by IAG geophysical survey team, while trenches were surveyed from July 5 to July 18 by French scientist, IAG and Russian scientist team.

In these three zones, detailed MALA ProEx GPR system (MALA Swedish trademark) measurements were conducted with three different frequencies, MALA 500 MHz and 250 MHz shielded, and unshielded MALA RTA 50MHz antennas with 3-4 parallel profiles each one, used with XV11 field control computer. We have chosen the distance between two profiles 1 m in all zones.

We have also performed seismic surveying and carried out one profile measurement at each trench excavation site. The seismic results are not shown here.

At the first trench excavation or strike slip structured zone, three GPR profiles of 90 m were performed by using GPR 250 MHz and 500 MHz antennas (Figure 2.6b). The trace interval (Δx) was 3 cm for both antennas and the investigation depth are approximately 7 m and 5 m for 250 and 500 MHz antenna, respectively. The trace interval of GPR RTA50 MHz antenna was 10 cm, and the penetration depth was approximately of 20 m. Table 2-1 shows the frequency, the acquisition parameters, and the length for each GPR profile. At 200 m and 1100 m south of the trench excavation site, two electrical resistivity profiles, have been measured, the length of which was 200 m and 280 m, respectively.

At the second trench excavation zone or back thrust structured zone, four GPR profiles of 73 m length were performed by using GPR 250 MHz and 500 MHz antenna (Figure 2.6c). The trace interval (Δx) was 3 cm for both antennas and the investigation depth are approximately of 7 m and 5 m for 250 and 500 MHz antenna, respectively. However, due to the proximity of the trench excavation site with a Mongolian family's ger, we chose to perform three profiles with GPR RTA 50 MHz antennas at a distance of 50 m to the west of the point. The distance between profiles was 15 m, the trace interval was 10 cm, their lengths were 70 and 115 m, and the penetration depth was approximately of 20 m (see Table 2-1).

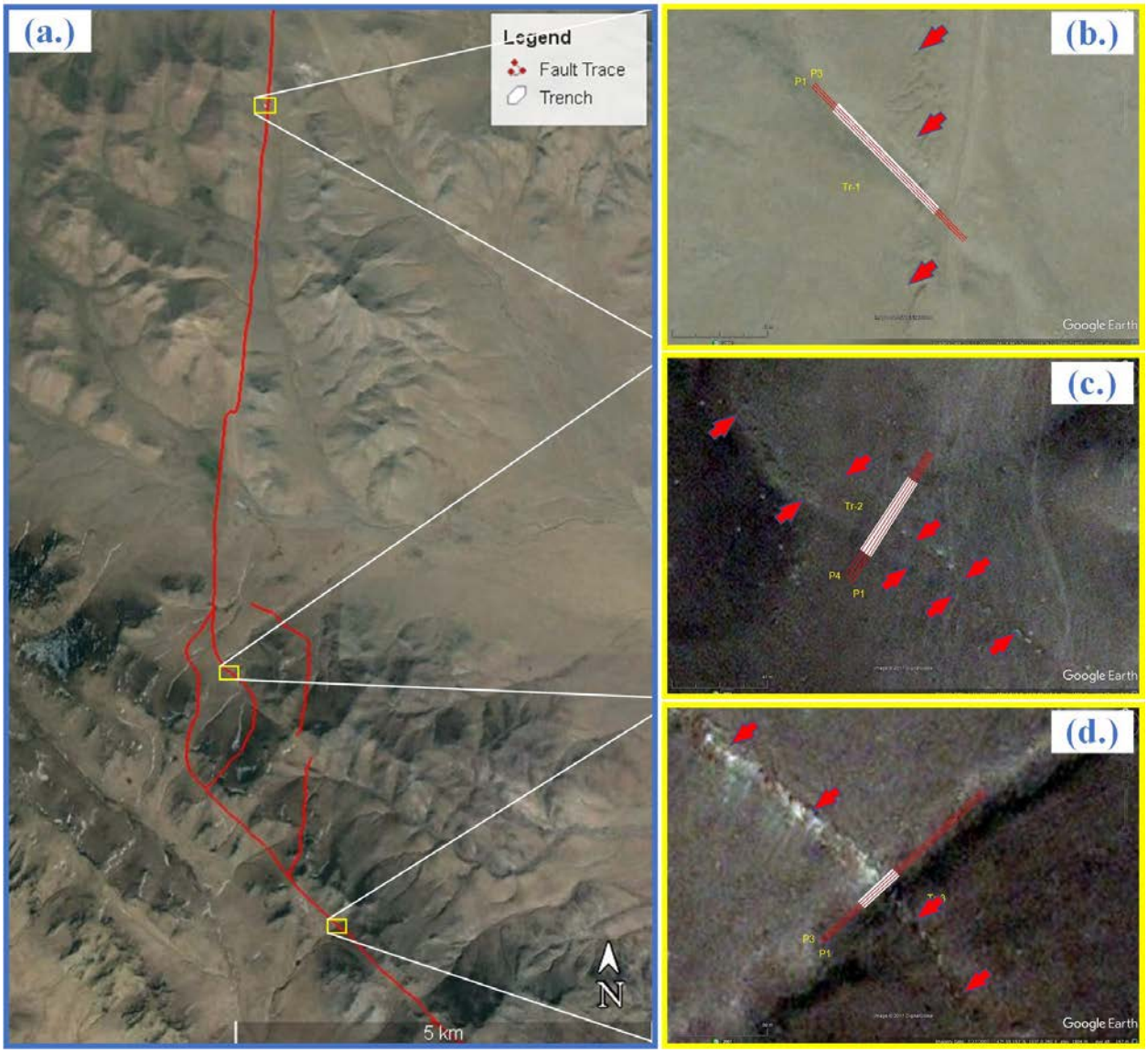

Figure 2.6 The location map of GPR profiles 2017 on the Mogod active fault. a) Main location of the studying three different structured zones, b) GPR profiles and trench location of the first right lateral strike slip structured zone-1, c) GPR profiles and trench location of the second area, back thrust structured zone-2, d) GPR profiles and trench location of the third area, reverse structured zone-3.

At the third trench excavation or reverse structured zone, three GPR profiles of 70 m ~~in~~ length, respectively, were conducted with 250 and 500 MHz antenna (Figure 2.6d). The penetration depth was of 7 m and 5 m. However, due to the limited location of the trench in the river channel along the flow direction, measurements with the GPR RTA50 MHz antenna were conducted of the same length overlapping the 1st and 2nd profiles (Table 2-1).

The topography of all GPR profiles was recorded using differential GPS (DGPS) system. The GPS antenna was mounted on a backpack carried by an operator who was following GPR paths. The recording step of the GPS was set to 1 second.

Table 2-1 Mogod GPR survey acquisition parameters.

	Site name	**Profile name**	**Antenna**	**Distance interval**	**Profile distance**	**Time window**
1.	Zone 1	Pr01-Pr03	500MHz 250 MHz RTA 50 MHz	0.03 m 0.03 m 0.1 m	90 m 90 m 190 m 215m	103 ns 141 ns 391 ns
2.	Zone 2	Pr01-Pr04	500MHz 250 MHz RTA 50 MHz	0.03 m 0.03 m 0.1 m	73 m 73 m 115 m	107 ns 142 ns 391 ns
3.	Zone 3	Pr01-Pr03	500MHz 250 MHz RTA 50 MHz	0.03 m 0.03 m 0.05 m	70 m 70 m 70 m	107 ns 142 ns 391 ns

3.1.3 Results and interpretation

Mogod fault rupture in the main shock occurred sequentially on two N-S right-lateral strike-slip segments, ending in thrust motion on a NW-SE fault at the southern end of the strike-slip faulting (Bayasgalan & Jackson, 1999b).

According to the results of GPR studies conducted in three parts of Mogod fault, the angle of inclination of the fault is almost 90º due to the strike slip structure of the first zone (Figure 2.6b), and it is not possible to distinguish the location of the fault plane due to almost 100% scattering.

However, the location of the fault plane is not well recorded because of the scattering of GPR waves due to the high angle structure and reverse segment in the third study zone (Figure 2.6d). This was also seen in the three profiles of IAG and French team, 2012 GPR survey.

The GPR results and interpretations are included in the Figure 2.7-Figure 2.11. In these figures we show the results of the surveys conducted in the transition zone (second zone) between the two different type fault structures, as the soil cracks is well defined. This transition zone is broken into three segments, and our study was conducted on a segment in the middle of those three segments. This segment is located at the foot of the mountain back side, and the fault scarp is folded to the northeast. It has folds that rise from the northeast or along the

direction of movement of the hanging wall block. From this analysis, it can be assumed that the dipping of this segment is from southwest to northeast. However, it can be clearly seen that this structure is formed in the opposite direction of the GPR results shown in Figure 2.7 and Figure 2.8. At the top of the scarp, there is a visible demarcation of the fault from northeast to southwest.

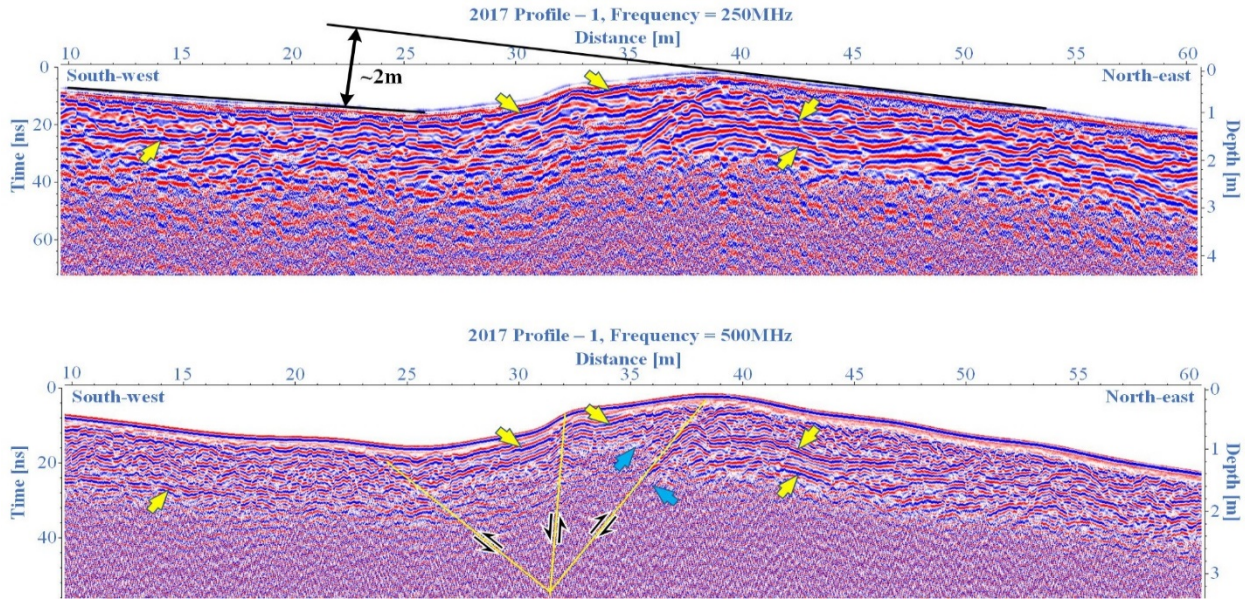

Figure 2.7 GPR result image of the Profile-1 (acquired the June 2017) interpretation of the zone 2 (back-thrust structured) of the Mogod active fault (Figure 2.6c). First figure is 250MHz antenna result image, yellow arrows show the reflections from layers. Second figure is 500 MHz antenna result image, blue arrow is same layer, orange line is strong reflected layers, black arrows indicated movement direction.

Stratified layers are visible within the back-thrust structure, clearly showing the direction of movement in this section. Figure 2.7, Figure 2.8, Figure 2.9 shows an interpretation of the results of the 250 MHz and 500 MHz antennas in GPR profile-1, profile -3, and profile-4, and these three profiles and interpretations show the same results. When measuring the surface displacement of the GPR Profile-1 acquired in the June 2017 in the back-thrust zone 2 (Figure 2.6c) from the topographic data, a vertical displacement of approximately 2 m is observed (Figure 2.7a). But the vertical displacement of the Mogod fault reverse structured section (Figure 2.6d) was determined to be 2.65-3.05 m, according to a study conducted in 2012 on the reverse fault structure (Marinière, 2013).

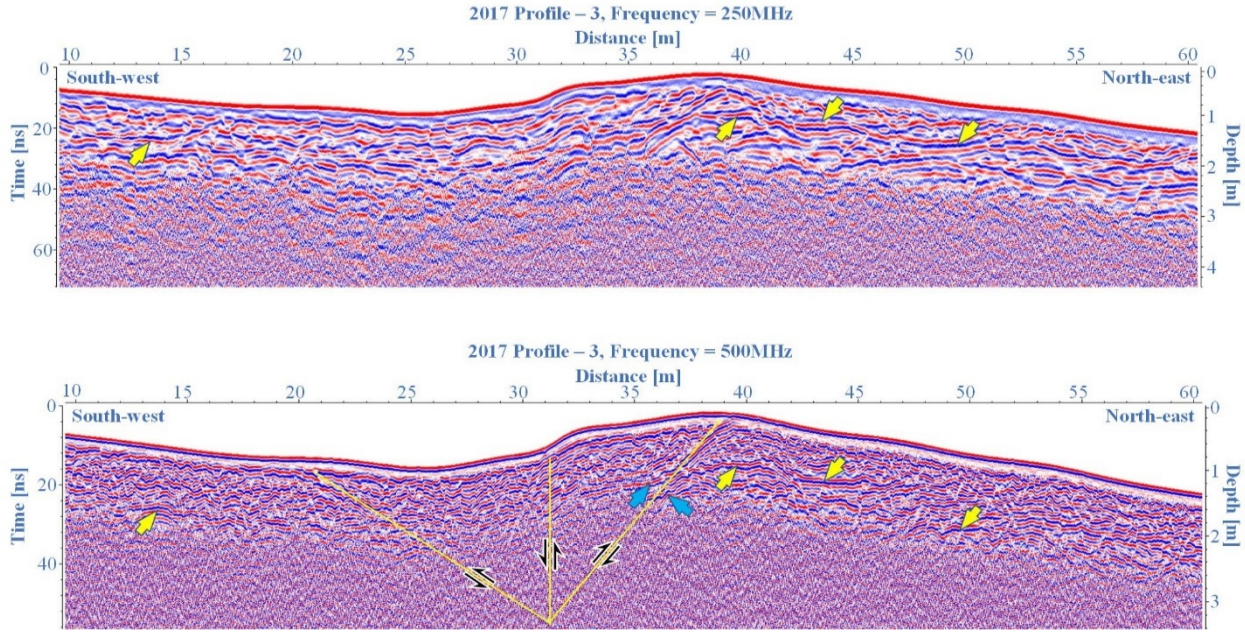

Figure 2.8 GPR result image of the Profile-3 (acquired the June 2017) interpretation of the zone 2 (back-thrust structured) of the Mogod active fault (Figure 2.6c). First figure is 250MHz antenna result image, yellow arrows show the reflections from layers. Second figure is 500 MHz antenna result image, blue arrow is same layer, orange line is strong reflected layers, black arrows indicated movement direction.

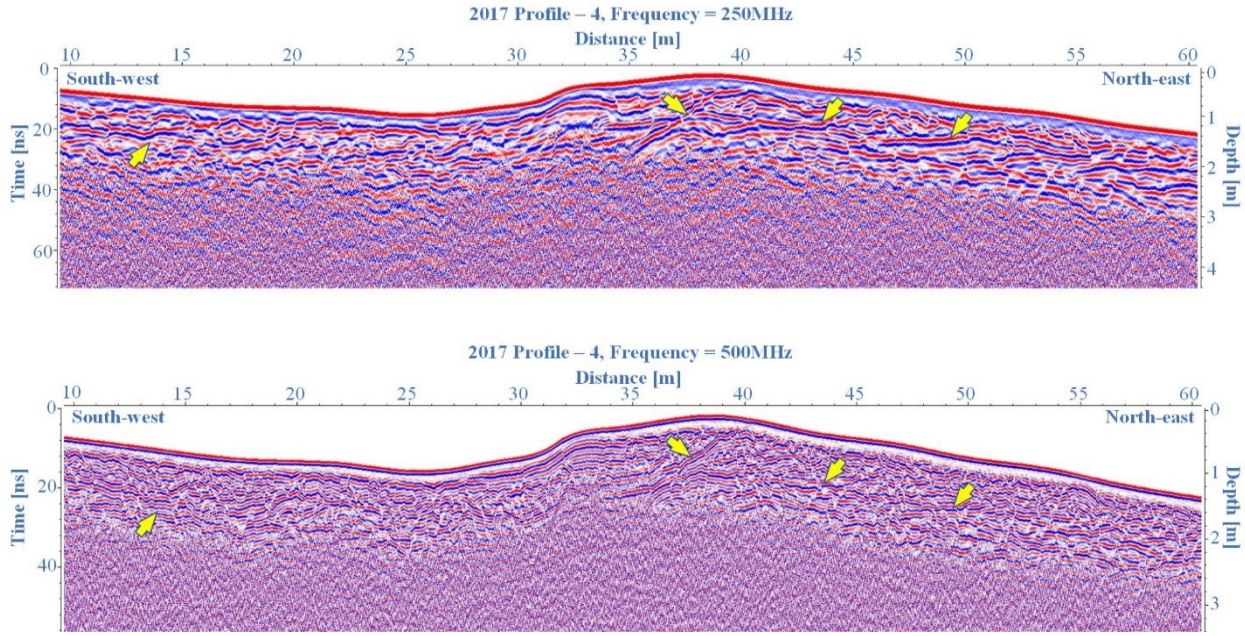

Figure 2.9 GPR result image of the Profile-4 (acquired the June 2017) interpretation of the zone 2 (back-thrust structured) of the Mogod active fault (Figure 2.6c). First figure is 250MHz antenna result image, yellow arrows show the reflections from layers. Second figure is 500 MHz antenna result image, orange line is strong reflected layers.

The paleo-seismological trench study was conducted in collaboration with French and Russian geologists and includes trench wall photos taken by French scientists Laurent Bollinger (CEA) and Yann Klinger (IPGP) The hand-logging on the west wall of the paleo-seismological trench clearly shows the yellow layer which was break up and its back-thrust structures (Figure 2.10). In the photos shown in Figure 2.11, the offsets are very clear. The movement and displacement of this structure on materials such as paleo-seismological trench photos and hand logging is consistent with the images of the GPR results shown in Figure 2.7-Figure 2.9. In particular, the back thrust structure between 35m-40m of the images of GPR result shown in Figure 2.7-Figure 2.9 is clearly visible.

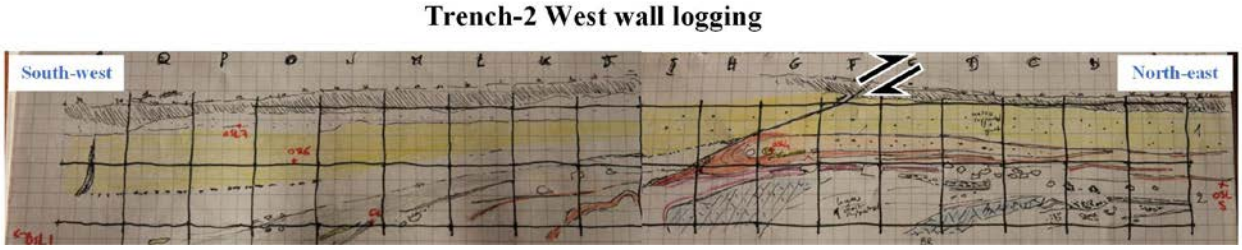

Figure 2.10 West wall logging of the paleo-seismic trench 2. Yellow layer was break up and thrusted structure, after (Laurent Bollinger (CEA), Yann Klinger (IPGP) 2017).

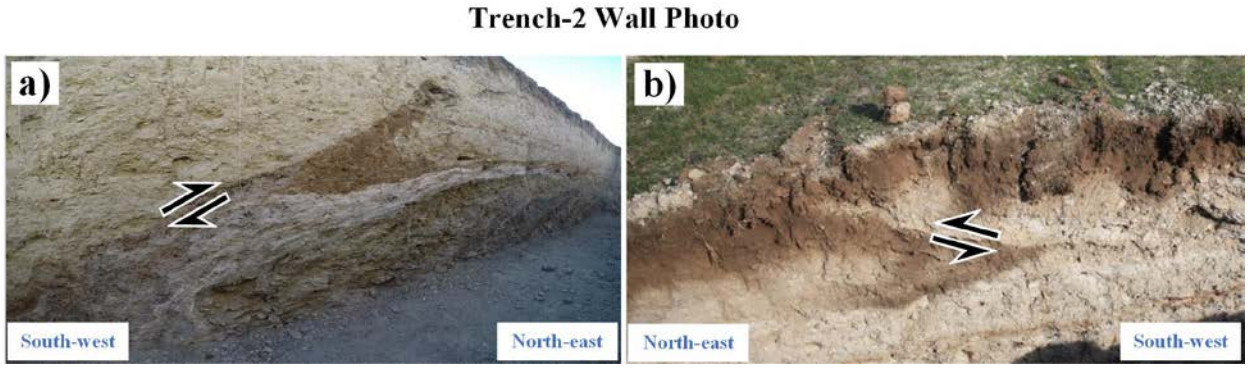

Figure 2.11 Photo of the paleo-seismic trench 2 wall. a) West wall photo and movement direction, b) East wall photo movement interpretation, after (Laurent Bollinger (CEA), Yann Klinger (IPGP) 2017).

3.2 The Mungunmorit (Kherlen) active fault zone

3.2.1 Location and Access

The Mungunmorit active fault is located on the Mungunmorit sum of the Tuv province at 190 km East of Ulaanbaatar capital city, Mongolia. There is a very nice road of 130 km asphalt and 60 km countryside road to access to the Mungunmorit sum center (see location on Figure 2.4). The study area lies within the northwestern flank of the upper kherlen basin. According to some researchers, the Mungunmorit fault is called the Kherlen fault because it is in the Kherlen river basin. The western margin of the basin is bounded by neo-tectonic fault separating it from mountain ranges (> 1800 m above sea level) that form the core part of the Khentii-daurian mega-dome (Smekalin, et al., 2015). The tectonic activity of the Khentii upland reached a maximum during the Mesozoic and then rapidly decreased toward the Cenozoic (Smekalin, et al., 2015). Determining the long-term strain rate would help in better determining its quaternary deformation history. Most of the paleo-seismologic studies in the Khentii upland are limited to trenching, usually constraining the earthquake events, which occurred during the Holocene or late quaternary due to limitations in sediments suitable for conventional radiocarbon dating (Ferry, et al., 2010; Imaev, et al., 2012; Smekalin, et al., 2015; Smekalin, et al., 2016).

The Mungunmorit fault is ~40 km long and borders the Kherlen river basin to the east. It has been identified as thrust in trenched locations (Smekalin, et al., 2015; Smekalin, et al., 2016), but the deflection of active channels implies that motion along this fault also has a strike-slip with dextral shift component.

3.2.2 Description & Survey Grids

The Mungunmorit active fault studying area of the 2013 year is located within the confines of several subfields, which are thrust structured field. A joint Geological/Geophysical field study of Mungunmorit Fault was conducted in 2013 by a team of researchers from the Institute of Astronomy and Geophysics and the Institute of the Earth's Crust Siberian Branch of Russian Academy of Sciences during a period of 14-days.

The ground penetrating radar survey covered several targeted areas of the thrust structured field. We carried out one long profile (of 230 m length) in 2013 named Pr1 and eleven parallel profiles in 2016 named Pr1 to Pr11 (of 50 m length) for the GPR Survey (see Figure 2.12).

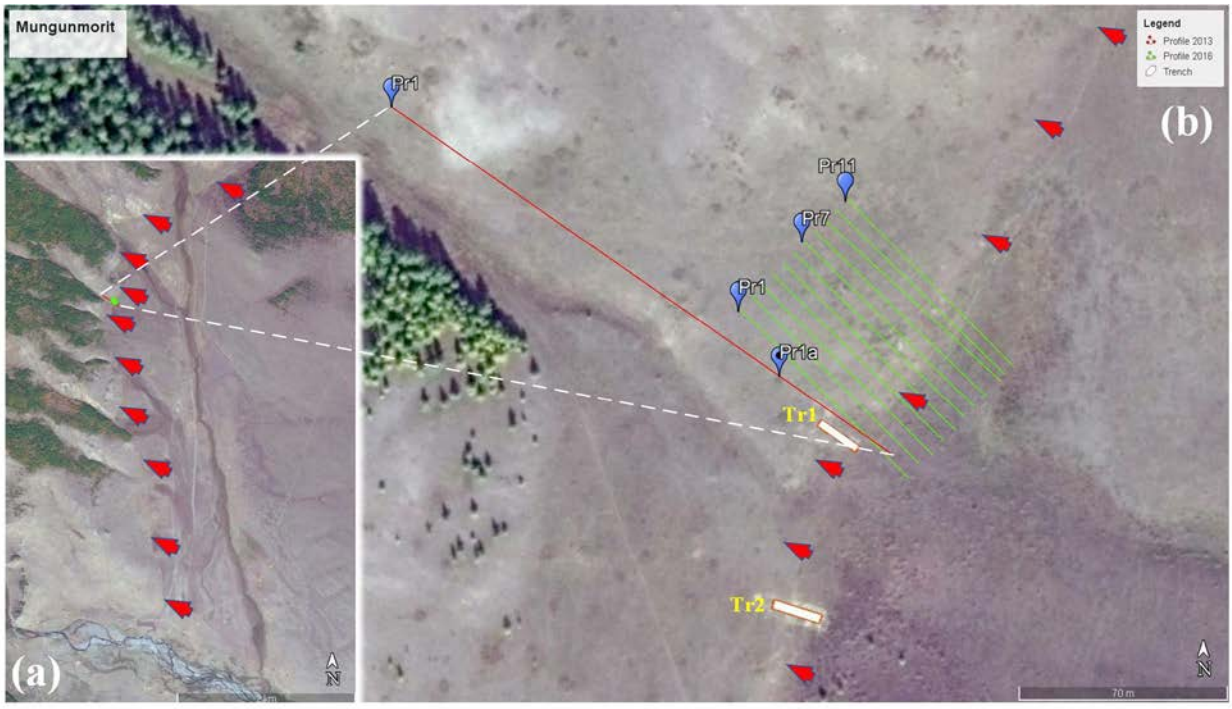

Figure 2.12 Location map of GPR profiles on the Mungunmorit active fault. a) Main location of GPR and trench study, red arrow is fault trace. b) GPR profiles and trench location, red line is GPR profile in 2013, green line is GPR profile in 2016, white square is paleo seismological trench, blue symbol is profile name and start point.

3.2.3 Survey design

We have used MALA ProEx GPR system (MALA Swedish trademark) with MALA RTA 50 MHz unshielded, and MALA 250 MHz shielded antennas and all the profiles are perpendicular to the fault trace (see Figure 2.13). The time window was selected 205 ns for the 250 MHz antenna and 501 ns for the RTA 50 MHz antenna. The trigger interval or distance interval was 0.02 meter in 2013 profiles and 0.05 meter in 2016 profiles for 250 MHz antenna (see Table 2-2).

The topography of all GPR profiles was recorded using differential GPS (DGPS) system. The GPS antenna was mounted on a backpack carried by an operator who was following GPR paths. The recording step of the GPS was set to 1 second. Saw-tooth effects were observed on the topographic profiles due to the small movements of the operator while he was walking along the profile. To filter out these unwanted effects, we have used a high degree polynomial curve fitting our data and used the topographic profiles filtered.

Table 2-2 Mungunmorit GPR survey acquisition parameters.

	Site name	**Profile name**	**Antenna**	**Distance interval**	**Profile distance**	**Time window**
1.	2013 Aug-10	Pr01	250 MHz RTA 50 MHz	0.02 m 0.3 m	230 m 220 m	205 ns 501 ns
2.	2016 Sep	Pr01-Pr11	250 MHz	0.05 m	80 m	130 ns

3.2.4 Results and interpretation

The Mungunmorit fault is located along the northwestern foothills of the Kherlen river basin. Therefore, the azimuth direction varies between approximately 20º and 171º. On the longest profile in 2013, some structures of low dipping angle were observed from the top of the mountain to the bottom or final thrust structure. Since we are studying the lowest or last part of the thrust component structure, we have interpreted the GPR images of this part of profiles (Figure 2.13). In Figure 2.13 shown zoomed section of the profile 1, that section started 196.5m to end of the profile 1 acquired august 2013. The scarps have a downward-sloping structure, and as a result of the GPR image of Figure 2.13 the layer indicated by the yellow arrow is placed above the layer indicated by the blue and green arrows. However, the layers indicated by the blue and green arrows show a thrust structure that overlaps at the bottom of the scarp due to compression. From these thrust structures along the total profile, the dipping angle is low, and the effect of a slow-moving like an excavator effect is observed.

Paleo-seismological trench studies are being carried out by Russian geologists. The paleo-seismological trench T1 (48.276443°, 108.513343°) was excavated only at the bottom of the Mungunmorit faults carp, from which three samples were taken for dating. Determining the displacements and kinematic history of the Mungunmorit fault requires more studies along the whole strand of the fault. Based on the trenching, paleo-seismic events associated with the Mungunmorit fault occurred at least twice (dated by radiocarbon dating: 1152–1702 B.C. and 5466–7201 B.C.; (Smekalin, et al., 2015)). The assumed magnitude of these earthquakes reached ca. 7.0. (Smekalin, et al., 2016)

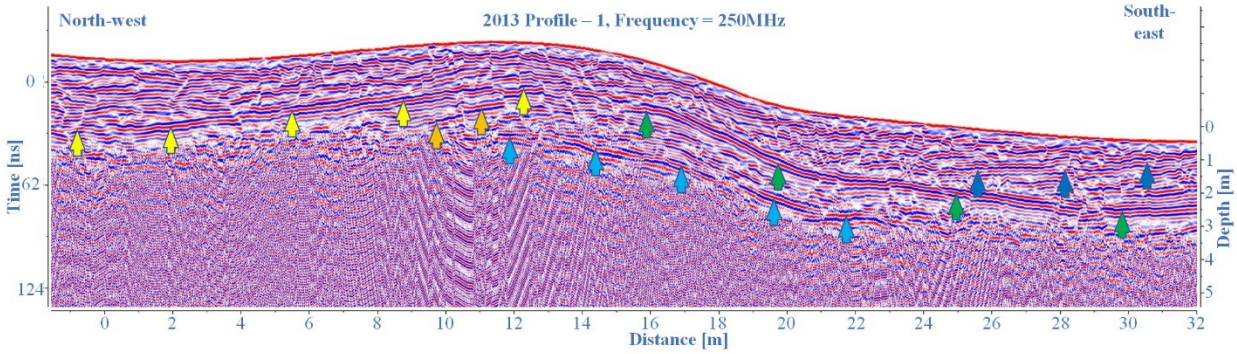

Figure 2.13 GPR result zoomed image of the profile P1a (acquired the August 2013) obtained with 250 MHz antenna in the Mungunmorit fault, location show in Figure 2.12. The GPR image shows a clear thrust structure with several layered structure under scarp (yellow, blue, green, and orange arrows) and ramp of the thrust structure.

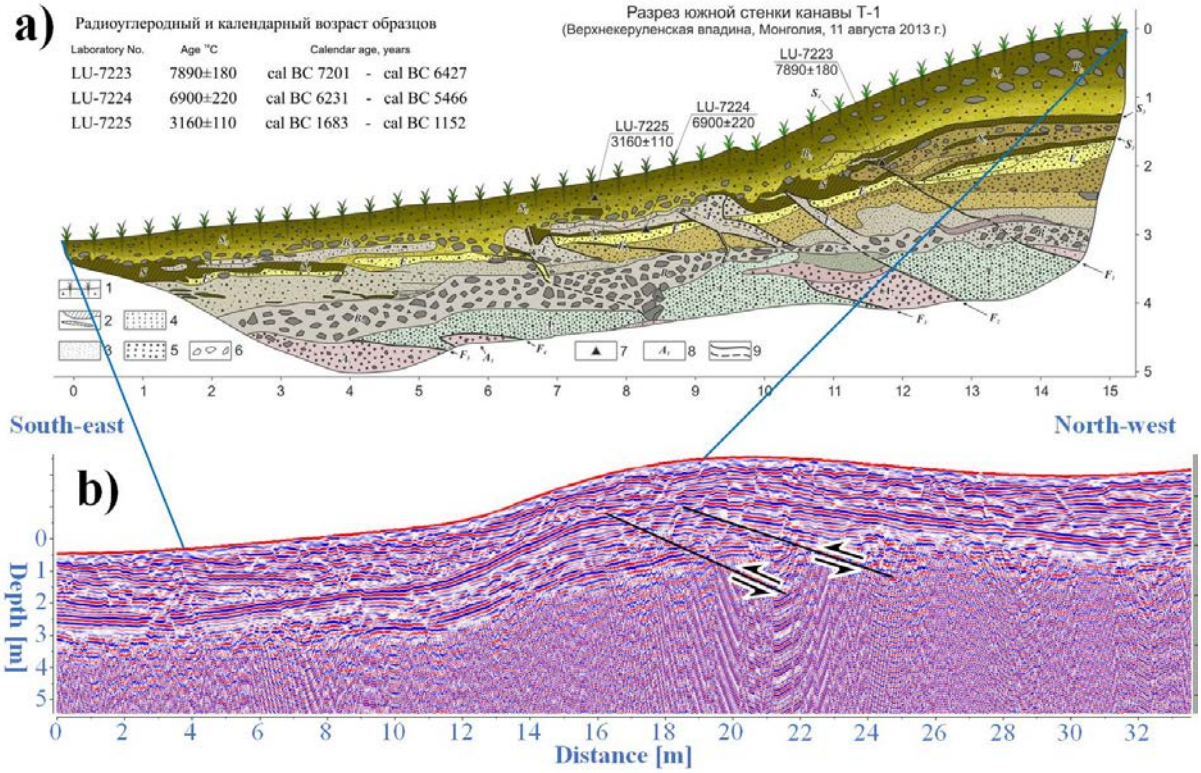

Figure 2.14 Comparison of the paleo-seismological trench logging and result of GPR image profile 1a. a) Section of the west wall of paleo-tranche T-1. After (Smekalin, et al., 2016), b) Result of GPR image and interpretation of fault dipping and movement, location of profile 1a (Pr1a) shown in Figure 2.12.

The result of GPR image and the log of the right wall of the trench are arranged to have the same scale in Figure 2.14. Figure 2.14a shows a paleo-seismological trench with geological

interpreted logging image, and Figure 2.14 shows the result of GPR image with interpretation. The GPR image shows the fractures and displacement of the layers below the scarp. The Trench was excavated approximately 15 meters away from the GPR profile nevertheless the results are very consistent.

An integrated geological and geophysical study of the Mungunmorit fault in 2013 and 2016 was conducted only on the segment with a thrust component structure. However, the main displacement of the Mungunmorit fault is a strike slip along the Kherlen river basin, and the angular difference between the thrust component structure and the strike slip structure is 138º-151º, which is the main condition for the formation of the thrust component structure.

4 Tensional structured fault examples

4.1 The Bayankhongor active fault zone

4.1.1 Study area and geological environment

The Bayankhongor Fault is part of a 350 km long systemic fault called the Southern Khangai Fault, which extends in a latitudinal direction along the latitude of Bayanbulag soum on the southwest side of the Khangai mountain range (Odonbaatar, et al., 2017). The Bayankhongor fault begins about 30 km west of Bayankhongor province center, extends approximately 85 km to the Bor Khairkhan mountain (Odonbaatar, et al., 2017).

This fault has already been studied by foreigner and domestic scientists through satellite images analysis and field route research. The Bayankhongor fault has been described as a thrust (Baljinnyam, et al., 1993), and a normal fault (Cunningham, 2001; Gantulga, 2018).

We conducted our GPR campaign in collaboration with administration of the Bayankhongor province within the framework of a seismic micro-zoning and mapping project. The Bayankhongor fault section stretches across the territory of Bayan-Ovoo and Galuut soums of Bayankhongor province along the foothills of the Jargalant mountain range. The study area is located 25 km northwest of Bayan-Ovoo soum and about 1 km from the gold mine stockpile (see Figure 2.15a). A geological study along the Bayankhongor fault shows a right lateral strike slip structure with horizontal displacement of 4-4.5 m and a vertical component of 2-8 m displacement scarps at 3 points. However, the main types and geodynamic conditions of the Bayankhongor fault have not yet been determined (Odonbaatar, et al., 2017). Along the fault trace, the scarp height is unevenly distributed with an average height of 1.5-3 m, and the high

scarps were formed by several strong earthquakes that occurred at this fault (Odonbaatar, et al., 2017).

Detailed paleo-seismological studies, based on the analysis of satellite images, show a more pronounced fault and a visible scarp at the foot of a thick mountain slope where the fault sediments have been accumulated (see Figure 2.15b).

4.1.2 Data acquisition method and survey parameters

In this study, we performed the MALA ProEx GPR system (MALA Geoscience, Sweden) measurements in the Common Offset (CO) acquisition mode, in which the distance (offset) between the transmitter and receiver antennas is kept constant. We used two types for antennas. That is shielded (MALA 250 MHz) and unshielded (MALA RTA 50 MHz) antennas with MALA ProEx fiber optic control system and MALA XV11 field computer. GPR measurements were collected in August 2014 and acquired three profiles with each antenna in the direction from the top to the bottom of the mountain (Figure 2.15b). Detailed acquisition parameters are shown in Table 2-3 and Table 2-4, respectively.

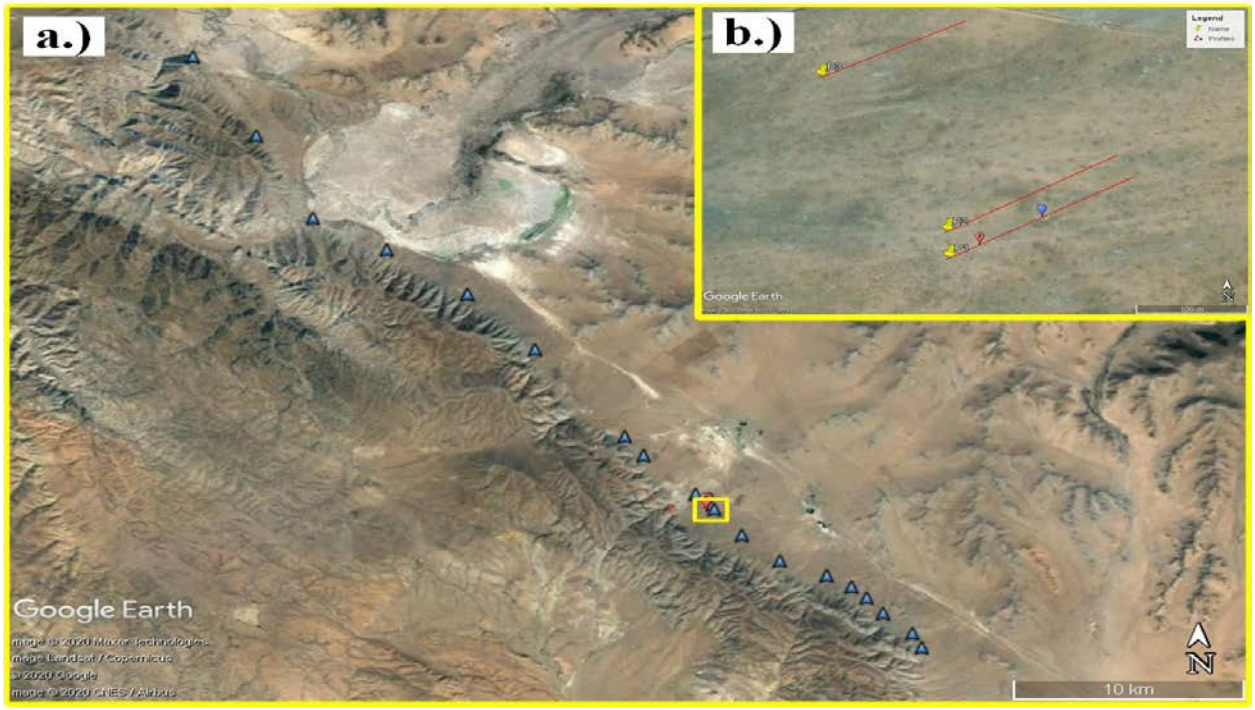

Figure 2.15 The location map of the study area of Bayankhongor fault. a.) Google Earth satellite image showing the survey area. The blue arrows indicate the fault mark, and the yellow rectangle indicates the GPR survey area. b.) An enlarged drawing of the GPR surveyed area. The red line indicates the GPR measurement profiles, the yellow line indicates the starting points and names of the profiles, and the red and blue points indicate the fault trace mark.

Table 2-3 Bayankhongor profiles and their lengths for different GPR antennas.

Name	250MHz	RTA50MHz	Start point	End point
Profile-1	200м	200м	46.405970° 100.190633°	46.406862°, 100.192840°
Profile -2	181.5м	181.5м	46.406260° 100.190611°	46.407099° 100.192647°
Profile -3	115м	150м	46.407918° 100.189137°	46.408546° 100.190858°

Table 2-4 Acquisition parameters of the Bayankhongor GPR profiles.

Name	250MHz		RTA50MHz	
	Step Interval (m)	**Time window** (ns)	**Step Interval** (m)	**Time window** (ns)
Profile-1	0.04	185	0.2	467.4
Profile -2	0.04	185	0.2	372
Profile -3	0.04	185	0.2	372

4.1.3 GPR Results and interpretation

During the GPR campaign conducted on this fault (Figure 2.15), we have used the 250 MHz and RTA 50 MHz antennas. The profile's coordinates and acquisition parameters are given in Table 2-3 and Table 2-4. Figure 2.16 shows the GPR image of profile 1 obtained with 250 MHz antenna: the first (Figure 2.16a) is shown without AGC applied, while the second one (Figure 2.16b) is shown with AGC applied. In Figure 2.16a we remark a sharply change of reflections around 38 m horizontally indicating two different sub-soils. This sharply changing of reflections remains even after AGC application (Figure 2.16a).

The penetrating depth of 250 MHz antenna is approximately 2.5-3 m, while for the RTA 50 MHz antenna it is 12 m (see Figure 2.17a). A comparison of the resulting GPR images obtained with GPR 250MHz and RTA 50MHz of the same profile (Figure 2.17a and Figure 2.17b) show that the fault plane zone is approximately on the same place, approximately at 33 m horizontally. However, in the location map of Figure 2.15b the fault trace mark is indicated by a red symbol.

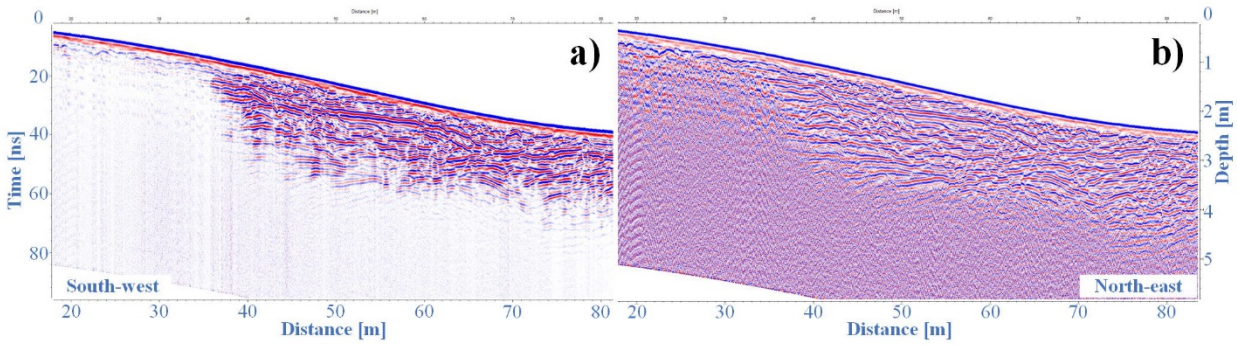

Figure 2.16 GPR image of profile 1 obtained with 250 MHz antenna. a.) The GPR image is obtained without the automatic gain control (AGC). b.) The GPR image is obtained after AGC amplification.

The GPR image shows a clear low angle normal (listric) structure with lot of layered structure near fault zone (Figure 2.17b). The resulting GPR image of the profile P1 performed with 250 MHz antenna from 72 m to 142 m is shown in Figure 2.17c, and a break in sediment accumulation is observed at around 102 m horizontally in this profile.

The yellow lines (Figure 2.17c) crossing each other at around 102 m horizontally seem to have the same angle related to the surface. The location of the fracture at 102 m is indicated by a blue symbol on a profile location map (Figure 2.15b), and the fault trace~~s~~, which we observed as a fracture scarp in the interpretation of the satellite image, passes through the blue symbol.

The Bayankhongor fault is considered to be a normal fault (Cunningham, 2001), and our GPR images of this fault show that the fault dipping, sediment accumulation pattern, and direction of movement are characteristic of low-angle normal fault structure or Listric fault (Figure 2.18) (Nyambayar, et al., 2018).

The scarps, which show an average of 1.5–3 m in height, do not present partial fault damage, but are often strewn with broad bands along the fault zone (Odonbaatar, et al., 2017). This is a signification of a normal fault structure, and landslides are common on the eastern slopes of the Jargalant Range, which are stepped along the expansion movement of the fault.

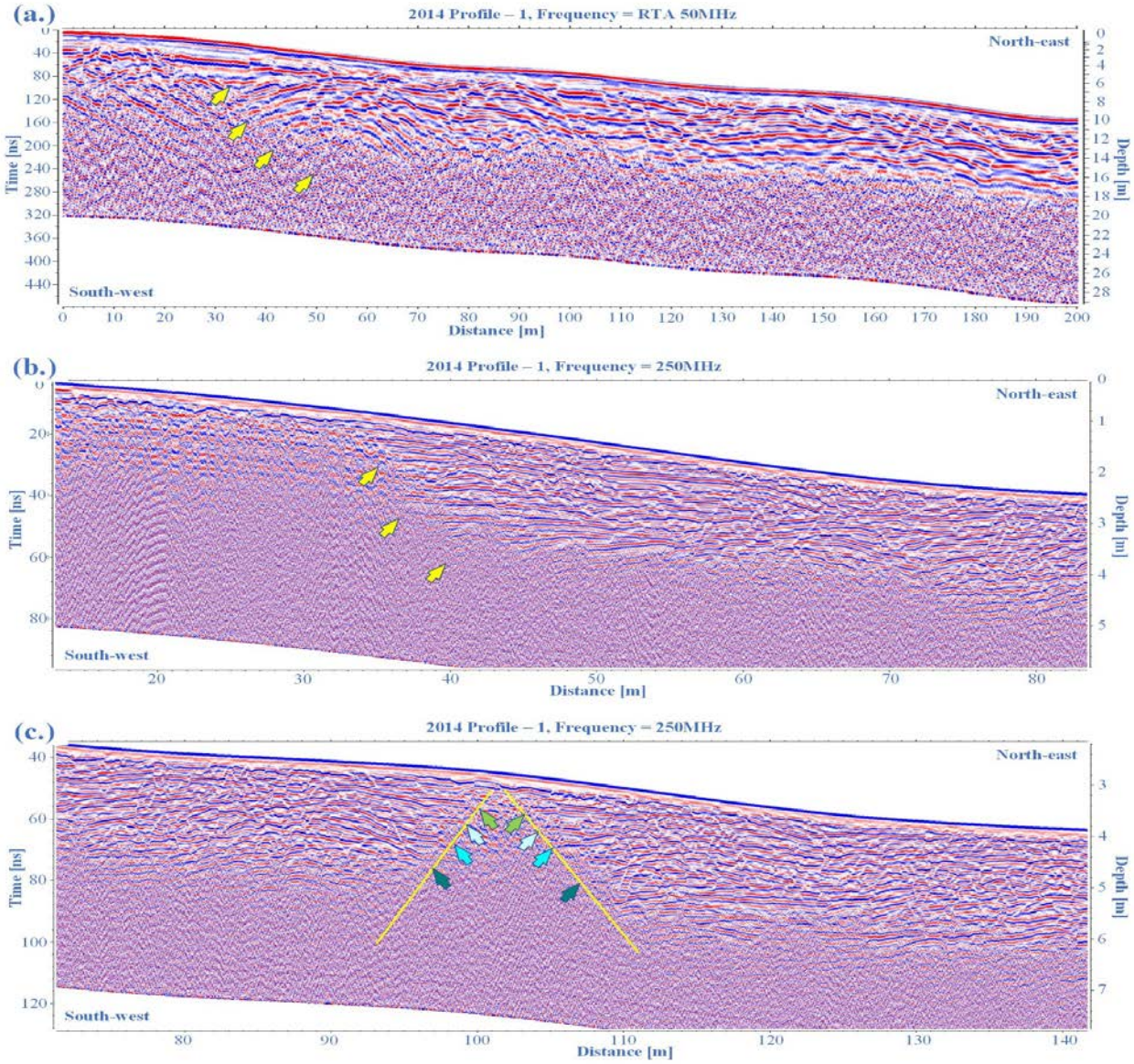

Figure 2.17 Interpretation of GPR RTA 50MHz and 250MHz antenna performance maps performed on the profile P1 (acquired the July 2014) in the Bayankhongor fault. The topographic corrections and depth conversion are performed using a velocity of 0.12 m/ns. a.) RTA 50MHz antenna result image, with a yellow arrow roughly outlining the location of the fault plane. b.) The resulting GPR image from 10 m to 85 m of the profile P1 with a 250MHz antenna. The yellow arrow outlines the fault zone. The GPR image shows a clear low angle normal (listric) structure with lot of layered structure near fault zone c.) The result image of the profile P1 performed with 250 MHz antenna from 72 m to 142 m, and a break in sediment accumulation is observed at around 102 m in this profile P1. The same layers that move in both directions are indicated by arrows of the same color. The yellow lines indicate the boundary between the two broken sections (Nyambayar, et al., 2018).

Another key feature of the Listric fault structure is the formation of a Paleo-lake in the depression below the fault, and the Galuut Paleo-Lake depression, a continuation of the Bayankhongor fault, 18 km from our study area to northwest side. Also, the location of the fault plane is unknown. The angle of the first dropped section of the Listric fault plane, or the part closest to the surface, is vertical or high angled structure of inclination gradually changes to a lower angle. Due to the structure, the GPR signal may not be scattered laterally from the fault plane.

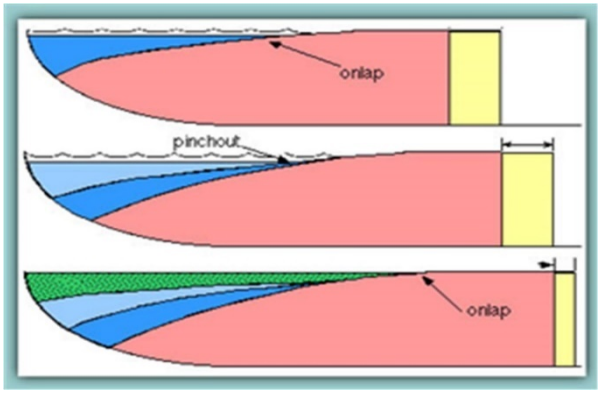

Figure 2.18 Low-angled normal fault structure or Listric fault model (University of SYDNEY, 2000).

5 Shear structured fault examples

5.1 The Emeelt active fault zone

5.1.1 Study area and geological environment

The seismic activity observed in the vicinity of Ulaanbaatar, capital city of Mongolia, is relatively low compared to the activity observed in western Mongolia. Nevertheless since 2005, the seismic activity around Ulaanbaatar has increased (Figure 2.19). At the west of Ulaanbaatar along two perpendicular directions, which determine two active faults: Emeelt fault, discovered in 2008 , that 45 km long minimum and situated about 10 km west of Ulaanbaatar and Hustay fault, 80 km long, with its NE part at less than 20 km west of Ulaanbaatar; their length and morphology indicate they can produce earthquakes of magnitude 6.5 to 7.5 (Schlupp, et al., 2012; Ferry, et al., 2010; Nyambayar, et al., Apr 2018). Most of the Mongolian population (1.5 million over 3.2 million) is concentrated at Ulaanbaatar, which is the main political and economic center of the country (Dugarmaa, et al., 2006; Nyambayar, et al., Apr 2018).

In the Emeelt fault zone, we studied in 2009-2012, the fault scarp and traces are clearly visible on the satellite image. Elsewhere, some traces are visible but very dim. Seismic activity at the Emeelt fault increased sharply in 2013. We have been conducting comprehensive geological and geophysical surveys on the Emeelt active fault since 2010, and some research and monitoring is still ongoing. We have been conducting a comprehensive geological and geophysical study in this area for 4 years in collaboration with researchers from the Strasbourg University of France, Institute of the Earth's crust Russia and Institute of Astronomy and Geophysics Mongolia. The first trench was excavated in 2009, and in 2010 a large three-segmented trench was excavated, and various geophysical surveys were conducted around it. One of the main studies of these geophysical surveys was the detailed study of MALA ProEx GPR system (MALA Swedish trademark). Measurements were made with MALA 500MHz shielded and MALA RTA 50MHz unshielded antennas to visualize the depth structure of Emeelt fault, and 500 MHz antennas were used in detailed paleo river channel studies to determine horizontal displacement.

5.1.2 Data acquisition and survey parameters

The Emeelt fault was geomorphologically recognized in 2009 and a preliminary trench (T1) was dug, after which we decided to perform GPR measurements to study the underground structure that may be affected by the fault. GPR survey should help us determine the optimal location of future trenches. Our first goal was to study any sediment near the T1 (47.909015°, 106.605226°) trench for three reasons. First, sediment provides stratigraphy, and if it is cut by a fault, it provides information on the geometry and dynamics of the fault, such as fault displacement, amplitude, and direction. Second, the sediment is usually an environment suitable for EM wave propagation, and third, the proximity of the trench allows us to directly compare the two data sets (geology and GPR). In this study, we mapped the fault depth and structure using a 50 MHz antenna. We recorded 1 profile 200 m long adjacent to the T1 trench to determine the fault zone (see Table 2-5). The location of the profiles and their GPR results together with comparison of the trench photo mosaic are shown in Figure 2.21a.

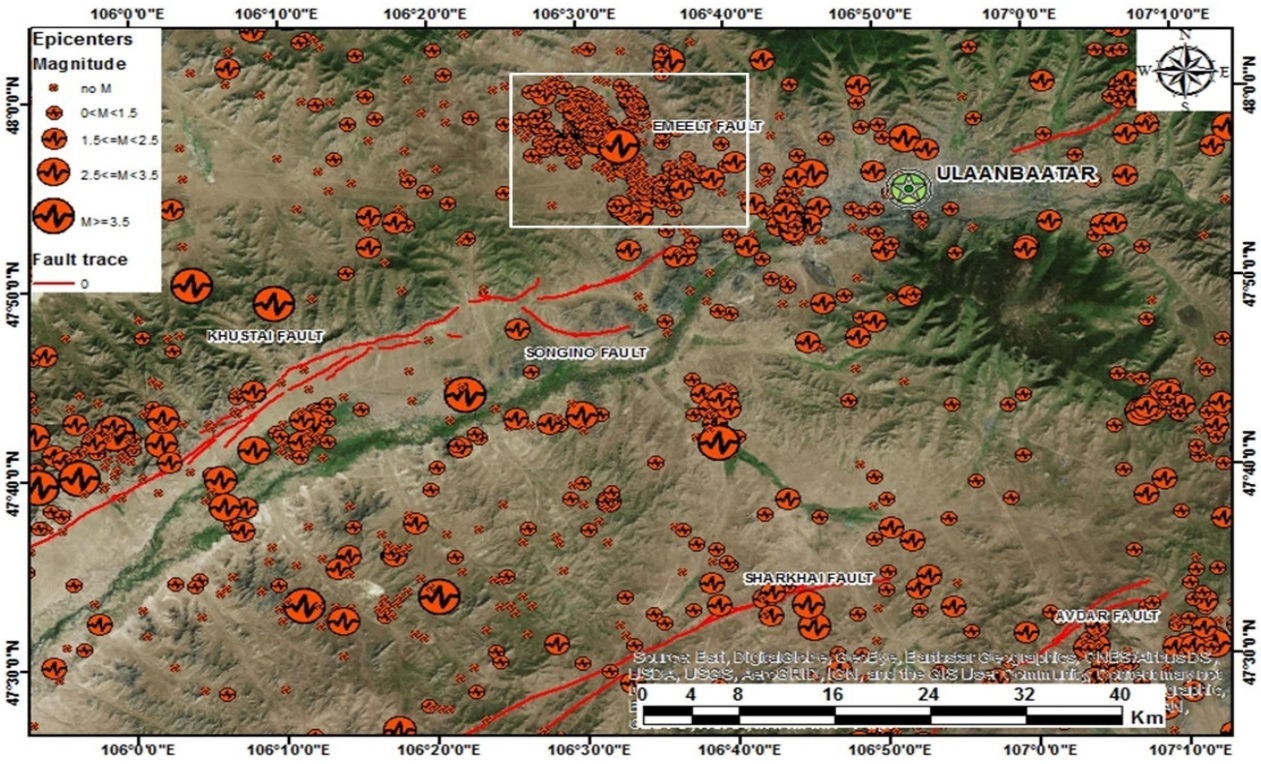

Figure 2.19 Seismic activity map around Ulaanbaatar capital city. Emeelt active fault location is white square. Red line is fault trace and red dots represent the seismic events since 2005 (after NDC data, IAG, MAS).

Table 2-5 Emeelt GPR survey acquisition parameters.

	Site name	**Profile name**	**Antenna**	**Distance interval**	**Profile distance**	**Time window**
1.	2010 June 27	Pr01-Pr04	RTA50 MHz	0.2 m	200 m	535 ns
2.	2013 May 30	Pr01-Pr07	RTA50 MHz	0.3 m	900-2000 m	500 ns

We also continued GPR studies on Emeelt fault in 2011 and 2013, the objective was to identify the traces and the geometry of Emeelt fault near the subsurface. However, from the survey planning to the end of the 2013 GPR survey. I did all the work myself, including GPR measurements, data processing, interpretation and satellite image analyses, and GPS measurements. Among these measurements, 7 profiles conducted in 2013 with a RTA50 MHz antenna were very effective (Table 2-5). The site showing a lot of incisions was selected to detect the faults as deep as possible by selecting areas with low environmental impact that would be suitable for measurement after the traces of faults were first identified and mapped on the satellite image. Figure 2.20 shows the location of the sixth profile (P-6) and the locations of

starting (47.940885°, 106.583281°) and ending points (47.935084°,106.574615°). This profile was selected following the mountain ridge, and because the sediment accumulation is on a thin rocky soil, the deep structure of the fault can be clearly seen. In addition, the direction of measurement was chosen from the top of the mountain to the bottom.

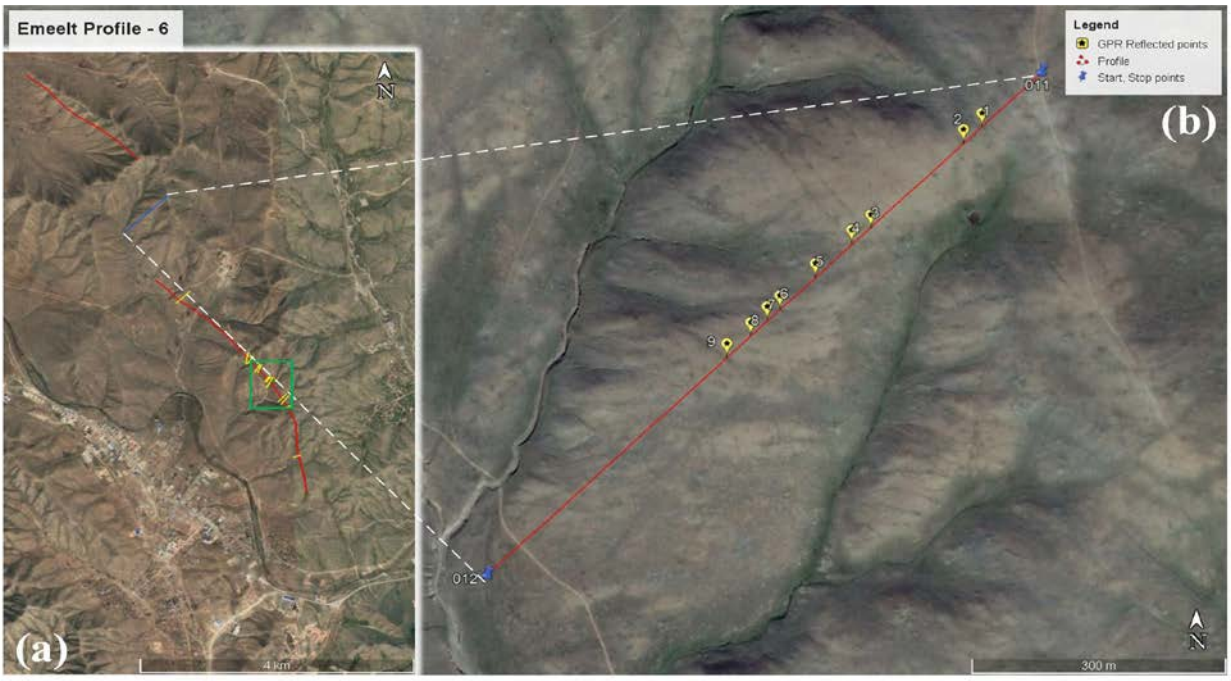

Figure 2.20 Location map Emeelt fault 2013 GPR survey. a) Main location GPR profile P6 and fault trace. Green square GPR survey 2010-2011 area. b) Zoomed detailed map of the GPR profile P6. Red line is RTA profile and yellow symbols are fault segments on the surface.

5.1.3 GPR Results and interpretation

The results of GPR measurements on active faults such as Emeelt and Hustai in 2010-2011 were used in the doctoral dissertation of one doctoral student at the University of Strasbourg, France ((Dujardin J.-R. , 2014). The results of the GPR measurements performed on the Emeelt active fault in 2010 are of good quality due to the low impact of soil moisture and provide significant information about the depth structure of the fault plane. From the results of the RTA50 MHz antenna, it is possible to clearly see the location of the fault and the dipping of the fault (Figure 2.21).

Although the sediment and rock boundaries are the same, the GPR output maps differ depending on the RTA50 MHz and 500 MHz antenna penetration depths. In addition, the dipping of the fault determined by the GPR results corresponds to the fault trace on the surface.

The dipping angle of the Emeelt fault was determined on the GPR result images and changed from 35º at the south part to 23º at the north side (Figure 2.21).

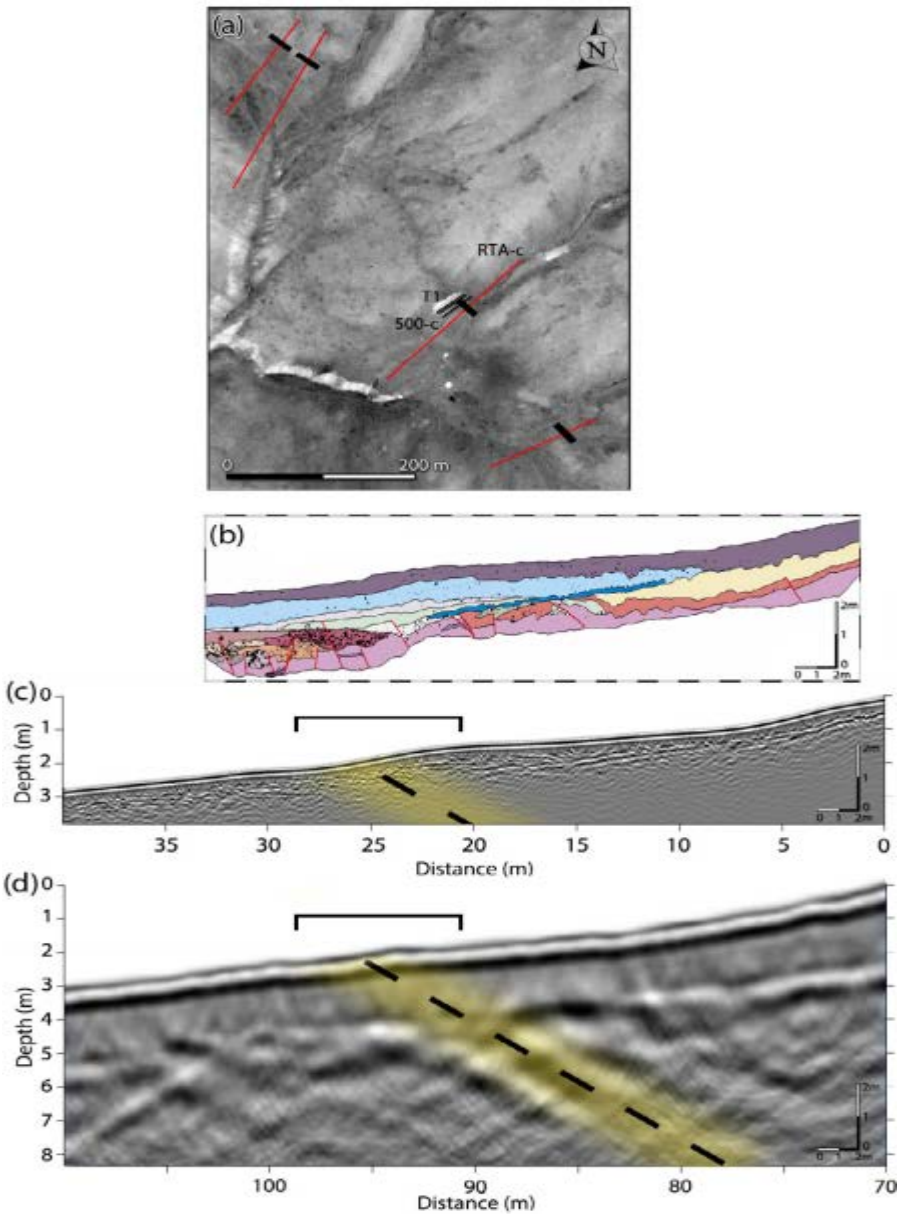

Figure 2.21 Emeelt fault 2010 GPR survey. a) RTA profiles (red lines) with the location of the fault at surface. b) T1 paleo-seismological trench west wall logging (first trench 2009 year). c) 500 MHz profile. d) RTA50MHz profile and black dashed line, surrounded by yellow zone, highlights the fault (after Dujardin, 2014).

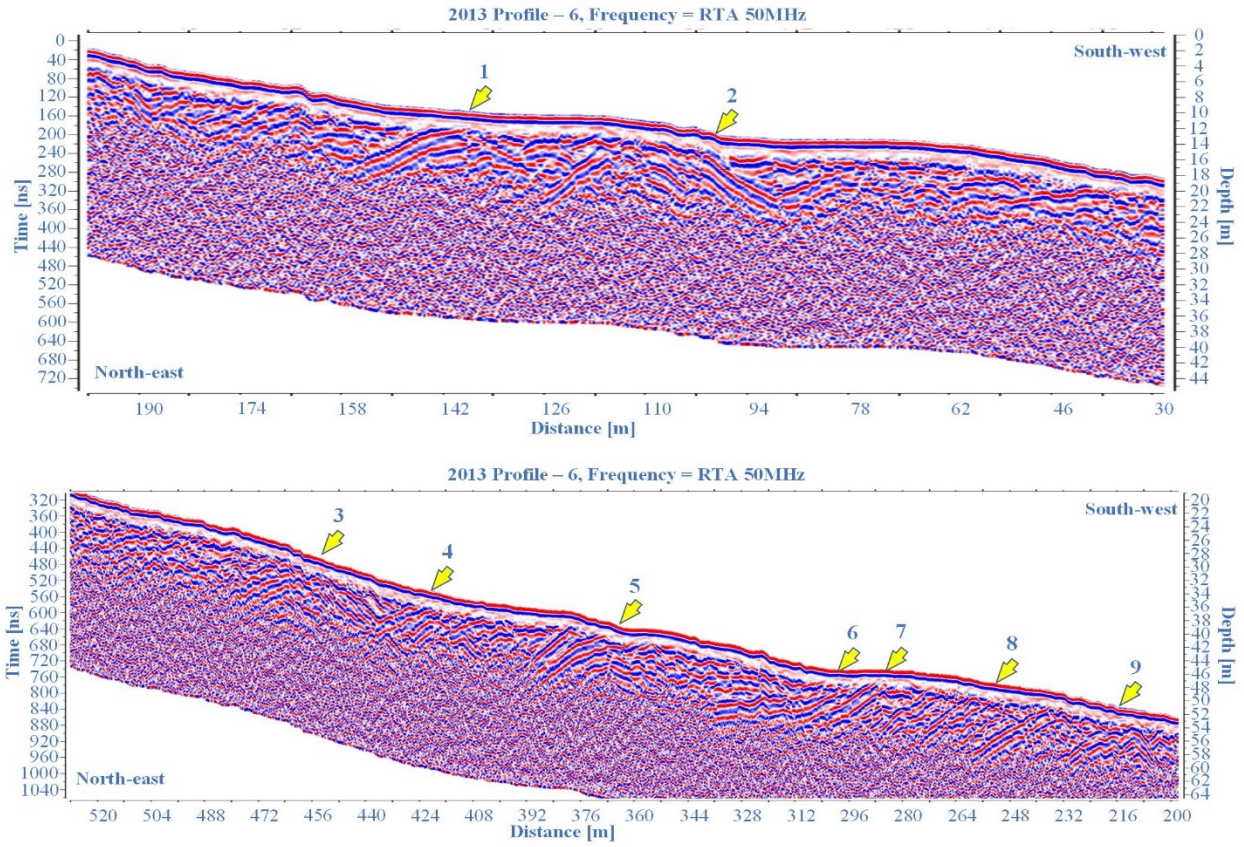

Figure 2.22 GPR result image of the profile P6 (acquired the May 2013) obtained with RTA 50 MHz antenna in the Emeelt fault. The GPR image shows a clear strong reflected and dipping angle structure (yellow arrows point soil fractured zone on the surface). First figure is first section of the profile P6 and second one is next section of the profile P6.

The 2010-2011 Integrated Geological and Geophysical Survey identified the Emeelt Fault as a right-lateral strike slip fault (Schlupp, et al., 2012). The results of GPR measurements conducted in 2013 on the Emeelt active fault are well mapped and provide a lot of in-depth information. Because the sections of these measurements are long, they contain a large amount of information. As an example, we show the result of the profile 6, which presents sub structures of several parallel fractures. The length of the profile-6 is approximately of 1000 m, and in Figure 2.22 we show only from 0 to 525 m in two parts. Also, at the beginning of the profile, between 80-130 m, the dipping of fractures indicated by 1 and 2 is in the different direction (Figure 2.22). However, between 250-510 m, the dipping is in same direction and there are several signs of fractures with different angles (Figure 2.22). The result of GPR image reveals the structure of the deep fault then locates it on the surface and places it on the line of the profile, which shows that it corresponds to the soil fault traces observed on the satellite image (Figure 2.20).

5.2 The Avdar active fault zone

5.2.1 Location and Access

Avdar Mountain Fault is located in the Tuv aimag, just south of the Zuunmod province center, 45 km straight from Ulaanbaatar capital city of the Mongolia, 24 km from Zuunmod province center, and about 20 km from the new international airport. The Avdar fault surface rupture extends from southwest to northeast, similar to Khustai and Sharkhai faults (Figure 2.4). There are two faults structure along the southern and northern slopes of the mountain on the satellite image, and we have mainly studied the faults in the southern part of the Avdar mountain fault (Figure 2.23).

In terms of seismic activity, earthquakes of 1.5-4.2 magnitude are quite common, and because of their proximity to the new international airport, they are also of interest to researchers. Avdar mountain faults have been identified as having a left lateral strike slip, like Khustai and Sharkhai faults (Abeer, 2015).

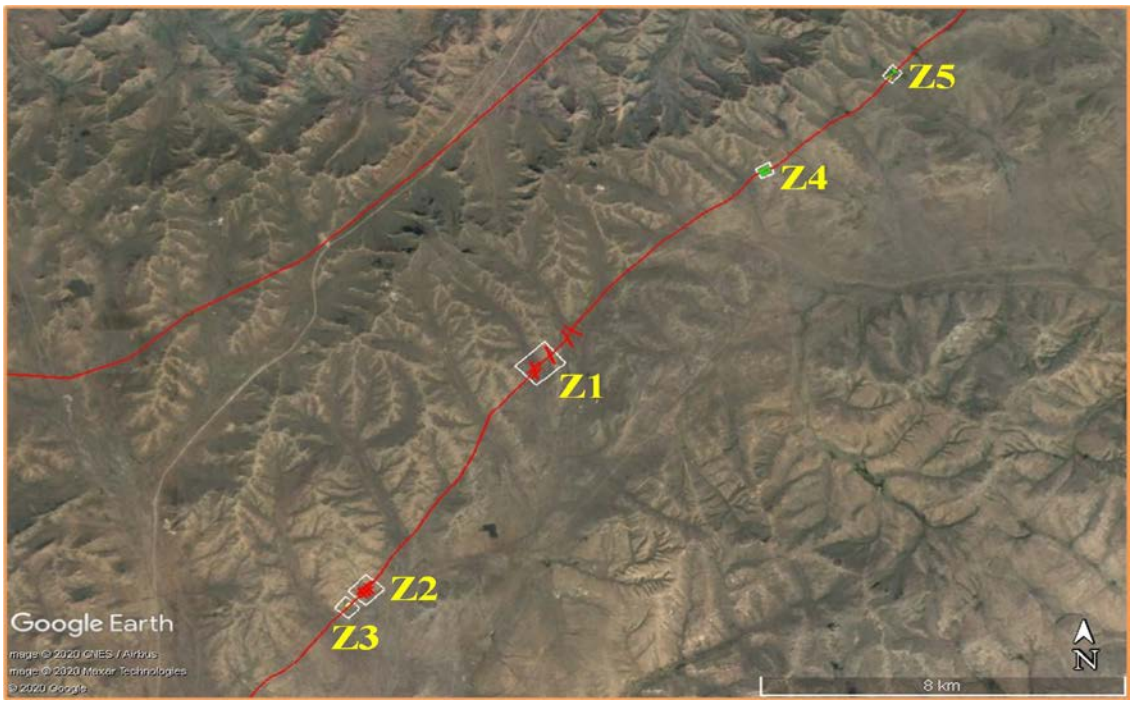

Figure 2.23 GPR survey locations map of the Avdar fault. Z1-Z2 are GPR zones surveyed in 2011. Z3 is surveyed in 2012 and Z4-Z5 are surveyed in 2016. Two red lines are Avdar fault traces.

5.2.2 Data acquisition and survey parameters

In 2011, when the Avdar mountain fault was discovered, a detailed study of the that active fault began. The Institute of Astronomy and Geophysics acquired a new GPR survey instrument of the MALA Geosciences Inc in 2011 as part of a detailed project to study active faults around Ulaanbaatar. The first GPR survey measurements were collected in October and November 2011 at Z1 (47.372177°,106.785050°) and Z2 (47.315682°,106.731789°) (Figure 2.23). On October 7, 2011, we acquired the GPR profiles 6 to 9, and on October 8, GPR profiles 1-5, 10, and 11 (Figure 2.24), using RTA 50MHz and 500 MHz shielded antennas, respectively (see Table 2-7). For the first time we have used the 250 MHz shielded antenna in a Avdar mountain fault study (Table 2-7).

After data processing and verifying the first GPR measurements, we conducted a more detailed geological and geophysical study in the southern part of the Avdar mountain fault in the summer 2012. That study was conducted by a joint team of the University of Strasbourg, France and the Institute of Astronomy and Geophysics. This joint survey included seismic, magnetic, and GPR survey measurements at Z2 and Z3 (47.311460°, 106.726288°), as well as a trench survey.

However, in 2016 another GPR campaign had been planned and did all the field measurements myself. This GPR survey was performed with 50 MHz and 250MHz antennas in the northern part of the Avdar mountain fault, Z4 (47.415778°, 106.847601°) and Z5 (47.439106°, 106.884190°) (see

Table 2-6), and this doctoral dissertation includes only examples of Z4 profiles (Figure 2.23). In Z4 zone, 4 parallel profiles of 160-180 m in length were collected at a distance perpendicular to the fault plane and 55-70 m between two profiles (Figure 2.30), apart to ensure underground fault information.

Topographic survey measurements of the sections were also performed using a trimble 5700 differential GPS system with RTK mode.

Table 2-6 Avdar 2016 GPR survey acquisition parameters.

	Site name	**Profile name**	**Antenna**	**Distance interval**	**Profile distance**	**Time window**
1.	2016 Z4	Pr01-Pr04	RTA50 MHz	0.05 m	160-180 m	391 ns
2.			250 MHz	0.05 m	160-180 m	160 ns

Table 2-7 Avdar 2011 GPR survey acquisition parameters.

	Site name	**Profile name**	**Antenna**	**Distance interval**	**Profile distance**	**Time window**
1.	2011 Z2	Pr01-Pr03	500 MHz	0.05 m	335-361 m	142 ns
2.			RTA50 MHz	0.2 m	335-361 m	528 ns
3.			250 MHz	0.05 m	335-361 m	111 ns
4.	2011 Z2	Pr04-Pr05	500 MHz	0.05 m	398-485 m	142 ns
5.			250 MHz	0.05 m	402-485 m	111 ns
6.	2011 Z1	Pr10	500 MHz	0.05 m	397 m	142 ns
7.			250 MHz	0.05 m	402 m	111 ns
8.	2011 Z1	Pr11	500 MHz	0.05 m	335 m	142 ns
9.			250 MHz	0.05 m	352 m	111 ns
10.	2011 Z1	Pr06	500 MHz	0.05 m	470 m	161 ns
11.			RTA50 MHz	0.2 m	461 m	676 ns
12.			250 MHz	0.05 m	469 m	111 ns
13.	2011 Z1	Pr07	500 MHz	0.05 m	495 m	161 ns
14.			RTA50 MHz	0.2 m	491 m	676 ns
15.			250 MHz	0.05 m	498 m	111 ns
16.	2011 Z1	Pr08	500 MHz	0.05 m	475 m	86 ns
17.			RTA50 MHz	0.2 m	461 m	676 ns
18.			250 MHz	0.05 m	484 m	111 ns
19.	2011 Z1	Pr09	500 MHz	0.05 m	511 m	86 ns
20.			RTA50 MHz	0.2 m	513 m	528 ns
21.			250 MHz	0.05 m	514 m	111 ns

5.2.3 GPR Results and interpretation

The Z2 fault zone is the area where the fault is most clearly visible on the surface (Figure 2.30). This is due to the fact that the water from the ravine is blocked by the wall at the bottom of the fault, and the accumulation of mud and sediments is clearly visible. Layers of sediments accumulated on both sides of the fault plane through three profiles in this section gave a strong reflection of the Ground Penetrating Radar wave (Figure 2.30). The fault plane is not very well visible, but some structures are observed (Figure 2.30). In the GPR profiles made in Z1, the structure of the fault is clearly visible by giving a strong reflection of the Ground Penetrating Radar wave from the fault plane, for which the angle of incidence can be determined. Profile 8 intersects the two segments (red mark) of the fault (Figure 2.30), and the Ground Penetrating Radar result image shows the structure of these faults below the surface by the distortion of the Ground Penetrating Radar wave reflection (Figure 2.30). In addition, there is a large accumulation of sediment between the two segments of the fault, and there are signs of

compression from the bottom or from the side of the second segment of the fault. The structure of this accumulation is similar to that of the Z2 sediment accumulation.

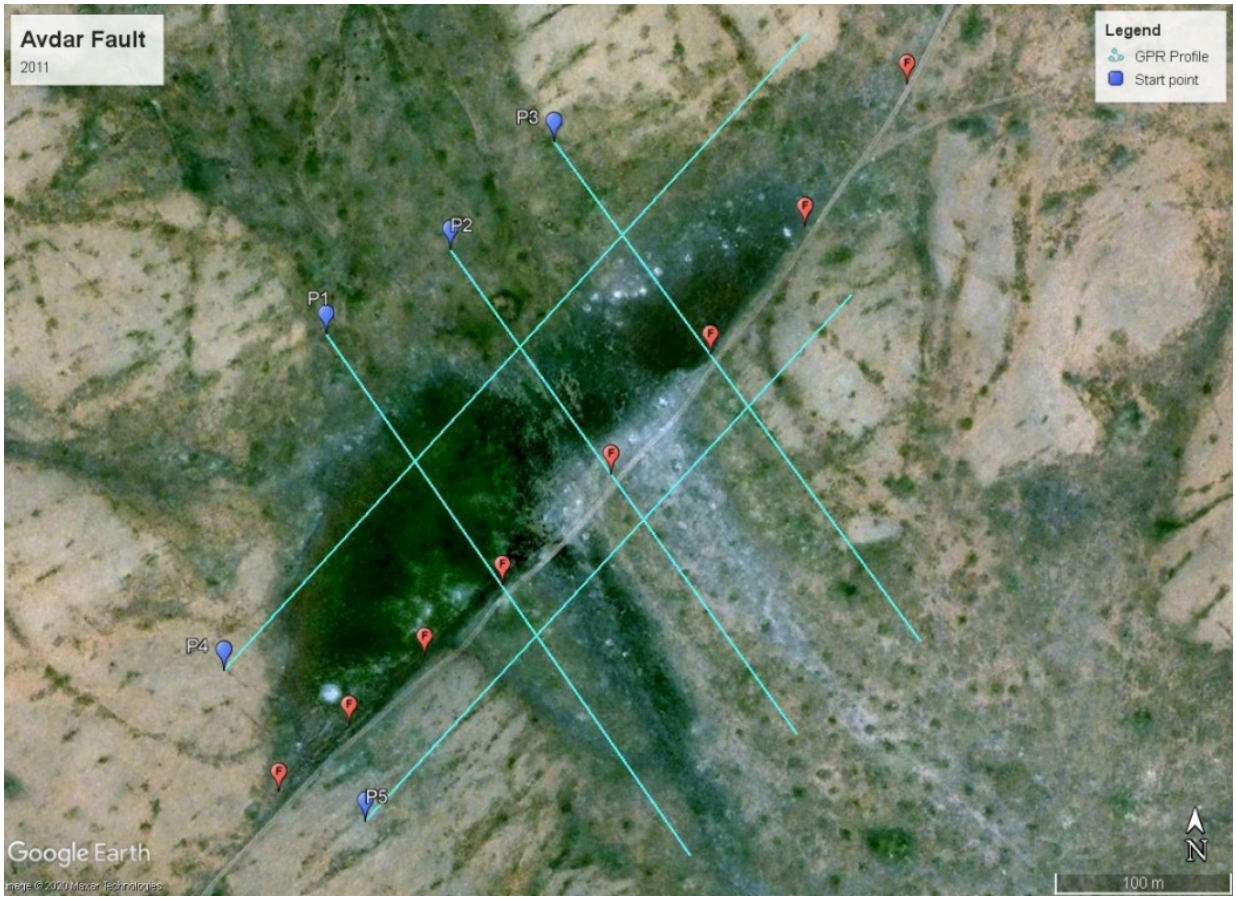

Figure 2.24 Location map of ground penetrating radar profiles in Z2 zone. The zone location is shown in Figure 2.23. Light blue lines indicate the profiles at the RTA50 MHz, 500 MH zand 250 MHz antenna. The blue symbols are indicating the start points and name of profiles. The red symbols are representing fault trace.

The ninth profile in this zone was made down the valley and also intersected two segments of the fault (Figure 2.30). The results of this profile show that in the first 250 meters, the sedimentary layer is clearly visible (indicated by the yellow arrow) and strongly reflected (Figure 2.30). If we look at the structure of this sediment, there is an effect of compression. At 270 and 370 meters of the profile, the traces of surface rupture and the direction of the deep structure almost coincide. From this, the angle of fall of the deep fault was calculated by converting it to the ratio of the actual quantity, and the two angles were almost identical and had a value of approximately 18.4º. It is possible to determine the direction of movement of the fault at the bottom of these two segments of the fault, which is 370 meters, which shows signs of normal fault structure. However, the nature of the fault in this section alone cannot be

considered a normal fault, and the displacement of all sections of the fault must be determined by careful identification and summarization.

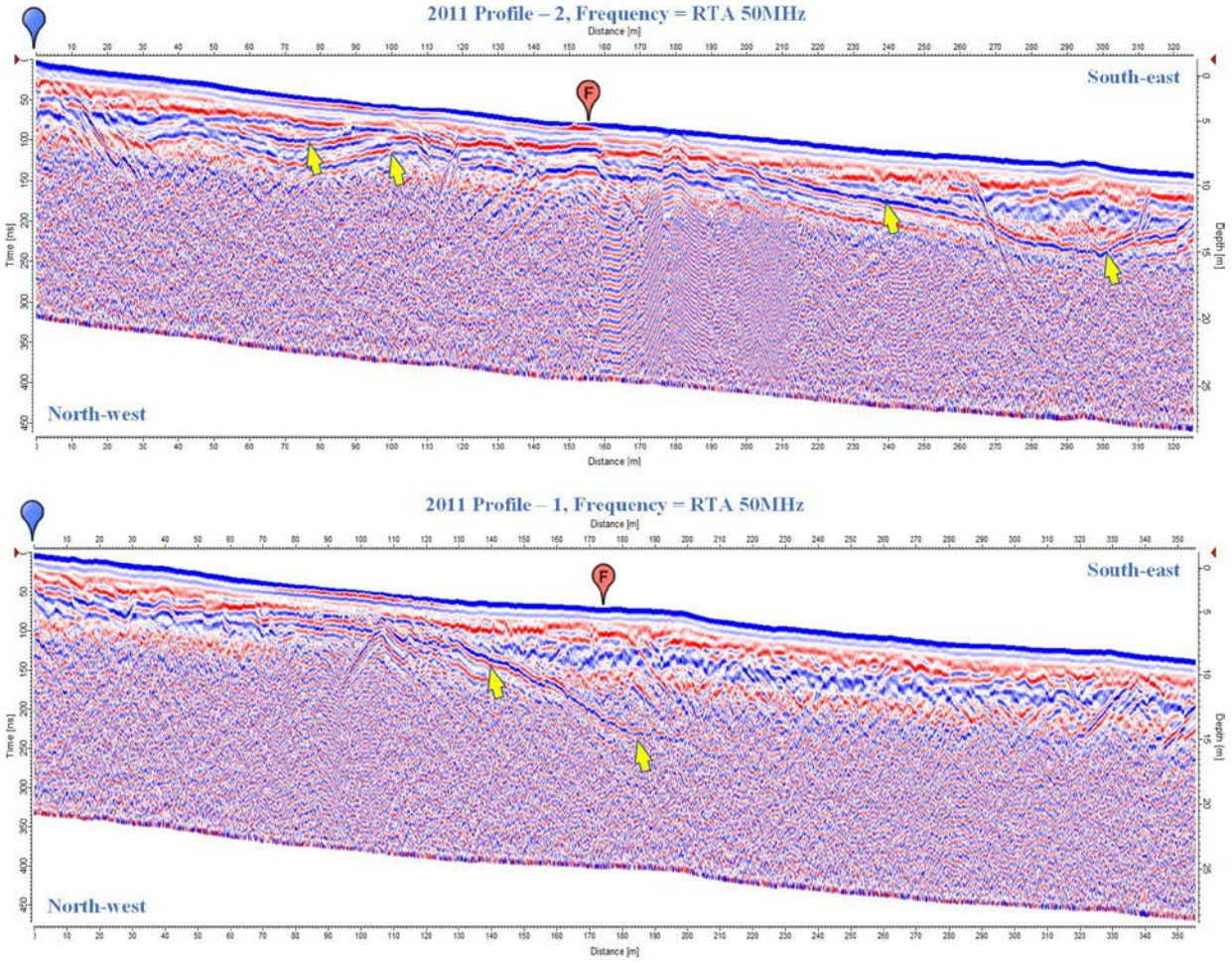

Figure 2.25 Result of GPR image of the profile P1 and P2 (acquired the October 2011) obtained with RTA 50 MHz antenna in the Avdar active fault. The GPR result image shows a clear layer structure (yellow arrows), and surface rupture location is red colored symbols (F), the blue symbols are measurement start point.

The 2016 Ground Penetrating Radar survey was conducted in some unexplored areas of the Avdar fault, which is important to confirm and refine the results of previous surveys. The location of the four parallel profiles made in 2016 can be seen in Figure 2.30. As an example, the results of two middle profiles, 2nd and 3rd, are included. Figure 2.30 shows the results of a 50 MHz antenna, which shows a three-stage structure of the fault. The structure at the first, 55 meters, gave a very strong reflection and continued at a considerable depth, up to a depth of about 10 meters. Its direction to the surface corresponds to the fault (F) mark on the surface

rupture. However, the structure of the fault in the 80 th meter or depression of the profile appears to be broad. The last part, the 110-meter structure, is a deep strip with a narrow strip.

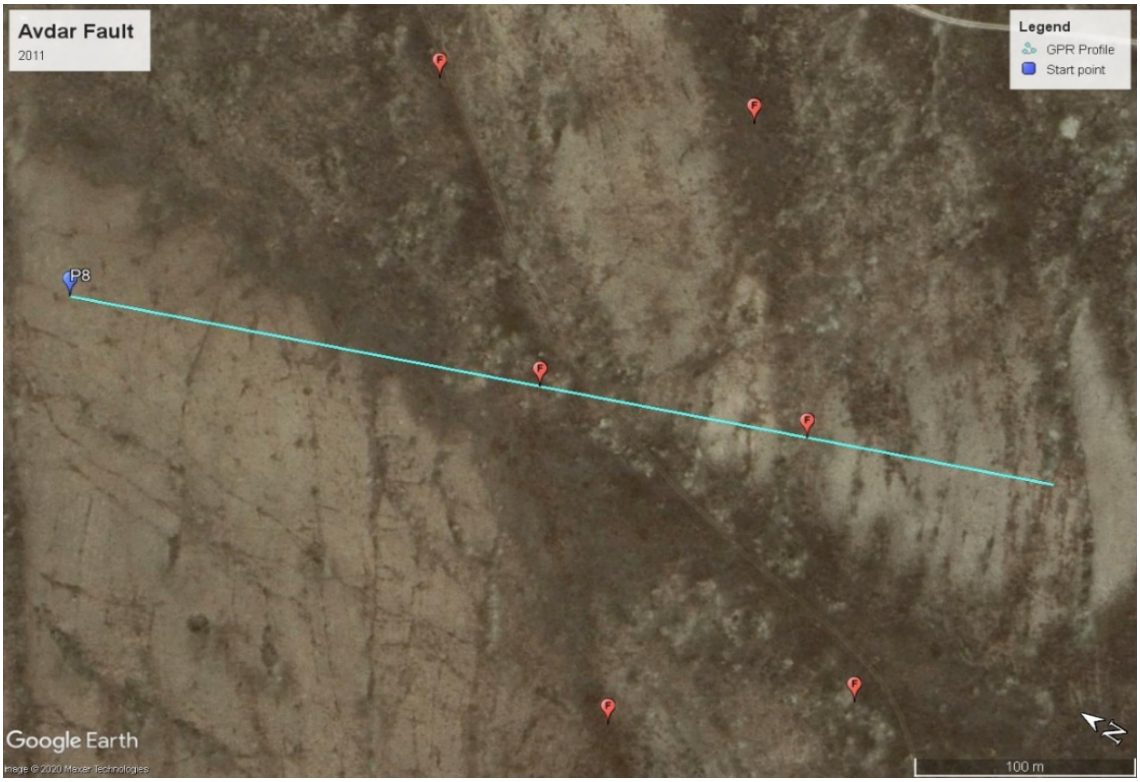

Figure 2.26 Location map of ground penetrating radar profiles in Z1 zone. The zone location is in Figure 2.23. Light blue lines indicate the profiles at the RTA50 MHz, 500 MHz,and 250 MHz antenna. The blue symbols are indicating the start points and name of profiles. The red symbols are representing fault trace.

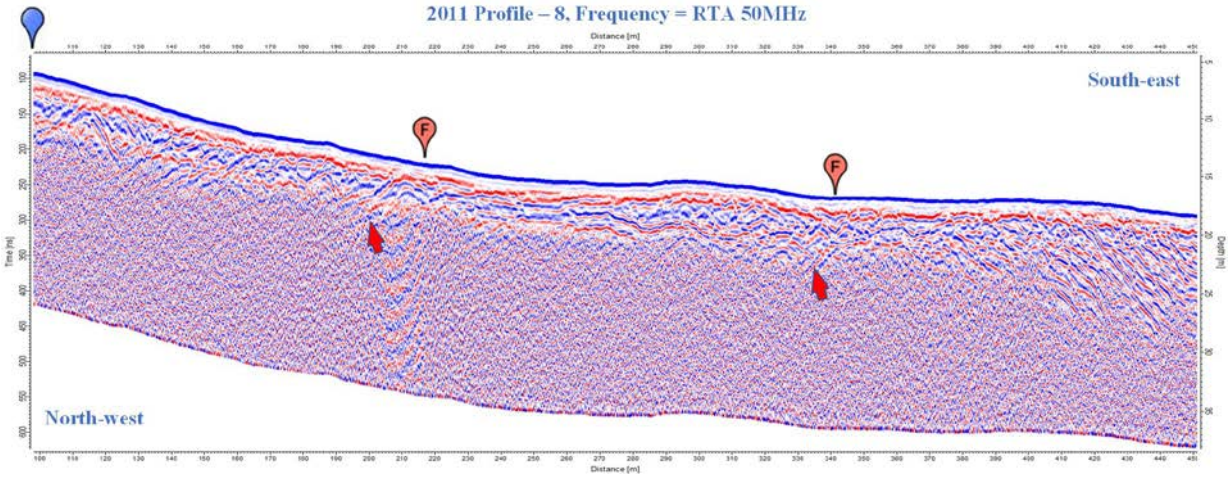

Figure 2.27 Result of GPR image of the profile P8 (acquired the October 2011) obtained with RTA 50 MHz antenna in the Avdar mountain fault. The GPR result image shows an

underground fault structure (red arrows) and surface rupture location is red colored symbols (F), the blue symbols are measurement start point.

The continuation of this fault segment is also consistent with the markings made on the surface rupture. In profile 3, the first clear anomaly is visible at 20 m and the second at around 130 m. The dip of the fault is the same as in the previous profiles, and the location of the fault corresponds to the fault trace point (F) marked on the surface rupture Figure 2.30. As a result of these profiles, vertical displacement of the normal structure and tensile effects are observed in some areas, such as 110 meters in Figure 2.30, 20 and 130 meters in Figure 2.30.

AL ASHKAR Abeer's doctoral dissertation on the Avdar and Sharkhai faults, the Avdar fault was defined as a left-lateral fault with a normal component (Abeer, 2015).

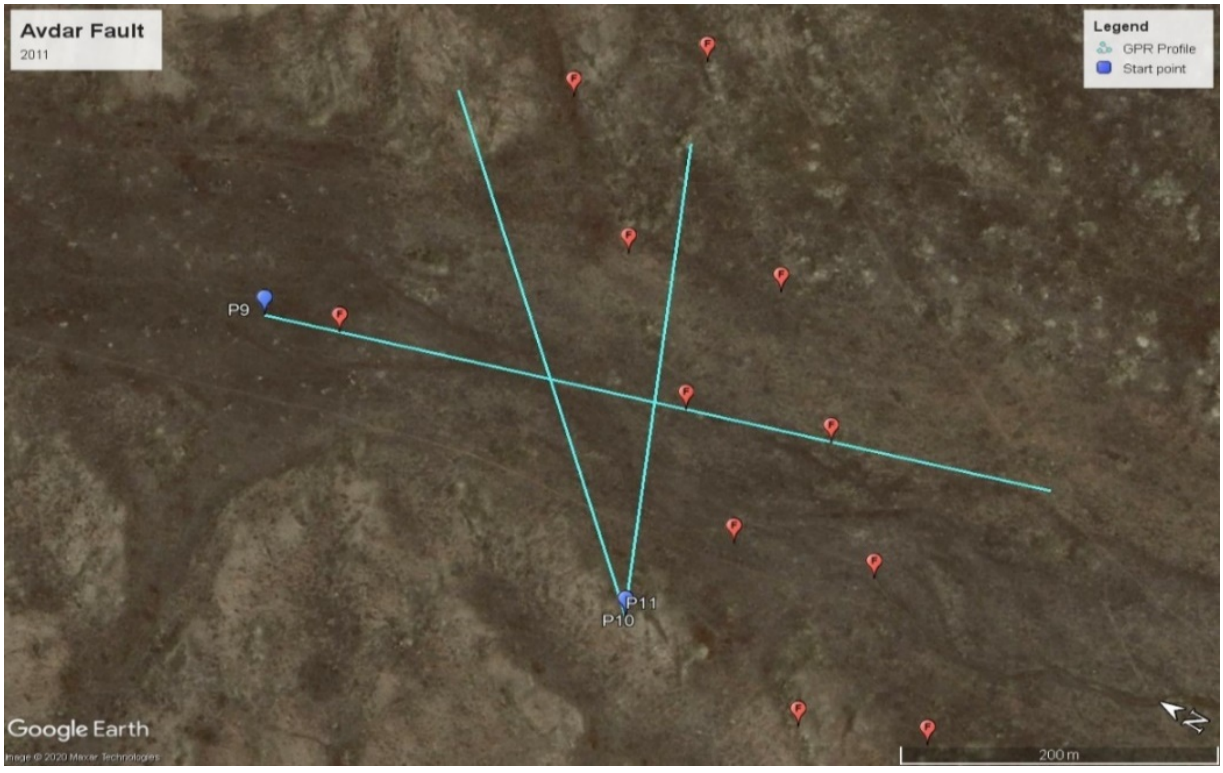

Figure 2.28 Location map of ground penetrating radar profiles in Z1 zone. The zone location is shown in Figure 2.23. Light blue lines indicate the profiles at the RTA50 MHz, 500 MHz, and 250 MHz antenna. The blue symbols are indicating the start points and name of profiles. The red symbols are representing fault trace.

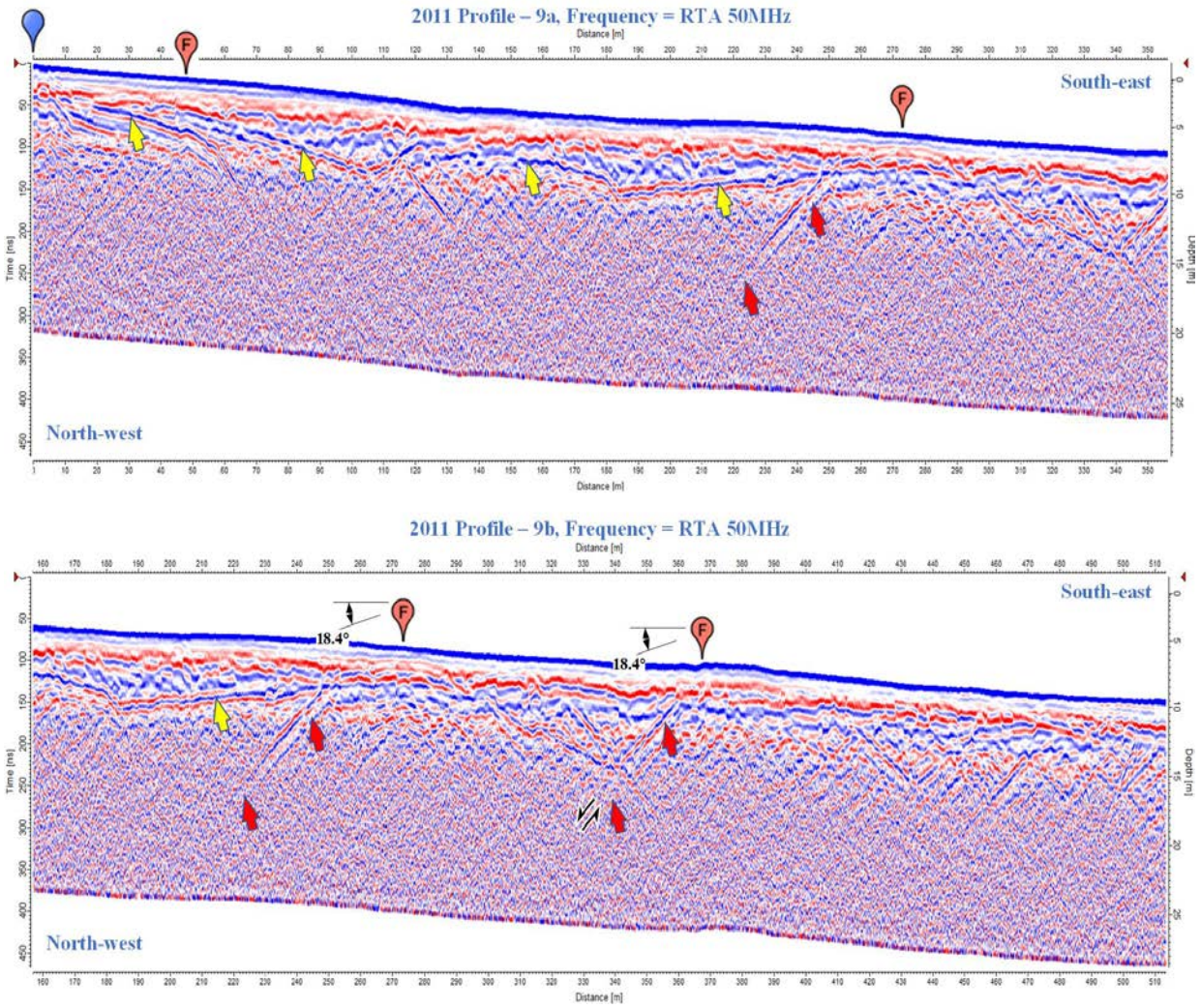

Figure 2.29 Result of GPR image of the profile P9 (acquired the October 2011) obtained with RTA 50 MHz antenna in the Avdar fault. The GPR image shows a clear fault structure (red arrows), and surface rupture location is red colored symbols (F), two dipping angles approximately of 18.4º, yellow arrows are pointing bed rock layer.

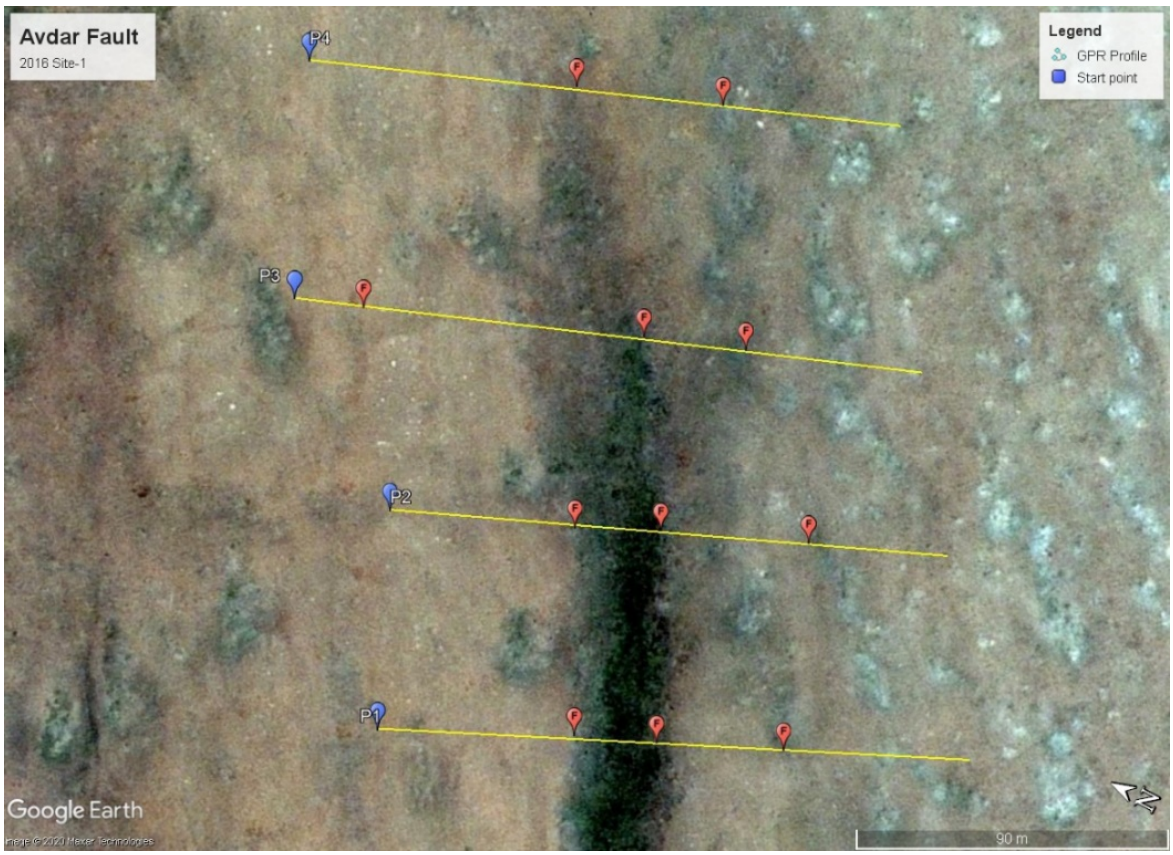

Figure 2.30 Location Map of GPR profiles in Z4 zone. The zone location is shown in Figure 2.23. Yellow lines indicate the profiles obtained with RTA 50 MHz and 250 MHz antenna. The blue symbols are indicating the start points and name of profiles. The red symbols (F) are representing surface rupture locations.

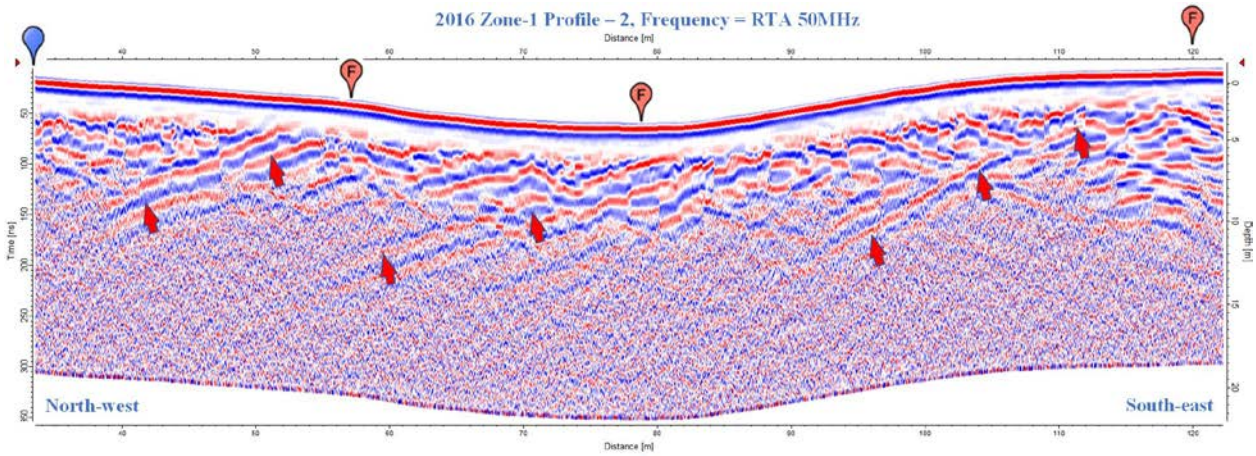

Figure 2.31 Result of GPR image of the profile P2 (acquired in August 2016) obtained with RTA 50 MHz antennae in the Avdar active fault. The GPR image shows a clear underground structure (red arrows), and surface rupture locations are shown by red colored symbol (F), the blue symbols indicate the starting points of measurements.

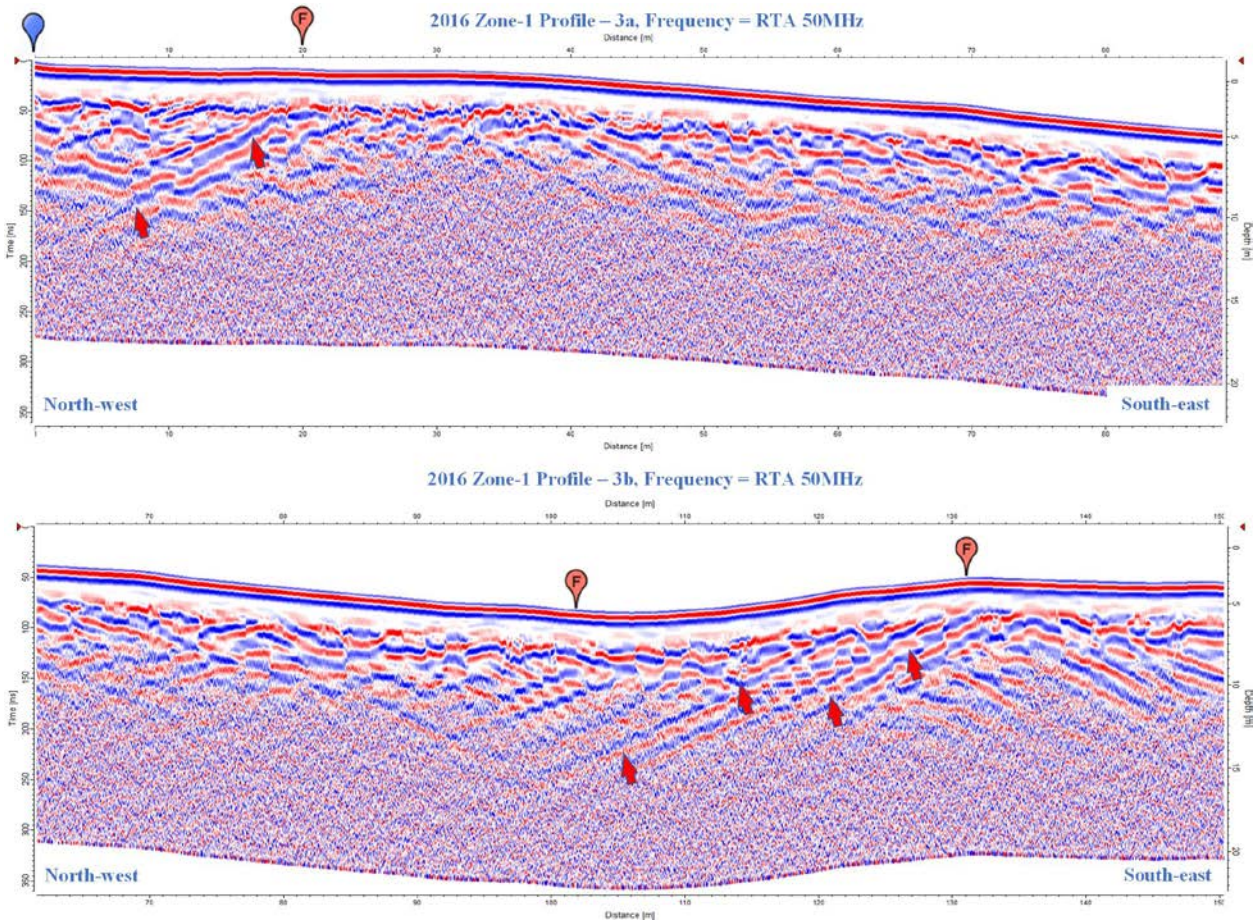

Figure 2.32 Result of GPR image of the profile P3 (acquired in October 2011) obtained with RTA 50 MHz antenna in the Avdar mountain fault. The GPR image shows a clear underground structure (red arrows), and surface rupture locations are shown by red colored symbol (F), the blue symbols indicate the starting points of measurements.

6 Application of 3D GPR data to characterization of active faults

Ground Penetrating Radar's three-dimensional survey methodology is classified into 3D layer surface, 3D Iso-surface, 3D time slice and 3D volume, where GPR 3D time slice and 3D layer surface techniques are widely used in fault studies. In collaboration with a IAG team and team of researchers from the University of Strasbourg in France, we conducted detailed three-dimensional Ground Penetrating Radar measurements to determine channel displacement in Emeelt fault between 2010 and 2011. This 3D measurement information was processed, visualized and interpreted using 3D layer surface and depth time slice techniques. The 3D layer surface processing, imaging, and interpretation work was performed by a team of researchers from the University of Strasbourg and is included in Dr. Jean-Rémi DUJARDIN's dissertation (Dujardin J.-R. , 2014). However, our Ground Penetrating Radar research team of the IAG did

the processing, imaging, and interpretation of the 3D time slice of the depth profiles, so I have included and compared my work in this section.

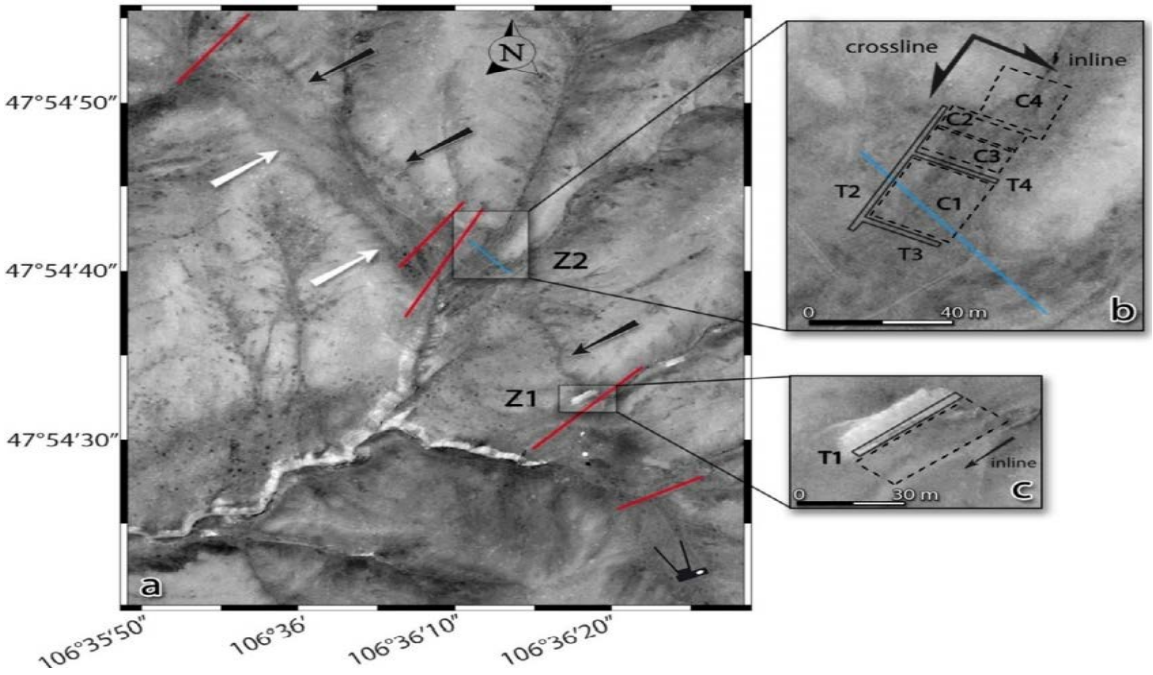

Figure 2.33 Location of ground penetrating radar profiles in Z1 and Z2 zones. The main location is in Figure 2.20. a) red lines indicate the profiles at the RTA50 MHz antenna. The black and white arrows are indicating the surface ruptures. b) Zoomed location map of the trenches (T2, T3 and T4) and GPR 3D cubes (C1, C2, C3 and C4), blue line is fault trace. c) Zoomed map of the T1 trench and 500MHz GPR profiles, after (Dujardin J.-R. , 2014).

6.1 Description & Survey Grids

The vertical resolution depends on the velocity of EM waves and the frequency of the antennae used. Following the λ/4 criterion (Wides, 1973; Jol, 1995; Zeng, 2009), it varies from 70 to 5 cm for frequencies of 50–500 MHz and velocities of 0.1– 0.14 m/ns. In general, features such as sedimentary structures, lithological boundaries, fractures and/or faults are clearly visible with GPR (Neal, 2004; Gross, et al., 2004; McClymont, et al., 2010), even when these features differ only by small changes in the nature, size, shape, orientation and packing of grains (Guillemoteau, et al., 2012). After the geomorphologic recognition of the Emeelt fault and a preliminary trench (T1) realized in 2009 (Figure 2.33), we decided to use GPR measurements to investigate subsurface deposits potentially affected by the fault on a wider area. The GPR observations should help us to decide location of future trenches. Our first objective was to study an alluvial fan situated close to the trench T1 (referred to as Z1 area) for three reasons. First, the sedimentary deposits provide a stratigraphy that, if offset by the fault, can give us

information on the geometry and dynamic of the fault, such as the dip, amplitude and direction of displacement with a non-destructive method. Second, sediments are usually favorable to EM propagation and third, the proximity of the trench will allow us to perform a direct comparison of both datasets (geology and GPR). In this survey we used a MALA 500 MHz shielded antenna to get detailed features at shallow depth and to have a depth of penetration and a wavelength consistent with the trench observations. We recorded 25 profiles of 40 m long on both sides of the trench T1 and parallel to it with the aim to cut through the fault. The space between profiles was 1 m and the recoding step was 0.03 m.

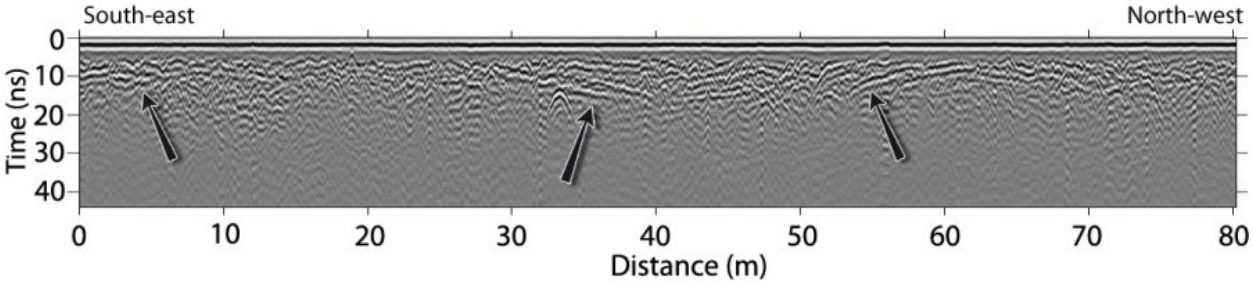

Figure 2.34. Example of a 500 MHz profile crossing paleo-channels and recorded in 2010 to verify the presence of the paleo-channel in the GPR data before the precise work on "cubes". Its location is displayed in Figure 2.33 (blue line). Black arrows highlight dipping reflections, which are related to the flanks of the channels, after (Dujardin J.-R. , 2014).

About 300 m north of Z1 area, the morphology shows two small streams crossing the fault and evidence of recent sedimentary deposits (Figure 2.33b). To check for the presence of hidden paleo-channels filled by sediments and cut by the fault, we recorded eleven profiles across and perpendicular to both streams using the 500 MHz antenna. The profiles were 80 m long with a recording step of 0.03 m. The profiles show a clear paleo-channel under the northernmost stream, well imaged by GPR (blue line on Figure 2.33b and Figure 2.34). Consequently, we decided to perform the pseudo-3D GPR survey in this area crossed by the fault (Z2 area). We opened simultaneously, due to field constraints, three trenches (T2, T3 and T4) in Z2 area; one across the fault (T2) and two parallel to it (T3 and T4). Their location and geometry are shown in Figure 2.33b. The GPR survey was separated in four distinct pseudo-cubes, denoted 1 to 4. Cubes C1 and C2 were recorded in 2010 while complementary cubes C3 and C4 were recorded in 2011.

Table 2-8. Emeelt 3D GPR survey acquisition parameters.

	Site name	Profile name	Antenna	Distance interval	Profile distance	Profile interval	Time window
1.	2010 July 01 (C1 cube)	Pr01-Pr107	500 MHz	0.02 m	25 m	0.25 m	82 ns
2.		Cr01-Cr26	500 MHz	0.02 m	26 m	1 m	82 ns

The main objective of this survey was to image the paleochannel in 3D in order to characterize any horizontal/vertical displacement caused by the fault. The pseudo-3D approach has become a common procedure and has successfully been used in the case of active fault studies (Malik, et al., 2007; Beauprêtre, et al., 2012). A full 3D acquisition schema requires an interval of a quarter wavelength grid spacing (Grasmueck, et al., 2005) in both in-line and crossline directions of the 3D cube. This would require one profile every five centimeters (for a mean velocity of 0.1 m/ns) with a 500 MHz antenna. The number of profiles would then be multiplied by five compared to our current survey. As a result, and due to time constraints on the field, we have chosen the pseudo-3D approach rather than a full 3D schema. The profiles were parallel to the fault direction and spaced each 25 cm. (see Table 2-8 for more details about the acquisition geometry).

The topography of all GPR profiles was recorded using differential GPS. The GPS antenna was mounted on a backpack carried by an operator who was following GPR paths. The recording step of the GPS was set to 20 cm. Saw-tooth effects were observed on the topographic profiles due to the small movements of the operator while he was walking. In order to get rid of these undesirable effects, a high degree polynomial curve fitting for the data was used, instead of using raw topographic profiles.

6.2 3D GPR processing

The processing of all GPR profiles has been performed with in-house software (Girard, 2002) written in MATLAB. We used a common flow procedure involving a constant shift to adjust the time zero; a DC filter to remove the low frequencies; a flat reflections filter to remove some clutter noise (ringing caused by multiple reflections between shielded antenna and the ground surface); a time varying gain function and finally a band-pass filter (elliptic tapered filter). The time varying gain function is a smoothed version of the trace envelope calculated by Hilbert transform. Band-pass filters are of 20-150 MHz and 100-800 MHz for the 50 and 500 MHz antennae, respectively. A velocity analysis, which is not presented here, has been done over the surveying area by analyzing diffraction hyperbolae present in the GPR data. It

gives a mean velocity of 0.135 and 0.095 m/ns for the data collected in 2010 and 2011, respectively. These values are constant and consistent for both frequencies (500 and 50 MHz antenna). The difference in velocity is explained by the unusual humid period during the survey in 2011 compared to the 2010 dry summer. Afterwards a Kirchhoff migration, which accounts for the topography (Lehmann & Green, 2000; Heincke, et al., 2005), and (Dujardin & Bano, 2013), has been applied before loading the data into seismic interpretation software (OpendTect). The topographic migration of each profile has been performed with a constant velocity.

6.3 GPR results and interpretation.

On the north of the Z1 area we recorded eleven profiles of 80 m long across the two streams to verify the presence of the paleo-channel in the GPR data and to help choose a location for the precise 3D work. One of these profiles is presented in Figure 2.34. The dipping reflections showing moderate continuity are indicated by black arrows. The middle and the right ones clearly define the flanks of a paleo-channel. Sub-horizontal reflections with moderate continuity and many diffraction hyperbolas lie in-between and are related to the sedimentary filling of the channel and the presence of many rocks. On the left side, another dipping reflection is observed. It is related to the edge of a second paleo-channel crossed by the profile. From those results, we decided to investigate the first channel in depth with the pseudo-3D surveys (Dujardin J.-R. , 2014). The acquisition geometry is presented in Table 2-8.

Figure 2.35a present a photomosaic from the north wall of trench T4. White wires in vertical and horizontal directions highlight the 1 m spacing gridding of the trench. The profile shown in Figure 2.35b is the northern most profile of the cube C1 and is 2.5 m away from the trench T4 wall. The photomosaic and the GPR profile have the same scale, and there is no vertical exaggeration. Three main units were identified in the trench and highlighted here by brown, yellow and orange colors. The brown unit is characterized by a silty-sandy material with some gravel scattered inside it. Locally, gravels are gathered in thin horizontal layers, highlighted by red lines. It corresponds to the filling of the channel. The two next units are characterized by yellowish coarser material. The first one (the yellow unit) is a layer of around 50 cm thick with centimetric stones. The last unit (orange one) is very similar to the yellow unit, but with many scattered centimetric stones.

After processing, all the profiles were merged in one single survey and loaded into seismic interpretation software (OpendTect) which allows 3D representations, depth slices and

horizon picking. We tried depth slices representation and attribute analysis to improve the quality of the interpretation, but the results were disappointing due to the space between the profiles. Horizon picking was much more time consuming but gave much more interesting results. Owing to the strong disparity of the reflections, which did not allow a semi-automatic picking, we picked the channel's flanks manually.

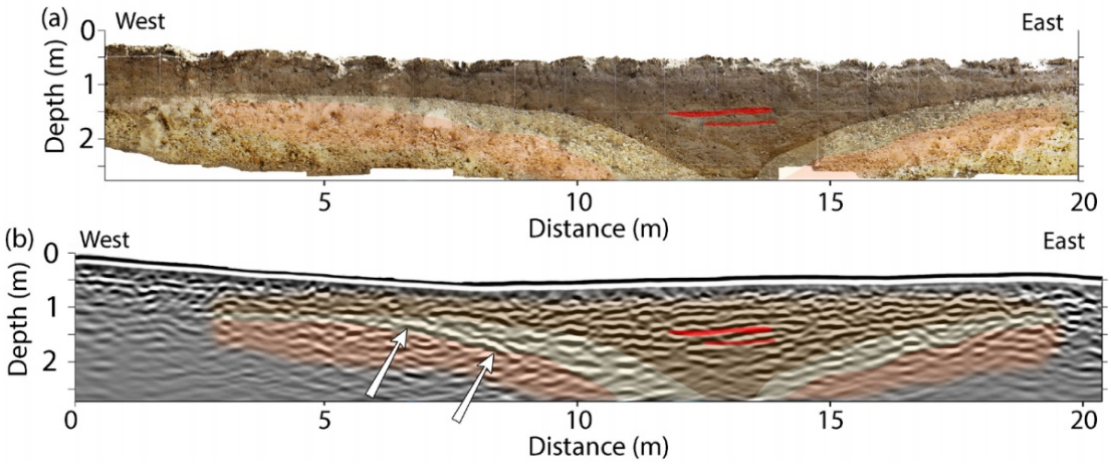

Figure 2.35 a) Photomosaic of the north wall of T4 trench and (b) northernmost profile of cube C1, 2.5 m away from the trench wall. Three main different units were identified in the trench highlighted here by brown, yellow and orange colors. They are superimposed on the trench and the profile for comparison. The brown is a thin brownish unit filling the channel, the yellow is a yellowish coarse deposits unit (centimetric sized), and the orange is a yellowish unit with fine material. Within the brown unit, a gravel lens is observed and highlighted by the red lines. A good consistency is observed between the GPR data and the trench. The gravel lens (red lines) is almost perfectly aligned with a reflection in the GPR profile. The left flank of the channel (limit between the yellow and the orange unit) is as well matching a reflection (arrows) and the yellow unit corresponds to an attenuated signal. On the east side, the unit's interfaces seem to match with dipping reflections but with a lateral offset that can be explained by the distance between the trench and the GPR profile (2.5 m) after (Dujardin J.-R. , 2014).

During this step, crossline profiles were of great importance as they permit a strong correlation of the reflections from one profile to the next one. The result of the manual picking is the 3D surface presented in Figure 2.36 in relation with GPR profiles (three in-lines and one crossline). The depth (from the most elevated point in the topography) is presented by color scale. Green lines on the profiles represent the picking, thus the intersection between the surface and the profiles. The red arrow indicates the flow direction. The displayed surface is obtained

by interpolating the picked profiles taken from cubes C2, C3 and C4. Afterwards, the main slope of the channel was subtracted to provide a better interpretability of the data. The removal of the main slope straightens the channel, and the geometry of the flanks is greatly enhanced. The result is superimposed on the aerial view (Figure 2.37). The channel appears very heterogeneous, and many bumps are observed at its bottom. The penetration depth, from 1.5 to 2 m, is often lower than the depth of the channel. The SE flank is straight on its upper part and starts enlarging at around 27 m distance from the SE corner of cube C1 (scale on Figure 2.37a). This enlargement is linked to the arrival in the sedimentary basin. The NW flank is as well straight in its deepest part except for the shift at around 49 m distance with right lateral amplitude of about 2 m (black arrow, Figure 2.37).

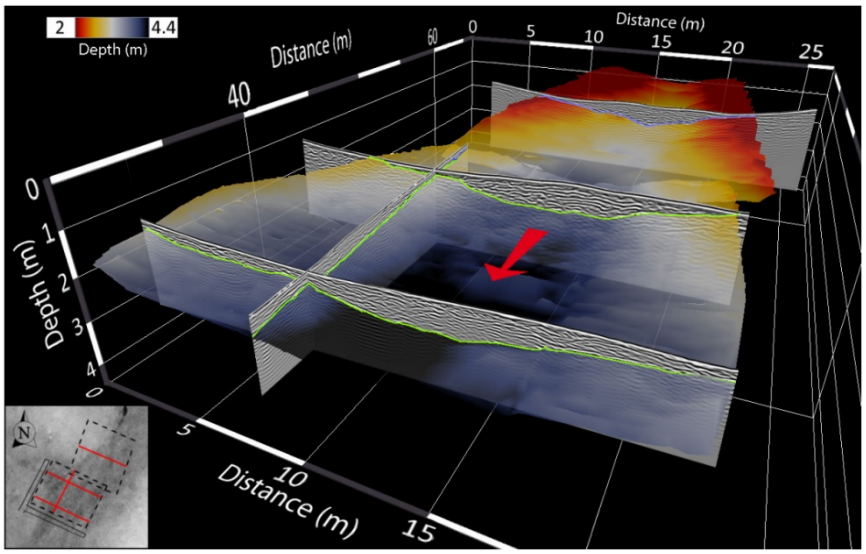

Figure 2.36 Four GPR profiles with the paleo-channel picked in green. The 3D surface (in colors) of the paleo-channel was deduced from the picking on all the profiles of the cube C2, C3 and C4. The red arrow shows the paleo-flow direction. The map on the down-left corner shows the relative position of the profiles, after (Dujardin J.-R. , 2014).

The picture in Figure 2.37b has been taken inside the trench T2 (area Z2), at the position of the pink asterisk. It shows evidence of the fault within a gravel layer with a dip toward the NNE. This dip direction was also determined at the surface as the fault trace moves upstream when crossing a local valley.

The locally apparent vertical offsets of reflections on some of these profiles cannot be directly related to a vertical component of the slip. Firstly, it is impossible to associate the reflections observed on each side of the fault zone because of the shallow penetration of 500 MHz signal and the very few sub-horizontal reflections. On the other hand, the right lateral

component can bring itself apparent vertical offsets in a context of interlocked alluvial deposits. However, a vertical component is suspected by the morphology and the dip of the fault near the surface, but its amplitude cannot be quantified by our GPR data.

On Z2 area, we observed a deep paleo-channel with a few 500 MHz profiles (down to about 2.5 m depth) fossilized by the filling material and crossing the fault. As we suspected a horizontal slip component from the linearity of the seismicity and the fault morphology, we decided to map the channel flanks across the fault by a pseudo-3D approach with numerous 500 MHz in-line and 82 crossline profiles that were acquired during 2010 and 2011 summers. A right lateral offset of about 2 m was imaged on the right downstream flank; it was preserved on the downstream right flank while it has been eroded on the downstream left flank (schema, Figure 2.37c). Afterwards, the filling of the paleo-channel fossilizes the paleo-morphology.

In the 3D channel reconstruction, we did not observe any clear vertical offset. Nevertheless, it does not prove its absence as the bottom of the channel was locally difficult to follow due the low penetration depth, which was of same depth as the bottom of the channel.

After GPR standard processing for the every profiles, the data of pseudo-3D analysis, we created a pseudo-3D data set and produced indepth-slice 2D result images using Matlab software. In the Matlab program, a pseudo-3D GPR data set of 107 profiles of the C1 cube was created, and the pseudo between them were interpolated and rehabilitated, and the depth-slices were made in 0.01 m or 1 cm increments. In the Figure 2.38 shows a three-dimensional entire data set image of the C1 cube between the T3 and T4 trenches of the Emeelt fault study area. The depth incisions were made in 1 cm increments to allow for animation of soil changes in the paleo river channel.

We continued this depth-slice processing to a depth of 1.31 m below ground surface and obtained a total of 122 horizontal profiles of the resulting images, which were combined to produce a moving animation of soil depth changes. In this animation, we can see the changes in the depth of the soil and how the paleo river channel flows through the water.

In addition, the results of the depth-slice show that the traces of soil eroded by the faults are not very clear. It also appears that some of the horizontal displacements along these fault boundaries can be identified.

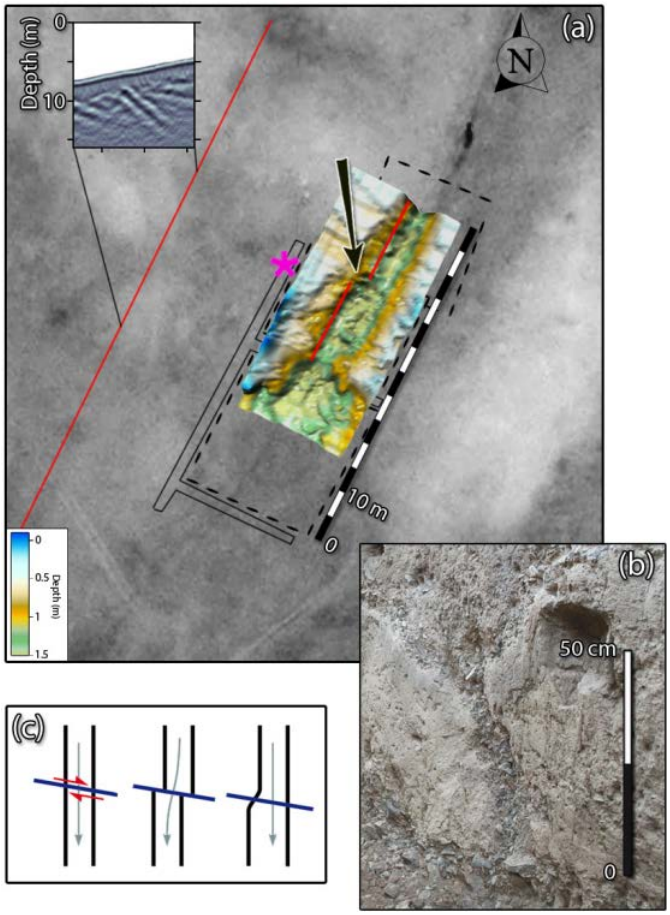

Figure 2.37 (a) Interpretation map of Z2 area. The interpolated 3D surface of the channel (after subtraction of its main slope) is superimposed on the satellite image. An offset of 2 m horizontally is observed on the NW flank of the channel (highlighted by the red lines and the black arrow), which is consistent with a right lateral strike-slip. The pink asterisk shows the location of picture (b) in the trench where evidence of the fault is observed. The closest RTA profile (upper left corner) shows the record and the location of the fault plane in depth. (c) Illustration of the evolution of the channel flanks due to the right lateral strike slip. The down left flank is preserved while the down right flank is eroded after the shift. The filling of the paleo-channel fossilizes the paleo-morphology, after (Dujardin J.-R. , 2014).

Some examples of the depth slice result images of the C1 pseudo-3D GPR data cube (acquired the June 2010) obtained with 500 MHz shielded antenna in the paleo river channel of the Emeelt active fault are shown in Figure 2.39. The interpreted depth slice result image 0.48m below ground surface presented in Figure 2.39a and depth slice result image 0.53 m below ground surface presented in Figure 2.39b, where blue arrows indicating fault traces location and the channel upside is rain water inlet side and channel downside are rainwater outlet side (Figure 2.39).

The results of the above two methods of the pseudo-3D GPR processing, imaging and analysis show that both methods are more effective in active fault studies or paleo-seismological studies. In particular, it is clearly shown that the horizontal displacement of the active fault and the location of the fault trace are predominant. It is also possible to identify traces or geometry of vertical displacements after further development of pseudo-3D GPR survey design and methodology.

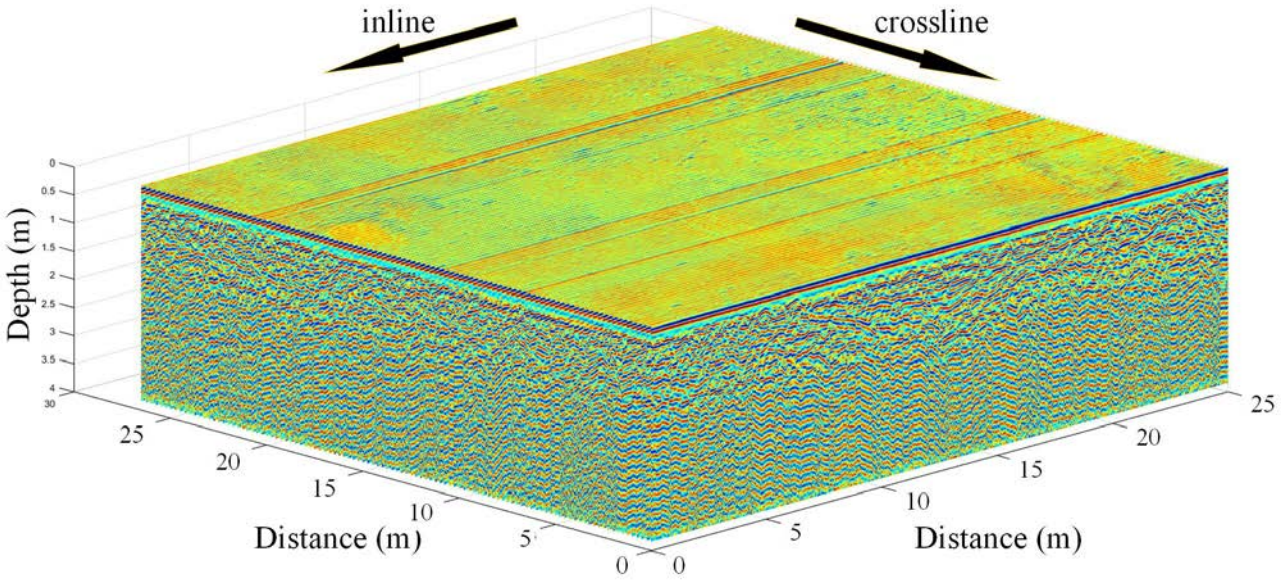

Figure 2.38 Pseudo-3D data cube of the C1 cube obtained with 500 MHz shielded antenna in the paleo river channel of the Emeelt active fault. Inline arrow pointed measurements direction of the GPR profiles parallel to the T3 and T4 trenches (see Figure 2.33 for the locations). Crossline arrow pointed measurement direction of the GPR crossed profiles.

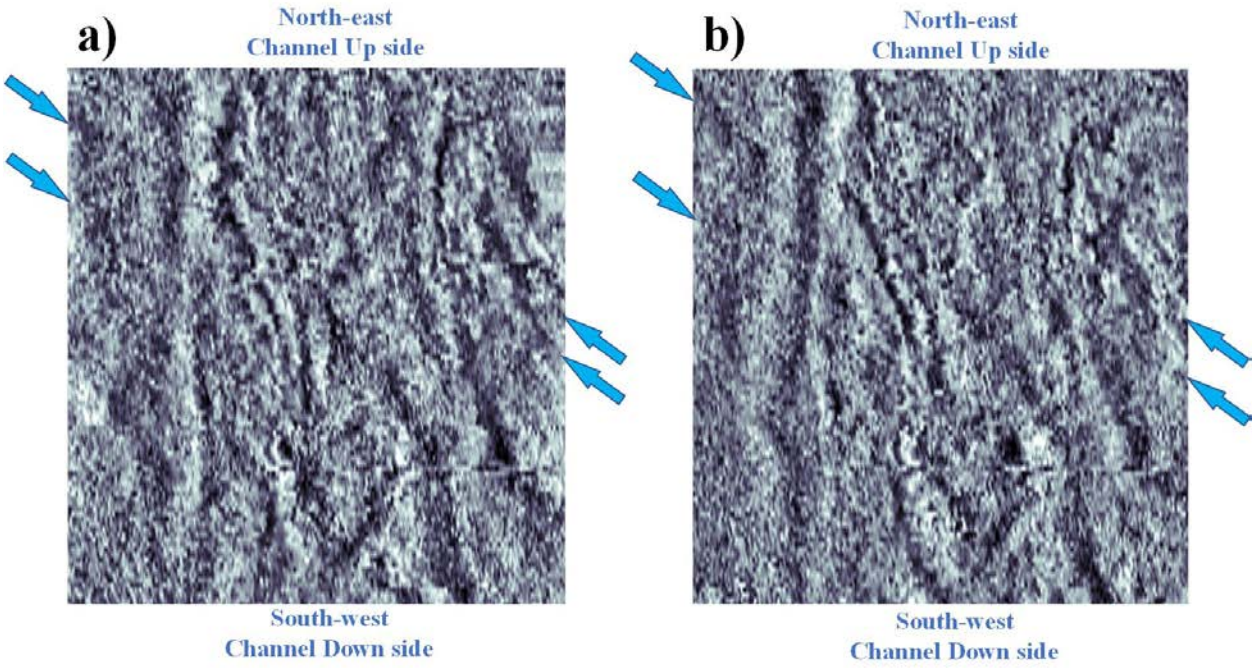

Figure 2.39 Result of depth slices images of the C1 pseudo-3D data cube (acquired the June 2010) obtained with 500 MHz shielded antenna in the paleo river channel of the Emeelt active fault. a) Depth slice 0.48 m below ground surface, b) Depth slice 0.53m below ground surface, blue arrows indicating fault traces. Channel upside is rainwater inlet side and channel downside are rainwater outlet side.

7 Conclusions

This work is a part of numerous studies on the characterization of active faults of Mongolia. For the first time we used GPR to explore and reveal the buried traces of a newly discovered active fault in area showing low slip rate. It is a challenge as we are in a context where the geomorphologic features have been heavily smoothed since the last event due to erosion processes combined with a very long return period probably of several thousands of years.

The results of two-dimensional and three-dimensional GPR surveys and analyzes conducted since 2010 on active faults in the central region of the Mongolia and around Ulaanbaatar capital city were presented. During this time, we imaged, mapped, analyzed, and interpreted GPR survey results for all types of active faults. Based on the survey objectives and after having reviewed the GPR survey results for the active fault characterization, the following can be concluded:

The combination of 500MHz, 250MHz with RTA 50MHz antenna produces three complementary and consistent datasets as they allow the imaging of different structures. A good consistency is observed between the 500 MHz antenna GPR profiles and trenching results.

Despite the low penetration depth of the GPR up to 15 m for the 50 MHz antenna, 5m for the 250 MHz antenna and 3 m for the 500 MHz antenna, it clearly provided several important pieces of information that improve our understanding of the active fault geometry and horizontal displacement.

One of the main results of this study is that it is possible to distinguish between compression and tensile effects of the active fault by combining the geomorphology of active faults and the imaging of underground structures imaged by GPR measurements.

It is also possible to reconstruct the structure of paleo-seismically active faults hidden under alluvial sediment accumulation and to determine the extent of the displacement with greater accuracy than traditional paleo-seismological methods..

The high efficiency of GPR studies in determining the optimal location for trench excavation has been reaffirmed.

Pseudo-3D profiles, recorded with a 500 MHz antenna over a paleo-channel crossing the Emeelt fault, provided information about the lateral displacement of 2 m caused by the fault and active fault trace locations. It could be associated to an earthquake with magnitude Mw of about 7 or several with magnitude Mw≥ 6.

The 50 MHz GPR profiles show a direct reflection, coming from the fault plane, giving access to the location, the dip angle and direction of the fault. In contrast, the linearity of the actual seismicity indicates a near vertical fault plane examples in GPR result of the Avdar, Bayankhongor and Emeelt active faults. To clarify that point, we need to investigate more in depth the active structure, by combining GPR with high resolution seismic profiles and very precise 3D relocation of the seismicity.

Chapter 3 : The characterization GPR-based technique of the Songino active fault, Ulaanbaatar, Mongolia.

1 Introduction

During the 20th century, Mongolia was one of the most seismically active intra-continental areas in the world with four large earthquakes (Magnitude around 8) along its active faults in the western part of the country (Schlupp, et al., 2012).

However, there is very low on the damages sustained by these strong earthquakes, which is due to Mongolia's small population, low urbanization, and low nomadic lifestyle. However, according to the reports of strong earthquakes around the world, the magnitude of the earthquake in our country is less than the magnitude of the earthquake of the other country, but many people were death and a lot of economic damage was caused (Table 3-1, Table 3-2.) However, it is clearly related to the urbanization, population density and settlement of these countries.

The capital city of Mongolia, Ulaanbaatar, is in a relatively low seismic zone, but at a time when the city's population and urbanization are increasing rapidly, it is impossible not to talk about the hazards of the earthquakes. Today, Ulaanbaatar is home to more than 50 percent of Mongolia's population approximately 1.6 million and is the only major economic, cultural, and commercial center, indicating that it is a high-risk area due to strong earthquakes (Dugarmaa, et al., 2006). The seismic activity observed in the vicinity of Ulaanbaatar (UB), capital of Mongolia, is relatively low compared to the activity observed in western Mongolia. Nevertheless, since 2005, the seismic activity around UB has increased (Dugarmaa, et al., 2006), and is organized at the west of UB along two perpendicular directions: the recently discovered Emeelt fault (about 25 km long) situated at about 10 km West of UB (Schlupp, et al., 2012; Munkhsaikhan, 2016) and Hustai fault (the main segment has a length of ~80 km) with its nearest at about 15 km West of UB (Ferry, et al., 2010; Ferry, et al., 2012).

The Songino fault (20 km long, situated 20 km West of UB) is located between Emeelt and Hustai faults. The length and morphology of these faults indicate that they can produce earthquakes of magnitude 6.5–7.5 (Schlupp, et al., 2012; Dujardin J.-R. , 2014; Munkhsaikhan, 2016). Therefore, the study of seismic hazard and the estimation of the probability of future destructive earthquakes are of first importance for the country. Since the last large earthquake, still unknown on the Songino fault, the fault geomorphology has been smoothed due to erosion

processes and a low slip rate (most likely less than 1 mm per year), thus the exact location of the fault is hidden in a several meter strip.

In such a context, the Ground Penetrating Radar (GPR) method gives good and useful results, can help to characterize faults by identifying offsets of radar reflections, and buried fluvial channel deposits (Beauprêtre, et al., 2012). The investigation depth depends on the electromagnetic (EM) attenuation of the medium and the frequency of the antenna used. The lower the frequency, the greater the penetration depth, which varies from a few centimeters in conductive materials up to 50 m for low conductivity (less than 1 mS m^{-1}) media (Jol, 2009). The vertical resolution depends on the velocity of EM waves and the frequency used. In general, features such as sedimentary structures, lithological boundaries, fractures and/or faults are clearly visible with GPR (Deparis, et al., 2007; Christie, et al., 2009; McClymont, et al., 2010), even when these features differ only by small changes in the nature, size, shape, orientation and packing of grains (Guillemoteau, et al., 2012).

Table 3-1 List of deadliest 21st century earthquakes

Rank	Fatalities	Magnitude	Location	Event	Date
1	227,898	9.1	Indonesia, Indian Ocean	2004 Indian Ocean earthquake and tsunami	December 26, 2004
2	160,000	7.0	Haiti	2010 Haiti earthquake	January 12, 2010
3	87,587	7.9	China	2008 Sichuan earthquake	May 12, 2008
4	87,351	7.6	Pakistan	2005 Kashmir earthquake	October 8, 2005
5	26,271	6.6	Iran	2003 Bam earthquake	December 26, 2003
6	20,896	9.0	Japan	2011 Tōhoku earthquake and tsunami	March 11, 2011
7	20,085	7.7	India	2001 Gujarat earthquake	January 26, 2001
8	8,964	7.8	Nepal	2015 Nepal earthquake	April 25, 2015
9	5,782	6.4	Indonesia	2006 Yogyakarta earthquake	May 26, 2006
10	4,340	7.5	Indonesia	2018 Sulawesi earthquake and tsunami	September 28, 2018
11	2,968	6.9	China	2010 Yushu earthquake	April 13, 2010
12	2,266	6.8	Algeria	2003 Boumerdès earthquake	May 21, 2003
13	1,313	8.6	Indonesia	2005 Nias-Simeulue earthquake	March 28, 2005
14	1,115	7.6	Indonesia	2009 Sumatra earthquake	September 30, 2009
15	1,000	7.4	Afghanistan	2002 Hindu Kush earthquakes	March 25, 2002

We have conducted many GPR campaigns in 2012, 2013, 2015 and 2017 on active fault areas around Ulaanbaatar city. In our study, we present only some preliminary results of GPR measurements performed along the Songino fault in 2013 and 2017 and discuss the results of a trench dug perpendicular to Songino fault in august 2013. The GPR profile's objective is to identify the near surface geometry of this fault (precise location, dip), describe underneath sedimentary sequence affected by past earthquakes, and the type of displacements and

amplitude. In this survey, we used 250 and 500 MHz shielded antenna and a 50 MHz rough terrain unshielded antenna.

Table 3-2 List of costliest 21st century earthquakes.

Rank	Damage $Billions	Magnitude	Event	Location	Date
1	$360	9.0	2011 Tōhoku earthquake and tsunami	Japan	March 11, 2011
2	$150	7.9	2008 Sichuan earthquake	China	May 12, 2008
3	$40	6.1	2011 Christchurch earthquake	New Zealand	February 22, 2011
4	$28	6.8	2004 Chūetsu earthquake	Japan	October 23, 2004
5	$16	6.3	2009 L'Aquila earthquake	Italy	April 6, 2009
6	$15.8	5.8	2012 Emilia earthquake	Italy	May 20, 2012
7	$15—$30	8.8	2010 Chile earthquake	Chile	February 27, 2010
8	$10	7.8	2015 Nepal earthquake	Nepal	April 25, 2015
9	$7.8—8.5	7.0	2010 Haiti earthquake	Haiti	January 12, 2010
10	$7.5	7.0	2016 Kumamoto earthquake	Japan	April 16, 2016

Tectonic setting around UB area

The Hustai fault (west area surrounded by red line in Figure 3.1) northeastern tip is located at 15 km west from Ulaanbaatar. This main fault of 80 km long may produce an M 7.5 earthquake. It displays continuous microseismicity with five M 4+ and an M 5.4 since 1974. Exploratory trenches located along the central section of the active trace reflect the transtentional nature of the fault with mixed normal and left lateral strike slip faulting geometries (Ferry, et al., 2010; Ferry, et al., 2012; Schlupp, et al., 2012). A detailed morphotectonic view of this fault is provided by combining high-resolution satellite images, digital elevation models, GPR images, magnetic mapping, geomorphology, and trenching investigations (Ferry, et al., 2010; Schlupp, et al., 2012; Dujardin J.-R. , 2014). The Emeelt fault (swarm area in Figure 3.1) located less than 10 km from the westernmost area of UB and its surface trace can be mapped over about 5 km along a N146 direction (Schlupp, et al., 2012; Dujardin J.-R. , 2014; Munkhsaikhan, 2016), and shows a right lateral strike slip with a small reverse vertical component (compression). It is capable to produce an earthquake with magnitude up to 6.7 (Schlupp, et al., 2012; Ferry, et al., 2010; Dujardin J.-R. , 2014; Munkhsaikhan, 2016).

The Songino fault (Blue Square of Figure 3.1) is located between Emeelt and Hustai faults; it has a length of ~20 km and is situated 20 km West of UB. In the area of the Songino fault, we have conducted many GPR campaigns in 2012, 2013, 2015 and 2017. In this study, we present results of 2D GPR measurements obtained in 2013 and 2017.

The Songino fault was first discovered in 2012 as part of a seismic hazard project around Ulaanbaatar capital city. The Songino fault is a fault between two large active faults the Hustai and the Emeelt. It also aims to confirm the results of research on the two active faults and to contribute to the unraveling of the geodynamic structure around Ulaanbaatar. Therefore, the main purpose of this work is to conduct a detailed study on the Songino fault and to establish its geodynamic correlation using the experience and knowledge gained in the study of active faults. This chapter presents all the results of a detailed Ground Penetrating Radar survey of the Songino fault.

2 Study area

2.1 Songino Fault zone

The Songino Fault (Blue Square of Figure 3.1), discovered in 2012, is located approximately 40 km west of Ulaanbaatar capital city of the Mongolia, between two large seismically active faults, that is Hustai and Emeelt. Figure 3.1shows the area around the Songino Fault, a study area, surrounded by a blue square. The main part of the Songino fault is branched at the eastern end of the Hustai active fault. The first azimuth of the Songino fault stretch starts at 166º or about 14º from south, then changes direction and the next azimuth continues at about 148º or southeast (SE), then also changes direction again and continues to 129º or southeast. The azimuth is reversed, and the azimuth is curved at 108º from south to east, and finally splits into 3-5 sections with a straight eastward direction.

The geomorphology of the Songino fault is clearly visible on the satellite image, and a high height scarp structure is observed at the beginning, at the branching point of the Hustai active fault. However, as the height of the Songino fault scarp gradually decreases, the fault scarp disappears in some places in the middle zone, and then the Songino faults scarp gradually increases again low rate and disappears.

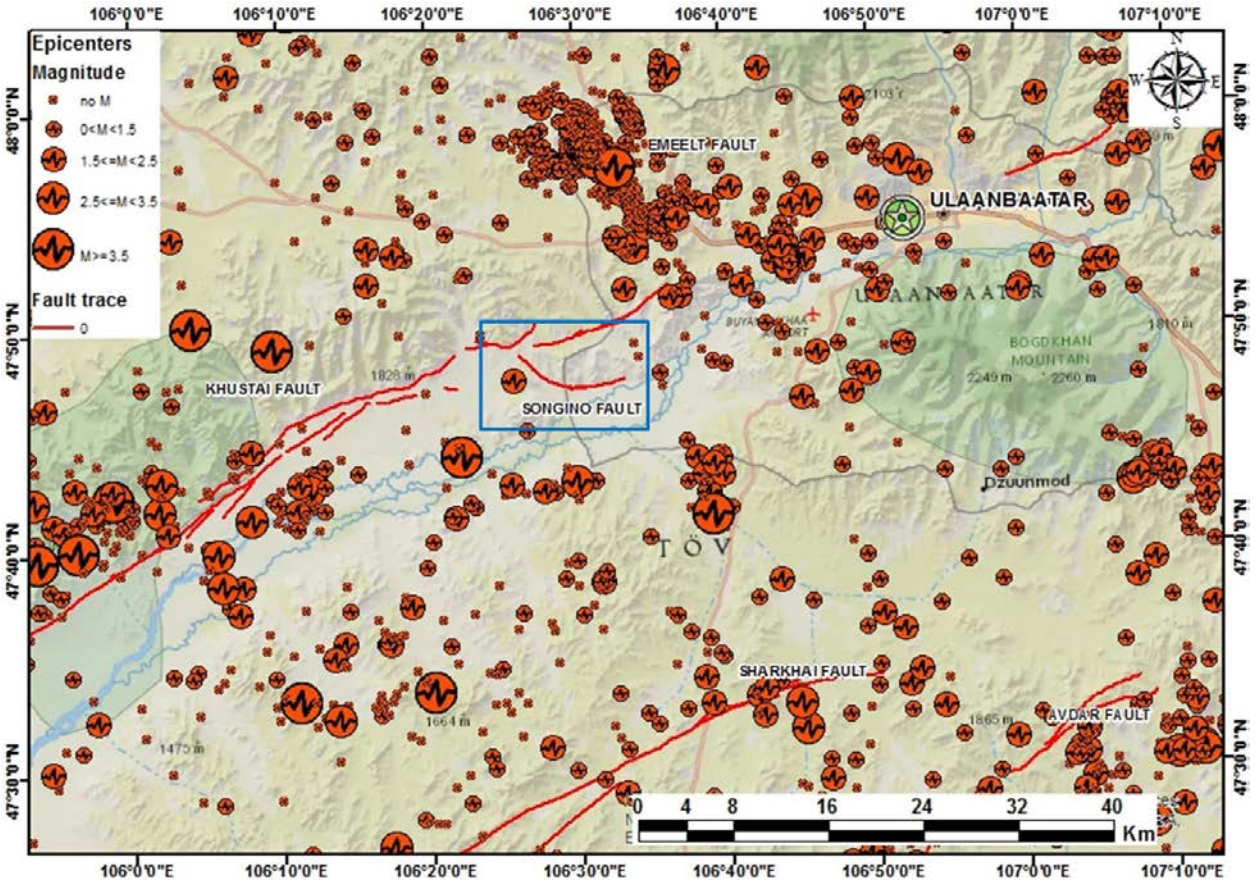

Figure 3.1 Seismicity maps (red dots) around Ulaanbaatar city from 1994 to 2014, after (Adiya 2016 and NDC data, IAG, MAS). The green asterisk indicates the UB urban area. Red lines indicate the trace of main active faults, after (Ferry et al., 2010, 2012; Al Ashkar 2015). The Hustai northeastern tip is located at 15 km west from UB and is of 80 km long; the Emeelt fault (swarm area) of 40 km long is situated less than 10 km from the westernmost area of UB; the Songino fault located between Emeelt and Hustai faults is about 20 km long and situated 20 km West of UB.

3 Methodology

Ground Penetrating Radar (GPR) is a high-resolution, near surface, geophysical method based on the propagation, reflection and scattering of high frequency (from 10 MHz to 2 GHz) electromagnetic (EM) waves in the Earth (Daniels, Gunton, & Scott, 1988; Jol, 2009; Van Dam, 2012). EM waves sent into the ground are reflected at interfaces of electric and dielectric contrast and the reflected signals are recorded. Those discontinuities can result from changes in the water content, the chemical composition, or the texture of the deposits. In sedimentary deposits, variations in grain size and water saturation are the main factors triggering reflections. GPR has proven its efficiency in many fields of geosciences but seems generally most efficient

in sedimentary deposits, marked lithological boundaries, fractures and/or faults (Gross, et al., 2004; Deparis, et al., 2007; McClymont, et al., 2010), even for subtle changes in the nature, size, shape, orientation and packing of grains (Guillemoteau, et al., 2012). In the sedimentological context, interpretation generally uses GPR-facies analysis, analogous to their use in seismic studies (Jol & Bristow, 2003; Neal, 2004). Ground Penetrating Radar (GPR) is a geophysical imaging method that detects reflections and diffractions of electromagnetic waves occurring at the dielectric, electrical and magnetic contrasts of the sub-surface within an electrically resistive medium. This is a relatively recent geophysical method which has found a wide field of applications over the last twenty years (Annan, 2002) for a background, and (Jol, 2009; Beres & Haeni, 2005) for a review. description of the main applications). By describing in the following the principle of propagation of electromagnetic waves, we will introduce the notions and the vocabulary inherent in this method, as well as the signal and noise sources that we will try to amplify and reduce, respectively, during the treatment.

4 GPR Data acquisition and processing

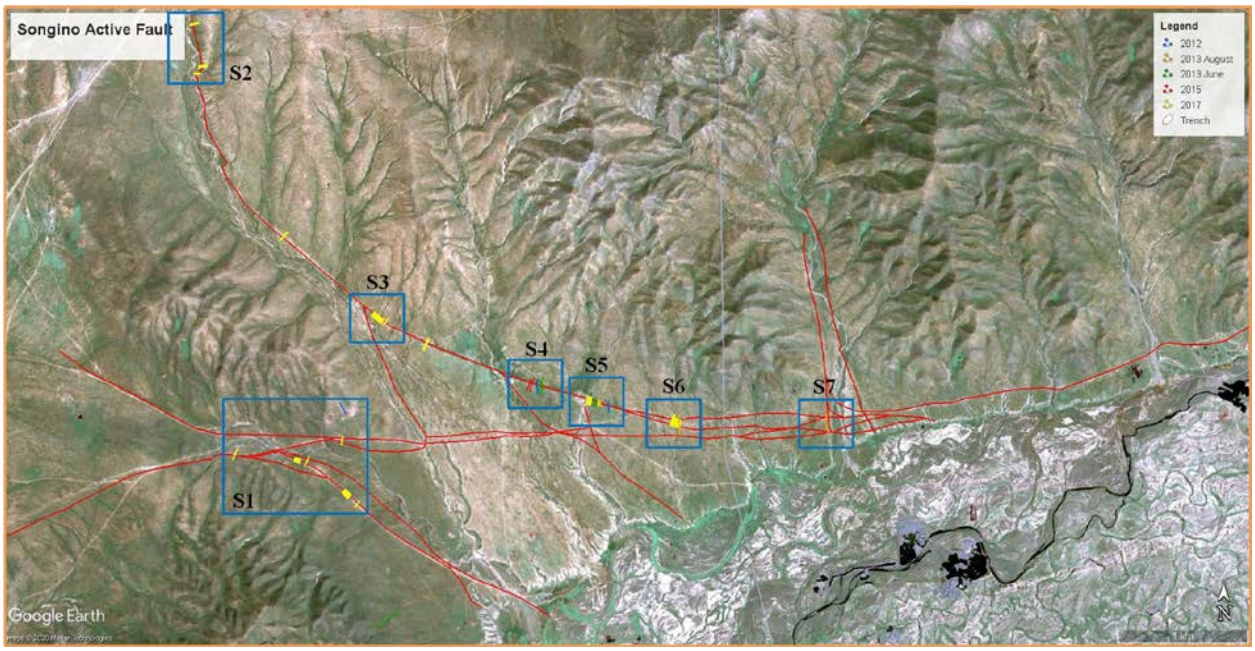

Figure 3.2 Location map of Songino fault and Ground Penetrating Radar survey areas. The red line shows the traces of the fault on the surface rupture of the Songino fault, the blue squares show the Ground Penetrating Radar measurements, the surveyed areas, and the Ground Penetrating Radarprofiles between 2012 and 2017 difference by color each year.

After the geomorphologic recognition of the Songino fault in 2012, we decided to use 2D GPR measurements to investigate subsurface deposits potentially affected by the fault on a wider area. The results should allow us to precise location of future trenches.

The first three Ground Penetrating Radar profiles measurements by MALA ProEx GPR system (MALA Swedish trademark) on the Songino fault were collected with MALA 250 MHz shielded and MALA RTA 50 MHz unshielded antennas in September 2012. These measurements were processed and analyzed between September and October 2012 while working at the University of Strasbourg, France. After analyzing the results of these initial measurements, GPR measurements were planned for the 2013 summer fieldwork. As planned, in June 2013, a joint team of scientists from the University of Strasbourg, France, and researchers from Institute of Astronomy and Geophysics continued the 2010 Emeelt active Fault GPR Survey. However, geological, and geomorphological studies of the Songino fault and the first part of the Ground Penetrating Radar survey were also carried out. At this time, we obtained 5 profiles perpendicular to the fault plane in only two zones, S4 and S5 Figure 3.2. Also, 3 crossed profiles were conducted parallel to the fault plane. We processed the day's GPR measurements in the evening and planned the following day's measurements, and because the results of the profiles conducted on S5 were very interesting, we repeated some of the previous profiles and enlarged them. We were very interested in the results of Ground Penetrating Radar measurements conducted in zone S5 in 2013 (see Figure 3.2), so we decided to study the Songino fault in more detail. After selecting the topic of my doctoral dissertation as Songino faults, I planned to conduct a more extensive GPR study of this fault, and in 2017, I conducted GPR measurements in the previous two zones and five other zones. First, satellite imagery was used to identify areas where horizontal and vertical displacements could be identified, and GPR measurement points were identified accordingly. In the GPR survey design, 3-4 parallel profiles at a distance interval of 1-2 m (Table 3-4) perpendicular to the fault trace were obtained to determine the horizontal displacement of the paleo river channel we collected parallel to the fault trace 6-8 profiles at a distance interval of 1-2 meters from each other (Table 3-4). In this study, we used a MALA ProEx GPR system equipped with a MALA 250 MHz and 500 MHz shielded antenna and the MALA RTA 50 MHz unshielded antenna. We overlapped the measurement locations of the 250 MHz and 50 MHz antennas to obtain different levels of fault depth information. However, the 500 MHz antenna measurement was used only for shallow depth surveys. A stack of the 16 has been used to improve the signal-to-noise ratio. A differential GPS system was used in conjunction with the GPR data line to measure location.

Details of the Ground Penetrating Radar survey measurements performed on the Songino fault can be found in Table 3-3, Table 3-4.

Table 3-3 Table of the GPR survey zone location parameters

	Zone name	Latitude	Longitude
1.	S1	47.788014°	106.455834°
2.	S2	47.816440°	106.445671°
3.	S3	47.797549°	106.464720°
4.	S4	47.793126°	106.480566°
5.	S5	47.792083°	106.485843°
6.	S6	47.790389°	106.494768°
7.	S7	47.790684°	106.509810°

Table 3-4 Songino fault GPR survey acquisition parameters.

	Site name	**Profile name**	**Antenna**	**Distance interval**	**Profile distance**	**Time window**	**Zone**
1.	2012 Sep-29	Pr01	250 MHz	0.06 m	97 m	150 ns	S1
2.			RTA50 MHz	0.2 m	96 m	504 ns	
3.		Pr02	250 MHz	0.06 m	115 m	150 ns	S5
4.			RTA50 MHz	0.2 m	111 m	504 ns	
5.		Pr03	250 MHz	0.06 m	90 m	150 ns	S4
6.			RTA50 MHz	0.2 m	91 m	504 ns	
7.	2013 June-14	Pr01	250 MHz	0.02 m	64 m	180 ns	S5
8.		Pr02	250 MHz	0.05 m	40 m	168 ns	
9.		Pr03	250 MHz	0.05 m	97 m	168 ns	S4
10.		Pr04	250 MHz	0.05 m	114 m	168 ns	
11.		Pr05	250 MHz	0.05 m	221 m	168 ns	
12.		Cr01	250 MHz	0.05 m	95 m	168 ns	S5
13.		Cr02	250 MHz	0.05 m	84 m	168 ns	
14.		Cr03	250 MHz	0.05 m	43 m	168 ns	S4
15.	2013 June-16	Pr01- Pr03	250 MHz	0.05 m	50-52 m	156 ns	S5
16.		Pr01- Pr03	500 MHz	0.02 m	50-52 m	109 ns	
17.		Cr01- Cr02	250 MHz	0.05 m	34 m	156 ns	
18.		Cr01- Cr02	500 MHz	0.02 m	34 m	109 ns	
19.	2013 June-17	Pr01	250 MHz	0.05 m	51 m	129 ns	S5
20.		Cr01	250 MHz	0.05 m	35 m	129 ns	
21.		Cr01	500 MHz	0.02 m	35 m	109 ns	
22.	2013 Aug-25	Pr01-Pr02	RTA50 MHz	0.3 m	151-171 m	502 ns	S6, S7
23.	2013 Aug-26	In-trench-01	250 MHz	0.02 m	40 m	206 ns	S5
24.			500 MHz	0.02 m	40 m	119 ns	
25.	2017 Aug-08	Pr01-Pr07	500 MHz	0.04 m	50 m	97 ns	S1
26.	2017 Aug-15	Pr01-Pr04	250 MHz	0.05 m	70-73 m	160 ns	S2
27.			RTA50 MHz	0.05 m	70-73 m	458 ns	
28.		Pr05-Pr07	250 MHz	0.05 m	55-53 m	160 ns	
29.			RTA50 MHz	0.05 m	55-53 m	458 ns	

30.		PPr8	250 MHz	0.04 m	77-81 m	160 ns	
31.		Pr01-Pr03	RTA50 MHz	0.05 m	78-83 m	458 ns	
32.		PPr7	250 MHz	0.05 m	66 m	160 ns	S3
33.		Pr01-Pr03	RTA50 MHz	0.05 m	66 m	458 ns	

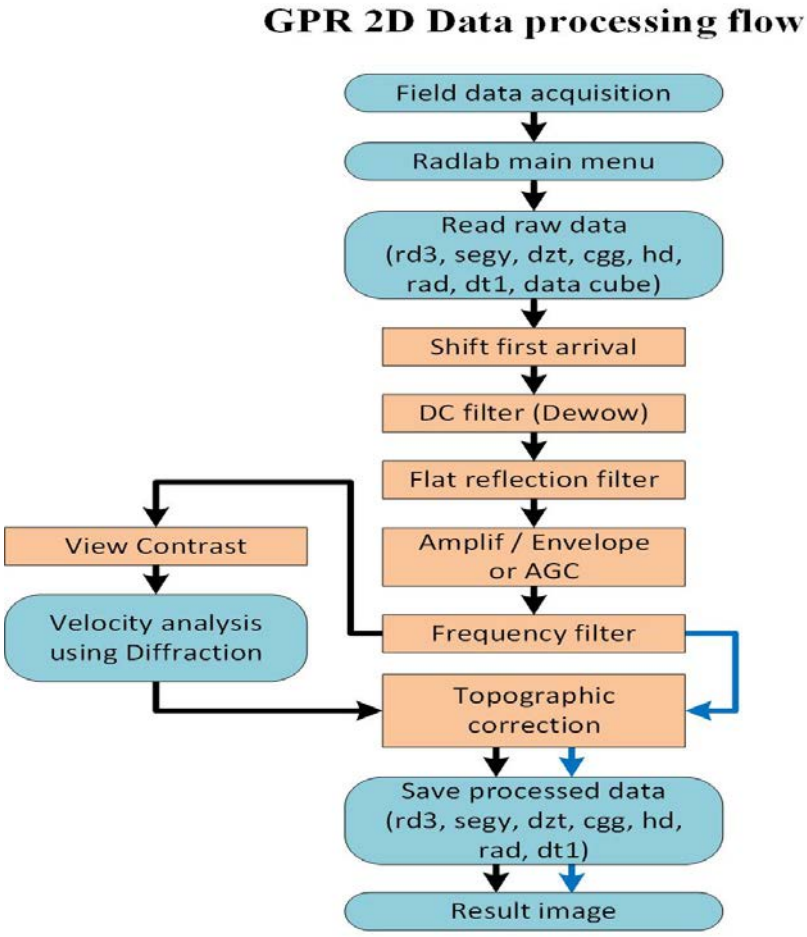

Figure 3.3 2D GPR data processing flow chart. Blue one is data input and output steps, orange one is GPR data processing steps. Black arrows following with velocity analysis, blue arrows following without velocity analysis.

The processing of all GPR profiles has been performed with an in-house software written in MATLAB (RadLab) (Girard, 2002; Dujardin J.-R. , 2014). The high quality of the data allows a very light workflow in four standard steps, which are described in detail elsewhere (Fisher, et al., 1992; Yilmaz & Doherty, 2001; Annan, 2001; Annan, 2002; Jol & Bristow, 2003; Neal, 2004; Annan, 2009). We used a common flow procedure including a constant shift to adjust the time zero, a dc filter to remove the low frequencies, a flat reflections filter to remove continuous flat reflections noise, a band-pass filter, a time varying gain function and finally the

topographic corrections (Annan, 2009; Cassidy N. , 2009). Band-pass filters are chosen to be 50–450 and 100–800 MHz for the 250 and 500 MHz antenna, respectively.

5 Analysis and visualization of the GPR images results

The results of the first Ground Penetrating Radar measurements conducted in 2012 on the Songino fault are also interesting. These measurements are collected by overlapping the 250MHz shielded and RTA 50MHz unshielded antennas on each profiles so that different levels of depth data can be seen. Figure 3.4 shows the location map of the first profile P1. This picture shows the traces of fracture along the road, and it is interesting to know whether the fracture was caused by fault or caused by the road. Before analyzing underground fracture structure on a Ground Penetrating Radar result image, we check and mark the satellite image analyze for signs of fracturethat intersect with the GPR profile. This is marked on the GPR profile of Figure 3.4b with the red symbol (F), and then the points are analyzed to see how they correspond to the traces of fault at depth. Based on the mapping and interpretation of the results of the first GPR profile on the study area, two parallel fractured structures are observed at 60 and more than 70 meters on the profiles (Figure 3.5).

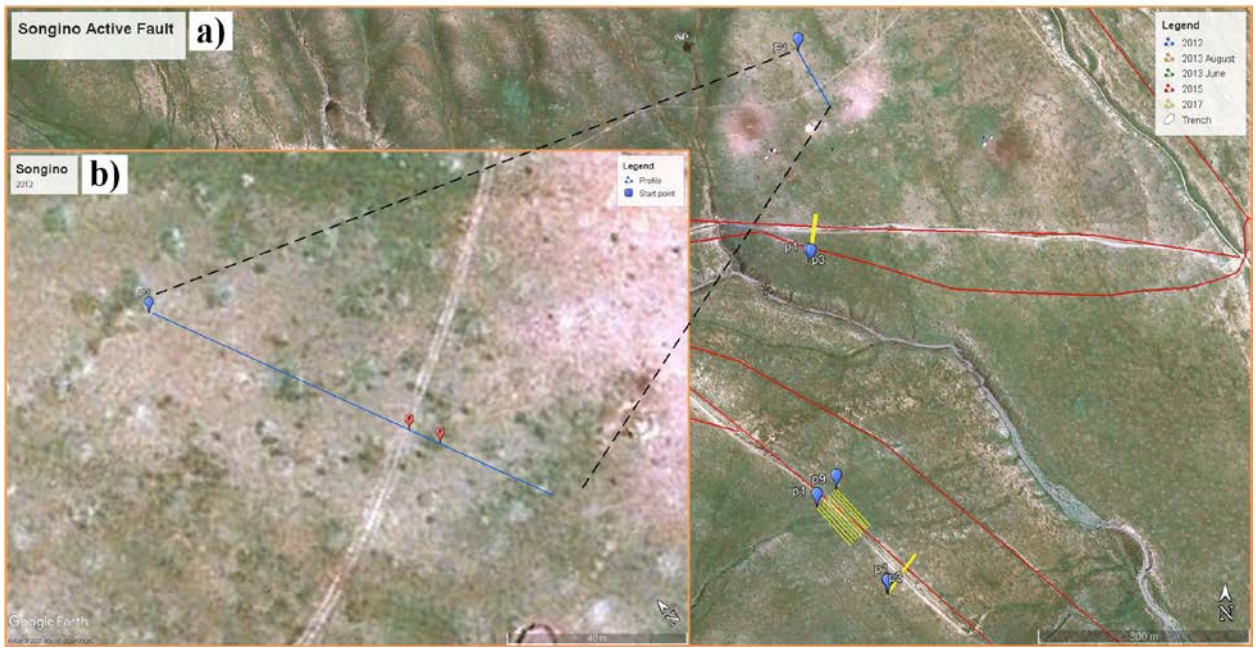

Figure 3.4 Location map of the first profile P1 acquired in 2012. a) Northeast corner of zone S1 (see Figure 3.2), b.) a magnified image of the profile area, blue line shows the profile acquired in 2012, blue symbols indicates the initial position of the measurement, red symbols (F) indicates the point of intersection with the traces of damaged structure on the surface rupture and the profile.

They show a south-west dipping structure on both profiles of 250 and 50 MHz antennas (Figure 3.5). It can also be seen that the direction of these fractures coincides with the markers red symbol (F) on the ground surface.

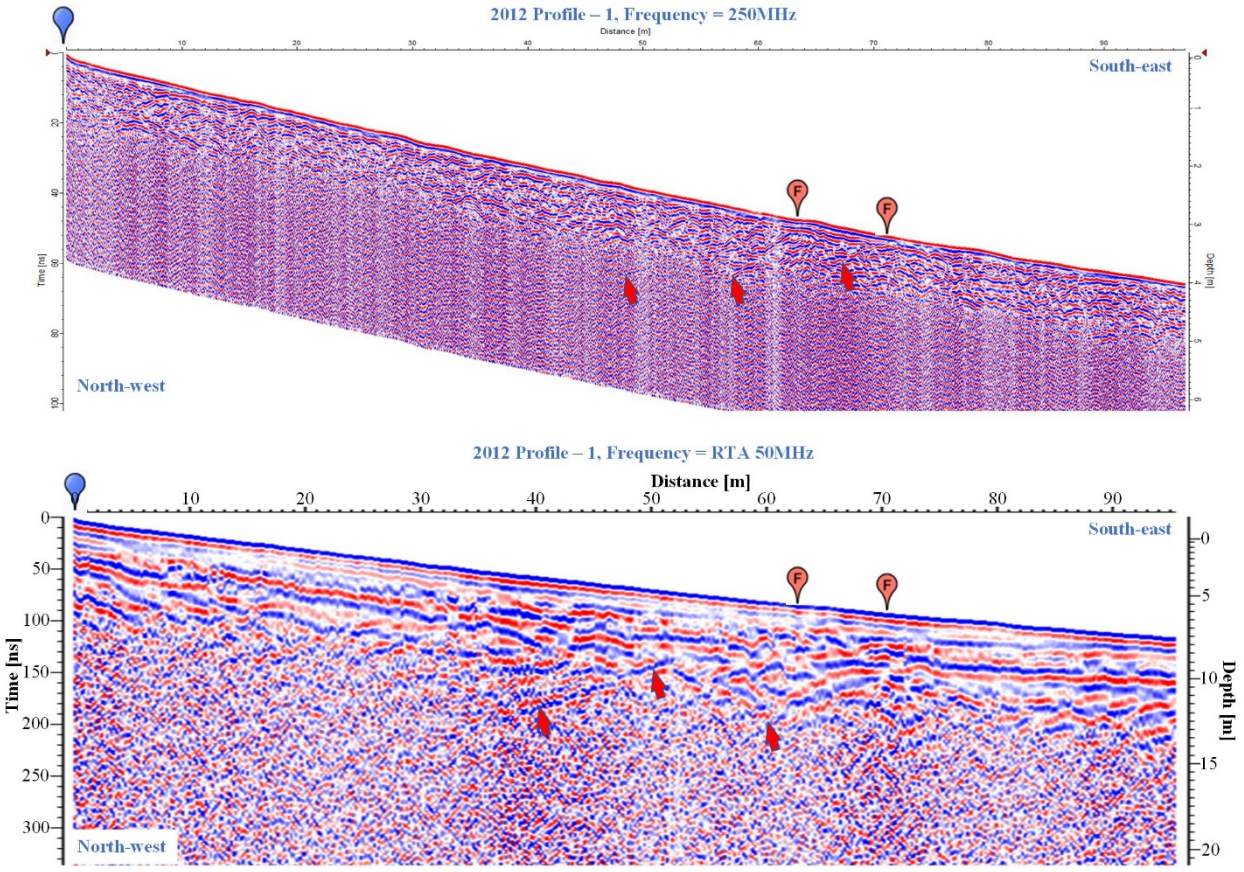

Figure 3.5 The result of GPR images of the first profile (acquired the September 2012) obtained with 250 MHz and RTA 50MHz antenna in the Songino fault study area S1 (see Figure 3.4). a.) result of GPR image obtained with 250 MHz antenna, b.) result of GPR image obtained with RTA 50 MHz antenna; blue symbol indicates the initial position of the measurement, red symbol (F) indicates the point of intersection with the fault traces on the surface rupture and the profile, red arrows are pointing underground high reflected GPR anomaly.

The location of the second profile of the 2012 Ground Penetrating Radar survey is shown in blue in Figure 3.6. Figure 3.7 shows the interpretation of the results of GPR images. The GPR image of RTA 50 MHz unshielded antenna shows a reflection at the bottom of the fault scarp. There is also a shorter but stronger reflection of the GPR signal in front of the scarp area. The GPR image of 250 MHz shielded antenna shows a layered structure of the sediment accumulation in the northern depression of the fault scarp. There is also a zone of fracture on the fault scarp, and in front of the fault scarp, there are three areas of fracture that are strongly

reflected. The location of these fractures corresponds to the markers red symbol (F) on the ground surface (Figure 3.7).

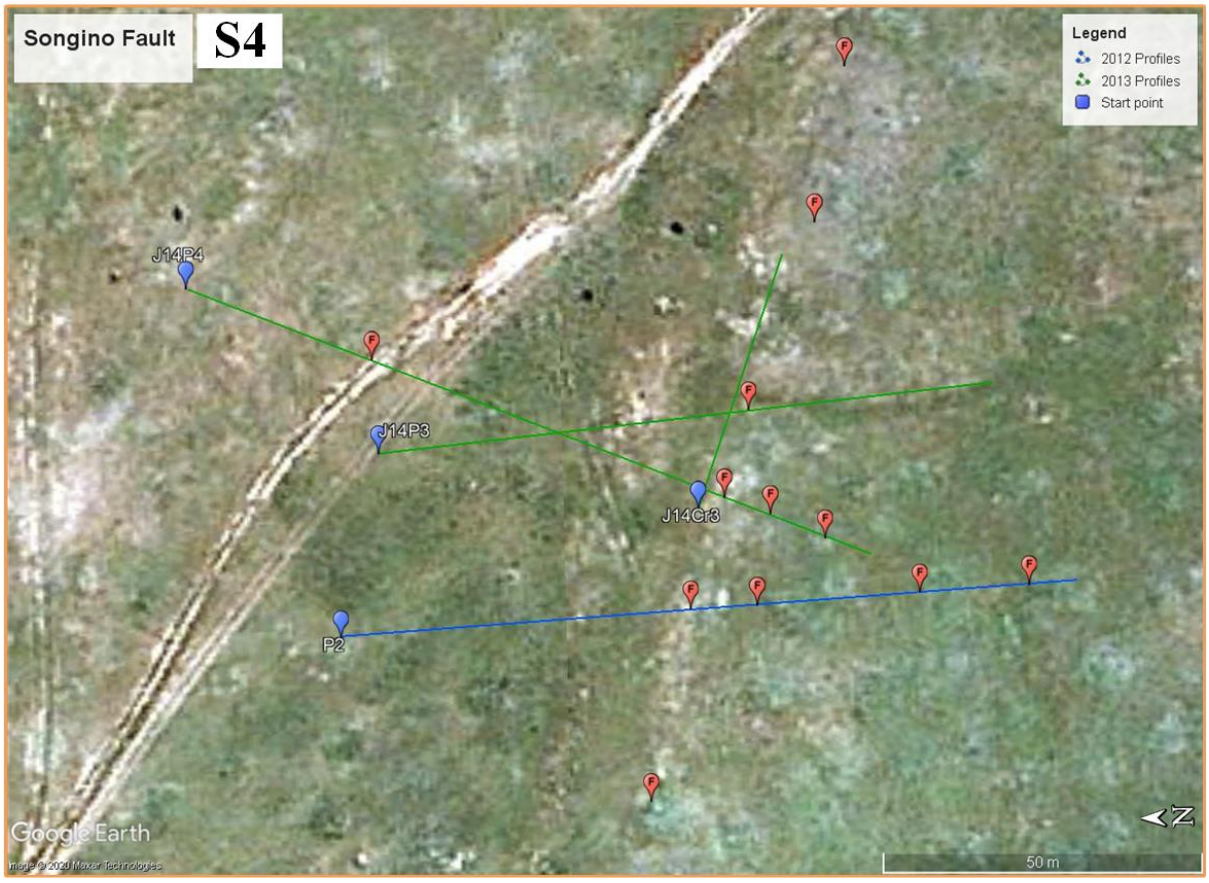

Figure 3.6 Location map of the GPR profile P2 acquired in 2012, S4 zone as shown in Figure 3.2. Blue line shows the second profile of 2012, blue symbol indicates the initial position of the measurement, red symbols (F) indicate the intersection of the fault traces on the surface rupture with the profile.

The location of the third profile acquired in 2012 (zone S5) is shown in Figure 3.8.

The results of this GPR profile, presented in Figure 3.8, show a better resolution with 250 MHz shielded antenna. In addition, below and after the fault scarp, sediment layers and traces of fractures are clearly visible (shown by red arrows in Figure 3.9). There is also a zone of clear reflections under the ground located between 20 and 40 meters horizontally, which is likely to be an ancient surface that has been submerged by fault (Figure 3.9). However, the resulting image of the RTA 50MHz unshielded antenna shows a similar structure of fractures and sediments as the result image of the 250 MHz shielded antenna. These structures, as determined by GPR profiles, are consistent with the fractured structures identified at the surface (Figure 3.9).

After the first GPR campaign conducted in zone S5 (Figure 3.2) in 2012, we performed a second one in 2013 on the same zone S5. The fault scarp are clearly visible in this area, and the vertical and horizontal displacements of the fault plane are likely to be kept clean. To the east of the deep paleo river channel, where horizontal displacements can be measured directly, we performed additional GPR measurements (Figure 3.10). On June 14, 2013, we acquired the profile-2 and on June 16, 2013, the same profile -2 (7 m longer than the one of June 14), the profiles are almost identical. In addition, two long and three short crossed profiles were conducted in parallel with the fault plane in S5 zone, and the results are very important in understanding the displacements and fault movements.

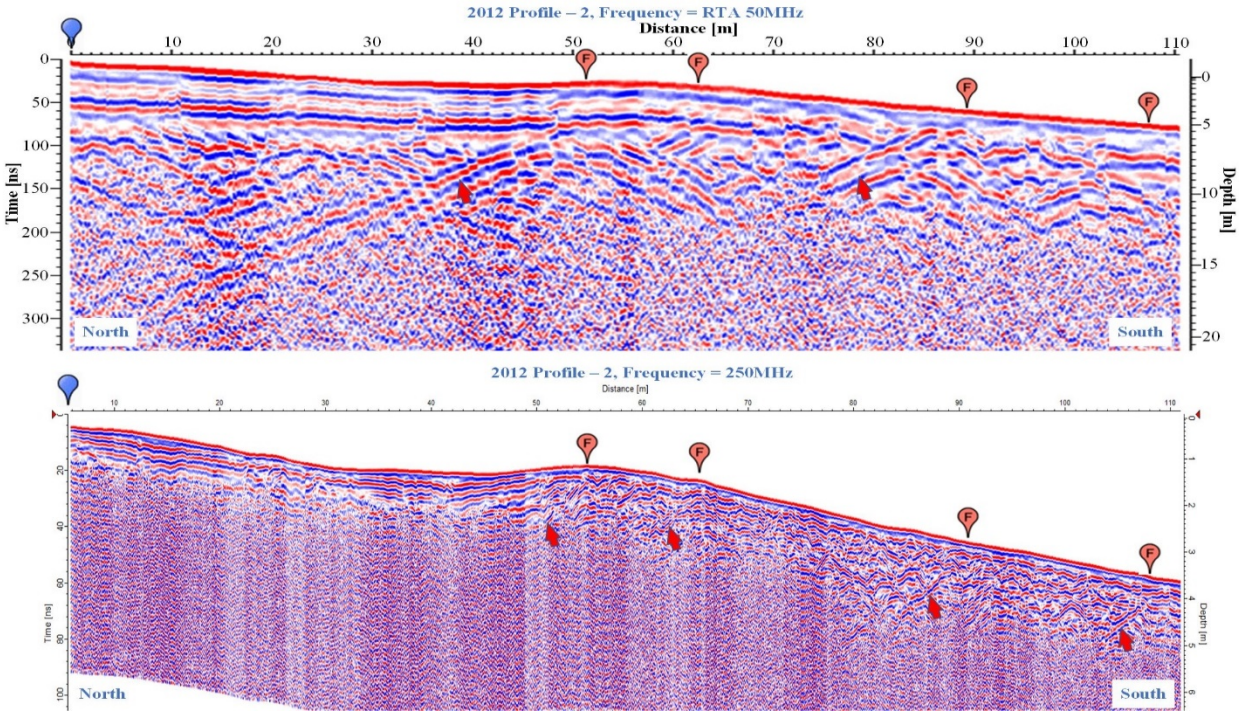

Figure 3.7 The result of GPR images of the second profile (acquired the September 2012) obtained with 250 MHz and RTA 50 MHz antenna in the Songino fault study area S4 (see Figure 3.6). a.) GPR profile obtained with RTA 50 MHz antenna, b.) GPR profile obtained with 250MHz antenna. Blue symbol indicates the initial position of the measurement, red symbols (F)indicate the point of intersection with the traces of damaged structure on the surface rupture and the profile, red arrows are pointing underground high reflected GPR anomalies.

Figure 3.11a shows the profile-2 of 14 June 2013, and the structure of the hidden layer below the ground surface shows a very strong reflection anomaly. From this S5 zone, it is possible to see the structure of the soil erosion below the fault scarp, but the location of the fault plane and the dipping angle of the fault plane are not visible. From the 250 MHz shielded

antenna result image, it is possible to analyze the direction of the fault movement, and the structural analysis shown in this section of the result image shows that the top side and mountain side of the fault sits down and forms a scarp, indicating normal structure of the scarp. In Figure 3.11b, however, the direction of the fault dipping, the direction and shape of the movement are similar to those of the profile image in the result of the profile along the fault (Figure 3.11).

The Figure 3.12 shows the results of the profile-2 obtained with 500 MHz shielded antenna on 16 June 2013. The result of the GPR image shows a strong GPR reflection between two layers as observed in the profile of 250 MHz shielded antenna (Figure 3.11a). It is indicated by the yellow arrow in Figure 3.12 provides more detailed information's concerning the nature of subsurface erosion and alluvial sedimentation.

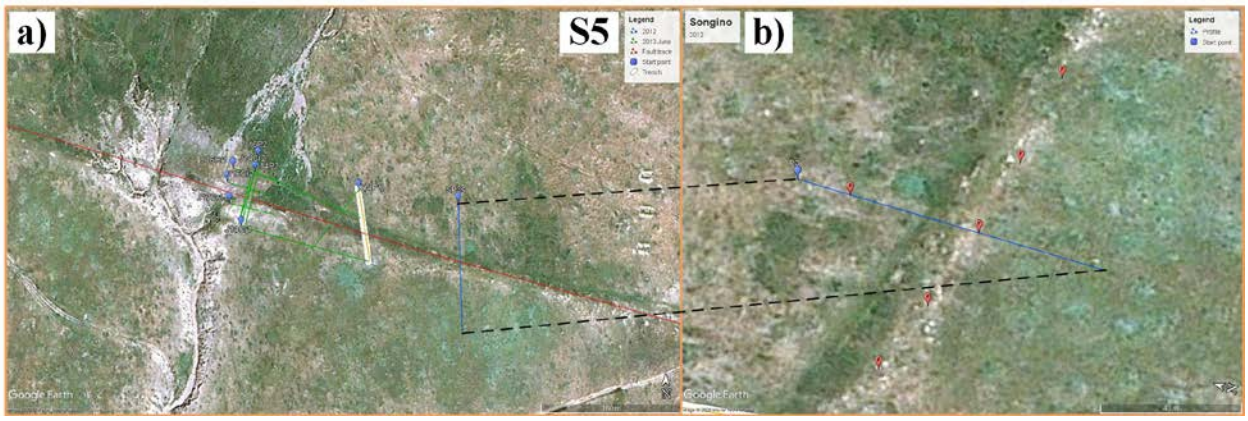

Figure 3.8 Location map of the third GPR profile (blue line) P3 acquired in 2012. Blue symbols indicate the initial position of the measurement. a) The GPR survey zone S5 as shown in Figure 3.2b) a magnified image of the profile area, red symbols (F) indicate the intersection of the fault traces on the surface rupture with the profile.

In August 2013, we completed a trench survey on the fault, and we performed GPR measurements inside the trench. Due to the fact that the excavation team of this study did not dig in the planned place, the results of the trench survey were not as we expected to be. However, the results of GPR images conducted in the trench floor provided some additional information about the movement of the fault zone sediments. The GPR images obtained with 250 MHz shielded antenna inside the trench (Figure 3.14a, location in Figure 3.13) show many parallel layers structure having the same dipping angle. However, the two layers around the fault scarp give a stronger reflection (indicated by the yellow arrow in Figure 3.14). Figure 3.14b shows the result of GPR image obtained with 500 MHz shielded antenna which is similar to the GPR image of previous Figure 3.14a. The vertical resolution in Figure 3.14b is higher

than the resolution Figure 3.14a. From the result of these two GPR images the direction of dipping angle of the strongly reflected layers coincides with the direction of dipping angle shown in Figure 3.11.

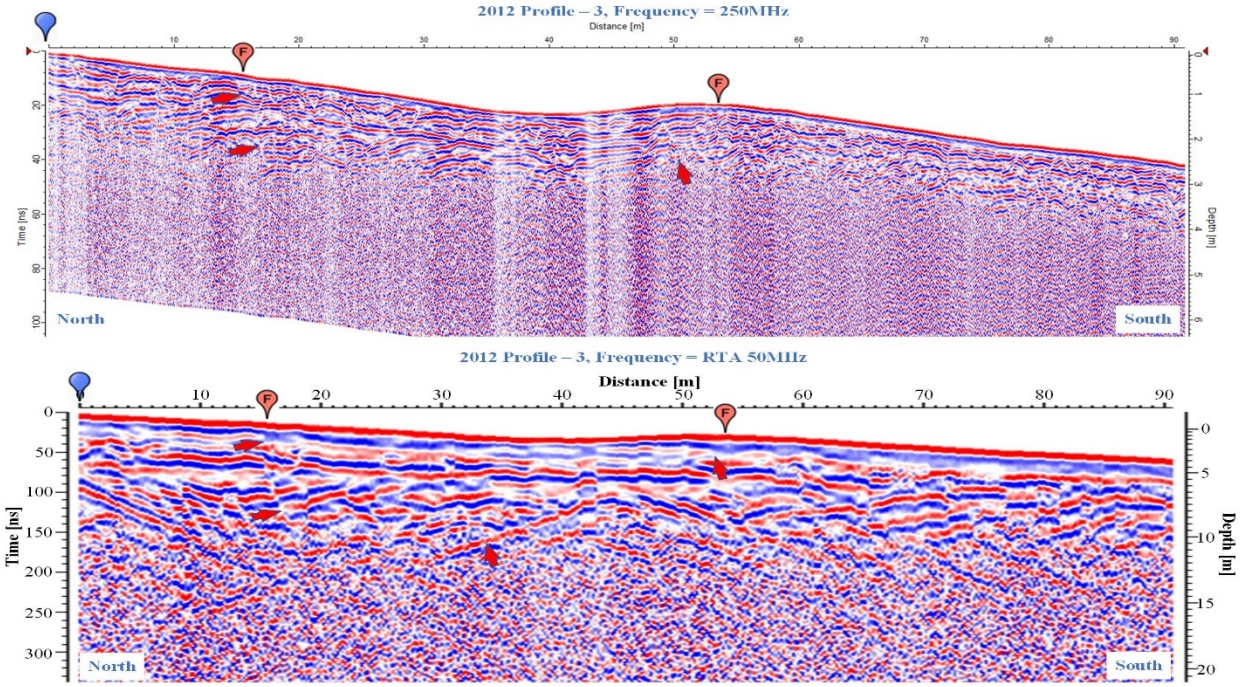

Figure 3.9 The result of GPR images of the third profile (acquired the September 2012) obtained with 250 MHz and RTA 50 MHz antenna in the Songino fault study area S5 (see location in Figure 3.8. a) Result of GPR image obtained with 250MHz antenna. b) Result of GPR image obtained with RTA 50 MHz antenna; the blue symbols indicate the initial position of the measurement, red symbols (F) indicate the intersection of the fault traces on the surface with the profile, red arrows are pointing underground high reflected GPR anomalies.

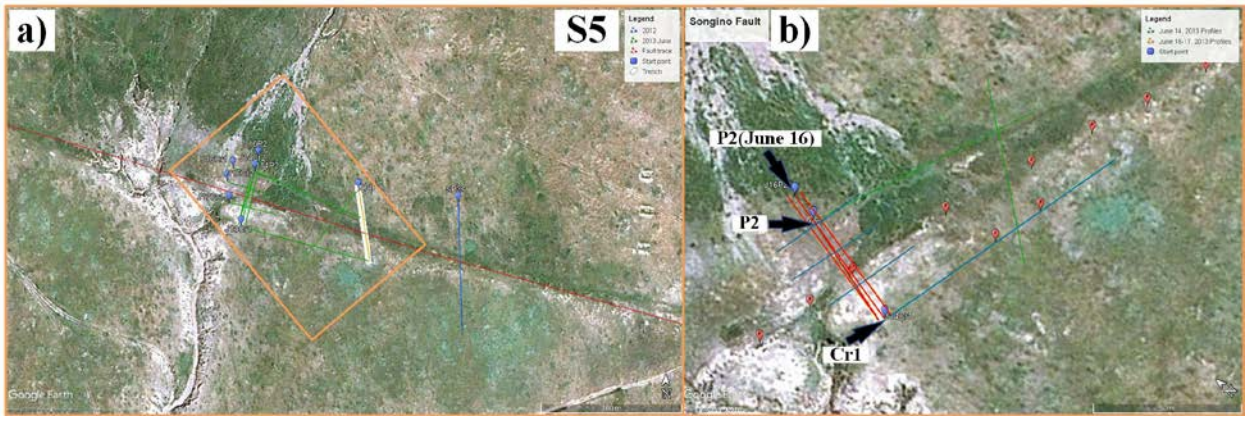

Figure 3.10 Location Map of the GPR profiles acquired in June 2013. a) The GPR survey zone S5 as shown in Figure 3.2. b) A magnified image of the profiles area (orange square); the red

lines show the GPR profiles of June 2012, blue line is crossed profile Cr1, the blue symbol indicates the initial position of the measurement, red symbols (F) indicate the intersection of the fault traces on the surface with the profile.

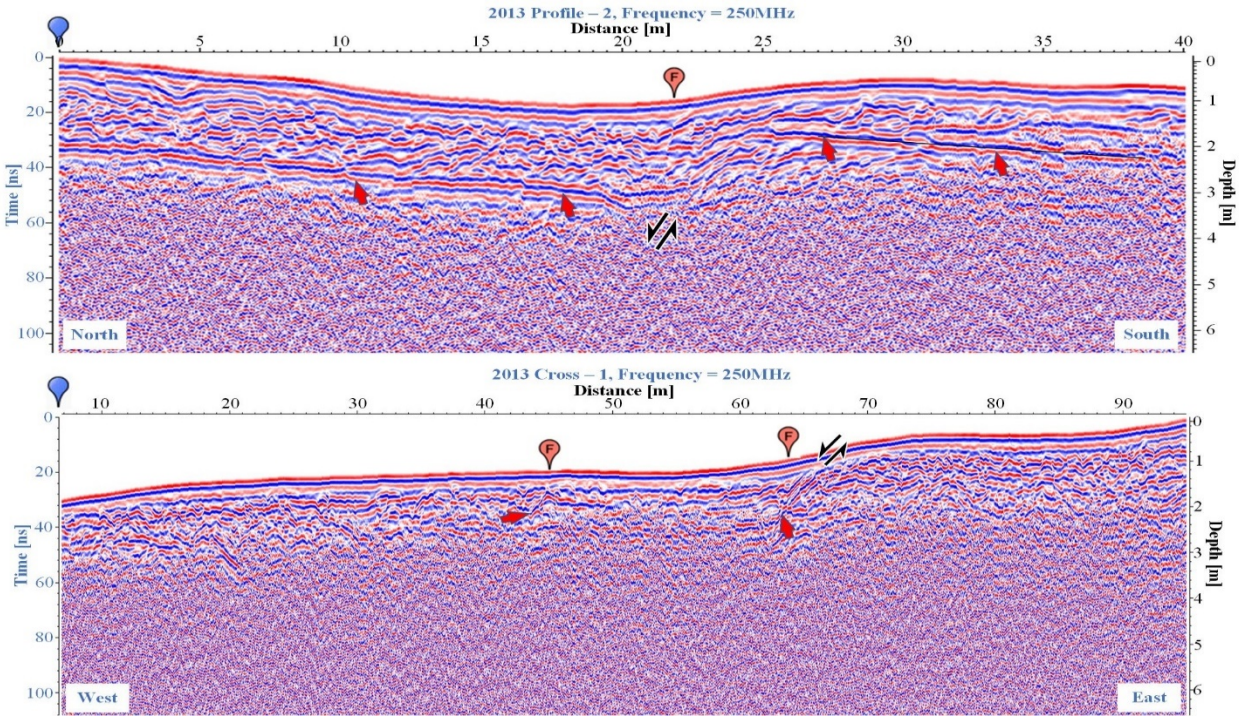

Figure 3.11 The result of GPR images of the profile P2 and crossed profile Cr1 (acquired the 14 June 2013) obtained with 250 MHz antenna in the Songino fault main study area S5 (see Figure 3.10). a) Result of GPR image of profile P2, it shows a clear normal structure and regional extensional effect with competent layer structure under scarp (red arrows). b) Result of GPR image of the crossed profile Cr1, red arrow is pointing underground high reflected GPR anomalies. The blue symbols indicate the initial position of the measurements, red symbols (F) indicate the intersection of the fault traces on the surface with the profile. The black arrows indicate movement direction of the two sides.

The map location of the profiles P3, P4 and crossed profile Cr3 collected in zone S4 on 14 June 2013 is shown in Figure 3.15. In Figure 3.16 we present the results of GPR profile P4 and the crossed profile Cr3. As a result, the GPR image of the profile P4, conducted with 250 MHz shielded antenna, shows good reflections on the south of the fault scarp. Unfortunately, no strong reflection is observed on the north side the fault scarp. In the first part of the profile, about 31 meters horizontally, there is an anomaly under the road. The GPR image of the crossed profile Cr3 (Figure 3.16b) shows an alluvial sedimentary layer structure in the depression, and at the end of the section there is a layer with a strong reflection adjacent to the left.

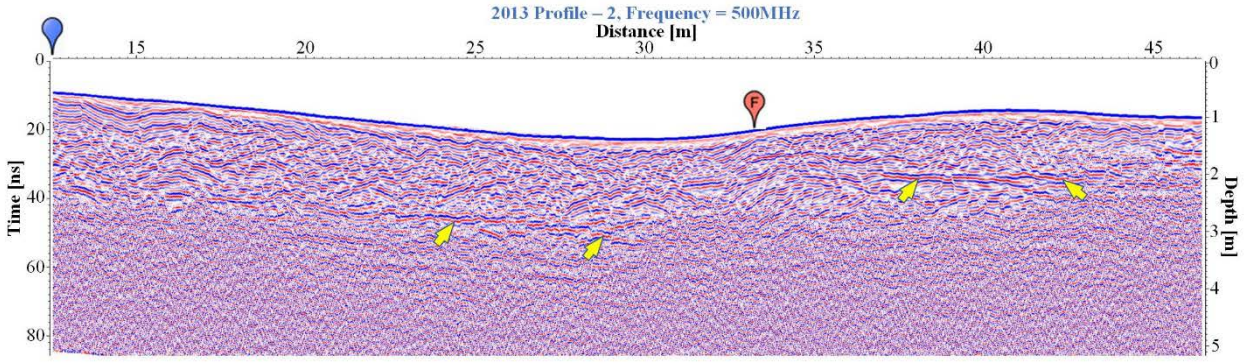

Figure 3.12 The result of GPR image of the profile P2 (acquired the 16 June 2013) obtained with 500MHz antenna in the Songino fault main study area S5 (see location in Figure 3.10). The GPR image shows a normal structure and regional extensional effect with competent layer structure under scarp (yellow arrows). The blue symbol indicates the initial position of the measurement, symbols (F) indicate the intersection of the fault traces on the surface with the profile.

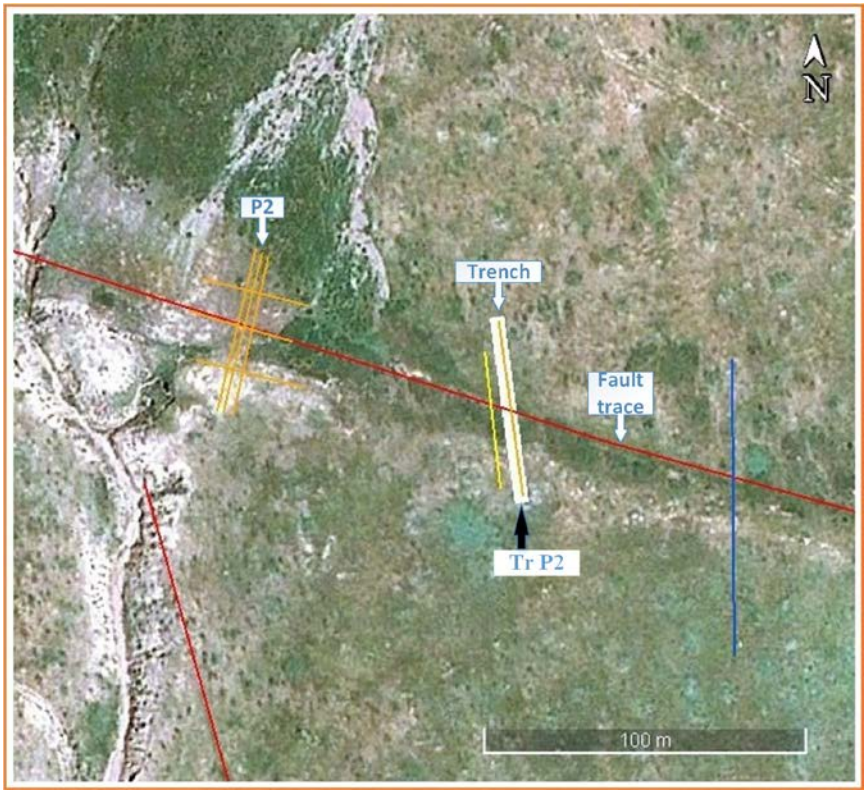

Figure 3.13 Location Map of the GPR profiles acquired in August 2013. The GPR survey zone S5 as shown in Figure 3.2. The red lines show the fault traces, white square shows trenching area.

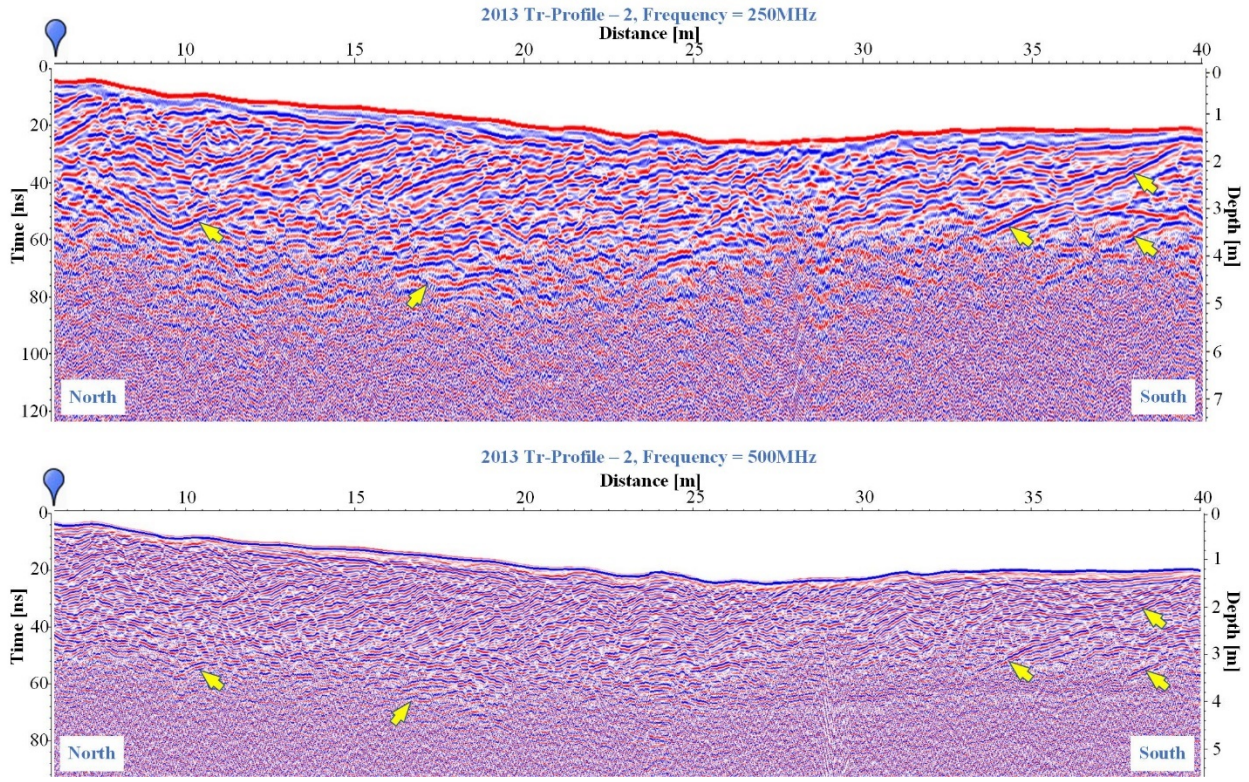

Figure 3.14 The result of GPR images of the profile P2 inside the trench (acquired the August 2013) obtained with 500MHz and 250 MHz antenna in the Songino fault study area S5 (see location in Figure 3.13). a) Result of GPR image of profile P2 obtained with 250 MHz. b) Result of GPR image of profile P2 obtained with 500 MHz antenna. The blue symbols indicate the initial position of the measurements, yellow arrows are pointing underground high reflected GPR anomalies.

Figure 3.17 shows the location map of the two profiles performed during the trench survey in August 2013. The satellite images of these zones S6 and S7 show very distinct traces of the surface rupture (indicated by red symbols in Figure 3.17). However, in the resulting images of these two profiles with a RTA 50 MHz unshielded antenna, the traces of these fractures are not strongly reflected, but are clearly recognizable (see Figure 3.18). Additionally, in the first 20 meters of the profile P1 we remark a very strong reflection. It is likely that there are traces of any sub-fractured structure at the beginning of the profile (Figure 3.18a).

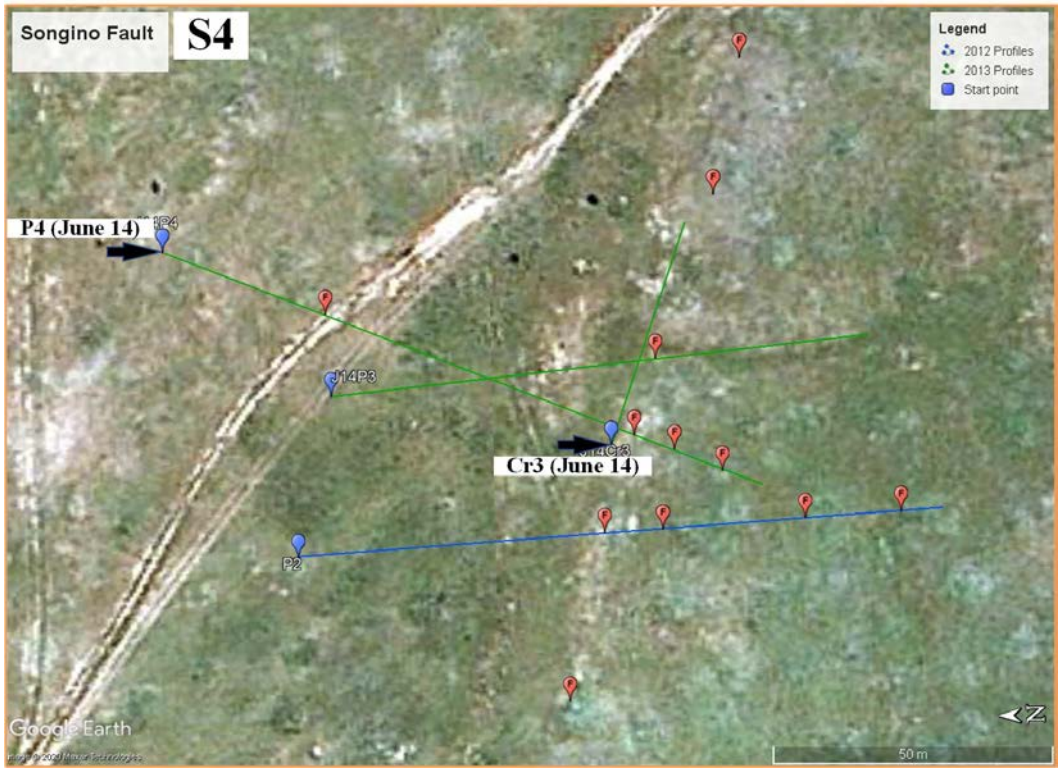

Figure 3.15 Location Map of the GPR profiles acquired on 14 June 2013. The GPR survey zone S4 as shown in Figure 3.2. The green lines show the GPR profiles of 14 June 2014, the blue symbols indicate the initial position of the measurements, red symbols (F) indicate the intersection of the fault traces on the surface with the profile.

In August 2017, additional GPR surveys of the Songino fault revealed measurements of horizontal displacement in some paleo river channels. Figure 3.19a shows the location map of the first paleo river channel inside the zone S1. This paleo river channel is crossed by 7 GPR profiles, their location is shown in Figure 3.19b. The fractures in this area do not show any scarps and are very well visible on satellite imagery (see Figure 3.19). In Figure 3.20 we show some results of GPR images obtained with a 500 MHz shielded antenna. The GPR images of profiles P1, P3 and P7 were used to identify and mark the center locations of hidden paleo river channels under the surface (marked by red symbol C in Figure 3.20). It is then plotted on a profiles location map to measure the actual displacement of the paleo river channel. From this measurement, the horizontal displacement of the paleo river channel was estimated to be approximately 11 meters (Figure 3.19).

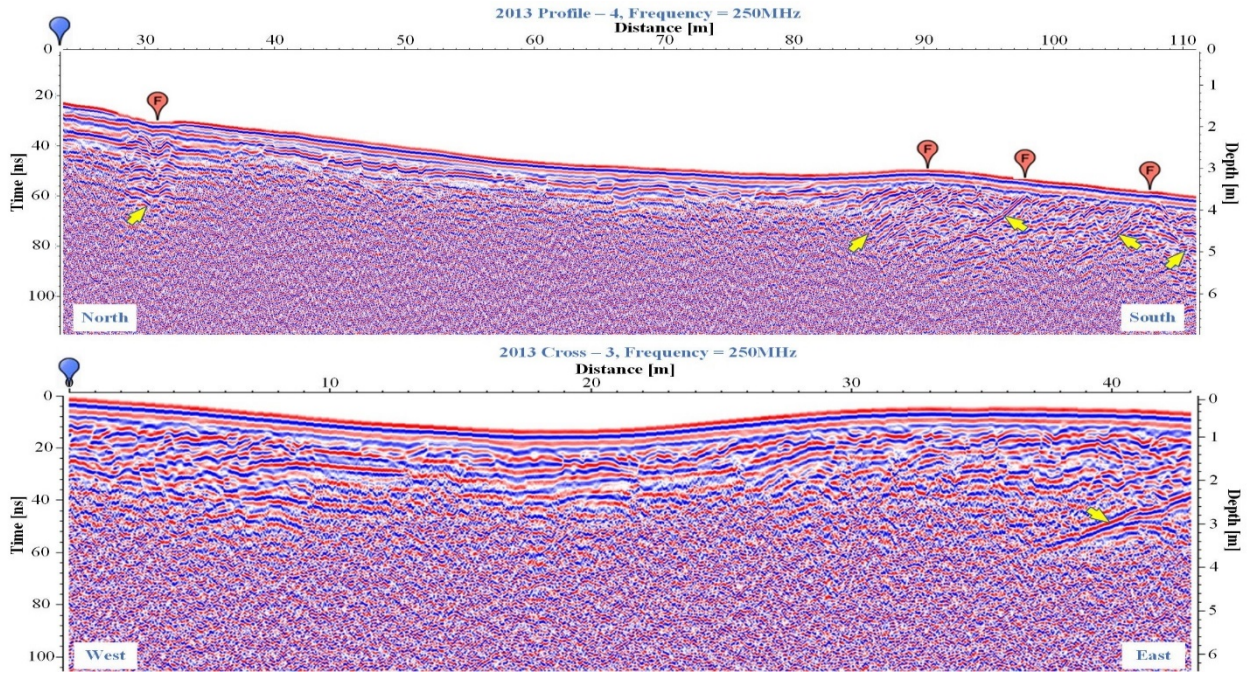

Figure 3.16 The result of GPR images of the profile P4 and crossed profile Cr3 (acquired in June 2013) obtained with 250 MHz antenna in the Songino fault study area S4 (see location in Figure 3.15). a) Result of GPR image of the profile P4. b) Result of GPR image of the crossed profile Cr3. The blue symbol indicates the initial position of the measurement, red symbols (F) indicate the intersection of the fault traces on the surface with the profile. The yellow arrows are pointing underground high reflected GPR anomalies.

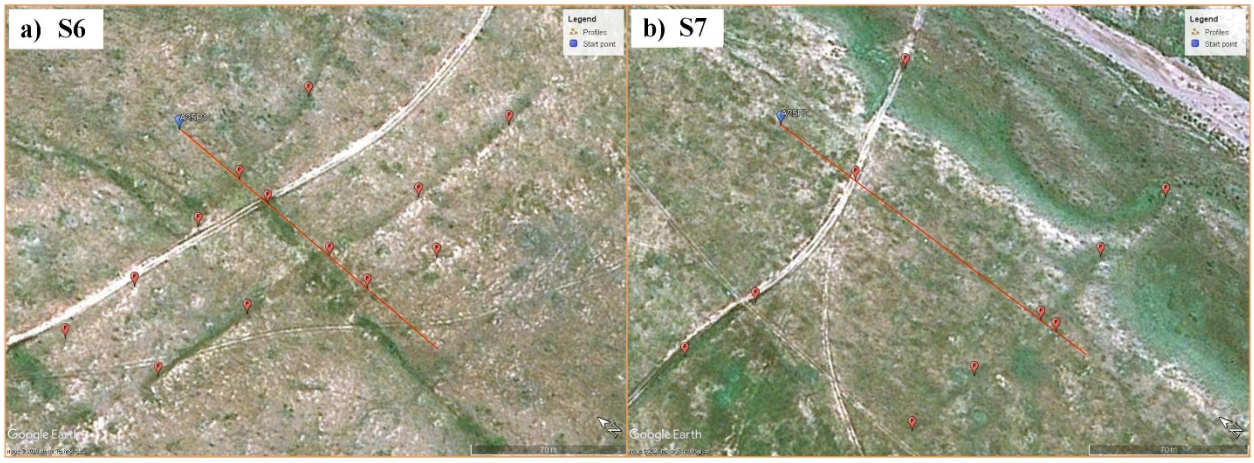

Figure 3.17 Location Map of the GPR profiles acquired in August 2013. a) GPR profile P1 of the survey area S6 shown in Figure 3.2. b) GPR profile P2 of the survey area S7 shown in Figure 3.2. The red lines show the GPR profiles, the blue symbol indicates the initial position of the measurement, red symbols (F) indicate the intersection of the fault traces on the surface rupture-with the profiles.

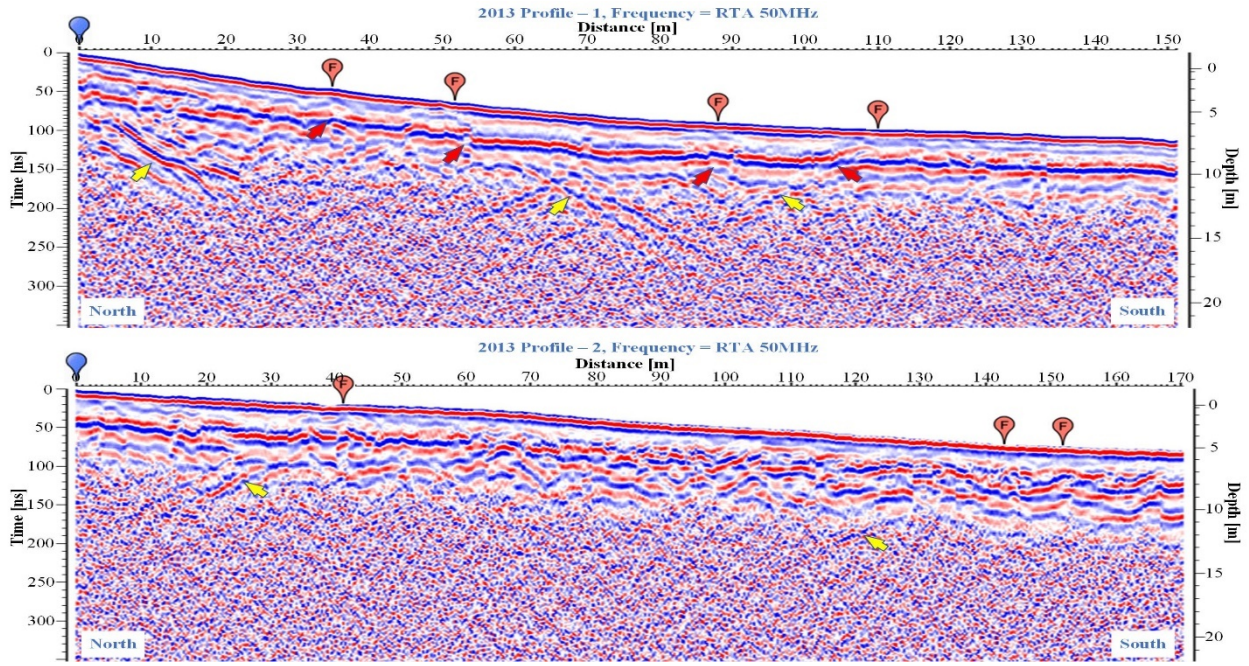

Figure 3.18 The results of GPR images of the profiles P1 and P2 (acquired in August 2013) obtained with RTA 50 MHz antenna in the Songino fault study areas S6 and S7 (see Figure 3.17). a.) GPR image of the profile P1, S6 zone (Figure 3.17a). b) GPR image of the profile P2, S7 zone (Figure 3.17b). The blue symbols indicate the initial position of the measurements, red symbols (F) indicate the intersection of the fault traces on the surface with the profiles. The yellow arrows are pointing underground high reflected GPR anomalies.

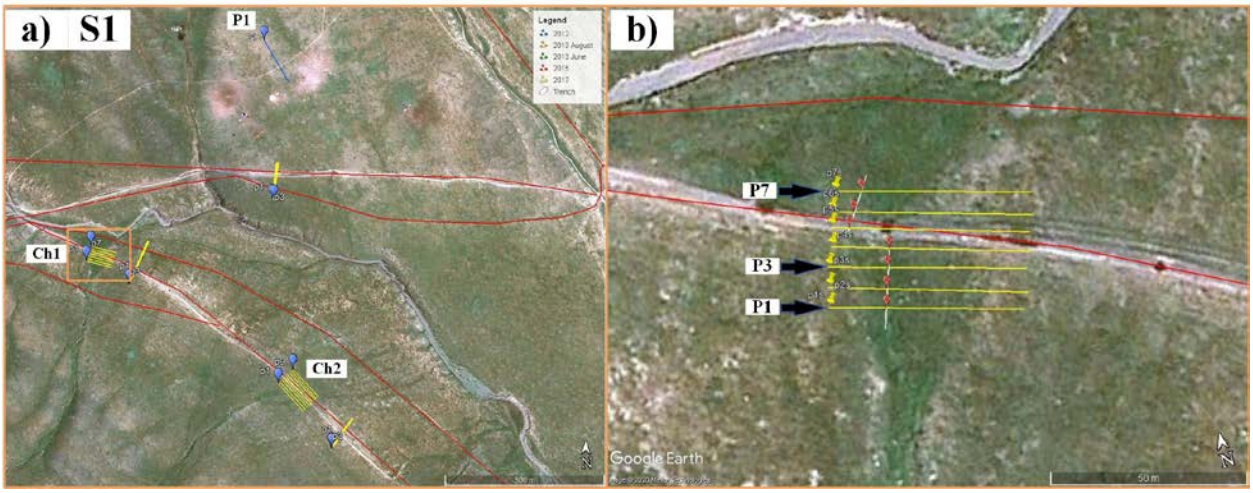

Figure 3.19 Location Map of the GPR profiles acquired in August 2017, S1 zone. a) The GPR survey zone S1as shown in Figure 3.2. b) A magnified map of the profile area (orange square), yellow lines indicate the GPR profiles crossing the paleo river channel. The red lines show the fault traces, the yellow symbols indicate the initial position of the measurements, red symbols (F) indicate the intersection of the fault traces on the surface rupture with the profile.

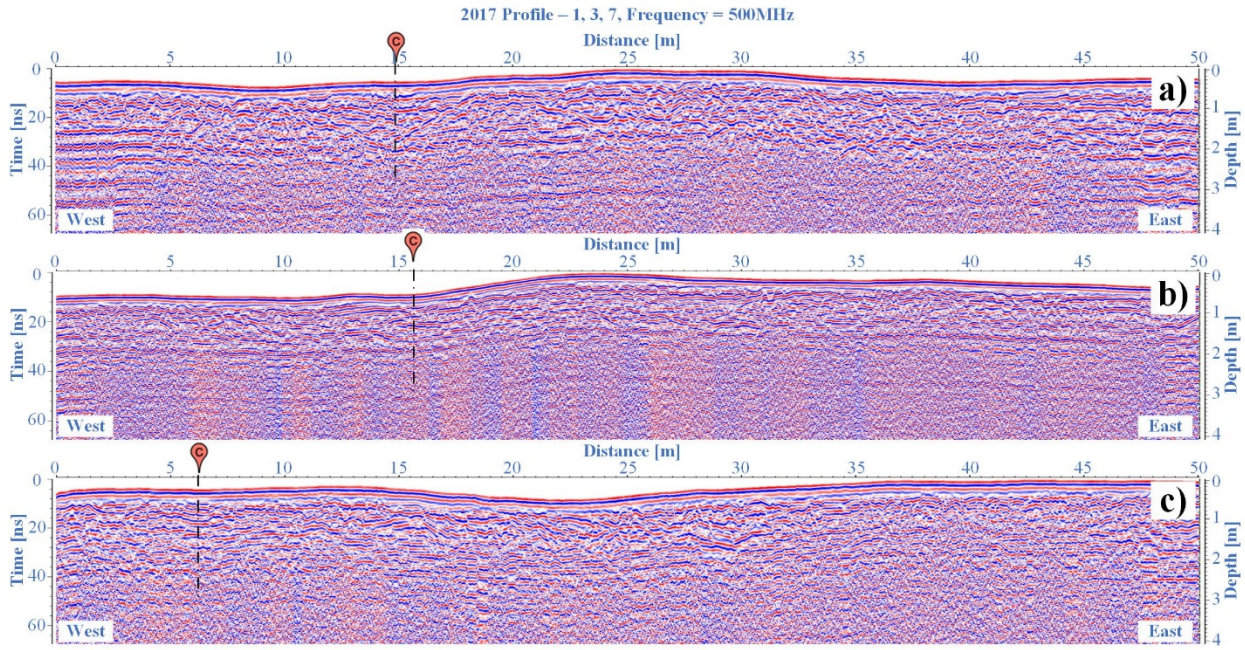

Figure 3.20 The results of GPR images of the profiles P1, P3 and P7 (acquired in August 2017) obtained with 500 MHz antenna in the Songino fault study area S1 (see Figure 3.19) of the paleo river channel. a) GPR image of the profile P1. b) GPR image of the profile P3, c) GPR image of the profile P7. The red symbols (C) indicate the center points of the paleo river channel.

The main area of GPR survey conducted in 2017 is zone S6. This is a zone of high scarp structure of the Songino fault caused by compression (see Figure 3.21). The zone is also divided into two sub-zones: PPr8 and 3D6. The highest scarp of the fault is in the PPr8 zone, the northern edge of the Songino fault. The Ground Penetrating Radar measurements collected here were not completely on the top of the scarp, and were intended to be collected in the vicinity of the fault Figure 3.21. In zone 3D6, however, the top of the scarp is reduced, so we could measure above the top. According to the results of measurements conducted in the PPr8 zone by the RTA 50 MHz unshielded antenna, compression effects are observed. These features are the interruption of the layers and the overlapping structure (Figure 3.22). Their movement also indicates the geodynamic environment in which these sediments accumulate.

For the first four profiles of the zone 3D6, the structure of the sediment under the influence of compression is more pronounced on the GPR images obtained with 250 MHz shielded antenna. This scarp shows fractures to the base and top, indicating traces of compression, as it can be clearly seen in Figure 3.23. The scarp height in this zone is approximately 8.4 meters, while the highest scarp in the PPr8 zone is approximately 21 meters

high. There are three GPR profiles in zone 3D6, and the compression-affected structure is very well illustrated in the GPR images obtained with 250 MHz shielded antenna. The profile shown in Figure 3.24a is obtained with 250 MHz shielded antenna, its image shows micro-folds formed under the ground, indicated by a blue arrow in Figure 3.24b. Additionally, the folds and movement characteristics of the soil sediments are clearly observed (marked by black arrows and white lines in Figure 3.24b). The scarp height in this area was approximately 2.1 meters. The angle created by the folded surface height was 5.7º. The location of this profile (P1) is in the transition zone where the azimuth of the Songino fault is changing.

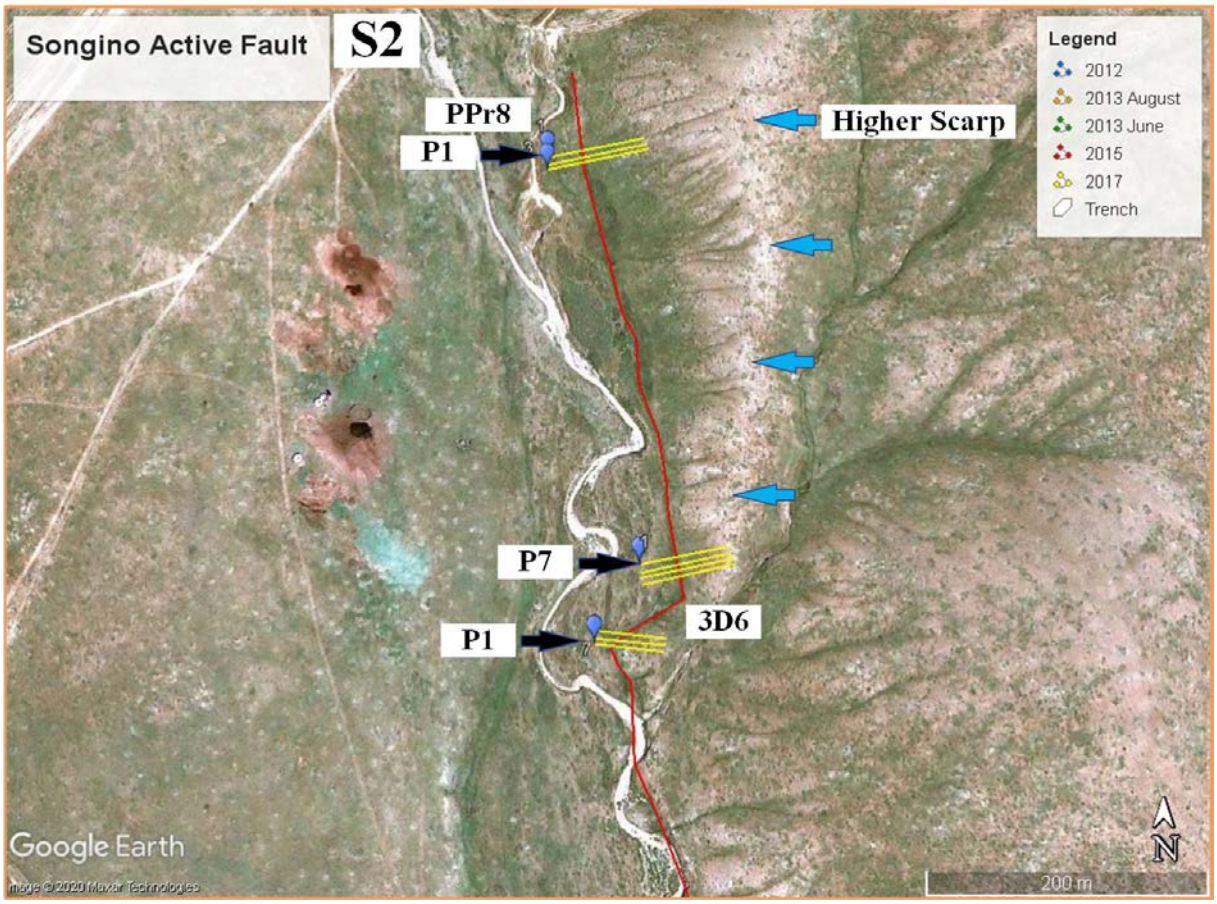

Figure 3.21 Location Map of the GPR profiles acquired in August 2017. The GPR survey of Songino fault thrust structured study area zone S2 as shown in Figure 3.2. The yellow lines indicate GPR profiles perpendicular to the fault traces. The red line shows the fault traces, the blue symbols indicate the initial position of the measurement, blue arrows are pointing to the Songino fault thrust structured fault scarp.

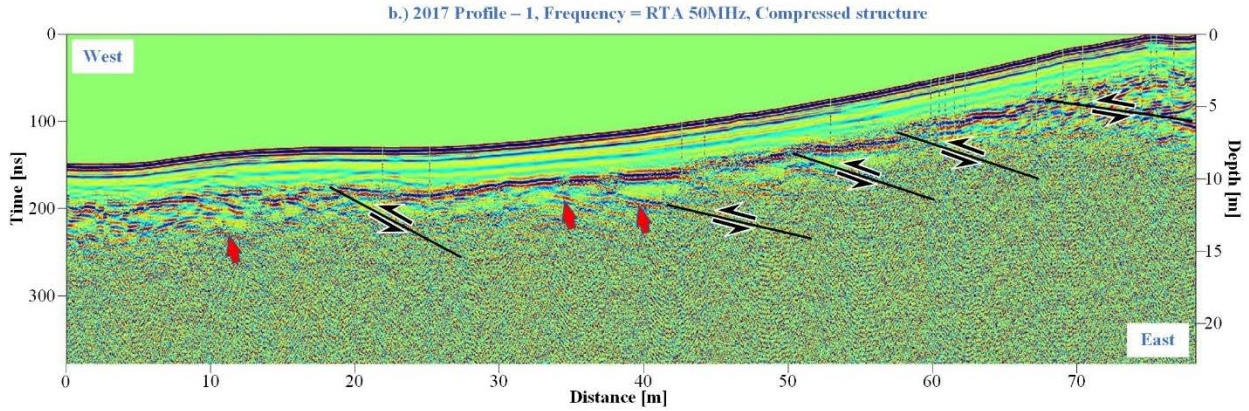

Figure 3.22 The result of GPR image of the profile P1 of PPr8 zone (acquired in August 2017) obtained with RTA 50 MHz antenna in the Songino fault study area S2 (see Figure 3.21). The red arrows indicate underground high reflected GPR anomalies, the black arrows show the movement direction.

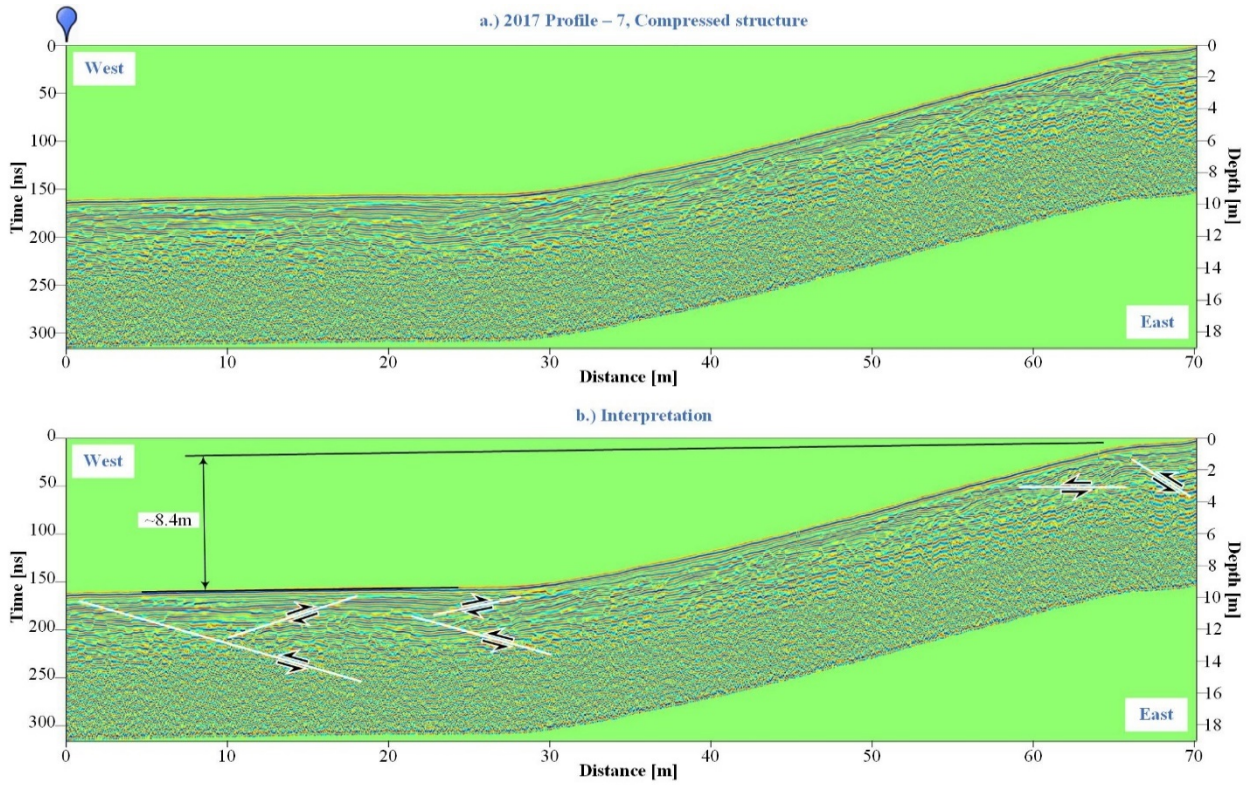

Figure 3.23 The result of GPR image of the profile P1of 3D6 zone (acquired the August 2017) obtained with 250MHz antenna in the Songino fault study area S2 (see location in Figure 3.21). a) GPR image of the profile P7, the blue symbol indicates the initial position of the measurement. b) Interpretation of GPR image of the profile P7, the white lines indicate fracture zones, the black arrows show the movement direction, the height of the scarp is approximately 8.4 meters in this area.

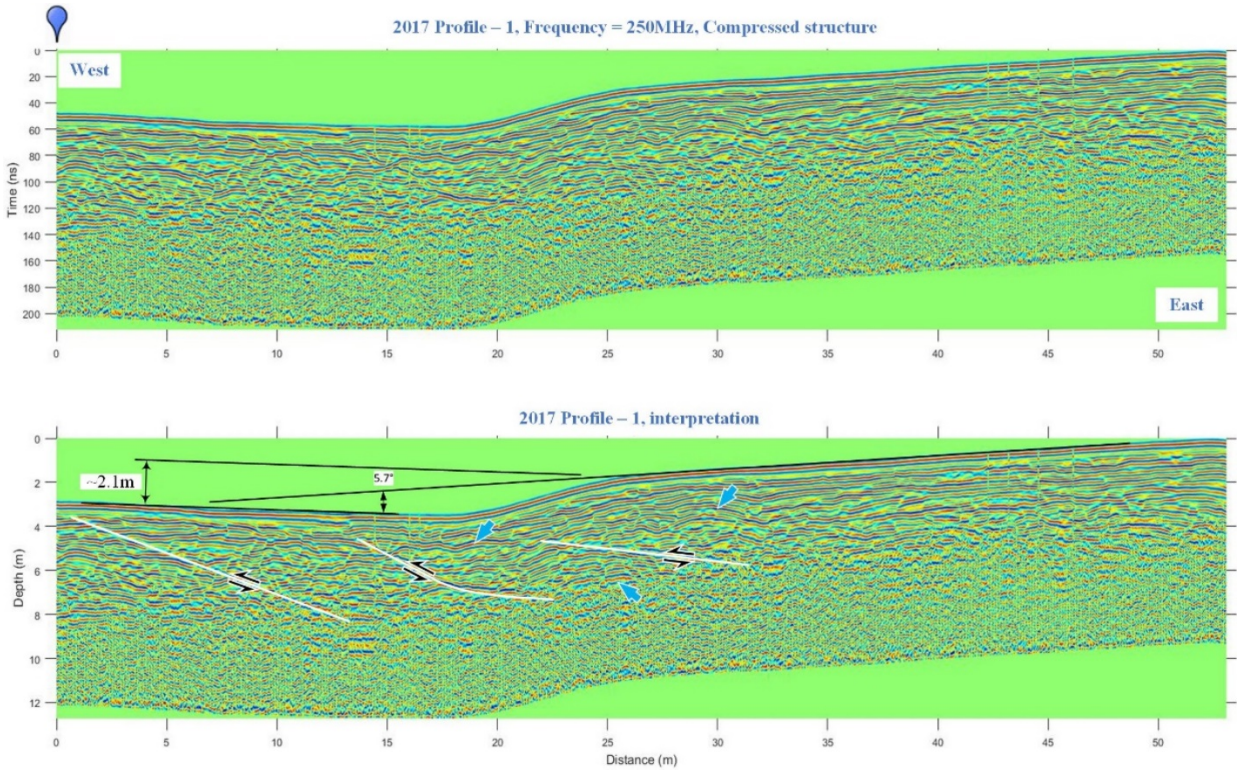

Figure 3.24 The result of GPR image of the profile P1 of 3D6 zone (acquired in August 2017) obtained with 250 MHz antenna in the Songino fault thrust structured study area S2 (see location in Figure 3.21). a.) GPR image of the profile P1, the blue symbol indicates the initial position of the measurement. b) Interpretation of GPR image of the profile P1. The GPR image shows a clear thrust structure with several ramp structure under scarp (white curve) and folding effects (blue arrows), the black arrows show the movement direction, the height of the scarp is approximately 2.1 meters in this area.

6 Conclusions

The GPR survey of Songino faults was carried out in several stages in a total of seven zones where horizontal and vertical displacements could be determined. Based on the results of the above detailed GPR studies and their interpretations, the following conclusions are made.

• GPR studies have been reaffirmed as a highly effective and important geophysical method for the study of fault zone structures and alluvial sediment accumulation.

• The results of GPR studies conducted in seven Songino fault zones show that the measurements made in the geodynamic environment of compression and tension are more effective. It means that the smaller the angle of dipping of faults and fractures, the clearer the

position of their planes and fracture zones. Especially in the normal fault structure, the displacement of the horizontal layers is strongly reflected by the GPR.

• Songino faults have a compressed structure on the northwest edge and have the highest scarp area (approximately 21 meters high from geomorphology analyze).

• The GPR study did not reveal any significant anomalies of the fault plane in the strike slip structured zone named S3 zone, and most of the radar waves may be irreversible due to the high angle of incidence of the fault plane in this zone.

• The GPR signal reflection is strongly anomalous in the area of the fault tensional zone or normal structure, and the structure below the fault scarp is clearly visible. The resulting image (Figure 3.11) provides a complete analysis of the movement in the area.

• Most of the budget for paleo-seismic surveys is spent on trench surveys, and GPR surveys have been shown to be important for the efficient use of the survey budget by determining the optimal location for trench excavations and making trench surveys more effective.

• It has been reaffirmed that it is possible to accurately determine the extent of their displacement by reconstructing paleo river channels that have been buried and hidden since the last earthquake.

A detailed GPR study of the Songino fault revealed a wealth of information on the structure, direction of movement, and alluvial sediment accumulation of the soil disturbances caused by the fault. Based on all of these data, a unified interpretation reveals that the Songino fault plane is a left-lateral strike slip from southeast to northwest. The compressional effect on the west part, or the high scarp sedimentary structure formed on the ground surface, is the effect of excavation at an angle of approximately 40° to the movement direction of the fault. The sediment with a normal-structured scarp on the east is the effect of the tensional of the structure, which bends in the direction of the Songino fault movement and forms an angle of about 21°.

Chapter 4 : The geological context of the Songino active fault, Ulaanbaatar, Mongolia.

1 Introduction

Mongolia's regional geology is commonly approached by employing tectonostratigraphic terrane analysis to aid in interpreting its structure and history. In this sense, a terrane is defined as a fault-bounded geologic entity or fragment that is characterized by a regional size and a distinctive geologic history that differs markedly from that of neighboring crustal blocks (Tomurtogoo & al, 2002). Thereby, workers have divided Mongolia into numerous individual terranes and super terranes, many extending beyond Mongolia's political borders (Badarch, et al., 2002; Tomurtogoo & al, 2002).

Two prevalent terrane division schemes frequently appear within the literature (Badarch, et al., 2002) has divided Mongolia into forty-five terranes that are grouped into eight different categories or zones: cratonal blocks, passive continental margins, metamorphic rocks of uncertain tectonic origin, island arcs, backarc/forearc basins, accretionary wedges, ophiolites, and volcanic/sedimentary overlap assemblages as shown in Figure 4.1. The other scheme, issued by the Mineral Resources Authority of Mongolia, employs seven different categories of Mongolian terranes: passive continental margins, turbidite basins, active continental margins, accretionary wedges, island arcs, ophiolites, and seamounts as shown on Figure 4.2. These two terrane zonation schemes reveal that the boundaries, orientations, positions, and categorization of these terranes can be interpreted differently. Thus, the interpretations of these zones, especially the cratonal zones and sedimentary basins, are the subjects of intense debate as they have important implications for constraining Mongolia's geodynamic history.

The boundary between the northern and southern Mongolian tectonic domains has been interpreted as a suture formed via closure of the Paleo-Asian Ocean due to the collision of the Sino-Korean craton with the Siberian craton (Ziegler, et al., 1996; Zorin, 1999; Badarch, et al., 2002; Li, 2006). The position of this important tectonic lineament is of great importance because it provides some of the first-order tectonic constraints on the geologic evolution represented by rocks found in Mongolia.

The Khustai fault is centrally situated east of the Mongolian Altai and Hangay Dome areas, south of the BF, and north of the TB where it serves as the tectonic boundary between

the Asralt Khairkhan (Haraa of (Badarch, et al., 2002), Figure 4.1) and Ulaanbaatar terranes; a boundary which strikes northeasterly from the eastern Hangay region into Russia Figure 4.2. When mentioned as a boundary fault between the juxtaposed terranes, this structure is referred to as the Tuul fault. The geology of the Asralt Khairkhan terrane has been variously interpreted as either a late Devonian backarc/forearc basin (Badarch, et al., 2002) or turbidite/accretionary basin (Tomurtogoo & al, 2002; Kelty, et al., 2005). The Ulaanbaatar terrane is regarded as part of the upper Devonian/ lower Carboniferous Hangay-Hentey turbidite basin that filled prior to closure of the Mongol-Okhotsk Ocean and is considered stratigraphically and lithologically correlative with the Tsetserleg terrane located to the west (Tomurtogoo & al, 2002). Both the Asralt Khairkhan and Ulaanbaatar terranes have been extensively intruded by late Triassic/early Jurassic plutons of the Hentey Batholith (stitch complex) (Kravchinsky, et al., 2002; Batulzii, et al., 2006).

During the twentieth century Mongolia experienced at least four 8+ magnitude (M) earthquakes, a fact that effectively highlights the country's geological penchant for very large magnitude earthquakes and overall high seismic activity despite being in an intracontinental setting. The causes of seismicity may be attributable to the Indo-Eurasian collision, uplifted regions possessing high heat-flow (i.e. Hangay dome), mantle plume phenomena, Baikalian extension, Pacific Plate subduction, or a combination of these possibilities (Tapponnier, et al., 1982; Zorin, et al., 2005). That Ulaanbaatar is at risk is well demonstrated by the close proximities of the September 24, 1998 Deren Earthquake (magnitude between 5.6-5.3, depending on the reference) and January 9, 2010 aftershock, both epicentered 150-km south of the Khustai fault, all events felt by residents in the city (Figure 4.4) (Dugarmaa, et al., 2003). Furthermore, a local seismic monitoring network operable since 1994 has shown the presence of microquake clusters epicentered around Ulaanbaatar (Dugarmaa, et al., 2003).

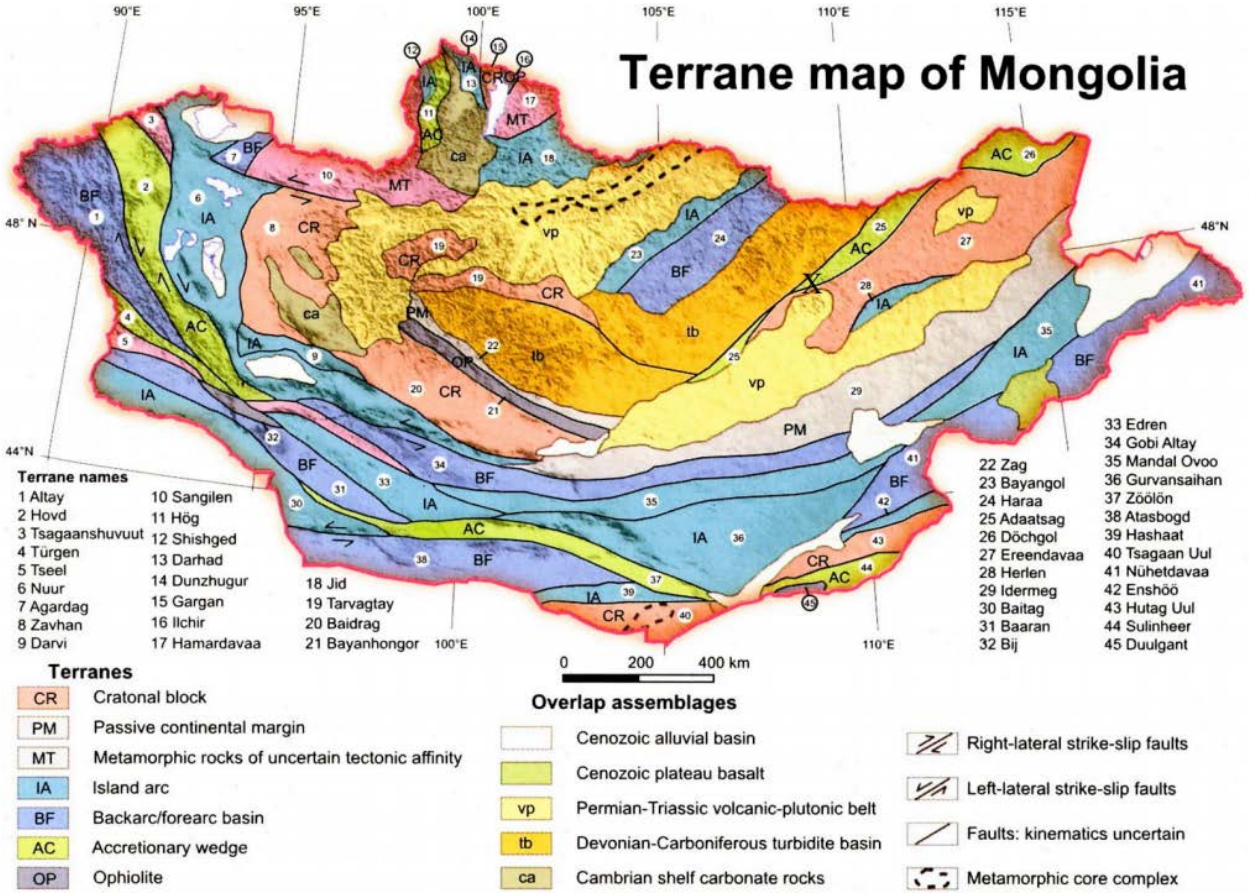

Figure 4.1 Simplified terrane map of Mongolia. Modified from (Badarch, et al., 2002; Lehmann, et al., 2010).

Since 1957, seismologists have been using a modern seismograph network to track the positions of earthquake hypocenters throughout the region. French and Mongolian geologists then used the resulting seismic data set (detectable events dating to between 1900 and 2000) to compile a map of earthquake epicenters located throughout Mongolia. A review of their map shows that the greatest concentrations of seismic events occur in the western half of the country and throughout the Lake Baikal region, whereas seismicity in the eastern half of the country has been much more subdued during this recent time period. The eastern region of the country has originated several recent earthquake clusters throughout the Gobi Desert, Hentey Mountains, and grassy steppe, most notably the Deren fault rupture near the town of Mandalgobi, with singular, smaller-magnitude events widely distributed but ebbing towards the east. The TRV is centrally located between these two seismic regions, approximately 300-km east of the January 5, 1968, Mogod Earthquake (M=7.0) epicenter (Bayasgalan, et al., 2005).

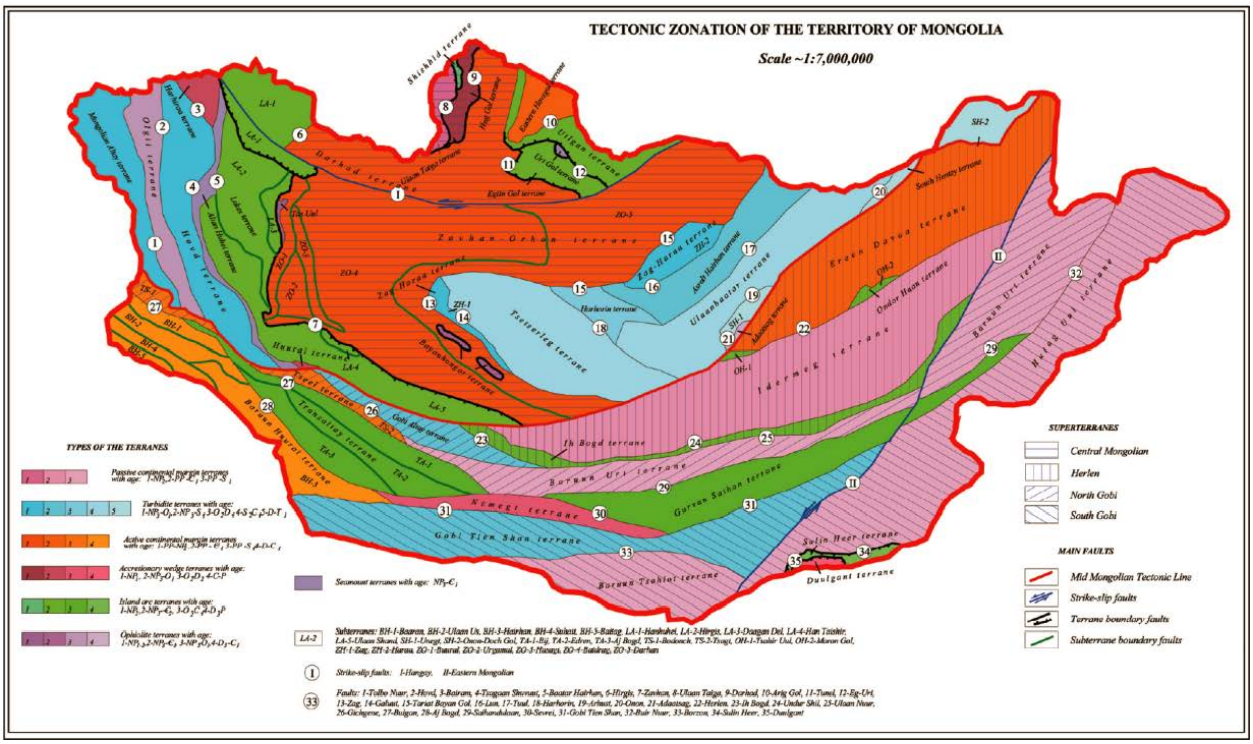

Figure 4.2 Tectonic zonation map of Mongolia. Modified from (Mineral Resources Authority of Mongolia, 1998).

The depths of earthquake hypocenters throughout Mongolia are also of great importance as they provide insights on crustal rheology as well as the information used for producing earthquake models of the region. (Bayasgalan, et al., 2005) reports that none of the earthquakes they analyzed originated at depths greater than 20 km, and that in central Mongolia, the depths were generally 8 events each resulting in hundreds of kilometers of surface rupture with an average offset of over 5 m (Pollitz, et al., 2003). Interestingly, the recurrence interval for large earthquakes (M 8+) on each of the aforementioned faults is between 2,000 and 8,000 years, therefore the presence of four 8+ magnitude earthquakes within a very short time span (~60 years) is likely anomalous (Calais, et al., 2002; Calais, et al., 2006; Dugarmaa, et al., 2003; Pollitz, et al., 2003). For example, the afore mentioned Bulnai Earthquake was closely preceded by the July 9, 1905 Tsetserleg Earthquake epicentered a short distance to the east (M=7.9-8.0). Though coincidental epicenter temporal and spatial clustering is a possibility, it is statistically unlikely. Furthermore, this clustering behavior resembles that of the Big Bear and Hector Mine earthquakes (epicentered in southern California during the 1990's), which were triggered by stress changes caused by the preceding Landers earthquake (Pollitz, et al., 2003). The other two M 8+ events were located further away and occurred several years later.

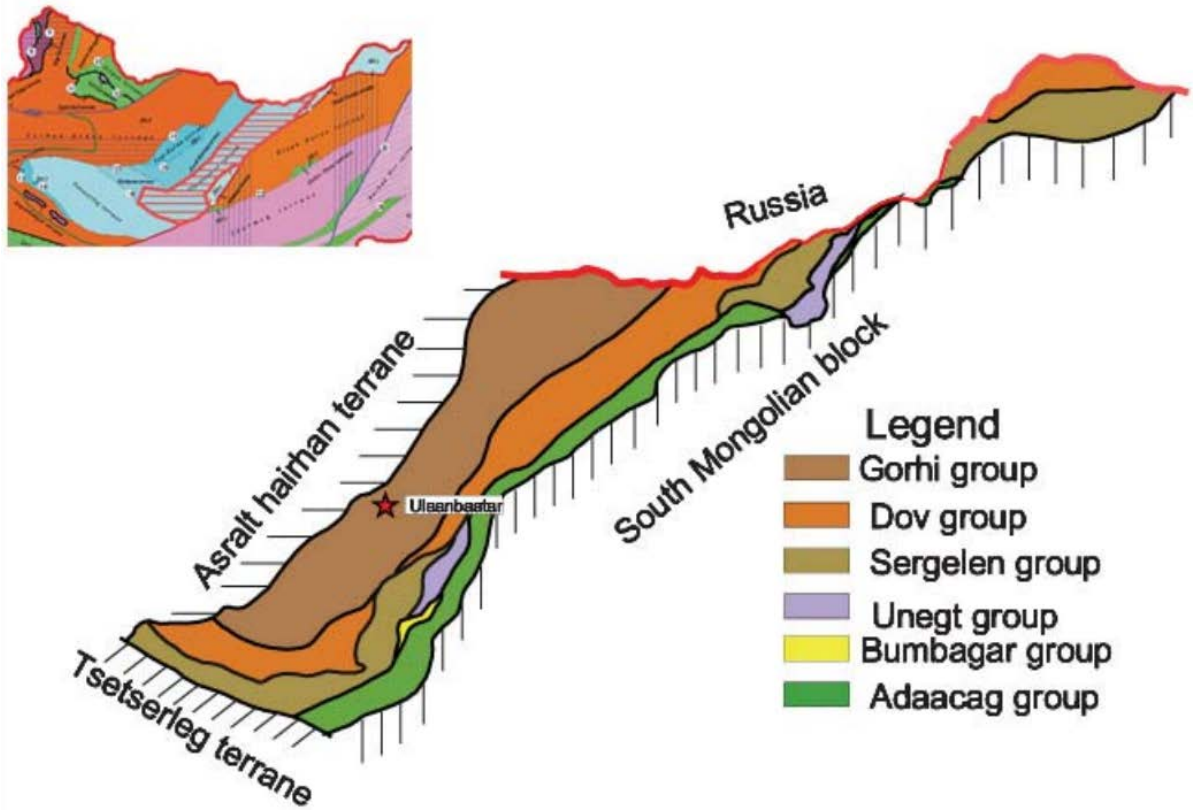

Figure 4.3 Schematic map of the Ulaanbaatar Terrane in the Hangay-Hentey zone of the Devonian Accretionary Complex. Distribution of stratigraphic groups with the Ulaanbaatar terrane. (Dorjsuren, et al., 2006).

The stress transfer models proposed by (Pollitz, et al., 2003) suggests that the Tsetserleg and Bulnai events likely triggered these later events as well, showing that these very large earthquakes could have far-reaching seismic “triggering” effects on fault systems throughout Mongolia for many years. The resulting temporal large earthquake cluster would transfer stress throughout the region, but with long periods of tectonic quiescence between seismic event periods (Dugarmaa, et al., 2003). The duration of these large earthquake clusters has not been extensively explored, but it has been suggested by one source that these changing stress fields may still be in place and is likely influencing GPS derived deformation rates (Calais, et al., 2002; Calais, et al., 2003; Calais, et al., 2006). Evidence for this post-seismic stress transfer is found within the apparent discrepancy between long-term fault movement rates, earthquake tensors, and the GPS data which has been collected since the mid-1990’s (Calais, et al., 2002; Calais, et al., 2003; Calais, et al., 2006).

The seismicity of the region around Ulaanbaatar from 1900-2000 and all earthquakes occur at depths of < 10 km. That the largest earthquakes to have occurred near Ulaanbaatar

during the twentieth century were the Mogod (1968) and Deren (1998) Earthquakes, both located ≥200 km away (Figure 4.4). The focal mechanisms for these earthquakes indicate strike-slip motions (dextral for the Mogod and sinistral for the Deren) with a possible thrust component associated with the Mogod event. Numerous M 3.5-4.5 events have occurred within 200-km of Ulaanbaatar, with a notable cluster of these earthquakes epicentered coincidentally along strike of the mapped trace of the Khustai fault.

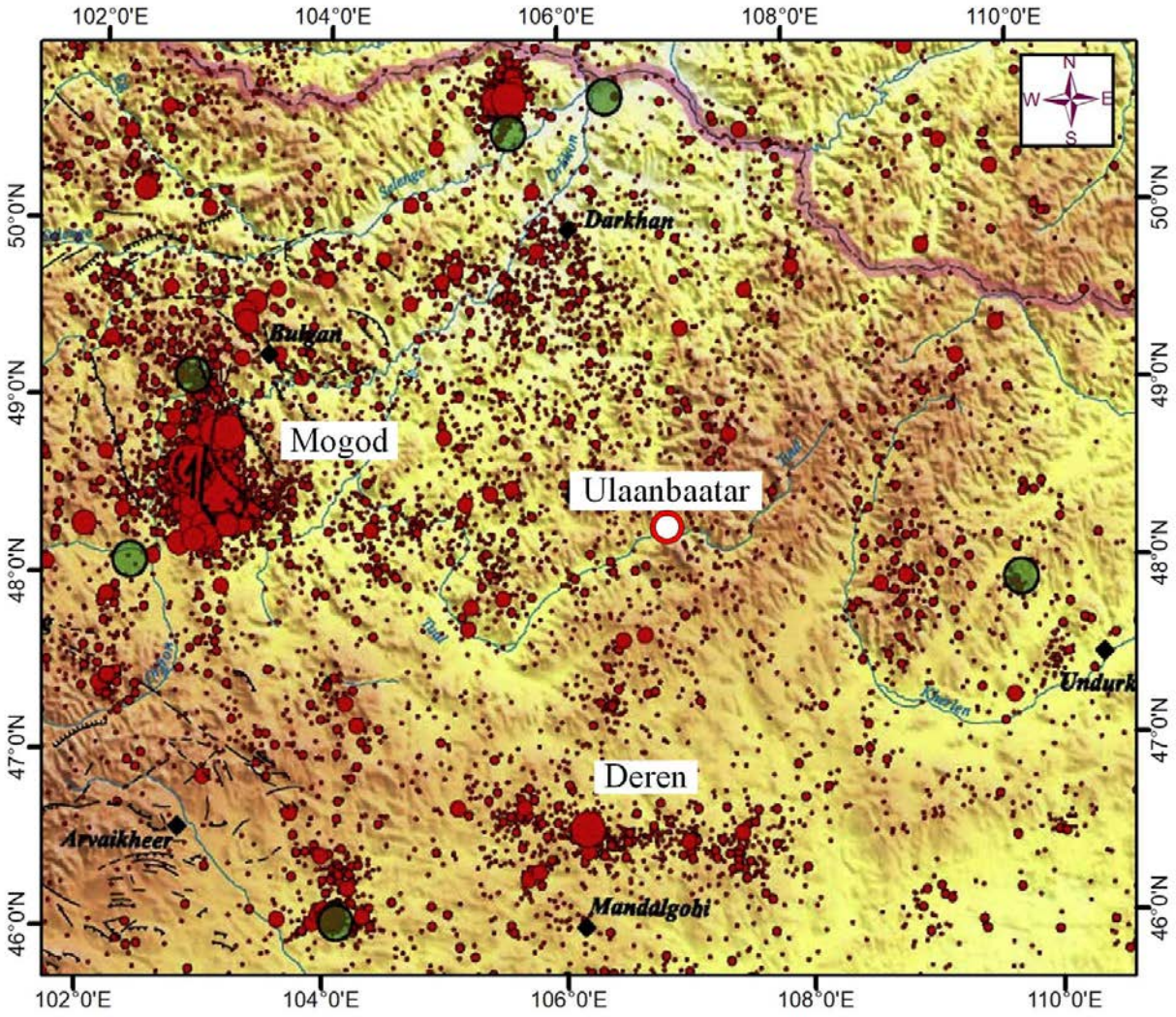

Figure 4.4 Seismicity map (1900-2000) of the region surrounding Ulaanbaatar capital city (modified from One century of seismicity in Mongolia 1900-2000).

2 Paleoseismologycal analyze.

The Paleoseismology studies prehistoric earthquakes, their location, time, and magnitude. Seismologists work with instrumental data during earthquakes, while paleoseismologists interpret the geological evidence of paleoearthquakes. Paleoseismology

allows us to study the distribution of earthquakes in space and over thousands and tens of thousands of years. Such long paleo-seismic stories, in turn, help us understand many aspects of neotectonics, such as earthquakes and tectonic regional patterns. Paleoseismology is a broad field of earthquake geology that includes the use of modern advanced tools and technologies, such as seismology, tectonic and structural geology, historical surface deformation (geodesy), and tectonic landscape geomorphology (tectonic geomorphology) (James & Alan, 2009).

The main driving force behind most paleoismic studies is the social need to assess the likelihood, severity, and danger of future earthquakes (Reiter, 1995; Gurpinar, 2005). Evidence of past earthquakes ranges from local deformation along the crustal fault (fault scarps, sag ponds, laterally offset stream valleys, monoclinic folded marine terraces, scarp-dammed lakes) to large-scale uplift and subsidence, can be. Features (deposits or landforms) formed during an earthquake are described as coseismic and are commonly contrasted with nonseismic features formed by processes of erosion, deposition, and deformation unrelated to large earthquakes. For example, seismogenic faults may creep between earthquakes or slip small amounts during small to moderate earthquakes that leave no signs of sudden slip. For this reason, nontectonic and nonseismic are better adjectives than aseismic (no detectable seismicity) for features unrelated to fault slip or strong earthquake shaking. The term aseismic should be restricted to seismology (James & Alan, 2009).

Paleoseismologists can only study and establish the paleoearthquakes that produce recognizable deformations (in the form of deformed stratigraphic units, displaced landforms, or earthquake-induced sedimentation) (James & Alan, 2009).

2.1 Songino fault trench

A detailed study of the trench is planned for August 2013 on the Songino active fault. In preparation for this, detailed GPR measurements were conducted in June 2013 in zone S5 by a research team from the University of Strasbourg, France, and the Institute of Astronomy and Geophysics, marking a trenching line. However, during the excavation of the trench in August 2013, a research team from the Institute of Astronomy and Geophysics was working with a research team from the Institute of the Earth’s Crust, Siberian branch of the Russian Academy of Sciences on the Mungunmorit active fault. The trench was excavated at a distance of about 100 m to the east of our planned profile P2 (acquired the 14 June 2013), with a deviation of about 60º, not perpendicular (90º) to the fault trace line, it is located (47°47'31.06"N, 106°29'11.72"E). It is wrong, but because the cost of digging a trench is high, we will not be

able to dig another trench again, so we will make a logging on the right wall of the trench and take an sample for dating (Figure 4.5).

As you can see from the photo mosaic of this trench (T1) wall, it is composed of dark brown soil, light yellow loam, orange clay and dark blue fine clay layers from top to the bottom. Beneath the dark blue fine-grained clay layer, a layer of highly fragmented and damaged bedrock is located below the fault scarp (Figure 4.5a, b). The bedrock disappears from the south to the north, and the accumulated layers of clay and earth also thicken and accumulate from the south to north. If we look at the stratification of the layers of these sediments, the oldest layer, the dark blue layer, is at the bottom, on the bedrock, and the youngest layer, the brown soil, is on the surface. According to the results of the dating samples taken from the two locations of the brown soil layer at the top of the trenches, the age of the veins entering the bottom of the soil is 5770 ± 40 (Figure 4.5b). However, the age of the sample taken from the case close to the surface of the accumulated thick part of the brown soil is 775 ± 25, which shows that it is relatively young (Figure 4.5b).

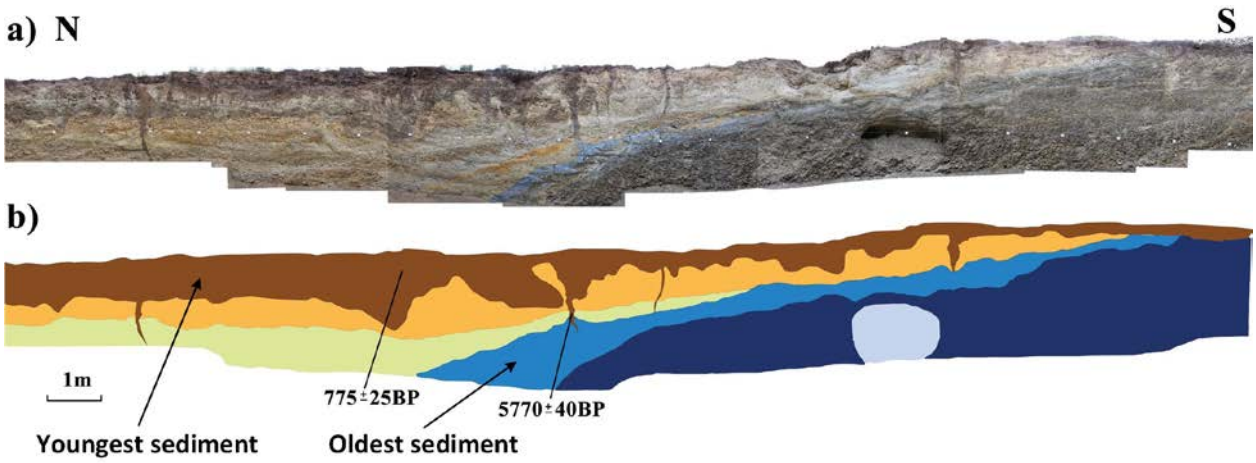

Figure 4.5 Comparison of the paleo-seismological trench photo mosaic and interpreted logging image of the Songino fault tensional structure, The trench(white square) location shown in Figure 3.13. a) Photo mosaic of the western wall of trench T-1 of the Songino fault. b) interpreted layers logging image and dating results, five main different units were identified in the trench shown here by brown, orange, yellow, blue, and dark blue colours. The brown is the soil layer (youngest), the orange and yellow are coarse and fine deposits unit, respectively, the blue is the clay layer (oldest) and dark blue is bedrock, whereas the grey one is a small cave.

Figure 4.6 shows a model for the interpretation of the T1 trench sediment accumulation of the Songino fault normal structure zone S5. The depression formed after the first earthquake

is filled with sedimentary deposits, forming the first and oldest sedimentary layers. After the second earthquake, the first layer settles down, and the depression is again filled with sediment, and the next second layer is formed. After several such earthquakes, several layers are formed, and the sequence, density, composition, and age of their accumulation are interrelated (James & Alan, 2009). The lowest layer is the oldest and most dense, while the top layer is the youngest and least dense.

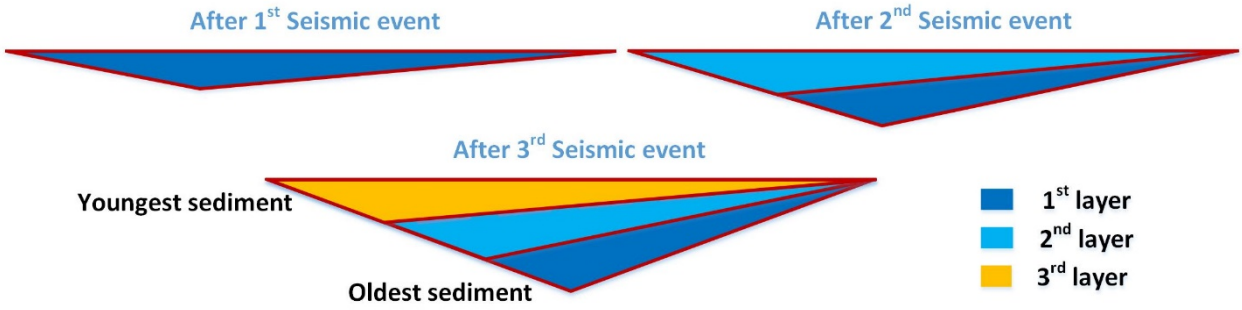

Figure 4.6 The paleo-seismological trench interpretation of sediment layered structure. The dark blue is 1st and oldest sediment and mud layer, the light blue is 2nd sediment layer and the orange one 3rd and youngest sediment layer. The trench photo mosaic in Figure 4.5.

2.2 Emeelt and Khustai trench dating

Integrated geological and geophysical surveys on Emeelt and Khustai active faults were carried out in 2009-2011 by a research team from the University of Strasbourg, France, in collaboration with Institute of Astronomy and Geophysics, Mongolian Academy of Sciences (MAS) research teams. As part of this work, trenches were surveyed at the Emeelt and Khustai active fault, and OSL dating samples were taken in September 2011 before burials were completed. The OSL dating samples were taken by our collaborators, Professor Sun Jimin and Dr. Wang Zhongcheng of the Institute of Geology and Geophysics, Chinese Academy of Sciences (CAS) and, in collaboration with the research team of the Institute of Astronomy and Geophysics, MAS. A total of seven samples were taken to determine the OSL dating of the Emeelt and Khustai active faults, and their laboratory analysis was performed in the optical luminescence laboratory of the Institute of Geology and Geophysics, CAS under the supervision of Professor Sun Jimin.

2.2.1 Emeelt and Khustai trench overview and sample collection

The ET Emeelt trench (47°54'47"N, 106°36'32"E, 1347m above sea level) is located on the Emeelt fault. The details of this section are shown in Figure 4.7. The surface layer of P1 is a deep brown gravel-bearing silt layer with a thickness of about 1.5 m, which is not affected by fault activity. The gravel is poorly sorted, and the maximum particle size can reach 15 cm. P2 is a gray-white gravel layer with a lot of silt sand, and the gravel size is generally 5-10 cm. The formation is thin and partially filled into the fracture. P3 Light yellow silt layer with uniform lithology and no gravel distribution. The stratum was affected by the fault activity and was horizontally broken. Four sampling points are set in the section of the ET trench (Figure 4.7). The sampling point of sample ET-1 is located at the bottom of the dark brown pebbly silt layer (P1), 1.1m from the surface. Sample ET-2 is a fault interstitial between the light-yellow silt layer (P3) and the overlying dark brown gravelly silt layer (P1), 1.2m from the ground surface. The sampling points of samples ET-3 and ET-4 are located at the top and middle and lower parts of the dislocated light-yellow silt layer (P3), 1.35m and 1.6m from the surface, respectively.

The KT Khustai trench (47°46'38.7"N, 106°14'45"E, 1248m above sea level) is located on the Khustai fault. The stratum of this section is inclined, as shown in Figure 4.8.

The section of the KT prospecting trough reveals the strata as follows:

L1 gray-black, black loess soil layer, the deposit is a fine-grained filling of the fault ridge, which has a clear boundary with the underlying L2 layer.

L2 is a gray-white gravel-bearing silt layer, the gravel size is generally 5-10cm, and the gravel size reaches 15cm, and the layer is dislocated.

L3 gray-brown silt layer with uniform lithology and no gravel distribution.

L4 reddish paleosol layer, which is relatively thin.

L5 gravel layer.

Three sampling points are set on the KT trench (Figure 4.8). The sampling point of sample KT-1 is located at the bottom of the black loess soil layer (L1), 0.15m from the surface. Sample KT-2 is in the middle of the gray-white gravelly silt layer (L2) on the hanging wall of the fault, while KT-3 is in the middle of the gray-brown silt layer (L3) in the footwall of the fault.

2.2.2 Optical luminescence dating results

As a sediment dating technology, optical luminescence technology has been rapidly developed in the last 20 years (Murray & Wintle, 2000; Wintle & Murray, 2006). In recent years, optical luminescence dating technology has been widely used in active fault study (Chen, et al., 2003; Chen, et al., 2009; Cheong, et al., 2003; Liu, et al., 2010; Nogueira, et al., 2011). The pretreatment and determination of the optical luminescence samples in this study were all completed in the optical luminescence laboratory of the Institute of Geology and Geophysics, Chinese Academy of Sciences. Among them, the equivalent dose of coarse-grained (90～125μm) quartz samples was measured by the single-piece regeneration method (SAR) (Wintle & Murray, 2006). In the annual dose rate, the test of the element content of uranium, thorium and potassium was completed in the Analysis and Test Research Center of the Beijing Geological Research Institute of Nuclear Industry. The relevant results are shown in Table 4-1 of the book. The dating results of the optical luminescence samples of the ET and KT grooves are shown in Table 4-2 of the book (refer to the calculation of the relevant annual dose (Prescott & Hutton, 1994; Adamiec & Aitken, 1998).

Table 4-1 Uranium, thorium, and potassium content in the sediment samples

Detector name	**Sample number**	**Th/μg*g^{-1}**	**K/%**	**U/ μg*g^{-1}**
ET Probe	ET-1	9.00	3.06	2.02
	ET-2	8.40	3.15	2.13
	ET-3	10.00	2.71	2.27
	ET-4	10.70	2.36	1.97
KI Probe	KI-1	8.67	1.97	5.07
	KI-2	6.24	1.43	3.46
	KI-3	7.35	2.05	2.45

Table 4-2 Basic data and OSL dating results of the samples from Emeelt and Khustai active faults.

Detector name	**Sample number**	**Sampling depth (m)**	**Equivalent dose (Gy)**	**Moisture content (%)**	**Cosmic rays (Gy/ka)**	**Annual dose rate (Gy*ka^{-1})**	**Optical luminescence age (ka)**
ET Probe	ET-1	1.1	40.7±4.0	2.68	0.22688	4.23±0.06	9.6±1.0
	ET-2	1.2	49.9±9.0	1.91	0.22086	4.34±0.04	11.5±2.0
	ET-3	1.35	44.6±5.0	3.94	0.22086	3.96±0.04	11.3±1.3

	ET-4	1.6	52.4±9.0	3.76	0.20940	3.61±0.05	14.5±2.5
KI Probe	KI-1	0.15	3.2±0.3	10.0	0.26603	3.68±0.05	0.87±0.08
	KI-2	0.5	67.5±13.6	3.88	0.26603	2.79±0.05	24.2±4.9
	KI-3	0.6	124.2±16.8	1.86	0.26603	3.29±0.05	37.8±5.1

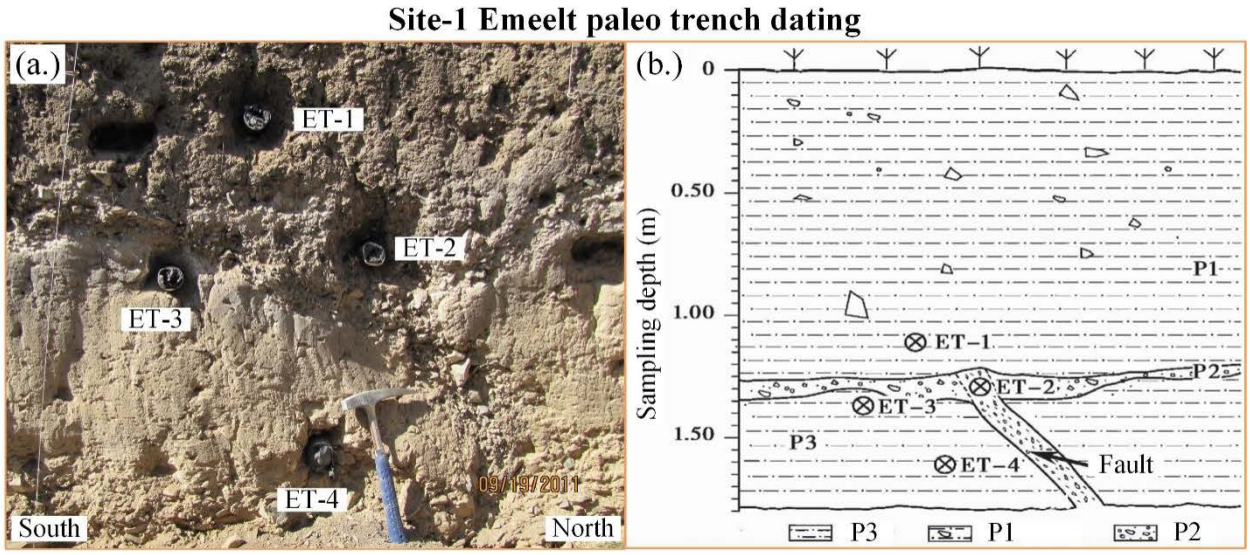

Figure 4.7 OSL dating result of west wall of the T2 trench, excavated in 2010, sampled in 2011, Emeelt active fault. The T2 trench location shown in Figure 2.33. a.) photo of sampling strategy from west wall of T2 trenching site, b.) interpreted image of sampling strategy for the dating.

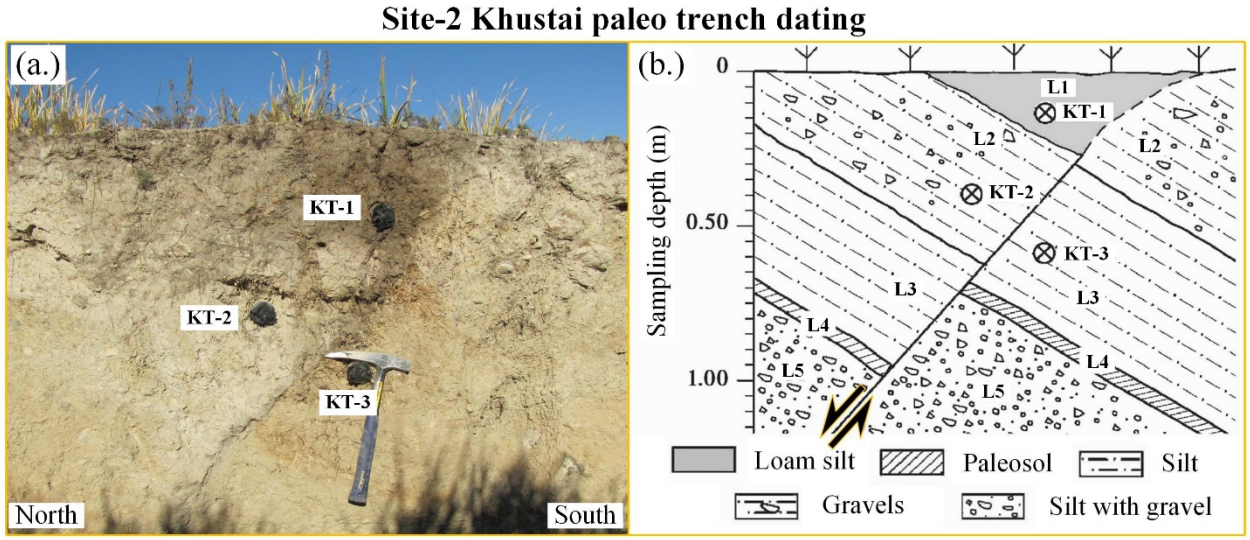

Figure 4.8 OSL dating result of east wall of the trench, excavated in 2011, sampled in 2011, Khustai active fault. a.) photo of sampling strategy from east wall of Khustai trenching site, b.) interpreted image of sampling strategy for the dating and fault movement.

2.3 Structural geological analysis.

We measured on the georadar image result of the Songino fault profile (Profile-2), vertical displacement of the fault scarp was approximately 1.5 m, and then vertical displacement was 0.8 m at the crossed profile (Cross-1). The directions is same of movement of the two normal structured scarp, but the length of the horizontal displacement of the subsurface two layers is approximately 5.2 m (Figure 4.9).

The main distinguishing feature of the Songino fault satellite map is that it consists of three main types of substructures, which can be compressional, tensional and strike slip (Figure 4.10). To the far west, at the tip with the compressional effect, there are three subsections with a stepped structure, which are clearly visible with a shear zone in the middle of two subsections. It is also look like horizontal folding effect. In addition, the three subsections of the hierarchy are also stepped in azimuth, moving from South-southeast to Southeast. The scarp formed in this compressional effect area is more than 22 m high at the northern tip and disappears as it moves forward. The next type of structure is a left-lateral strike slip structure that moves in a horizontal direction. You can see that this strike slip is moving in an almost straight line. There are almost no fault scarp in this horizontal transition area of the left lateral strike slip, and it is not possible to identify the fault zone and traces on the ground surface. The left extensional zone, on the other hand, is tilted to the east at an angle of about 20 ° from the strike slip structure and is gradually curved. The scarp of this normal structure also have a gradually increasing scarp structure from the strike slip structure to the east end. In Figure 4.10a shows the displacement of three earthquakes on the Songino fault, and the location of the first trace of the crack is shown in red. The blue and yellow colors show how the traces of the fault change and move during the next two earthquakes. The black arrow indicates the general direction of the Songino fault, and the three different colored curves and the distance between them indicate the amount of movement in which part of the Songino fault. In Figure 4.10b shows how the elongation direction of the Songino fault changes by how many degrees, and shows which deformation effects occur in which part.

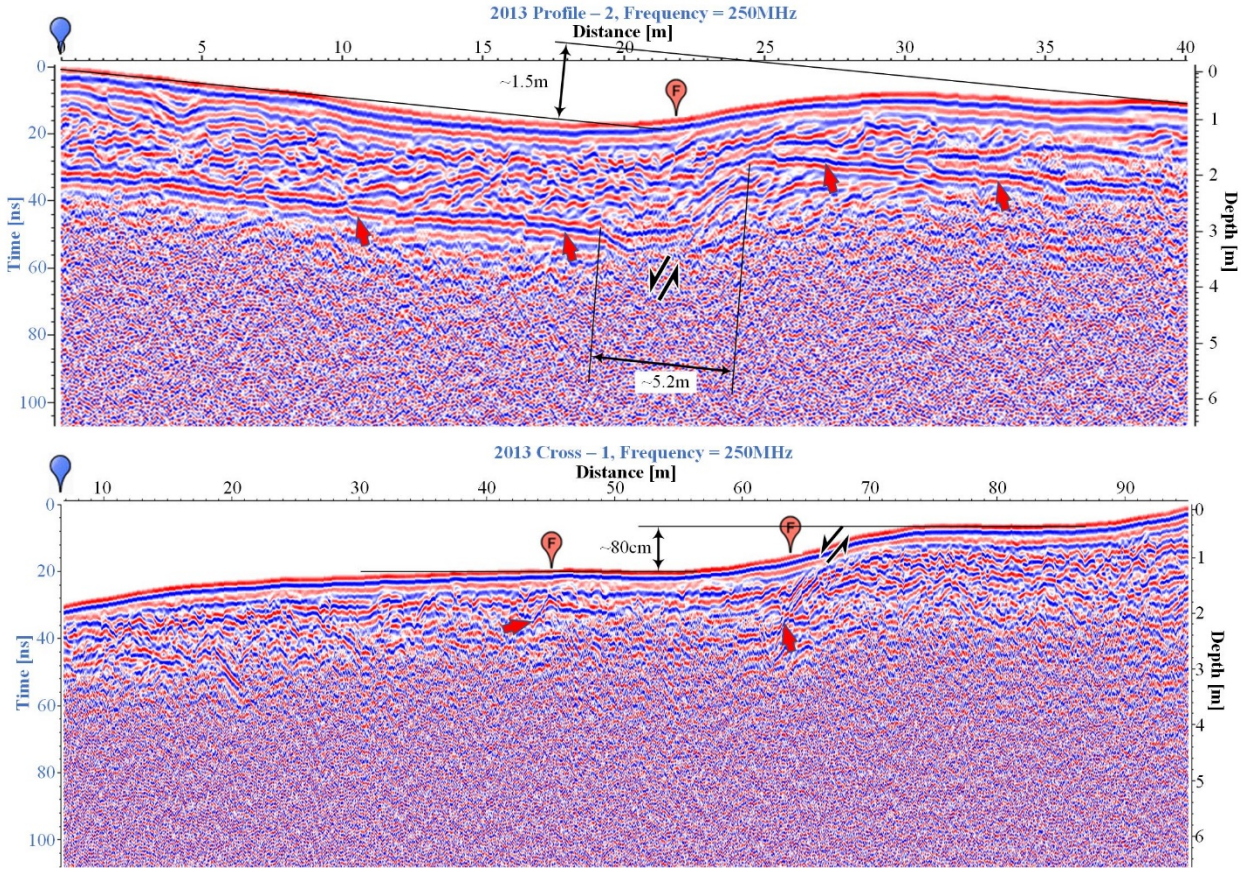

Figure 4.9 The GPR result image of the profile P2 and crossed profile Cr1 (acquired the 14 June 2013) obtained with 250 MHz antenna in the Songino fault main study area S5 (Figure 3.10). a.) result image of the profile P2, the GPR result image shows a clear normal structure and regional extensional effect with competent layer structure under scarp (red arrows). b.) result image of the crossed profile Cr1, red arrow pointed underground high reflected GPR anomaly. The blue symbol indicates the initial position of the measurement, red symbol (F) indicates the point of intersection with the traces of damaged structure on the surface rupture and the profile. The black arrows indicate movement direction of the two side.

The azimuth of the Songino fault trace structure starts at about 166º and changes its direction twice, then extends to about 129.1º for strike slip structure. However, the azimuth of the end normal structure is approximately 108.3º. This shows that there is a difference about 20.5º between the normal and strike slip structures, and about 37.1º difference between the strike slip and thrust structures, and a total of about 58º difference between the normal and thrust structures (Figure 4.10b). The main direction of movement of the Songino fault is along the strike slip structure in the middle, and the thrust structure on the opposite side of its direction of movement (approximately 37.1º) is under compressional effect. However, the strike slip

structure located along the movement (approximately 20.5º) is tensional in the opposite direction (Figure 4.10b).

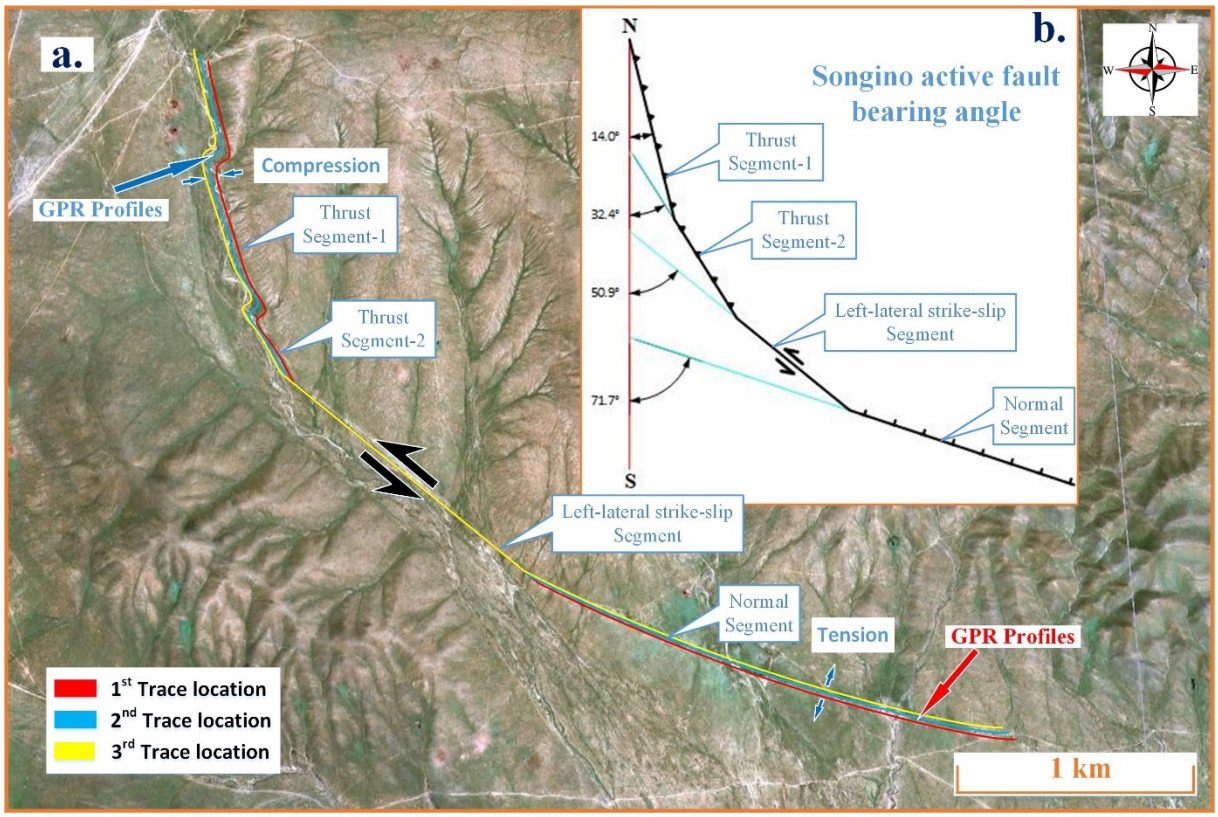

Figure 4.10 The Songino active fault modelling. a. red line indicates the 1st trace location of the Songino fault, Blue line represent 2nd trace location after 1st seismic event, Yellow one is 3rd trace location after 2nd seismic event. b. four different direction fault trace bearing angle and fault interpretation.

The next analysis was to measure the displacement value of the most obvious paleo river channel (approximately 33 m displacement) and calculate the angle (in which the difference is 105.6º with the normal structure trace) (Figure 4.11). This calculation calculates how many meters of displacement can occur in other parts of the Songino fault when the paleo river channel moves 33m. In Figure 4.12, the small angle curvature structure of the thrust structure and the normal structure are averaged to simplify the calculation. According to the final results of the calculation, the horizontal displacement on the normal structure is 11.22 m, the horizontal displacement on the strike slip structure is 32.03 m, and the horizontal displacement on the thrust structure is 19.32 m of the Songino fault (Figure 4.12). It can be seen that a 19.32 m long zone sediment was compressed on the highest scarp section of the Songino fault thrust structure, and it is clear that the compressed sediment was lifted up to form a high scarp, but there is less

displacement compared to the existing scarp height over 20 m. It is not possible for scarp to form because the strike slip is structurally moving along its own axis. In terms of structural differences, it is estimated that a tensional displacement should have occurred at a distance of 11.22 m, which is twice as much as the displacement, which is not yet consistent with the results of satellite image and georadar studies. Thus, it is clear that the main movement of Songino fault is not only a straight movement along the strike slip structure, but also a combined movement with a rotational moment.

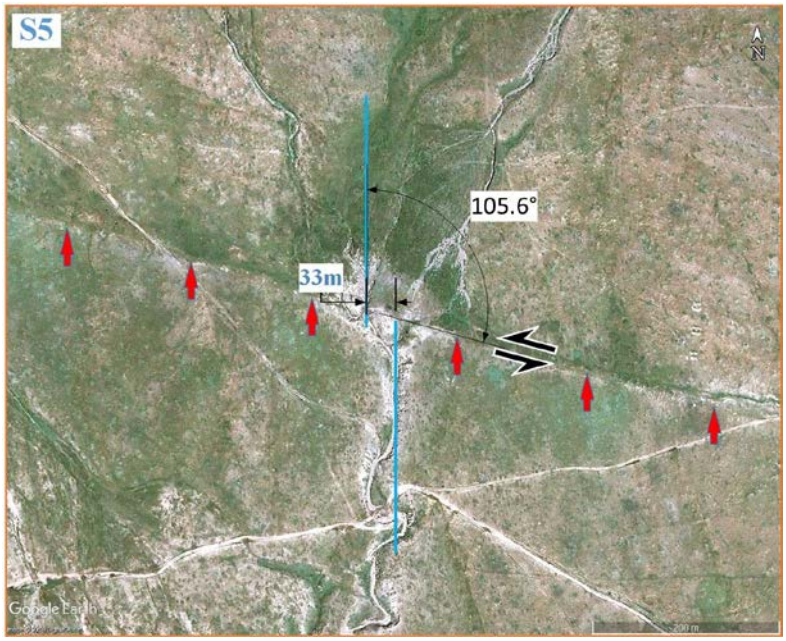

Figure 4.11 Paleo River channel displacement on the S5 zone of the Songino active fault. Blue line pointed paleo river channel axis line and displacement is approximately 33m. Black arrow shown fault movement direction and red arrows shown Songino fault trace on the ground surface. The angle of the axis line of the paleo river channel to fault trace line direction, it is 105.6º.

Figure 4.13 shows the structure of the effects of sedimentation due to the strike-slip fault and the surrounding fault structure. In this example, the effects on right-lateral strike-slip fault accumulation are shown to be opposite to the Songino fault structure, but the fault line structure and formation effects are the same. From this, it is clear that the structure of the fault caused by the Songino fault on the west side compressional zone is push-up oblique thrust structure and the structure formed on the left side extensional zone has pull-apart oblique normal structure.

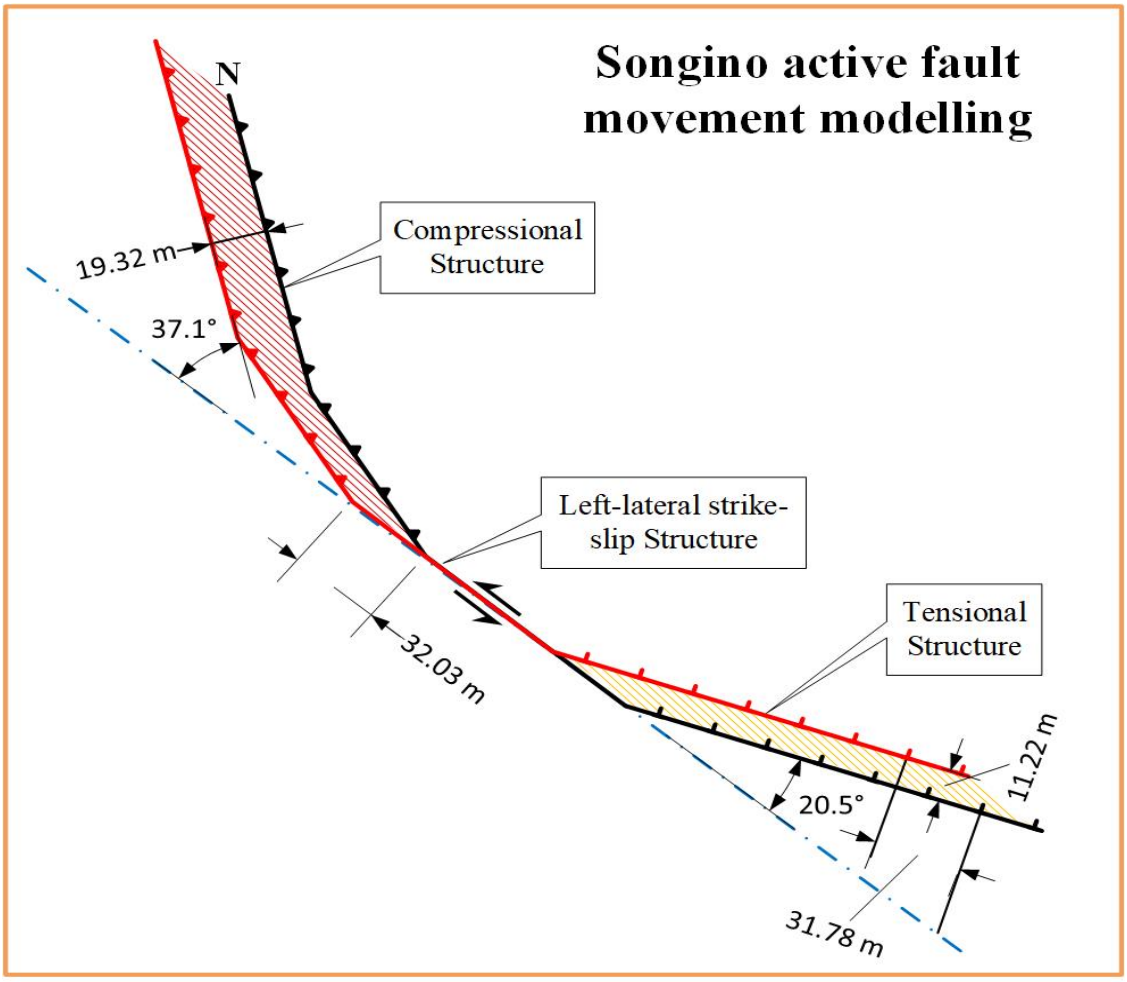

Figure 4.12 Songino active fault movement modeling. Blue dashed line is axis line of strike slip direction. Black lines shown first and before earthquake location of the Songino fault trace. Red lines shown last and after earthquake location of the Songino fault trace. Thrust dextral structure in the compressional zone and normal sinistral structure in the tensional zone. Brown area (from red line to black line) is indicated compressional sediment zone and yellow area (from red line to black) is indicate tensional sediment zone.

The cumulative left lateral strike slip horizontal displacement from a satellite image analyze and measured offset markers were approximately 29m (Figure 4.13). This offset value has over 3m difference from estimated value in Figure 4.12. This may be related to the errors and other measurement faults as well as other measurement linear stretches in calculated by the calculating.

But the estimated value of the horizontal displacement in the normal structured zone is 11.22m (Figure 4.12), and then a measured horizontal displacement value on the GPR result

image of the profile P2 is approximately 5.2m (Figure 4.9), difference between that values is approximately 6m.

This great difference is confirmed by the following. This is: Two big paleo river channels are located between the GPR P2 profile (acquired the 14 June 2013) and the beginning point location of the normal structure. All the substructures on these two paleo-river channels around and contains all the different migrations of their own migration. Also, the substructures of our predicts are evidence to divide this stretching defective deformer power and multiple substructures fracture.

Figure 4.13 Reconstruction of the paleo-river channel movement on the left lateral strike-slip zone. Cumulative left lateral strike slip offset is approximately 29meter. Google Earth 2009.

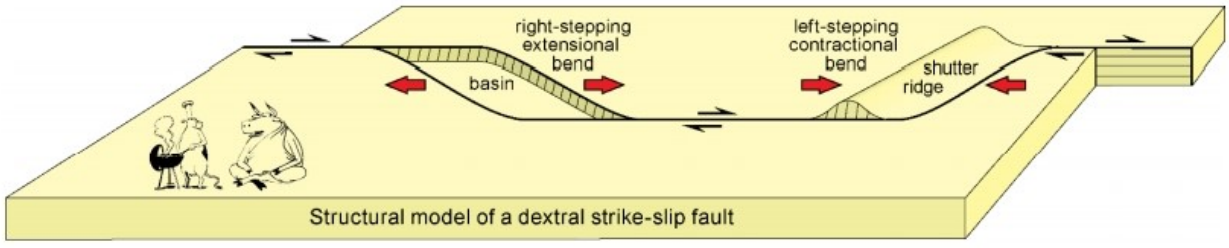

Figure 4.14 Strike slip faulting and sedimentation. This is dextral strike-slip fault example. Left side extensional zone with pull-apart oblique normal structure, Right side compressional zone with push-up oblique thrust structure (Burg, 2017).

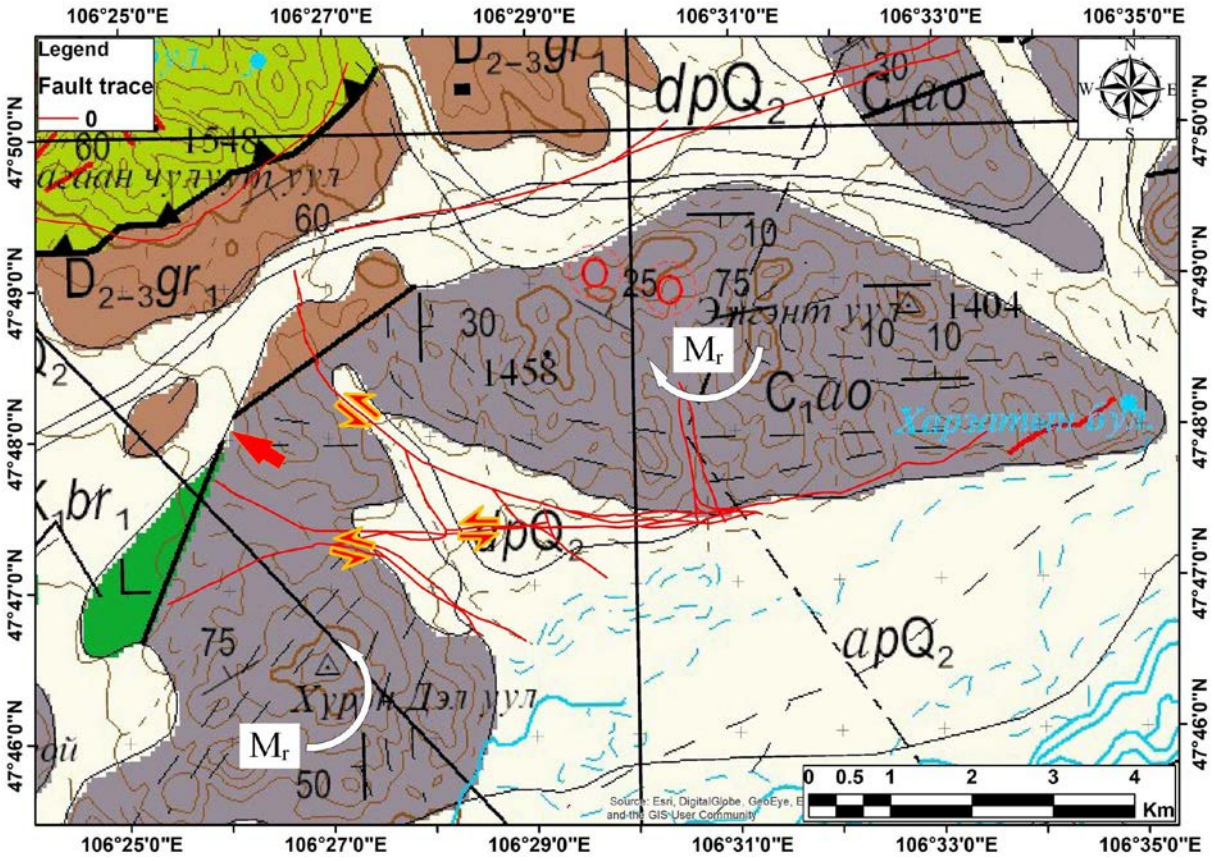

Figure 4.15 Geological background map of the Songino active fault area. Red lines indicated fault trace location of the Songino fault. Red arrow pair point to the movement directions. Mongolian Geological Map-200 project, 2005, scale 1:200 000, map number is 5732.

One of next analyzes was to map the Songino fault trace from satellite image to combine with the georeferenced geological map on the GIS program. In the geological map, the geological environment of the Songino fault is composed of Lower Carboniferous age rocks of the Altanovoo Formation, two mountains named Khuren Del and Ergent and Quaternary sediments between them (Figure 4.15). The geodynamic environment of these mountains is compressed by the movement of Khustai faults from the southwest and northeast (Figure 4.15). However, the compression brings the two mountains Khuren Del and Ergent, closer together and together they provide pressure to the northwest, Tsagaan Chuluut (Figure 4.15). The main fault sections of the Songino fault are located in the Quaternary sediments located between the two mountains Khuren Del and Ergent. The impact of compression from two mountains Khuren Del and Ergent on mount Tsagaan Chuluut can also be seen in the thrust fault structure at the foot of Mount Tsagaan Chuluut (Figure 4.15).

An explanation of the origin and development of the northwestern thrust structure of the Songino fault is given in detail in the work of (Burg, 2017). The mechanical development of folds-and-thrusts-structure is compared to the piling up of loose sand in front of a bulldozer as it is pushed up a slope (Burg, 2017).

In the critically tapered, stable wedge, equilibrium between three main elements exists:

- Frictional resistance to sliding along the base, which refers to the basal traction of the wedge.

- Forces pushing at the rear of the wedge, which express the regional tectonics.

- The shape of the wedge, which is controlled by various factors such as frontal or basal accretion, internal deformation, sedimentation, surface, and tectonic erosion (Burg, 2017).

A change of one or more of these factors generates within-wedge deformation caused by internal stress release to regain or maintain stability. The gravitational potential energy, due to elevation of the hinterland, creates both horizontal and vertical stresses. If the surface of the wedge becomes too steep because of excessive thickening, then the basal plane is unable to support the load and the wedge collapses forward. If the surface of the wedge is too gentle, then not enough gravitational force is transmitted down to the basal plane to allow slip to occur and the topography builds up while the wedge deforms internally by forming folds, faults, and penetrative strain (Burg, 2017).

It is clear that mount Ergent moved northwest due to Khustai fault, spawning sediments in the northwestern part of Songino fault to form the highest scarp in the that area. This can be seen from the folds of the highest scarp on the northwest side of the Songino Fault and the river channel formed behind it, and the structure of the scarp structure is similar to the ramp-1 layer structure of the thrust structure shown in Figure 4.16.

The western boundary of mount Ergent, which pushes the sediment, is the boundary of the bulldozer push-up plane. During the push-up, the push-up plane is likely to rise as slowly along the sliding plane as shown in Figure 4.17.

The northwest thrust structure of the Songino-fault is a wedge-shaped bulldozer effect, and the materials in this wedge-shaped area are composed of Quaternary soft sedimentary material, which folds at the ends to form a highest topographic scarp structure.

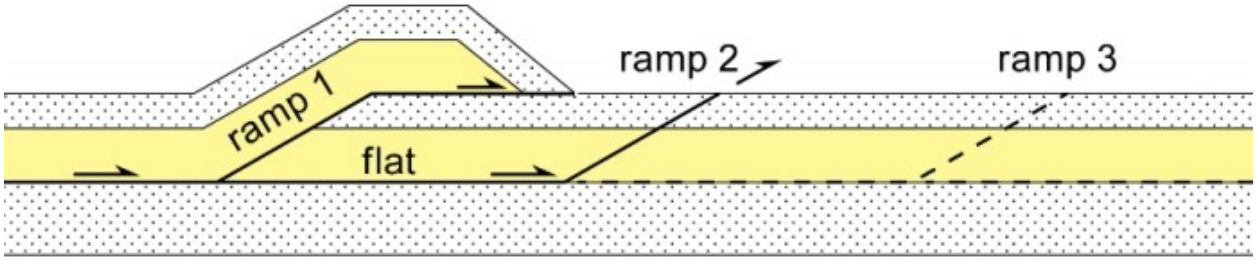

Figure 4.16 Development of a thrust structured scarp. Ramp1 is older and ramp3 is younger one (Burg, 2017).

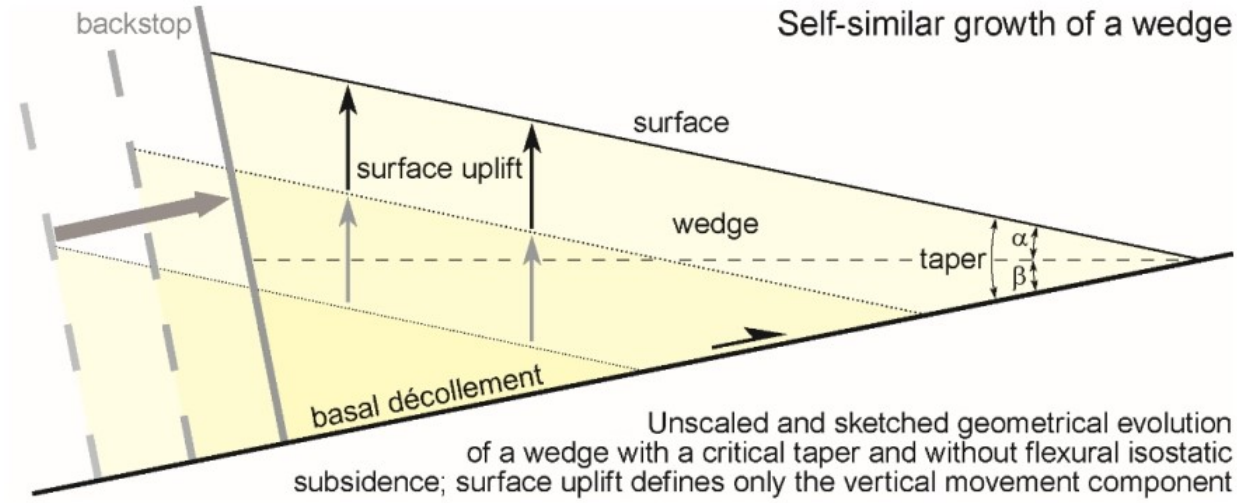

Figure 4.17 Geometry and growth of a wedge structure and bulldozer effect (Burg, 2017).

3 Conclusions

This chapter seeks to identify the geological environment of the Songino fault and the factors that contribute to it, and this study believe that this goal has been achieved to some extent. These include: By carrying out optical luminescence chronology research on the trench sections of the Songino, Emeelt and Khustai active faults for Paleo-seismologic dating, combined with the faults of the formation, the following preliminary understandings are obtained:

1) Based on the optical luminescence age of the fault dislocation strata and its overlying strata on the ET trench, it is inferred that the time of the latest activity of the Emeelt active fault is between (9.6±1.0) ka and (11.3±1. 3) ka.

2) Based on the optical luminescence ages of the fault dislocation strata and the overlying deposits on the KT trench, it is inferred that the time of the latest fault activity of the Khustai active fault is between (0.87±0.08) ka and (24.2±4.9) ka, it may be closer to (0.87 ± 0.08) ka from today.

3) Based on the optical luminescence age of the fault dislocation strata and its normal structured overlying strata on the T-1 trench, it is inferred that the time of the latest activity and age of last top layer of the Songino active fault is (5.77±0.04) ka.

The vertical displacement of the scarp of the normal-structured section was approximately 1.5 m in the perpendicular profile to the Songino fault trace, and the vertical displacement was approximately 0.8 m in the parallel profile along the, while the height of the vertical displacement in the northwest thrust structure of the Songino fault was the highest. At its highest point, it was approximately 22 m high.

There is a difference about 20.5º between the normal and strike slip structures, and about 37.1º difference between the strike slip and thrust structures, and a total of about 58º difference between the normal and thrust structures.

In addition, the horizontal displacement of the normal structured section was 33 m, and from this value, the geometric calculations were used to determine the displacement on the other structures, including 19.32 m for the thrust structured section and then 32.03 m on the left-lateral strike slip section, which is the main transition of the Songino fault.

Finally, the correction between the geological map and the traces of fault line elongation determined the direction of the Songino fault movement and the surrounding sediments, the cause of the accumulation damage, and the relationship.

Chapter 5 General discussions and conclusions

1 General discussion

The objective of this thesis work, and more broadly of the framework of a seismic micro-zoning and mapping project of the Ulaanbaatar capital city, was to develop a new paleo-seismological approach based on high-resolution GPR imagery, which would make it possible to find the traces of a larger number of strong past earthquakes. That has been possible to image shallow structure to 2-3 meter and but limited for the deep structure to 5-30 meter until now with existing paleo-seismological methods. That it is possible to do so until now with existing GPR method for deep structure. The corollary objective was to use these traces to document the displacements produced by these past earthquakes, and to use these quantifications to better estimate the seismic hazard relating to the faults analyzed. The approach followed consisted in exploring the near surface. The first 5-30 meters of the ground, using GPR, which is a non-destructive, inexpensive, and rapid implementation. Previous studies had demonstrated the potential of GPR imagery to detect zones of active deformation, in particular fault planes, in the first 10 meters of the ground (Smith & Jol, 1995; Audru, et al., 2001; Gross, et al., 2004; McClymont, et al., 2009a). In this work, we demonstrated its additional potential to detect morphological markers buried and preserved in the subsurface. Our work is leading to new information on the history of the surface deformation along the Songino, Khustai, Emeelt and other faults, which will help to better constrain seismic hazard estimates for these major faults of the Ulaanbaatar capital city.

GPR has proven its efficiency in many fields of geosciences but seems generally most efficient in sedimentary deposits, marked lithological boundaries, fractures and/or faults (Gross, et al., 2004; Deparis, et al., 2007; McClymont, et al., 2010), even for subtle changes in the nature, size, shape, orientation and packing of grains (Guillemoteau, et al., 2012).

In the sedimentological context, interpretation generally uses GPR-facies analysis, analogous to their use in seismic studies (Jol & Bristow, 2003; Neal, 2004). Ground Penetrating Radar (GPR) is a relatively recent geophysical method which has found a wide field of applications over the last twenty years (Annan, 2002) for a background, and (Jol, 2009; Beres & Haeni, 2005; Dujardin J.-R. , 2014; Nyambayar, et al., 2018) for a review. description of the main applications).

At the beginning time of this doctoral dissertation, the innovative and advanced method of modern geophysical study, the GPR method, was not widely used in Mongolia. Therefore,

since 2010, we have been working to introduce and localize this survey methodology throughout Mongolia, in many fields. In particular, the aim is to usefully in paleoseismology surveys, and in the future to use a combination of many advanced techniques and technologies to improve the results and quality of surveys.

The structure of underground surveillance for GPR is divided into three main parts: 1. point targets or object, 2. line targets or cylindrical structure, and 3. planar targets. However, the surface of faults, fractures, and geological sediments forms a planar structure, so it is very well reflected in GPR waves Figure 5.1. In determining the location of the fault and fracture plane, its dipping angle and the angle of the accumulated sedimentary layer are very important basements.

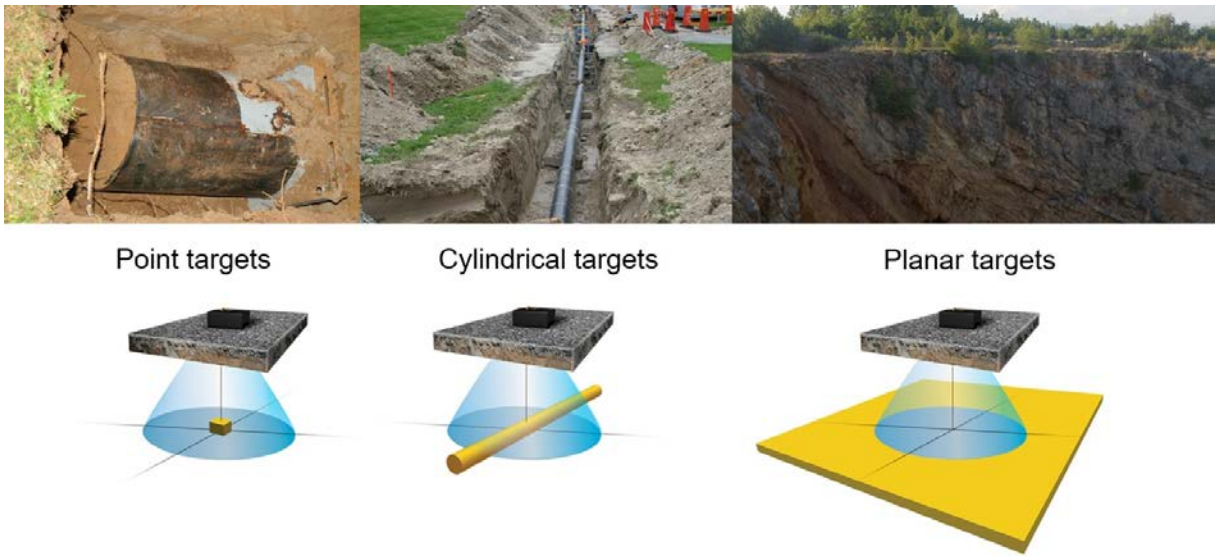

Figure 5.1 GPR target description (GEOSCANNERS, 2021).

The location of the fault and fracture plane are not exactly visible in the example of a normal fault structure with a high angle, but the contrasting layers on both sides of the normal fault structure are almost parallel to the ground surface, which gives a very clear and strong reflection. However, since the vertical structure of the high angle does not any reflection and attenuated completely for the GPR signal, the location of the layers that give a very strong reflection reveals the vertical structure between them for the GPR facies (Figure 5.2). Also, on a low angle normal fault structure, due to the high angle structure near the surface, it also has the effect of completely attenuated and chaotic propagation, which does not any reflections the fault plane. This is especially true when the GPR signal energy intensity is high near to the ground surface, and which given a chaotic propagation effect (Figure 5.2), and when the downward GPR signal energy intensity decreases, it have been a complete attenuation effect

for the GPR facies. In such an environment, the location of the fault and fracture plane is determined by the location and reflections of the lateral accumulated sedimentary layers (Figure 5.3).

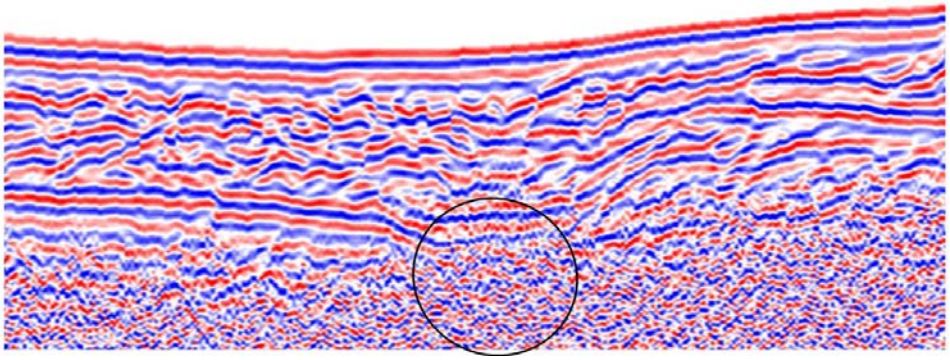

Figure 5.2 The facies used in the interpretation of the 250MHz GPR result images on the high angle normal structure zone. Clear strongly horizontal reflection layer, it is almost parallel to the surface topography. A strongly attenuated signal and don't have any reflection in the high angle vertical structure of the high angle normal structure (black circle).

In the case of low dipping angle thrust structures, both the plane of the fault, fracture and the accumulation of ambient sediments are easier to detect and imaging because they provide better reflection anomaly on GPR waves. In such structure, the thrust structure and displacement of the sediment layers differ significantly for the GPR signal facies. It is also easy to identify the fault zone because the phase shifts of the GPR waves are clearly visible at the displacement of the sediment layers (Figure 5.4).

Figure 5.3 The facies used in the interpretation of the 250MHz GPR result images on the high angle fault structure. a) First example of the interpretation, 1. Clear horizontal reflection layer and chaotic background, 2. Clear horizontal reflection layer and strongly attenuated signals. b) Second example of the interpretation, upside of 1. And 2. Chaotic background with no layer continuity, downside of 1. And 2. Clear horizontal reflection layer and strongly attenuated signals.

The phase shift of the GPR signal in the fault and fracture plane environment and the location of the movement and displacements of the layers of sedimentary deposits were used to

evaluate the geodynamic environment between them and to determine the state of compression and extention.

The findings of this study clearly show that georadar surveys conducted on active faults in the central region of Mongolia and around Ulaanbaatar have yielded many good results. The results of the thrust structured surface can be seen in the examples of Mogod active fault (Figure 2.7, Figure 2.8, Figure 2.9) and Mungunmorit active fault (Figure 2.13). However, the results of two different types of normal structured fault surface can be seen in the examples of Bayankhongor active fault (Figure 2.17) and Songino fault (Figure 3.11) surfaces. It is also possible to accurately determine the results of the horizontal displacement of the fault by the displacement of the mountain river channel, which can be seen in the imaging of the results of the Emeelt active fault (Figure 2.34, Figure 2.35). It is also possible to see from the Emeelt active fault example that the results of high-precision measurements of 3D GPR imaging can be used to reconstruct and imaging traces of underground canyons and to accurately determine the extent of horizontal displacement by means of profiles (Figure 2.37, Figure 2.38, Figure 2.39). Based on the overall results of the GPR study conducted in this study, it is assumed that the 250MHz, 500MHz shielded antennas and RTA50MHz unshielded antenna of the GPR provide complete underground hidden structural information on soil erosion for all types of active faulting.

Also, a good consistency is observed between the GPR data result imaging and the trench study results (Figure 2.10, Figure 2.14, Figure 2.35).

A lot of experience and knowledge has been gained from the GPR study of active faults of the central region and around Ulaanbaatar of Mongolia. Based on that experience and knowledge, a detailed GPR study was conducted on the Songino fault between the Khustai and Emeelt active faults.

The results of the Songino fault GPR study show that the results of this study are sufficient to fully meet the objectives of this study. In particular, the compressional effects to the thrust structural fault scarp and subsurface can be clearly seen in the results of studies conducted in the Songino fault thrust structured section. It is also possible to get a very clear result imaging of the high angle normal structure from the results of GPR imaging in the normal structured section of the Songino fault.

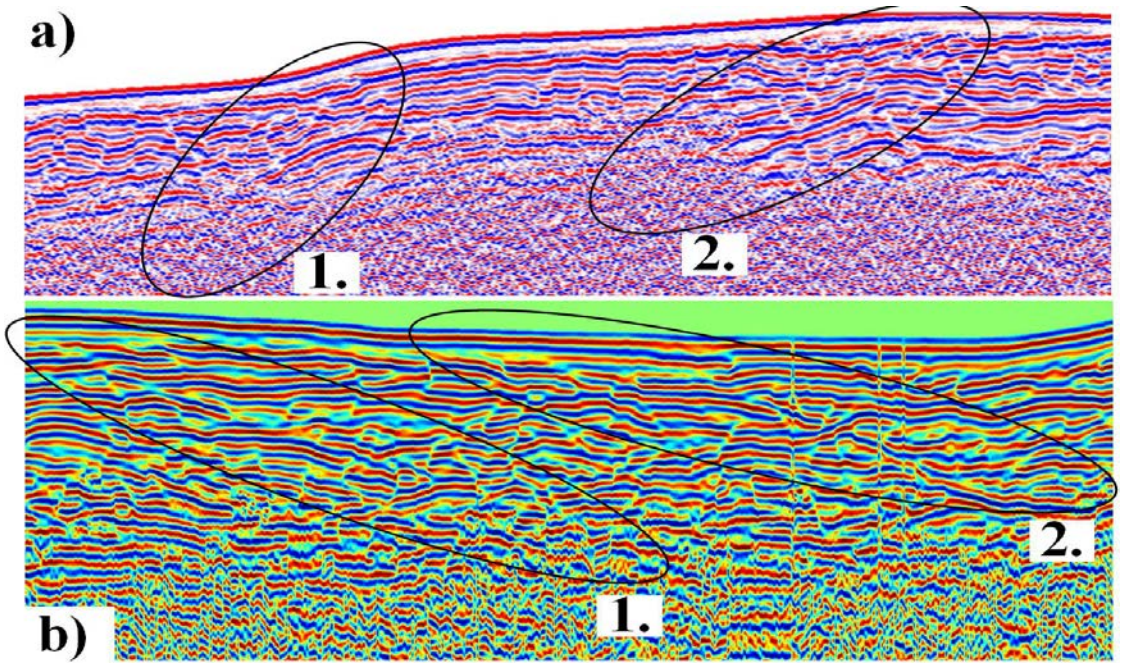

Figure 5.4 The facies used in the interpretation of the 250MHz GPR result images on the low angle thrust fault structure. a) First example of the interpretation, 1. Clear horizontal reflection layers and phases changed, 2. Clear horizontal reflection diverged layers. b) Second example of the interpretation, 1. And 2. Clear horizontal and low angle reflection layers and strongly attenuated signals.

According to the results of a detailed study of Songino fault trenches conducted in August 2013, the accumulated form of sediment accumulation is stacked in from south to north direction, and each layer has a thickened structure in from south to north direction. In many respects, the structure of this part of the Songino fault indicates a normal structure, such as the fact that the younger layers have the structure of the previous older layers leaning from front to back. According to the latest analysis of the accumulated brown soil, the age of the sample taken at a depth of 1.2 m above the ground, where the three old layers were cut, is 5770 ± 40 BP, which may indicate the time of the last activation of the Songino fault. However, the age of the samples taken from the 0.4 m depth of the topsoil brown soil is 775 ± 25 BP, which indicates a much later soil accumulation. The accumulation of Songino fault sediments has four main types, and it would be helpful to determine the relationship between the frequency of earthquakes in the fault if samples were taken from each layer and analyzed for their age.

Stratum is the natural carrier for recording fault activity. Trenches were excavated for Emeelt and Khustai faults, and the time of fault activity was inferred by analyzing the stratigraphic relationship of the trench sections.

The section of the ET trench on the Emeelt fault shows that the fault activity caused the light-yellow silt layer (P3) to be dislocated; during the fault activity, the material in the gravel layer (P2) was involved in the fault fracture zone and became the material in the fault zone; The brown gravel-bearing silt layer (P1) has no faults and is not affected by fault activity. Therefore, the time of the latest fault activity on this fault should be somewhere in between. The sample ET-1 was collected from the bottom of the dark brown gravel-bearing silt layer (P1), and its age is (9.6±1.0) ka. The samples ET-3 and ET-4 were collected from the light-yellow silt layer (P3). Among them, the sampling point of ET-3 is located at the top of the formation, and its optical luminescence age represents the minimum age of formation of the dislocation formation, namely (11.3±1.3) ka. Therefore, the time of the latest fault activity of the Emeelt active fault is between (9.6±1.0) ka (ET-1) and (11.3±1.3) ka (ET-3).

The section of the KT trough on the Khustai active fault shows that the fault activity caused the gray-white gravel-bearing silt layer (L2), the gray-brown silt layer (L3), the reddish palaeo-soil layer (L4) and the gravel layer (L5) to produce dislocations. This indicates that the latest activity of the fault was later than the formation of the gray-white gravel-bearing silt layer (L2). The KT trench shows that the fault is a normal fault. When the fault is active, the two disks of the fault are relatively dislocated, resulting in a height difference on the surface. In addition to the inclination of the stratum itself, a local depression is formed there. The surface material is mixed with a large amount of organic matter to fill the depressions, forming a black loess layer (L1). Therefore, the fault activity is earlier than the formation of the black loess soil layer (L1). The dating results of the three optical luminescence samples KT-1, KT-2, and KT-3 on the KT profile are (0.87±0.8) ka and 35 volumes of paleo-seismic geology (24.2±4.9) ka respectively and (37.8±5.1) ka. Since the sample KT-1 was collected from the bottom of the black loess soil, its optical luminescence age represents the age when the black loess soil began to form. Therefore, this age can be used to define the lower limit of the fault activity time. The samples KT-2 and KT-3 come from the gray-white gravel-bearing silt layer (L2) and the gray-brown silt layer (L3), respectively, and their optical luminescence ages represent the formation ages of the corresponding fault strata. Therefore, the optical luminescence age of KT-2 can define the upper limit of the fault activity time. The formation of the black loess soil layer may be very close in time to the fault activity. Therefore, the latest activity time of the Khustai active fault is between (0.87±0.8) ka and (24.2±4.9) ka and may be closer to (0.87±0.8) ka.

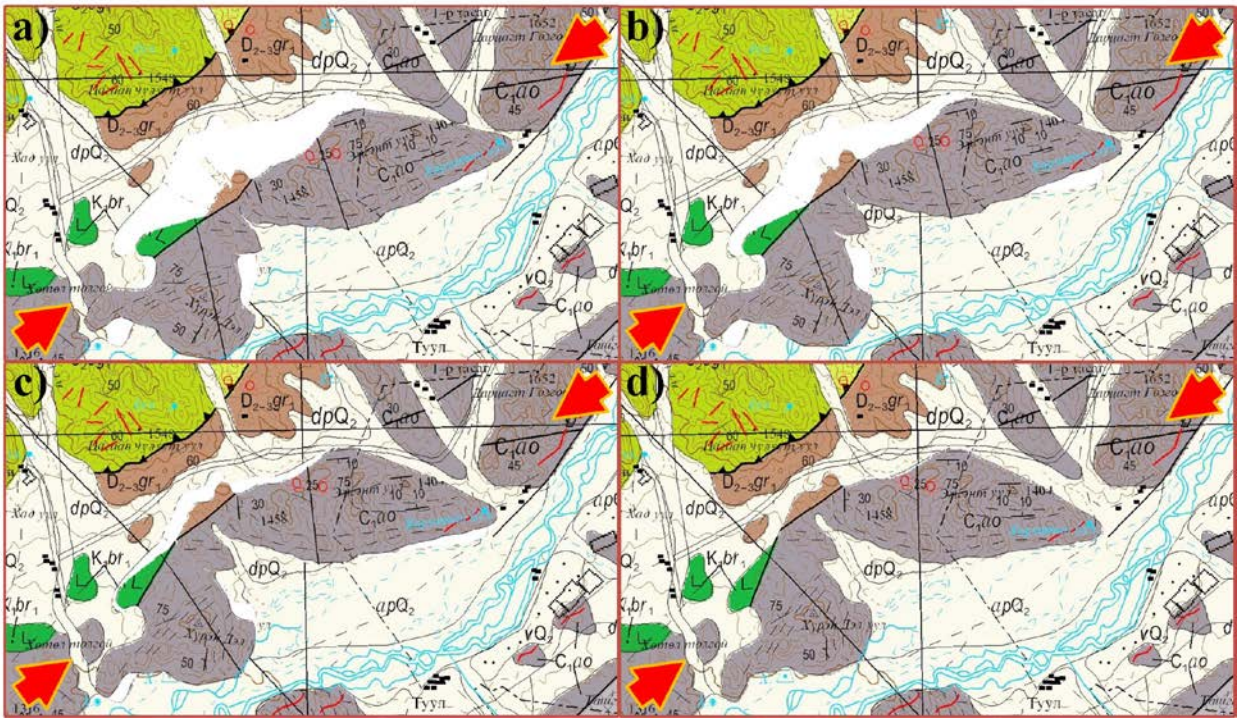

Figure 5.5 Structural evolution of the Songino fault area. a) Past first location, b) Past second location, c) Past third location, d) Present location

According to the geological map of the Songino fault area, the that fault is caused by the movement of two Carboniferous aged mountains, and it is clear that the fault and fracture was caused on the Quaternary sediments between them.

The boundary of the continuous elongation of the normal structure of the Songino fault is branched from the eastern edge of zone c5, divided into several sections with only horizontal transitions, without scarps. This is directly related to the nature of the Quaternary sediments, accumulation density and strength in the environment. Also, this substructured part is located to the southwest of the fist-shaped structure in the southern part of the Ergent mountain. Therefore, it is clear from Figure 4.15 that the forces acting on the this site are in a position to create the branching substructure of the faulting fractures.

The movement of the Carboniferous “Ergent” and “Khuren Del” mountains has a bending and compressional effect due to the force of the “Khustai” and “Emeelt” active faults, which have caused left lateral strike slip main component, compressional and tensional effects on the Quaternary sediments between them (Figure 5.5).

This study is only a detailed study of the main structure and substructures around the Songino fault. Within the scope of this doctoral dissertation work, the main movements of the Songino fault and the auxiliary parts of the sub fracture were identified and modeled.

2 Advantages and limitations

The paleo seismological GPR approach has some limitations: The first being that it can only be applied to electrically resistive materials. In addition, the acquisition is fast, but the data processing is tedious, mainly because of the separate acquisition of the GPR profiles and their location but also because of certain processing and analysis steps that cannot be fully automated. This concerns the data editing step which requires viewing and verifying each of the profiles.

The second one, pseudo-3D acquisition geometry has some drawbacks, being the inability to correct artifacts from 3D effects and especially out-of-plane reflections. Pseudo-3D acquisition, however, turns out to be a good compromise between acquisition, processing and analysis time, and spatial coverage. The use of ground penetrating radar as an imaging method also provides images of the subsoil with a high resolution compared to other existing methods and avoids the drawbacks of inversion (data smoothing and non-uniqueness of the solution).

The acquisition of several parallel profiles also helps to avoid misinterpretations of the images obtained by distinguishing noise and signal artifacts. While noise and artifacts vary from profile to profile, the signal is coherent. The interpolation between the profiles therefore makes it possible to keep only the signal.

A final limitation is that the GPR approach allows only the co-seismic displacements of past strong earthquakes to be determined, but not their ages. Knowledge of these movements is nevertheless sufficient to estimate the number and magnitudes of the strong events identified. Good combination is the GPR result with the ages (dating) result found.

3 General conclusions

At the beginning time of this doctoral dissertation, the innovative and advanced method of modern geophysical study, the GPR method, was not widely used in Mongolia. Therefore, since 2010, we have been working to introduce and localize this survey methodology throughout Mongolia, in many fields. In particular, the aim is to usefully in paleoseismology surveys, and in the future to use a combination of many advanced techniques and technologies to improve the results and quality of surveys.

This work is a part of numerous studies on the characterization of active faults of Mongolia. For the first time we used GPR to explore and reveal the buried traces of a newly discovered active fault in area showing low slip rate. It is a challenge as we are in a context where the geomorphologic features have been heavily smoothed since the last event due to erosion processes combined with a very long return period probably of several thousands of years. Despite the low penetration depth of the GPR up to 15 m for the 50 MHz antenna, 5 m for the 250 MHz antenna and 3 m for the 500 MHz antenna, it clearly provided several important pieces of information that improve our understanding of the active fault geometry and horizontal displacement.

The results of two-dimensional and three-dimensional GPR surveys and analyzes conducted since 2010 on active faults in the central region of the Mongolia and around Ulaanbaatar capital city were presented. During this time, we imaged, mapped, analyzed, and interpreted GPR survey results for all types of active faults. Based on the survey objectives and after having reviewed the GPR survey results for the active fault characterization, the following can be concluded:

The combination of 500MHz, 250MHz with RTA 50MHz antenna produces three complementary and consistent datasets as they allow the imaging of different structures. A good consistency is observed between the 500 MHz antenna GPR profiles and trenching results.

One of the main results of this study is that it is possible to distinguish between active fault compression and tensile effects by combining the geomorphology of active faults and the imaging of underground structures imaged by GPR measurements.

It is also possible to reconstruct the structure of paleo seismic active faults under alluvial sediments and to determine the extent of horizontal displacement more accurately than traditional paleo-seismological methods.

Most of the budget for palaeoseismological research is spent on trenching, and GPR studies have been shown to be important in determining the optimal location for trench excavation.

Pseudo-3D profiles, recorded with a 500 MHz antenna over a paleo-channel crossing the Emeelt fault, provided information about the lateral displacement of 2 m caused by the fault and active fault trace locations. The 50 MHz GPR profiles show a direct reflection, coming from the fault plane, giving access to the location, the dip angle and direction of the fault. It is

clear gives from these examples that different frequency antenna of the GPR images provide information on different geological structures. In contrast, the linearity of the actual seismicity indicates a near vertical fault plane examples in GPR result of the Avdar, Bayankhongor and Emeelt active faults. To clarify that point, we need to investigate more in depth the active structure.

The GPR survey of Songino faults was carried out in several stages in a total of seven zones where horizontal and vertical displacements could be determined. Based on the results of the above detailed GPR studies and their interpretations, the following conclusions are made.

GPR studies have been reaffirmed as a highly effective and important geophysical method for the study of fault zone structures and alluvial sediment accumulation.

The results of GPR studies conducted in seven Songino fault zones show that the measurements made in the geodynamic environment of compression and tension are more effective. It means that the smaller the angle of dipping of faults and fractures, the clearer the position of their planes and fracture zones. Especially in the normal fault structure, the displacement of the horizontal layers is strongly reflected by the GPR.

Songino faults have a compressed structure on the northwest edge and have the highest scarp area (approximately 21 meters high).

GPR studies do not reveal strong anomalies in the strike slip structured zone, which is likely to have a high angle of collapse in this zone.

The GPR signal reflection is strongly anomalous in the area of the fault tensional zone or normal structure, and the structure below the fault scarp is clearly visible. The resulting image provides a complete analysis of the movement in the area.

It has been reaffirmed that it is possible to accurately determine the extent of their displacement by reconstructing paleo river channels that have been buried and hidden since the last earthquake.

A detailed GPR study of the Songino fault revealed a wealth of information on the structure, direction of movement, and alluvial sediment accumulation of the soil disturbances caused by the fault. Based on all of these data, a unified interpretation reveals that the Songino fault plane is a left-lateral strike slip from southeast to northwest. The compressional effect on the west part, or the high scarp sedimentary structure formed on the ground surface, is the effect of excavation at an angle of approximately 40° to the movement direction of the fault. The

sediment with a normal-structured scarp on the east is the effect of the tensional of the structure, which bends in the direction of the Songino fault movement and forms an angle of about 21°.

Identify the geological environment of the Songino fault and the factors that contribute to it, and this study believe that this goal has been achieved to some extent. These include: By carrying out optical luminescence chronology research on the trench sections of the Songino, Emeelt and Khustai active faults for Paleo-seismologic dating, combined with the faults of the formation, the following preliminary understandings are obtained:

Based on the optical luminescence age of the fault dislocation strata and its overlying strata on the ET trench, it is inferred that the time of the latest activity of the Emeelt active fault is between (9.6±1.0) ka and (11.3±1. 3) ka. On the KT trench, it is inferred that the time of the latest fault activity of the Khustai active fault is between (0.87±0.08) ka and (24.2±4.9) ka, it may be closer to (0.87 ± 0.08) ka from today. The T-1 trench, it is inferred that the time of the latest activity and age of last top layer of the Songino active fault is (5.77±0.04) ka.

The vertical displacement of the scarp of the normal-structured section was approximately 1.5 m in the perpendicular profile to the Songino fault trace, and the vertical displacement was approximately 0.8 m in the parallel profile along the, while the height of the vertical displacement in the northwest thrust structure of the Songino fault was the highest. At its highest point, it was approximately 22 m high.

There is a difference about 20.5º between the normal and strike slip structures, and about 37.1º difference between the strike slip and thrust structures, and a total of about 58º difference between the normal and thrust structures.

In addition, the horizontal displacement of the normal structured section was 33 m, and from this value, the geometric calculations were used to determine the displacement on the other structures, including 19.32 m for the thrust structured section and then 32.03 m on the left-lateral strike slip section, which is the main transition of the Songino fault.

The main object of this doctoral dissertation, the main structure of the Songino fault, is a left lateral strike slip displacement fault, and the within two side effects of this movement are: the thrust structure of the north-west side structure will have a rotational thrust structure and the normal structure of the south-east side structure will have the same rotational normal structure. However, the stress that causes this Songino fault is defined as the compressive effect of the “Khustai” and “Emeelt” active faults.

References

Abeer, A. (2015). *Tectonique active de la région d'Oulan Bator, Mongolie: Analyse morpho-tectonique et paléosismologique des failles actives de Sharkhai et Avdar.* Strasbourg, France: ED413, UM7516, University of Strasbourg.

Adamiec, G., & Aitken, M. (1998). Dose-rate conversion factors: Update. *Ancient TL*, 16; 37-50.

Annan, A. P. (1993). Practical processing of GPR data. *In Proceedings of the second government workshop on ground penetrating radar.*

Annan, A. P. (2001). Ground Penetrating Radar Work-shop Notes. *Sensors and Software.* Ontario, Canada: Sensors and Software Incorporated.

Annan, A. P. (2002). GPR—History, Trends, and Future Developments. *Subsurface Sensing Technologies and Applications*, 3(4): 253-270.

Annan, A. P. (2009). Electromagnetic Principles of Ground Penetrarting Radar. In H. M. Jol, *Ground Penetrating Radar: Theory and Applications* (pp. 3-40). Amsterdam, Netherlands: Elsevier Science.

Audru, J. C., Bano, M., Begg, J., Berryman, K., Henrys, S., & Niviere, B. (2001). GPR investigations on active faults in urban areas: the Georisc-NZ project in Wellington, New Zealand. *Earth and Planetary Science*, 333(8): 447-454.

Badarch, G., Cunningham, W., & Windley, B. F. (2002). A new terrane subdivision for Mongolia; implications for the Phanerozoic crustal growth of Central Asia. *Journal of Asian Earth Sciences*, 21; 87-110.

Bakun, W. H., & Lindh, A. G. (1985). The Parkfield, California, Prediction Experiment. In C. Kisslinger, & T. Rikitake, *Practical Approaches to Erathquake Prediction and Warning* (pp. 285-304). Dordrecht: Springer Netherlands.

Baljinnyam, I., Bayasgalan, A., Borisov, B. A., Cisternas, A., Dem'yanovich, M. G., Ganbaatar, L., . . . Vashchilov, Y. Y. (1993). Ruptures of major Earthquakes and active deformation in Mongolia and its surroundings. *Geological Society of America*, 181.

Bano, M. (2000). *Imagerie de la proche surface par géoradar.* Institut de Physique du Globe de Strasbourg.

Bano, M., Duringer, P., Ghienne, J. F., & Schuster, M. (1999). Ground penetrating radar study of dry aeolian environment. *69th SEG meeting Expanded Abstracts*, (pp. 586-589). Housten, USA.

Barry, T. L., & Kent, R. W. (1998). Cenozoic magmatism in Mongolia and the origin of central and east Asian basalts, in Mantle Dynamics and Plate Interactions in East Asia. *Geodynamics*, 27: 347-364.

Batulzii, D., Yin, A., & Kelty, T. (2006). Timing, composition, and tectonic setting of igneous complex with and around the Hangay-Hentey flysch basin. In D. Tomurhuu, B.

Natal'in, Y. Ariunchimeg, S. Khishigsuren, G. Erdenesaikhan, & (eds), *Second International Workshop and Field Excursions for IGCP Project-480. Structural and tectonic correlation across the central Asian orogenic collage: implications for continental growth and intracontinental deformation: Abstracts and Excursion Guidebook* (pp. 65-66). Ulaanbaatar: Institute of Geology and Mineral Recourses, Mongolian Academy of Sciences.

Bayasgalan, A., & Jackson, J. A. (1999b). A re-assessment of the faulting in the 1967 Mogod earthquake in Mongolia. *Geophysical Journal International*, 138: 784-800.

Bayasgalan, A., Jackson, J., & McKenzie, D. (2005). Lithosphere rheology and active tectonics in Mongolia; relations between earthquake source parameters, gravity and GPS measurements. *Geophysical Journal International*, 163; 1151-1179.

Beauprêtre, S., Garambois, S., Manighetti, I., Malavieille, J., Sénéchal, G., Chatton, M., . . . Romano, C. (2012). Finding the buried record of past earthquakes with GPR based palaeoseismology: a case study on the Hope fault, New Zealand. *Geophysical Journal International*, 189: 73-100.

Benedetti, L., Finkel, R., King, G., Armijo, R., Papanastassiou, D., Ryerson, F. J., . . . Stavrakakis, G. (2003). Motion on the Kaparelli fault (Greece) prior to the 1981 earthquake sequence determined from 36CI cosmogenic dating. *Terra Nova*, 15: 118-124.

Benson, R. C., Glaccum, R. A., & Noel, M. R. (1984). *Geophysical Techniques for Sensing Buried Wastes and Waste Migration.* Dublin: Office of Research and Development.

Beres, M., & Haeni, F. (2005). Application of Ground-Penetrating-Radar Methods in Hydrogeo- logie Studies. *Ground Water*, 29(3): 375-386.

Bozkurt, E. (2001). Neotectonics of Turkey-a synthesys. *Geodinamica Acta*, 14(1): 3-30.

Burg, J. (2017). *Strike-slip faults*. From ETH Zürich and Universität Zürich: https://www.files.ethz.ch/structuralgeology/jpb/files/english/5wrench.pdf

Burg, J. (2017). *Thrust systems*. From ETH Zürich and Universität Zürich: https://www.files.ethz.ch/structuralgeology/JPB/files/English/4thrustsyst.pdf

Cai, J., McMechan, G. A., & Fisher, M. A. (1996). Application of ground-penetrating radar to investi- gation of near-surface fault properties in the San Francisco Bay region. *Bulletin of the Seismological Society of America*, 86(5): 1459-1470.

Calais, E., & Amarjargal, S. (2000). New constraints on current deformation in Asia from continuous GPS measurements at UlanBaatar, Mongolia. *Geophysical Research Letters*, 27; 1527-1531.

Calais, E., Dong, L., Wang, M., Shen, Z., & Vergnolle, M. (2006). Continental deformation in Asia from a combined GPS solution. *Geophysical Research Letters*, 33; L24319.

Calais, E., Vergnolle, M., Déverchère, J., San'kov, V., Lukhnev, A., & Amarjargal , S. (2002). Are post-seismic effects of the M = 8.4 Bolnay earthquake (1905 July 23) still influencing GPS velocities in the Mongolia-Baikal area? *Geophysical Journal International*, 149; 157-168.

Calais, E., Vergnolle, M., Sankov, V., Lukhney, A., Miroshnitchenko, A., Amarjargal, S., & Déverchère, J. (2003). GPS measurements of crustal deformation in the Baïkal-Mongolia area (1994-2002): Implication for current kinematics of Asia. *Journal of Geophysical Reasearch*, 108: 2051.

Canada: Geoscan. (n.d.). From Geoscan web site: http://www.geoscan.ca/ground-penetrating-radar-gpr.html

Caputo, R., Salviulo, L., Piscitelli, S., & Loperte, A. (2007). Late Quaternary activity along the Scorciabuoi Fault (Southern Italy) as inferred from electrical resistivity tomographies. *Annals of Geophysics*, 50(2): 213-224.

Cassidy, N. (2009). Ground Penetrating Radar data processing, modelling and analysis. In H. M. Jol, *Ground Penetrating Radar: Theory and Applications* (pp. 141-176). Amsterdam, Netherland: Elsevier.

Cassidy, N. (2009). Theory and Applications, chapter Ground Penetrating Radar data processing, modelling, and analysis. In H. Jol, *Ground Penetrating Radar Theory and Applications* (pp. 141-176). Amsterdam, Netherland: Elsevier.

Cassidy, N. J. (2009). Ground Penetrating Radar Data Processing, Modelling and Analysis. In H. M. Jol, *Ground Penetrating Radar Theory and Applications* (pp. 141-176). Amsterdam, Netherland: Elsevier.

Cavinato, G., Carusi, C., Dall'Asta, M., Miccadei, E., & Piacentini, T. (2002). Sedimentary and tectonic evolution of Plio–Pleistocene alluvial and lacustrine deposits of Fucino Basin (central Italy). *Sedimentary Geology*, 148(1): 29-59.

Chen, Y. G., Chen, Y. W., Chen, W. S., Lee, K. J., Lee, L. S., Lu, S. T., . . . Lin, Y. N. (2009). Optical dating of a sedimentary sequence in a trenching site on the source dault of the 1999 Chi-Chi earthquake, Taiwan. *Quaternary International*, 199(1-2); 25-33.

Chen, Y. G., Chen, Y. W., Chen, W. S., Zhang, J. F., Zhao, H., Zhou, L. P., & Li, S. (2003). Preliminary results of long-term slip rates of 1999 earthquake fault by luminescence and radiocarbon dating. *Quaternary Science Reviews*, 22; 1213-1221.

Cheong, C. S., Hong, D. G., Lee, K. S., Kim, J. W., Choi, J. H., Murray, A., . . . Chang, H. (2003). Determination of slip rate by optical dating of fluvial deposits from the Wangsan Fault, SE Korea. *Quaternary Science Reviews*, 22; 1207-1211.

Christie, M., Tsoflias, G. P., Stockli, D. F., & Black, R. (2009). Assessing fault displacement and off-fault deformation in an extensional tectonic setting using 3-D ground-penetrating radar imaging. *Journal of Applied Geophysics*, 68; 9-16.

Cunningham, W. (2001). Cenozoic normal faulting and regional doming in the southern Hangay region, Central Mongolia: implications for the origin of the Baikal rift province. *Tectonophysics*, 331: 389-411.

Daëron, M., Klinger, Y., Tapponnier, P., Elias, A., Jacques, E., & Sursock, A. (2007). 12,000-year long record of 10 to 13 paleoearthquakes on the Yammouneh Fault, Levant fault system, Lebanon. *Bulletin of the Seismological Society of America*, 97(3): 749-771.

Daniels, D. J., Gunton, D. J., & Scott, H. F. (1988). Introduction to subsurface radar. *IEE Proceedings*, 135; 278-320.

Davis, J. L., & Annan, A. P. (1989). Ground penetrating radar for high resolution mapping of soil and rock stratigraphy. *Geophysical Prospecting*, 37: 531-551.

Demanet, D., Renardy, F., Vanneste, K., Jongmans, D., Camelbeeck, T., & Meghraoui, M. (2001). The use of geophysical prospecting for imaging active faults in the Roer Graben, Belgium. *Geophysics*, 66(1): 78-89.

Deparis, J., Garambois, S., & Hantz, D. (2007). On the potential of ground penetrating radar to help rock fall hazard assessment: a case study of a limestone slab, Gorges de la Bourne (French Alps). *Engineering Geology*, 94; 89-102.

Dorjsuren, B., Bujinlkham, B., Minjin, C., & Tsukada, K. (2006). Geological settings of the Ulaanbaatar terrane in the Hangay-Hentey zone of the Devonian accretionary complex, Central Asian orogenic belt. *International Geoscience Program*, IGCP-480.

Dugarmaa, T., Schlupp, A., Adija, M., Ankhtsetseg, D., Bayar, G., Munkhuu, D., . . . Baasanbat, T. (2003). Seismic map of Mongolia and site effect microzoning at the capital, Ulaanbaatar. *American Geophysical Union, Fall Meeting 2002, Abstract* (pp. #S71B-1100). American Geophysical Union.

Dugarmaa, T., Schlupp, A., Bayasgalan, A., Ulziibat, M., Odonbaatar, C., Ankhtsetseg, D., . . . Bayarsaikhan, C. (2006). *Earthquake hazard assessment of Ulaanbaatar, the capital city of Mongolia. Earthquake micro-zoning map.* Ulaanbaatar: RCAG, MAS.

Dujardin, J.-R. (2014). *Imagerie géoradar (GPR) en milieu hétérogène Application aux failles actives en Mongolie et aux dépôts pyroclastiques du Tungurahua (Equateur).* Strasbourg, France: IPGS, UMR7516, University of Strasbourg.

Dujardin, J.-R., & Bano, M. (2013). Topographic migration of GPR data: Examples from Chad and Mongolia. *Comptes Rendus Geoscience*, 345; 73-80.

Ferry, M., Meghraoui, M., Girard, J. F., Rockwell, T. K., Kozaci, O., Akyuz, S., & Barka, A. (2004). Ground-penetrating radar investigations along the North Anatolian fault near Izmit, Turkey. *Geological Society of America*, 32: 85-88.

Ferry, M., Schlupp, A., Ulziibat, M., Munschy, M., & Fleury, S. (2012). Tectonic Morphology of the Hustai Fault (Northern Mongolia). *EGU General Assembly 2012* (pp. 14: EGU2012-5803). Vienna, Austria: Geophysical Research Abstracts.

Ferry, M., Schlupp, A., Ulziibat, M., Munschy, M., Fleury, S., Baatarsuren, G., . . . Ankhtsetseg, D. (2010). Tectonic Morphology of the Hustai Fault (Northern Mongolia), A Source of Seismic Hazard for the city of Ulaanbaatar. *EGU General Assembly.* Vienna, Austria.

Fisher, S. C., Stewart, R. R., & Jol, H. M. (1992). Processing ground penetrating radar (GPR) data. *CREWES Research Report*, Vol. 4, pp. 11-1.

Gantulga, B. (2018). *Late Cenozoic landscape evolution in the Khangay Mountains, Mongolia.* Raleigh, North Carolina: North Carolina State University.

GEOSCANNERS. (2021). *GEOSCANNERS geophysical survey solutions*. From www.geoscanners.com

Girard, J. F. (2002). *Imagerie géoradar et modélisation des diffractions multiples.* Strasbourg: Université Louis Pasteur.

Grasmueck, M., Weger, R., & Horsemeyer, H. (2005). Full resolution 3D GPR imaging. *Geophysics*, 70(1); K12-K19.

Gross, R., Green, A. G., Holliger, K., Horstmeyer, H., & Baldwin, J. (2002). Shallow geometry and displacements on the San Andreas Fault near Point Arena based on trenching and 3D georadar surveying. *Geophysical Research Letters*, 29(20): 1973-1977.

Gross, R., Green, A. G., Horstmeyer, H., & Begg, J. H. (2004). Location and geometry of the Wellington Fault (New Zealand) defined by detailed three-dimensional georadar data. *Journal of Geophysical Research*, 109: B05401.

Guillemoteau, J., Bano, M., & Dujardin, J.-R. (2012). Influence of grain size, shape and compaction on georadar waves: examples of aeolian dunes. *Geophysical Journal International*, 190; 1455-1463.

Gurpinar, A. (2005). The importance of paleoseismology in seismic hazard studies for critical facilities. *Tectonophysics*, 408(1-4); 23-28.

Heincke, B., Green, A. G., van der Kruk, J., & Horstmeyer, H. (2005). Acquisition and processing strategies for 3D georadar surveying a region characterized by rugged topography. *Geophysics*, 70: K53-K61.

Huang, J., & Chen, W. P. (1986). Source mechanisms of the Mogod earthquake sequence of 1967 and the event of 1974 July 4 in Mongolia. *Geophysics Journal International*, 84: 361-379.

Imaev, V. S., Smekalin, O. P., Strom, A. L., Chipizubov, A. V., & Syas'ko, A. A. (2012). Seismic-hazard assessment for Ulaanbaatar (Mongolia) on the basis of seismogeological studies. *Russian Geology and Geophysics*, 53: 906–915.

Inc, S. &. (2020). From Sensors & Software Inc Web site: https://www.sensoft.ca/

Inc., S. &. (2001). *EKKO-for-DVL pulseEKKO 100 User's Guide Version 1.0.* Mississauga, ON L4W 3R7, Canada: Sensors & Software Inc. .

Jackson, D., & Kagan, Y. (2006). The 2004 Parkfield earthquake, the 1985 prediction, and characteristic earthquakes: Lessons for the future. *Bulletin of the Seismological Society of America*, 96(4B): 397-409.

James, P. M., & Alan, R. N. (2009). Introduction to Paleoseismology. In P. M. James, *Paleoseismology* (pp. 1; 1-27). Elsevier Inc.

Jan, V. S. (2015). *GPS for Land Surveyors.* CRC Press.

Jewell, C., & Bristow, C. (2004). GPR studies in the Piano di Pezza area of the Ovindoli-Pezza Fault, Central Apennines, Italy: extending paleoseismic trench investigations

with high resolution GPR profiling. *Ground Penetrating Radar, 2004. Proceedings of the Tenth International Conference on* (pp. 21-24). Near Surface Geophysics.

Jol, H. M. (1995). Ground-penetrating radar antennae frequencies and transmitter powers compared for penetration depth, resolution and reflection continuity. *Geophysical Prospecting*, 43: 693-709.

Jol, H. M. (2009). *Ground Penetrating Radar: Theory and Applications.* Amsterdam, Netherland: Elsevier.

Jol, H. M., & Bristow, C. S. (2003). GPR in sediments: advice on data collection, basic processing and interpretation, a good practice guide. . *Geological Society, London, Special Publications*, 211: 9-27.

Kelty, T. K., Yin, A., Dash, B., Gehrels, G., Bei, X., Rice, K., & Katsuk, O. (2005). Detrital-zircon geochronology of the Hangay-Hentey basin: implications for the tectonics of the Mongol-Okhotsk Ocean, Mongolia. *Geological Society of America Abstracts with Programs*, 37; 7, 56.

Khil'ko, S. D., Kurushin, R. A., Kochetkov, V. M., Baljinnyam, I., & Monkhoo, D. (1985). Strong earthquakes, paleoseismological and macroseismic data, in Earthquakes and the Bases of Seismogenic Zoning of Mongolia. *Nauka Trans*, 41: 19-83.

Kim, J., Cho, S., & Yi, M. (2007). Removal of ringing noise in GPR data by signal processing. *Geosciences Journal*, 11(1): 75-81.

Kravchinsky, V. A., Cogné, J. P., Harbert, W. P., & Kuzmin, M. I. (2002). Evolution of the Mongol-Okhotsk Ocean as constrained by new palaeomagnetic data from the Mongol-Okhotsk suture zone, Siberia. *Geophysical Journal International*, 148; 34-57.

Lahmann, F., & Green, A. G. (2000). Topographic migration of georadar data: implications for acquisition and processing. *Geophysics*, 65(3): 836-848.

Lehmann, F., & Green, A. G. (1999). Semi automated georadar data acquisition in three dimensions. *Geophysics*, 64: 719-731.

Lehmann, F., & Green, A. G. (2000). Topographic migration of georadar data: implications for acquisition and processing. *Geophysics*, 65(3): 836-848.

Lehmann, F., Klostermann, J., & Pelzing, R. (2001). Paleoseismological investigations at the Rurrand Fault, Lower Rhine Embayment. *Netherlands Journal of Geosciences*, 80(3/4): 139-154.

Lehmann, J., Schulmann, K., Lexa, O., Corsini, M., Kröner, A., Štipská, P., & al, e. (2010). Structural constraints on the evolution of the Central Asian Orogenic Belt in SW Mongolia. *American Journal of Science*, 310; 575-628.

Li, J. (2006). Permian geodynamic setting of northeast China and adjacent regions: closure of the Paleo-Asian Ocean and subduction of the Paleo-Pacific plate. *Journal of Asian Earth Sciences*, 26; 207-224.

Liberty, L., Hemphill-Haley, M., & Madin, I. (2003). The Portland Hills Fault : uncovering a hidden fault in Portland, Oregon using high-resolution geophysical methods. *Tectonophysics*, 368(1): 89-103.

Liu, J., Guan, P., Shen, X., Xu, Y., Shen, J., Jing, F., & Hong, S. (2010). Paleoearthquake studies along the Nalinlaka Fault of the Late Pleistocene in Lhasa, Tibet. *Earthquake Research in China*, 24(4); 467-477.

Liu-Zeng, J., Klinger, Y., Sieh, K., Rubin, C., & Seitz, G. (2006). Serial ruptures of the San Andreas fault, Carrizo Plain, California, revealed by three dimentional excavations. *Journal of Geophysical Research*, 111(B2): B02306.

Lu, Q., Sato, M., Liu, C., Zeng, Z., & Feng, X. (2010). Characterization of the shallow structures of the Deren Fault by ground penetrating radar. *2010 IEEE International Geoscience and Remote Sensing Symposium.* Honolulu, Hawaii, USA: IEEE Geoscience and Remote Sensing Society.

Malik, J. N., Sahoo, A. K., & Shah, A. A. (2007). Ground penetrating radar investigation along Pinjore Garden Fault: implication toward identification of shallow sub-surface deformation along active fault, NW Himalaya. *Current Science*, 93(10); 1427-1442.

Malik, J., Sahoo, A., Shah, A., Shinde, D., Juyal, N., & Singhyi, A. (2010). Paleoseismic evidence from trench investigation along hajipur fault, himalayan frontal thrust, nw himalaya : Implications of the faulting pattern on landscape evolution and seismic hazard. *Journal of Structural Geology*, 32(3): 350-361.

Manighetti, I., Campillo, M., Bouley, S., & Cotton, F. (2007). Earthquake scaling, fault segmentation and structural maturity. *Earth and Planetary Science Letters*, 253: 429-438.

Manighetti, I., Campillo, M., Sammis, C., Mai, M., & King, G. (2005). Evidence for self-similar, triangular slip disributions on earthquakes: implications on earthquake and fault mechanics. *Journal of Geophysical Research*, 110: B05302.

Marco, S., Rockwell, T., Heimann, A., Frieslander, U., & Agnon, A. (2005). Late Holocene activity of the Dead Sea Transform revealed in 3D palaeoseismic trenches on the Jordan Gorge segment. *Earth and Planetary Science Letters*, 234(1): 189-205.

Marco, S., Stein, M., Agnon, A., & Ron, H. (1996). Long-term earthquake clustering: a 50,000-year paleoseismic record in the Dead Sea Graben. *Journal of Geophysical Research*, 101(B3): 6179-6191.

Marinière, J. (2013). *Analyse géomorphologique (GPS) et GPR pour l'étude des failles actives en Mongolie.* Strasbourg, France: IPGS, EOST, University of Strasbourg.

McCalpin, J. (2009). *Paleoseismology, 2nd edition.* Imprint: Academic Press.

McClymont, A. F., Green, A. G., Kaiser, A., Horstmeyer, H., & Langridge, R. M. (2010). Shallow fault segmentation of the Alpine fault zone, New Zealand, revealed from 2- and 3-D GPR surveying. *Journal of Applied Geophysics*, 70(4); 343-354.

McClymont, A. F., Villamor, P., & Green, A. G. (2009a). Assessing the contribution of off-fault deformation to slip-rate estimates within the Taupo Rift, New Zealand, using 3-D ground penetrating radar surveying and trenching. *Terra Nova*, 21(6): 446-451.

McNeilan, T., Rockwell, T., & Resnick, G. (1996). Style and rate of Holocene slip, Palos Verdes fault, southern California. *Journal of Geophysical Research*, 101(B4): 8317-8334.

Mineral Resources Authority of Mongolia. (1998). *Tectonic Map of Mongolia at a scale of 1:1,000,000.* Ulaanbaatar, Mongolia: Mongolian Academy of Sciences, Institute of Geology and Mineral Resources.

Munkhsaikhan, A. (2016). *Seismic activity near Ulaanbaatar: Implication for seismic hazard assessment.* Strasbourg: IPGS, UMR-716, Doctoral School of Earth and Environmental Sciences - ED 413.

Murray, A. S., & Wintle, A. G. (2000). Luminescence dating of quartz using an improved single-aliquot regenerative-dose protocol. *Radiation Measurements*, 32(1); 57-73.

Natsag-YÏm, L., Baljinnyam, I., & Monhoo, D. (1971). Mongolian earthquakes, in Seismic Regionalization of Ulan Bator. *Nauka*, 54-82.

Neal, A. (2004). Ground-penetrating radar and its use in sedimentology: principles, problems and progress. *Earth Science Reviews*, 66; 261-330.

Nguyen, F., Garambois, S., Chardon, D., Jongmans, D., Bellier, O., & Hermitte, D. (2003). Slow active fault detection and imaging using multiple geophysical methods : the Trevaresse thrust (Provence, France). *Journal of Applied Geophysics*, 338-353.

Nogueira, F. C., Bezerra, F. H., & Fuck, R. A. (2011). Quaternary fault kinematics and chronology in intraplate northeastern Brazil. *Lournal of Geodynamics*, 49(2); 79-91.

Noon, D., Stickley, G., & Longstaff, D. (1998). A frequency-independent characterisation of GPR penetration and resolution performance. *Journal of Applied Geophysics*, 40(1): 127-137.

Noriega, G., Arrowsmith, J., Grant, L., & Young, J. (2006). Stream channel offset and Late Holocene slip rate of the San Andreas fault at the Van Matre Ranch site, Carrizo Plain, California. *Bulletin of the Seismological Society of America*, 96(1): 33-47.

Nyambayar, T., Bano, M., Schlupp, A., Ulziibat, M., & Tseedulam, K. (2018). The results of the work determined the type of the active fault by GPR sensing. *Geophysics and Astronomy*, 5: 65.

Nyambayar, T., Bano, M., Schlupp, A., Ulziibat, M., Battogtokh, D., & Byambakhorol, B. (Apr 2018). Studying active faults by combing GPR images with morphotectonic and trenching results. Ulaanbaatar, Mongolia. *EAGE-HAGI 1st Asia Pacific Meeting on Near Surface Geoscience and Engineering* (pp. Volume 2018, p.1 - 5). Yogyakarta, Indonesia: European Association of Geoscientists & Engineers.

Odonbaatar, C., Ulziibat, M., Bayasgalan, A., Battogtokh, D., Baatarsuren, G., & Nyambayar, T. (2017). *Earthquake hazard assessment and micro-zoning survey: Bayankhongor soum of the Bayankhongor province center.* Ulaanbaatar: IAG, MAS.

Palumbo, L., Benedetti, L., Bourles, D., Cinque, A., & Finkel, R. C. (2004). Slip history of the Magnola fault (Apennines, Central Italy) from 36CI surface exposure dating: evidence for strong earthquakes over the Holocene. *Earth and Planetary Science Letters*, 225(1-2): 163-176.

Pollitz, F., Vergnolle, M., & Calais, E. (2003). Fault interaction and stress triggering of twentieth century earthquakes in Mongolia. *Journal of Geophysical Research*, 108; 16-1 to 16-14.

Prentice, C., Crosby, C., Harding, D., Haugerud, R., Merrittc, D., Gardner, T., . . . Baldwin, J. (2003). Northern California LiDAR data; Atool for mapping the San Andreas fault and Pleistocene marine terraces in heavily vegetated terrain. *AGU Fall Meeting Abstracts*, (pp. Volume 1, page 06).

Prescott, J. R., & Hutton, J. T. (1994). Cosmic-ray contributions to dose-rates for luminescence and ESR dating: Large depth and long-term time variations. *Radiation Measurements*, 23(2-3); 497-500.

Reiter, L. (1995). Paleoseismology-A user's perspective. In S. L, B. S. D, & Eds, *Perspective in Paleoseismology* (pp. 6; 3-6). Association of Engineering Geology Special Publication.

Reynolds, J. M. (2011). *An Introduction to Applied and Environmental Geophysics, 2nd Edition.* Wiley.

Rockwell, T., Lindvall, S., Herzberg, M., Murbach, T., Dawson, D., & Berger, G. (2001). Paleoseismology of the Johnson Valley, Kickapoo, and Homestead Valley faults : clustering of earthquakes in eastern California shear zone. *Bulletin of the Seismological Society of America*, 90: 1200-1236.

Rockwell, T., Ragona, D., Ucarkus, G., Ferry, M., Meltzner, A. J., Klinger, Y., . . . Akbalik, B. (2009c). *Palaeoseismology: Historical and Prehistorical Records of Earthquake Ground Effects for Seismic Hazard Assessment.* London: The Geological Society, Special Publications.

Rubin, C. M., & Sieh, K. (1997). Long dormancy, low slip rate, and similar slip-per-event for the Emerson fault, eastern California shear zone. *Journal of Geophysical Research*, 102(B7): 15319-15333.

Salvi, S., Cinti, F. R., Colini, L., Addezio, G., Doumaz, F., & Pettinelli, E. (2003). Investigation of the active Celano–L'Aquila fault system, Abruzzi (central Apennines, Italy) with combined ground-penetrating radar and palaeoseismic trenching. *Geophysical Journal International*, 155(3): 805-818.

Schlagenhauf, A., Gaudemer, Y., Benedetti, L., Manighetti, I., Palumbo, L., Schimmelpfennig, I., . . . Pou, K. (2010). Using in situ Chlorine-36 cosmonuclide to recover past earthquake histories on limestone normal fault scarps: a reappraisal of methodology and interpretations. *Geophysical Journal International*, 182: 36-72.

Schlagenhauf, A., Manighetti, I., Benedetti, L., Gaudemer, Y., Finkel, R., Malaveille, J., & Pou, K. (2011). Earthquake supercycles in Central Italy, inferred from 36CI exposure dating. *Earth and Planetary Science Letters*, 307(3): 487-500.

Schlupp, A., Ferry, M., Ulziibat, M., Baatarsuren, G., Munkhsaikhan, A., Bano, M., . . . Demberel, S. (2012). Investigation of active faults near Ulaanbaataar. Implication for seismic hazard assesment. *The 9th General Assembly of Asian Seismological Commission* (pp. 265-267). Ulaanbaatar, Mongolia: International scientific cooperation for prevention and mitigation seismic disaster.

Schwartz, D. P., & Coppersmith, K. J. (1984). Fault behavior and characteristic earthquakes: Examples from the Wasatch and San Andreas Fault Zones. *Journal of Geophysical Research*, 89(B7): 5681-5698.

Shimazaki, K., & Nakata, T. (1980). Time-predictable recurrence model for large earthquakes. *Geophysical Research Letters*, 7(4): 279-282.

Sieh, K. (1981). A Review of Geological Evidence for Recurrence Times of Large Earthquakes. In S. David, & R. Paul, *An International Review* (pp. 181-207). American Geophysical Union.

Sieh, K. (1996). The repetition of large earthquake ruptures. *Proceedings of the National Academy of Sciences*, 93(9): 3764-3771.

Sieh, K., Natawidjaja, D., Meltzner, A., Shen, C., Cheng, H., Li, K., . . . Edwards, R. (2008). Earthquake supercycles inferred from sea-level changes recorded in the corals of west Sumatra. *Science*, 322(5908): 1674-1678.

Slater, L., & Niemi, T. (2003). Ground-penetrating radar investigation of active faults along the Dead Sea Transform and implications for seismic hazards within the city of Aqaba, Jordan. *Tectonophysics*, 368(1): 33-50.

Smekalin, O. P., Chipizubov, A. V., & Imaev, V. S. (2015). Paleoseismogenic dislocations in the Upper Kerulen basin (southern Henteyn-Daurian mega-arch). *Russian Geology and Geophysics*, 56: 1780–1790.

Smekalin, O. P., Chipizubov, A. V., & Imaev, V. S. (2016). Seismogeology of Verkhnekerulen basin (Khentei, Northern Mongolia). *Geodynamics & Tectonophysics*, 7: 39-57.

Smith, D., & Jol, H. (1995). Ground penetrating radar : antenna frequencies and maximum probable depths of penetration in Quaternary sediments. *Journal of Applied Geophysics*, 33(1): 93-100.

Sperl, C. (1999). *Determination of spatial and temporal variations of soil water content in an agro-ecosystem with ground penetrating radar (in German).* Munich, Germany: Technische Universitat Munchen.

Steelman, C., & Endres, A. (2011). Comparison of petrophysical relationships for soil moisture estimation using GPR ground waves. *Vadose Zone Journal*, 10(1): 270-285.

Stolt, R. H. (1978). Migration by fourier transform. *Geophysics*, 43(1): 23-48.

Streich, R., van der Kruk, J., & Green, A. G. (2007). Vector-migration of standard copolarized 3D GPR data. *Geophysics*, 72: J65-J75.

Sun, J., & Young, R. A. (1995). Recognizing surface scattering in ground-penetrating radar data. *Geophysics*, 60(5): 1378-1385.

Tapponnier, P., & Molnar, P. (1979). Active faulting and cenozoic tectonics of the Tien Shan, Mongolia, and Baykal Regions. *Journal of Geophysical Research*, 84: 3425-3459.

Tapponnier, P., Peltzer, G., Le Dain, A. Y., Armijo, R., & Cobbold, P. (1982). Propagating extrusion tectonics in Asia; new insights from simple experiments with plasticine. *Geology*, 10; 611-616.

Tapponnier, P., Zhiqin, X., Roger, F., Meyer, B., Arnaud, N., Wittlinger, G., & Jingsui, Y. (2001a). Oblique stepwise rise and growth of the Tibet Plateau. *Science* , 294(5547): 1671-1677.

Telford, W. M., Geldart, L. P., & Sheriff, R. E. (1990). *Applied Geophysics second edition.* Cambridge University Press.

Tomurtogoo, O., & al, e. (2002). *A brief explanatory note to the Tectonic Map of Mongolia at a scale of 1:1,000,000.* Ulaanbaatar, Mongolia: Mongolian Academy of Sciences, Institute of Geology and Mineral Resources.

University of SYDNEY. (2000). From University of Sydney Web site: http://www.geosci.usyd.edu.au/users/prey/Teaching/Geol-3101/EReport03/GroupB/Report1/structures.html

Van Dam, R. L. (2012). Landform characterization using geophysics - Recent advances, applications and emerging tools. *Geomorphology*, 137(1); 57-73.

Vanneste, K., Radulov, A., De Martini, P., Nikolov, G., Petermans, T., Verbeeck, K., . . . Shanov, S. (2006). Paleoseismologic investigation of the fault rupture of the 14 April, 1928 Chirpan earthquake (M 6.8), southern Bulgaria. *Journal of Geophysical Research*, 111(B1): B01303.

Vanneste, K., Verbeeck, K., & Petermans, T. (2008). Pseudo-3D imaging of a low-slip-rate, active normal fault using shallow geophysical methods : The Geleen fault in the Belgian Maas River valley. *Geophysics*, 73(1): B1-B9.

Vergne, J., Wittlinger, G., Hui, Q., Tapponier, P., Poupinet, G., Mei, J., . . . Paul, A. (2002). Seismic evidence for stepwise thickening of the crust across the NE Tibetan plateau. *Earth and Planetary Science Letters*, 203(1): 25-33.

Wang, M., & Shen, Z.-K. (2020). Present-Day Crustal Deformation of Continental China Derived From GPS and Its Tectonic Implications. *Journal of Geophysical Research: Solid Earth*, 125, e2019JB018774.

Weldon, R., Scharer, K., Fumal, T., & Biasi, G. (2004). Wrightwood and the earthquake cycle: What a long recurrence record tell us about how faults work. *GSA Today*, 14(9): 4-10.

Wesnousky, S., Prentice, C., & Sieh, K. (1991). An offset Holocene stream channel and the rate of slip along the northern reach of the San Jacinto fault zone, San Bernardino Valley, California. *Geological Society of America Bulletin*, 103(5): 700-709.

Wides, M. B. (1973). How thin is a thin bed? *Geophysics*, 38; 1176-1180.

Wikipedia. (2001). From https://mn.wikipedia.org/wiki

Wintle, A. G., & Murray, A. S. (2006). A review of quartz optically stimulated luminescence characteristics and their relevance in single-aliquot regeneration dating protocols. *Radiation Measurement*, 41(4); 369-391.

Wittlinger, G., Tapponnier, P., Poupinet, G., Mei, J., Danian, S., Herquel, G., & Mas-son, F. (1998). Tomographic evidence for localized lithospheric shear along the Altyn Tagh fault. *Science*, 282(5386): 74-76.

Yeats, R., Sieh, K., & Allen, C. (1997). *The Geology of Erthquakes.* New York: Oxford University Press.

Yetton, M., & Nobes, D. C. (1998a). Recent vertical offset and near-surface structure of the Alpine Fault in Westland, New Zealand, from ground penetrating radar profiling. *New Zealand Journal of Geology and Geophysics*, 41(4): 485-492.

Yilmaz, O. (1987). *Seismic data processing.* V.2; 526p: Society of Exploration of Geophysics-Investigations in Geophysics.

Yilmaz, O., & Doherty, S. M. (2001). *Seismic data analysis : processing, inversion, and interpretation of seismic data.* Tulsa, OK: Society of Exploration Geophysics.

Zachariasen, J., Sieh, K., Taylor, F., Edwards, R., & Hantoro, W. (1999). Submergence and uplift associated with the giant 1833 Sumatran subduction earthquake: Evidence from coral microatolls. *Journal of Geophysical Research*, 104(B1): 895-919.

Zeng, H. (2009). How thin is a thin bed? An alternative perspective. *Geophysics*, 28; 1192-1197.

Ziegler, A. M., Rees, P. M., Rowley, D. B., Bekker, A., Li, Q., & Hulver, M. L. (1996). Mesozoic assembly of Asia: Constrains from fossil floras, tectonics, and paleomagnetism, In An Yin and Harrison, M. (eds.). *The tectonic Evolution of Asia*, 371-400.

Zorin, Y. A. (1999). , Geodynamic of the western part of the Mongolia-Okhotsk collisional belt, Trans-Baikal region (Russia) and Mongolia. *Tectonophyiscs*, 306; 33-56.

Zorin, Y. A., Turutanov, E. K., Kozhevnikov, V. M., Rasskazov, S. V., & Ivanov, A. V. (2005). Cenozoic upper mantle plumes in east Siberia and central Mongolia and subduction of the Pacific Plate. *Doklady Earth Sciences*, 409; 723-726.

Appendixes

Appendix 1: Seismicity of Mongolia (1900-2000)

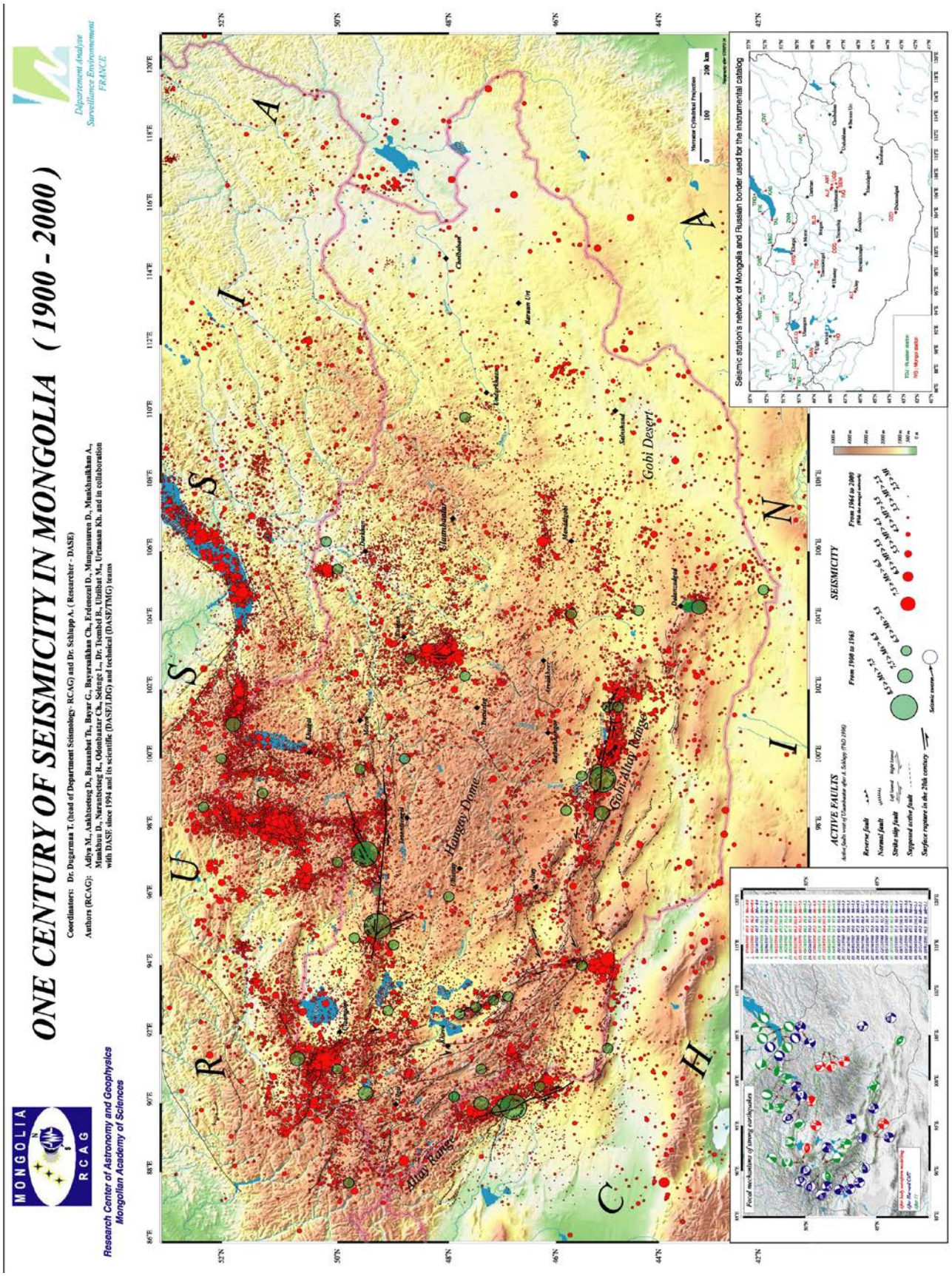

Appendix 2: Terrane map of the Mongolia

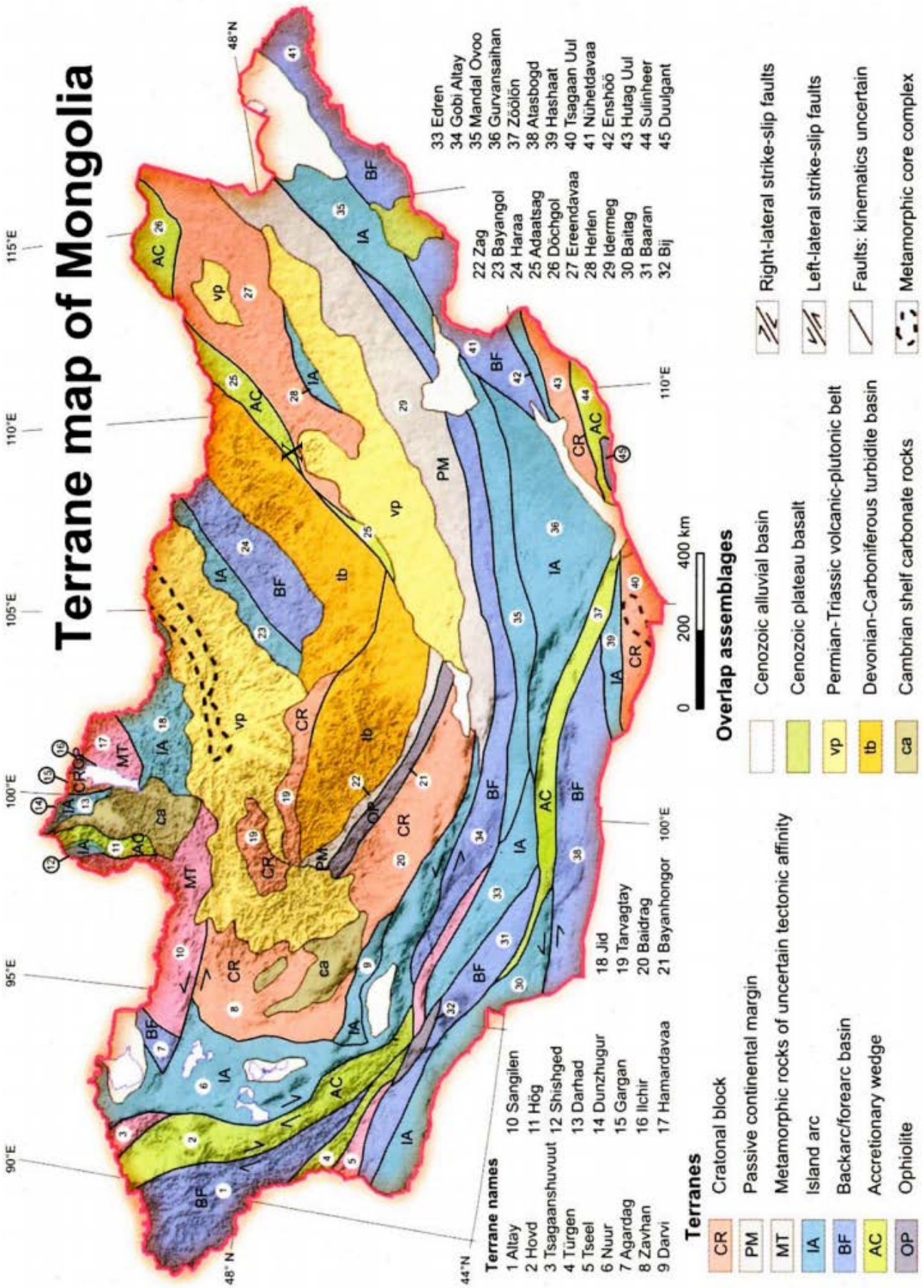

Appendix 3: Tectonic zonation of the territory of Mongolia

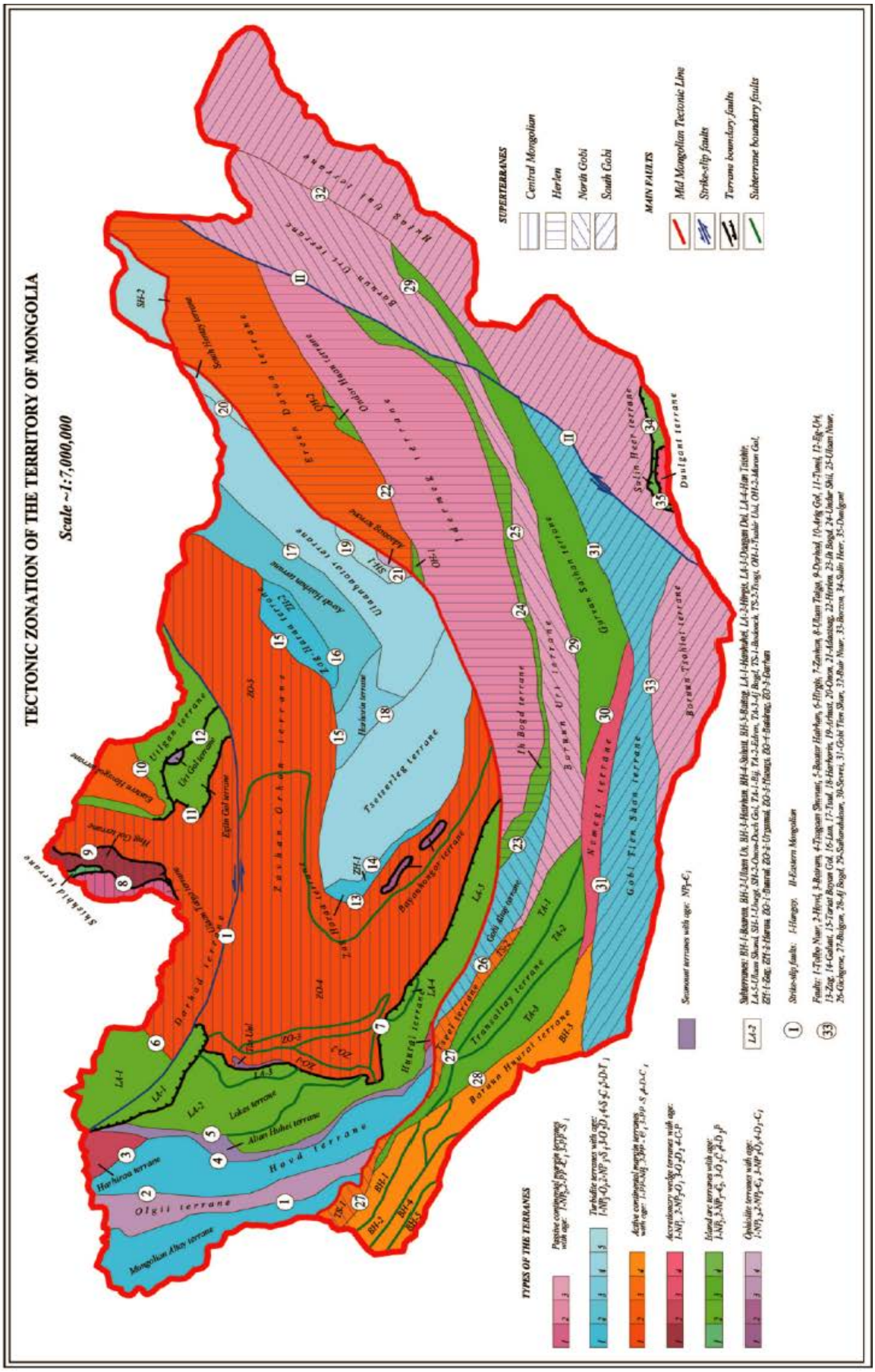

Université de Strasbourg

NYAMBAYAR
Tsend-Ayush

Caractérisation des Failles Actives en 2D et 3D par la technique d'Imagerie géoradar et Interprétations des Résultats

L'objective de cette thèse de doctorat est de déterminer et d'expliquer les caractéristiques et les paramètres des failles actives à l'aide de technologies de pointe modernes, telles que les techniques d'imagerie 2D et 3D du géoradar. Cette recherche a été réalisée à l'aide d'antennes 500, 25 et RTA 50 MHz. Les techniques d'imagerie géoradar 2D et 3D ont été combinées avec les résultats d'analyse d'images satellites, de levés géologiques quaternaires et de sondages paléosismologiques de tranchées pour la datation.

La structure des failles actives avec effet de compression est montrée par les failles actives de Mogod et Mungunmorit, la structure de l'effet d'extension est présentée par la faille active de Bayankhongor, et la structure de l'effet de décrochement est interprétée par les exemples des failles actives d'Avdar et d'Emeelt.

La faille de Songino est située entre les failles paléosismiques de Hustai et d'Emeelt situées à l'ouest d'Ulaanbaatar. Une étude GPR détaillée de cette faille a identifié trois types différents de structures et de mouvements observés en surface. Le mouvement principal de la faille de Songino est un décrochement latéral dextre du sud-est au nord-ouest, et ce mouvement s'est avéré être causé par la compression entre les failles actives de Hustai et d'Emeelt. Son chevauchement (compression) et sa structure normale (extension) des deux côtés sont dues à la structure en courbure de cette faille.

La datation des échantillons des paléo chenaux montrent que la faille Emeelt date, en moyenne, de 10 000 ans, la faille de Hustai environ de 900 ans et la faille Songino environ de 6 000 ans pour les derniers événements.

Mots-clés : Géoradar, faille active, Mongolie, paléoséismologie

The purpose of this doctoral dissertation is to determine and explain the characteristics and parameters of active faults using modern advanced technology, such as 2D and 3D imaging techniques of GPR. This research was performed using 500, 250 and RTA 50 MHz antennas. The GPR 2D and 3D imaging techniques were combined with the results of satellite image analysis, quaternary geological survey, and palaeoseismological trench survey for dating.

The structure of active faults with compression effect is shown by the example of Mogod and Mungunmorit active faults, the structure of tensional effect is presented by Bayankhongor active fault, and the structure of strike slip effect is interpreted by the examples of Avdar and Emeelt active faults. In addition, the results of the 3D GPR imaging are shown by depth slices on the example of the Emeelt active fault.

The Songino Fault is located between the Hustai and Emeelt paleoseismic faults located west of Ulaanbaatar. A detailed GPR study of this fault identified three different types of surface fractured structures and movements. Songino fault have a basic left lateral strike slip movement from southeast to northwest, and this movement has been found to be caused by compression between the Hustai and Emeelt active faults and and its thrust and normal structure on both sides are due to the curvature structure of the that fault

The paleochannel dating samples show that the Emeelt fault is on average 10,000 years, the Hustai fault is about 900 years, and the Songino fault is about 6,000 years for last event.

Key words: GPR, Active faults, Mongolia, paleoseismology